AD/A-003 005

SPUTTERED THIN FILM RESEARCH

A. J. Shuskus, et al

United Aircraft Research Laboratories

Prepared for:

Office of Naval Research
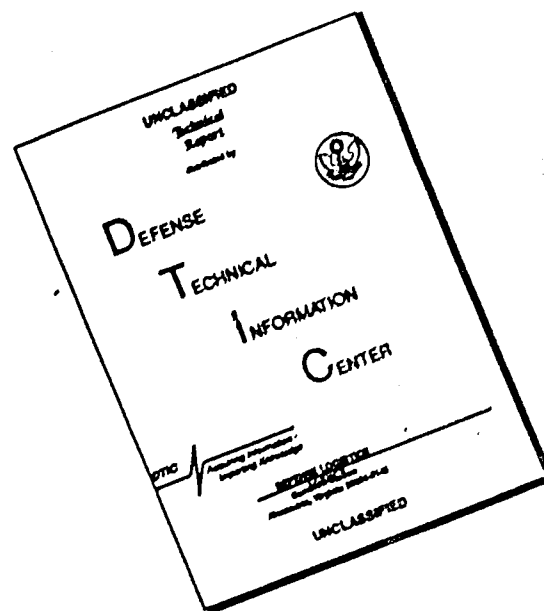Advanced Research Projects Agency

November 1974

DISCLAIMER NOTICE

THIS DOCUMENT IS BEST QUALITY AVAILABLE. THE COPY FURNISHED TO DTIC CONTAINED A SIGNIFICANT NUMBER OF PAGES WHICH DO NOT REPRODUCE LEGIBLY.

REPORT DOCUMENTATION PAGE		READ INSTRUCTIONS BEFORE COMPLETING FORM
1. REPORT NUMBER N921337-15	2. GOVT ACCESSION NO.	3. RECIPIENT'S CATALOG NUMBER AD/A·003005
4. TITLE (and Subtitle) Sputtered Thin Film Research		5. TYPE OF REPORT & PERIOD COVERED Semi-annual Report (Summary) For the period of 15 April, 1972 to 30 Sept. 1974.
		6. PERFORMING ORG. REPORT NUMBER
7. AUTHOR(s) A. J. Shuskus, D. J. Quinn, E. L. Paradis, J. M. Berak, D. E. Cullen, T. M. Reeder		8. CONTRACT OR GRANT NUMBER(s) N00014-72-C-0415
9. PERFORMING ORGANIZATION NAME AND ADDRESS United Aircraft Research Laboratories East Hartford, Connecticut 06108		10. PROGRAM ELEMENT, PROJECT, TASK AREA & WORK UNIT NUMBERS ARPA Order #2173
11. CONTROLLING OFFICE NAME AND ADDRESS Advanced Research Projects Agency 1400 Wilson Boulevard Arlington, Virginia 22209		12. REPORT DATE November 1974
		13. NUMBER OF PAGES 211
14. MONITORING AGENCY NAME & ADDRESS(if different from Controlling Office) Department of the Navy Office of Naval Research 800 North Quincy Street Arlington, Virginia 22217		15. SECURITY CLASS. (of this report) Unclassified
		15a. DECLASSIFICATION/DOWNGRADING SCHEDULE

16. DISTRIBUTION STATEMENT (of this Report)

17. DISTRIBUTION STATEMENT (of the abstract entered in Block 20, if different from Report)

18. SUPPLEMENTARY NOTES

19. KEY WORDS (Continue on reverse side if necessary and identify by block number)

Reactive Sputtering, Heteroepitaxy, Thin Films Single Crystal Zinc Oxide, Titanium Dioxide, Aluminum Nitride, Gallium Nitride, Strontium Titanate, Gallium Arsenide, Gallium Aluminum Arsenide Alloys, Tungsten Oxide, Neodymium Ultraphosphate, Optical Waveguiding, Surface Acoustic Wave

20. ABSTRACT (Continue on reverse side if necessary and identify by block number)

The reactive rf sputtering technique was applied to the preparation of a wide variety of materials. The results of a two and one half year investigation are summarized. Single crystal films of ZnO, TiO_2, WO_3 AlN and GaN were grown on one or more of the insulating crystalline substrates of Al_2O_3, $MgAl_2O_4$, SiC and $LiNbO_3$. Data on the deposition parameters, structure and optical waveguiding characteristics of the heteroepitaxial structures are

(20)

presented. Surface acoustic wave delay lines were fabricated to evaluate the piezoelectric properties of the ZnO and AlN films grown.

Reactive sputtering using sublimed arsenic as the sputtering gas inside a heated vacuum chamber was used to grow epitaxial films of GaAs. The controlled growth of single crystal alloys of $Ga_{1-x}Al_xAs$ at low temperatures was also demonstrated. Structural, optical and electrical characteristics of these films are presented.

Conditions were determined for the deposition of amorphous neodymium ultraphosphate films. Low loss optical wave guide structures were fabricated. Flouresence lifetime data is presented for sputtered neodymium ultraphosphate and lanthanam diluted neodymium ultraphosphate films.

Charge storage characteristics of MIS structures were investigated. These employed a composite insulator formed by sputtering 1000$\overset{\circ}{A}$ of strontium titanate over a 20$\overset{\circ}{A}$ thick thermally grown silicon dioxide layer on silicon. Data is presented on charge retentivity and the flat band voltage shifts obtained as a function of voltage pulse amplitude and duration.

UNITED AIRCRAFT CORPORATION
RESEARCH LABORATORIES
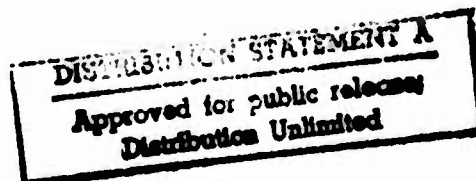East Hartford, Connecticut

N921337-15

Fifth Semi-Annual Report Under Contract N00014-72-C-0415
Summary of Work Performed for the Period
15 April 1972 to 30 September 1974

Report N921337-15

Interim Technical Report Under Contract N00014-72-C-0415
Summary of Work Performed
For The Period 15 April 1972 to 30 September 1974

Sputtered Thin Film Research

ARPA Order No. 2173, Amendment No. 2, Project Code 3D10

TABLE OF CONTENTS

TABLE OF CONTENTS
(con'd)

TABLE OF CONTENTS
(con't)

TABLE OF CONTENTS
(con'd)

N921337-15

FIGURE CAPTIONS

3-1. ZnO rf sputtering facility (RL-72-107-B).

3-2. Schematic of the major internal components of the sputtering system.

3-3. Sensor temperatures rise as a function of time after start up recorded for a quadrupole magnetic field configuration.

3-4. Effect of magnet coil pair separation distance on substrate temperature profile for a quadrupole field configuration.

3-5. Effect of magnet coil pair midplane location on substrate temperature profile for a quadrupole field configuration.

3-6. Effect of magnet strength on substrate temperature profile for a quadrupole field configuration.

3-7. Comparison of deposition rate and substrate temperature profiles for several quadrupole field configurations.

3-8. Effect of magnet coil pair separation distance on substrate temperature profile for a longitudinal field.

3-9. Effect of magnet coil pair midplane location on substrate temperature profile for a longitudinal magnetic field configuration.

3-10. Effect of magnet field strength on substrate temperature profile for a longitudinal magnetic field configuration.

3-11. Comparison of deposition rate and substrate temperature profile for a longitudinal field configuration.

3-12. Electron micrograph of ZnO film sputtered on ($1\bar{1}02$) oriented sapphire substrate for two values of a longitudinal magnetic field. The upper film (A) was deposited with a current of 45 amps dc in the coils and the lower film (B) was deposited with 425 amp dc in the coils. The film deposited at the higher field is much smoother.

3-13. Electron micrograph of TiO_2 films sputtered on (0001) oriented sapphire substrate. The upper film (A) was deposited with no magnetic field, the lower film (B) was deposited in the presence of a longitudinal magnetic field. The texture of the film sputtered in the presence of the longitudinal field is clearly superior.

APPENDIX   I

AI-1.   Electron microscope surface replication of as received sapphire substrate.

APPENDIX II

AII-1.   Repeatability of silicon substrate temperature.

AII-2.   Thermal expansion of single crystal sapphire.

AII-3.   Sapphire substrate temperature as a function of heater temperature.

APPENDIX III

AIII-1.   Apparatus for studying waveguiding in thin films.

AIII-2.   Sample table and attenuation measuring apparatus.

AIII-3.   Experimental setup for optical attenuation measurements.

LIST OF TABLES

1.0 SUMMARY

As a consequence of the change in program objectives in the follow-on phase of the present contract it was decided to make this report a summary of the results achieved over the period April 15, 1972 through September 30, 1974. The purpose of this program was to establish the feasibility of employing reactive rf sputtering for synthesis and deposition of selected semiconductor and high permittivity insulating films suitable for integrated optics or electronic applications. A secondary objective of the program was to fabricate devices, where feasible, and to assess the potential of the mateiral prepared in selected device applications. A large fraction of the effort encompassed the preparation and evaluation of heteroepitaxial structures of selected semiconductors and insulators grown on insulating crystalline substrates. Epitaxial films of ZnO, AlN, GaN, GaAs, $Ga_{1-x}Al_xAs$, InSb, TiO_2 and WO_3 were successfully grown by reactive sputtering on one or more of the following substrates of sapphire, spinel, gallium arsenide and silicon carbide and lithium niobate. We believe that this work constitutes the first successful effort to grow single crystal films of these materials by reactive sputtering.

The relative merits of ammonia and nitrogen were compared for the growth of AlN and GaN films. Ammonia proved to be preferred over nitrogen since epitaxy could be achieved at lower substrate deposition temperatures. The effect of magnetic field on surface finish was investigated. It was demonstrated the the surface finish could be greatly improved by deposition of films in a nearly axial field configuration which had a strong longitudinal component and a weak radial component in the vicinity of the target. This configuration reduces the bombardment of the substrate by secondary electrons which has an adverse effect on film structure and texture.

A number of advantages surfaced for films grown by reactive sputtering compared to those prepared by chemical vapor deposition (CVD) techniques. High quality ZnO films could be grown at deposition temperatures of $600^{\circ}C$ versus $850^{\circ}C$ for CVD films. No lithium diffusion was required to enhance the resistivity of the films grown by sputtering nor surface polishing required to remove surface irregularities. Surface acoustic wave delay lines were fabricated on AlN and ZnO films with the interdigital transducers deposited on the as-grown surfaces and showed excellent piezoelecteic response comparable to films formed by CVD.

Evaluation of the optical waveguiding characteristics of the heteroepitaxial structures showed that the lowest propagation loss was obtained with ZnO films on sapphire. At a wavelength of 0.6328µm scattering losses as low as 2dB/cm were obtained with as-grown ZnO films. Post deposition annealing is required of CVD films to achieve comparable loss values.

Waveguide loss in rutile grown on (0001) sapphire was measured to be as low as 20dB/cm, and 30dB/cm was observed with AlN films on (0001) sapphire substrates.

Considerably higher attenuation figures were obtained with GaN and WO_3. No comparable data is available for these materials grown by CVD. The high loss in waveguide structures employing TiO_2, AlN, GaN and WO_3 is attributed to strain which is a consequence of the elevated growth temperature and differences in thermal coefficients of expansion between film and substrate.

Reactive sputtering using sublimed arsenic as the sputtering gas inside a heated vacuum chamber was used to grow epitaxial films of gallium arsenide. The controlled growth of single crystal alloys of $Ga_{1-x}Al_xAs$ at low temperatures was also demonstrated. Sputtered gallium arsenide films grown between 330°C and 565°C have been found to show inordinately low carrier Hall mobilities due to lattice defects.

Conditions were determined for the deposition of amorphous neodymium ultra-phosphate films. This material holds the potential for the fabrication of lasers, amplifiers and passive waveguide components in monolithic form. The amorphous films sputtered from a NdP_5O_{14} target exhibit low optical attenuation (less than 1dB/cm) at 1.059μm. Absorption of the films in the neodymium pump band is high, and the flouresence lifetime, 8μsec, appears to at least allow pulsed laser operation. Lifetimes have been increased to 16μsec in the sputtered films through neodymium dilution using lanthanum. These sputtered films have all the basic properties required of a thin film laser material.

Charge storage characteristics of MIS (metal-insulator-semiconductor) structures were investigated. These employed a composite insulator formed by sputtering 1000Å of strontrum titanate over a 20Å silicon dioxide layer thermally grown on silicon. Switching voltages for the structures employing strontium titanate were considerably lower than that required for the conventional charge storage memory elements fabricated with either silicon nitride or aluminum oxide. Charge retention of these structures lasted approximately a day. Additional work is requested to take advantage of the reduced operating voltages offered by the strontium titanate structures as electrically reprogrammable memory elements. High transconductance, low threshold voltage strontium titanate MIS transistors were also fabricated.

Five publications have resulted from the research efforts to date. Two additional papers have been submitted for publication and several other manuscripts are in preparation.

The viability of reactive rf sputtering as a useful technology for the growth of single crystal films has been amply demonstrated for a wide variety of materials One of the principal advantages of this approach is the relative simplicity of the process development required in comparison to CVD.

The lower deposition rates which are obtained by reactive sputtering may be a disadvantage in the preparation of "thick" films, but it insures finer control over thickness in the growth of thin layers. The degree of success achievable in the preparation of heteroepitaxial structures rests primarily in the compatibility of the film and the substrate on which it is grown. This is illustrated by the difference in optical waveguide attenuation figures obtained with ZnO films on sapphire and WO_3 films on sapphire. Similar limitations are faced with CVD. The use of reactive sputtering for the preparation of epitaxial and heteroepitaxial structures should be considered for many more applications than it has in the past.

2.0 INTRODUCTION

Numerous applications exist for semiconductors and dielectrics in thin film form which essentially exhibit the same electrical and optical properties as they do in bulk single crystal form. In many cases these applications require the fabrication of structures which not only combine materials having appreciable differences in thermal coefficients of expansion, but also incompatible high temperature properties. For semiconductor device applications, low temperature deposition techniques are important since side reactions are suppressed and device degradation is minimized. In order to overcome these problems, a low temperature deposition process is mandatory. This in itself will not prove to be adequate unless the process will yield films with high purity and good structure. In fact, many applications require use of single crystal films. The primary objective of this program is to establish the feasibility of employing reactive rf sputtering for synthesis and deposition of selected high quality semiconductor and high permittivity insulating films suitable for optical and electronic applications. The secondary objective of the program is to fabricate devices where feasible to assess the potential of the grown material in selected device applications.

Sputtering is the technique of bombardment of a solid or liquid target with positive ions of sufficient energy to cause emission of atomic or molecular species from the target surface. The sputtering mechanism is generally accepted as a process of momentum transfer from the bombarding ion to the atomic or molecular species in the target. RF sputtering is a technique using high-frequency alternating voltages applied to the target electrode of an otherwise conventional sputtering system. In this way insulating or refractory materials can also be sputtered. There are, however, many compounds that tend to decompose under direct physical sputtering. This loss of stoichiometry is due to the breaking of chemical bonds by the impact of the sputtering ion and can be very serious if one of the constituents has a high vapor pressure or a low sticking coefficient. A technique often employed is to compensate for the loss of the volatile material by adding it to the sputtering atmosphere. This technique of compensating for component loss when sputtering a compound target is sometimes called reactive sputtering but the term is usually reserved for the process of sputtering elemental targets by a reactive gas.

RF reactive sputtering was chosen as the mode of deposition for several reasons:

(1) The method is capable of producing high purity films through the use of high purity elements and gases.

(2) Lower deposition temperatures, due to the high arrival energy of the sputtered species, can be used to achieve good quality epitaxial growth.

(3) In the event of a chemical reaction between the target material and sputtering gas producing an insulating layer on the target, the sputtering

process will not be interrupted.

(4) Economical preparation of a wide variety of III-V compound semiconductors and their alloys, high-dielectric constant insulators, and refractory materials is possible in many cases without the complex and time-consuming process development required in conventional chemical vapor deposition techniques.

(5) Control over stoichiometry and homogeneity are easily accomplished through variation in the growth parameters, (e.g., substrate temperature, target composition, type and partial pressure of sputtering gases, etc.).

(6) Fine control over thickness, due to the low growth rates, inherent in the sputtering process, is possible.

These potential advantages form a strong basis for the utilization of reactive sputtering in the synthesis of thin-film materials. The application of RF sputtering to single-crystal expitaxial growth is of primary importance and has not drawn much attention in the past.

This report is a summary of a two-and-one-half-year effort in the investigation of reactive sputtering of some technologically important materials. The versatility of RF reactive sputtering is immediately evident when one considers the wide variety of materials that have been deposited by this technique. Single crystal films of TiO_2, ZnO, GaN, AlN, InSb, GaAs, and $Ga_{1-x}Al_xAs$, and expitaxial layers of WO_3, which are twinned due to domain formation, have been grown. In addition, there is reported work on polycrystalline $SrTiO_3$ MIS structures and amorphous neodymium ultraphosphate optical waveguide structures. All the heteroepaxial structures grown were evaluated with regard to their optical waveguiding capabilities. Surface acoustic wave delay lines were fabricated to evaluate the piezoelectric properties of AnO and AlN films. The results of these investigations are presented in the following sections.

3.0 EPITAXIAL THIN FILM DEPOSITION OF ZnO

3.1 ZnO Sputtering System

Films of ZnO were prepared by rf sputtering from a 99.99% pure target of the compound in an argon and oxygen ambient. The argon was 99.999% pure and the oxygen was 99.994% pure. The sputtering chamber was pumped with a turbomolecular pumped backed with a standard mechanical pump. Pumping speed of the turbomoleuclar pump is about 250 liters pre second in the millitorr range. Since the chamber has a volume of about 25 liters, this represents a change of sputtering gas about 10 times per second. The chamber is of stainless steel construction. Copper gasketed seals as well as viton A "O" ring seals are used. The system typically was evaculated to about 2×10^{-6} torr before deposition began. Figure 3-1 is a photograph of the ZnO sputtering facility.

Substrates were heated by placing them on a thin high purity Al_2O_3 slide which was in direct contact with a tantalum strip heater. The heater temperature was monitored with a chormel-alumel thermocouple spot welded to the heater. The correlation between the heater temperature and substrate temperature had been established as described in Appendix II.

The sputtering gas was admitted through two precision micrometer valves. The argon flow was first adjusted to yield a certain percentage of the total desired sputtering pressure, and then the oxygen flow was adjusted to bring the pressure up to 100% of the desired pressure.

A special feature of this sputtering system is the variety of magnetic fields which can be produced in the region of the substrate and cathode. The fields are produced by a pair of solenoids concentric to the cathode and substrate holder. Spacing between the coils and position of the coil pair midplane is variable. Figure 3-2 illustrates the relative position of these components. The coils can be connected so that their fields either add or oppose. In this way the fields can be changed from a predominantly axial one to a quadrupole one. In previous work with this system extensive measurements were made to determine the effect of these fields on the substrate temperature and film deposition uniformity (Ref. 1).

3.2 Magnetic Field Experiments

Temperature measurments were made at six locations along a radius of the substrate holder for various magnetic field strengths and configureations. The temperature sensors were made from a 1.27 cm diameter by 0.55 cm high stainless steel rod with a chromel-alumel thermocouple spot welded in a 0.30 cm deep groove on the underside of the steel slug. The sensors were held in place simply by their own weight. The substrate holder temperature is controllable and was kept

FIG. 3-1

OVERALL VIEW OF ZnO SPUTTERING SYSTEM
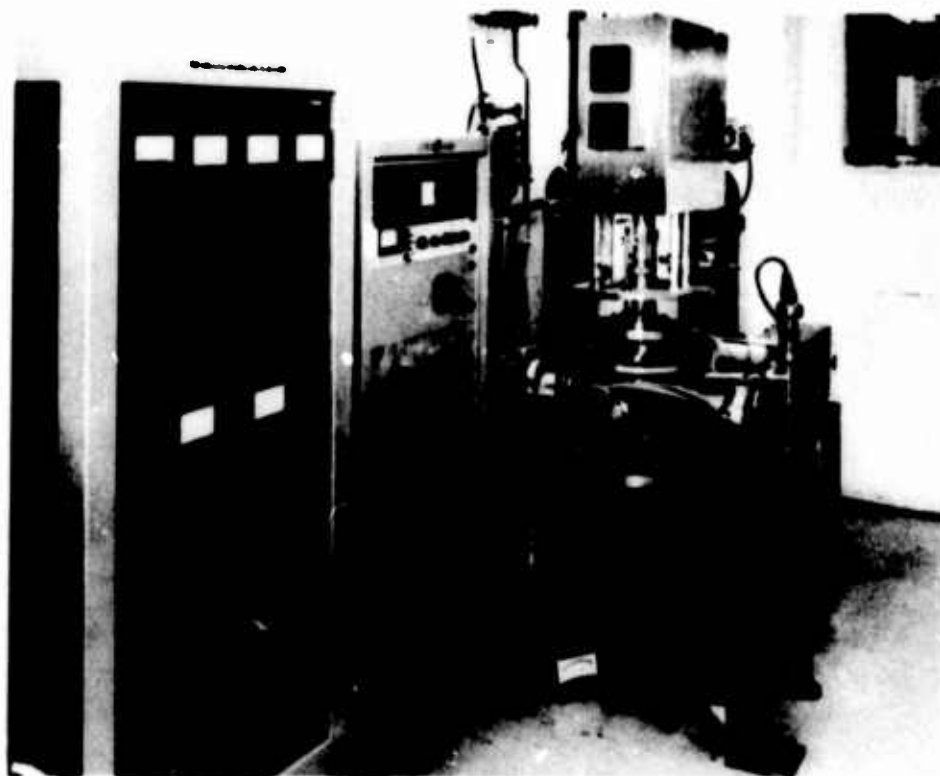
CLOSE-UP OF TARGET AND MAGNET ASSEMBLY

UPPER
MAGNET
COIL

ZnO
TARGET

N12-27-1

FIG. 3-2

SCHEMATIC OF THE MAJOR INTERNAL COMPONENTS OF THE SPUTTERING SYSTEM

UPPER COIL

GROUND SHIELD

TARGET

LOWER COIL

SUBSTRATE HOLDER

N04-106-2
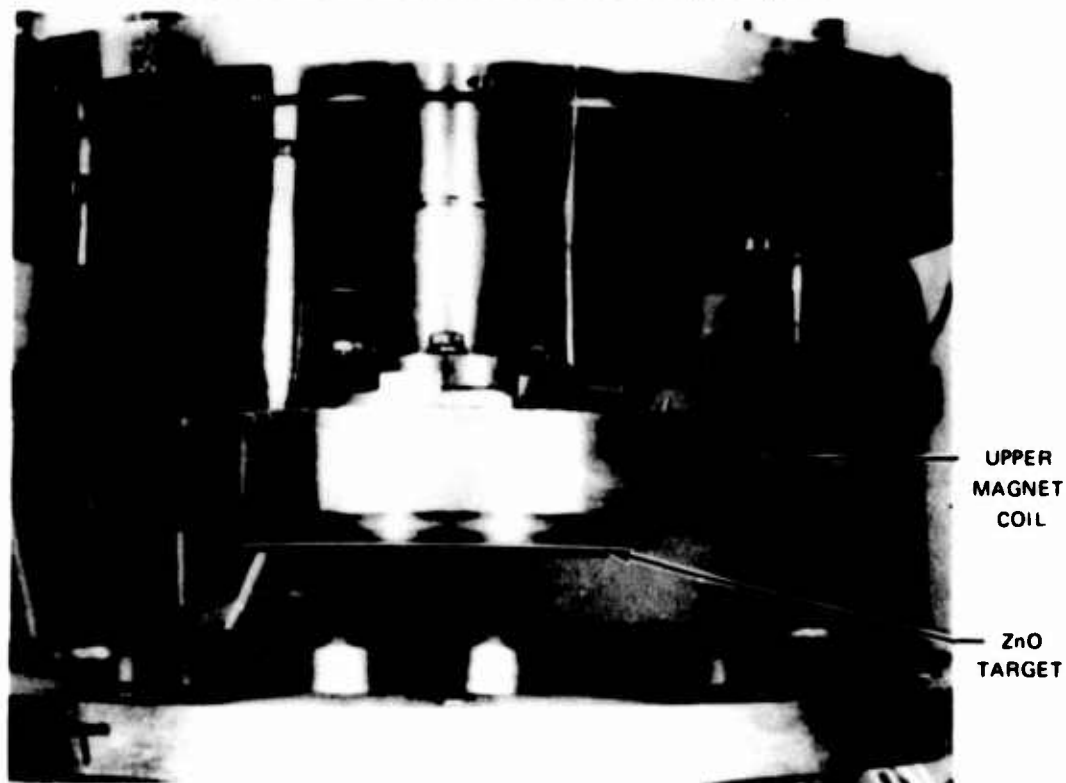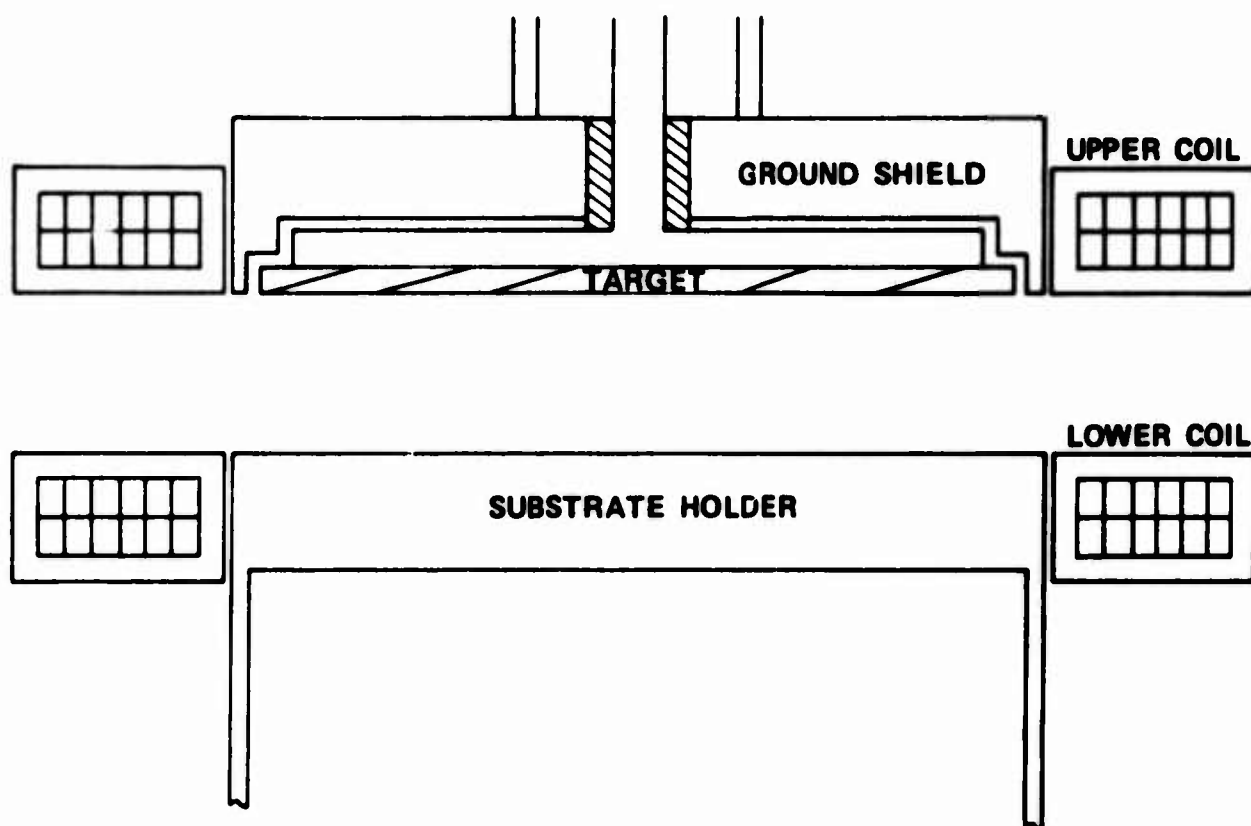
at a constant 10°C. Sensor temperatures were recorded before start up of each run
so that the raise in temperature could be determined. Sensor temperatures were
normally between 10 and 20°C at start-up.

The sputtering target was a 15.25 cm diameter hot pressed ZnO disc. The rf
power input to the target for this series of tests was 5.5 watts/cm^2. Essentially
equilibrium temperature of the sensors was arrived at after about 10 minutes of
operation, (Fig. 3-3). Temperature profiles were taken after 11.5 minutes of
operation and for many of the same runs after only 1.5 minutes of operation. In
general, the shape of the temperature profile for the shorter runs was similar to
that for the longer runs. However, temperatures were much higher for the longer
runs.

The sputtering gas was an 80 - 20 percent mixture of argon and oxygen at
10mtorr.

Film thickness was measured with a profilometer capable of 10^5 magnification.
Thickness samples were prepared for measuring by selectively etching away the ZnO
film down to the substrate.

3.2.1 Quadrupole Field

From previous work (Ref. 3-1), the quadrupole configuration looked promising
for reducing substrate temperature since the temperature at the outer edge was
much less than at the center. For this reason, the quadrupole configuration was
the first investigated. Figure 3-4 shows the temperature profiles determined for
quadrupole configurations with the magnetic coils at various separations. The
midplane of the coils was held at a constant distance of 0.7 cm below the plane
of the target. The overall shape of the profile is not altered too greatly as the
separation distance is varied; however, the general trend is to reduce the
temperature at the outer edge of the substrate as the coils are separated.

For a constant coil separation of 2.5 cm, much greater changes in temperature
profile are seen when varying the position of the coil midplane. Figure 3-5 shows
that the magnitude and position of the peak temperature continues to decrease and
move outwardly as the coil pair midplane is moved further away from the target.

Increasing the strength of the quadrupole field for a given coil separation
and midplane position has the effect of depressing the peak temperature and moving
it toward the center as seen in Fig. 3-6. It would appear that the quadrupole
configuration and strength which produced the temperature profile of the 400 amp
curve in Fig. 3-6 would come closest to satisfying the requirement for the least
temperature perturbation to the substrate. However, a deposition profile for the
outer 4.5 cm shows (curve I, Fig. 3-7) that the deposition rate can fall off by

FIG. 3—3

SENSOR TEMPERATURE RISE AS A FUNCTION OF TIME AFTER START UP FOR QUADRUPOLE MAGNETIC FIELD CONFIGURATION
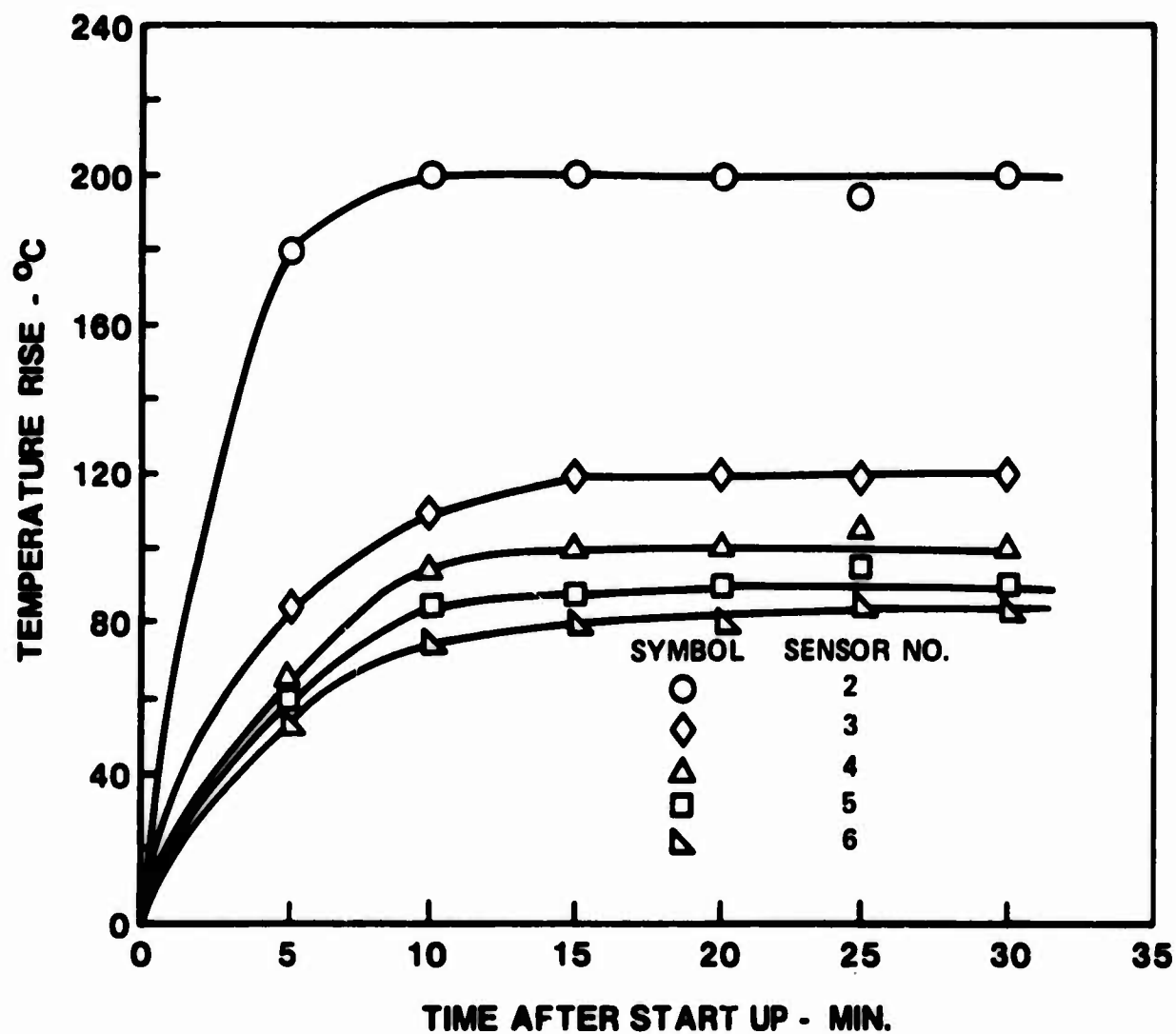
FIG. 3—4

EFFECT OF MAGNET COIL PAIR SEPARATION DISTANCE ON SUBSTRATE TEMPERATURE PROFILE FOR A QUADRUPOLE FIELD CONFIGURATION

QUADRUPOLE FIELD
MAGNET CURRENT — 300 AMPS
TARGET INPUT POWER — 5.5 WATTS/cm^2
COIL PAIR MIDPLANE BELOW TARGET — 0.7 cm

○	1.2	
◇	2.5	COIL PAIR
△	3.8	SEPARATION — cm
□	5.1	

N04—143—4

FIG. 3–5

EFFECT OF MAGNET COIL PAIR MIDPLANE LOCATION ON SUBSTRATE TEMPERATURE PROFILE FOR A QUADRUPOLE FIELD CONFIGURATION

QUADRUPOLE FIELD

MAGNET CURRENT – 300 AMPS

TARGET INPUT POWER – 5.5 WATTS/cm^2

COIL PAIR SEPARATION – 2.5 cm

O	0.6	ABOVE	COIL PAIR MIDPLANE WITH RESPECT TO TARGET – cm
◇	0.7	BELOW	
△	1.8	BELOW	
□	3.3	BELOW	

N04 – 143 – 3

12

FIG. 3–8

**EFFECT OF MAGNETIC FIELD STRENGTH ON SUBSTRATE TEMPERATURE PROFILE FOR
A QUADRUPOLE FIELD CONFIGURATION**

QUADRUPOLE FIELD

TARGET INPUT POWER – 5.5 WATTS/cm^2

COIL PAIR SEPARATION – 5.1 cm

COIL PAIR MIDPLANE
BELOW TARGET – 0.7 cm

○ 100
△ 300 MAGNET CURRENT
□ 400 AMPS

13

FIG. 3 7

COMPARISON OF DEPOSITION RATE AND SUBSTRATE TEMPERATURE PROFILES FOR SEVERAL QUADRUPOLE FIELD CONFIGURATION

QUADRUPOLE FIELD
TARGET INPUT POWER = 5.5 WATTS/cm^2

	I	II	III
COIL PAIR SEPARATION – cm	5.1	–	2.5
COIL PAIR MIDPLANE BELOW TARGET – cm	0.7	–	0.2
MAGNET CURRENT – AMPS	400	0	400

TEMPERATURE RISE °C

DEPOSITION THICKNESS - MICRONS

RADIAL POSITION - cm
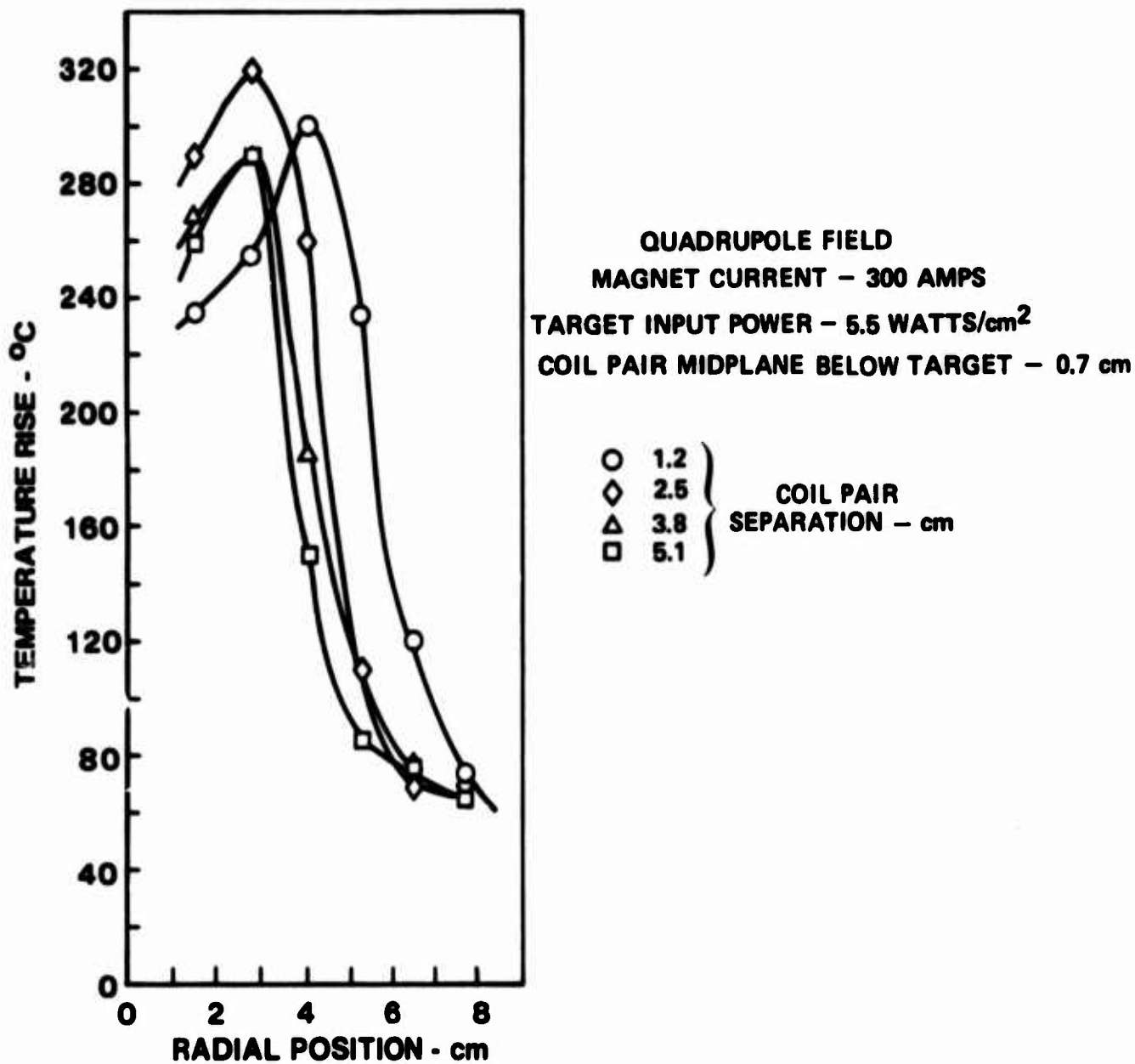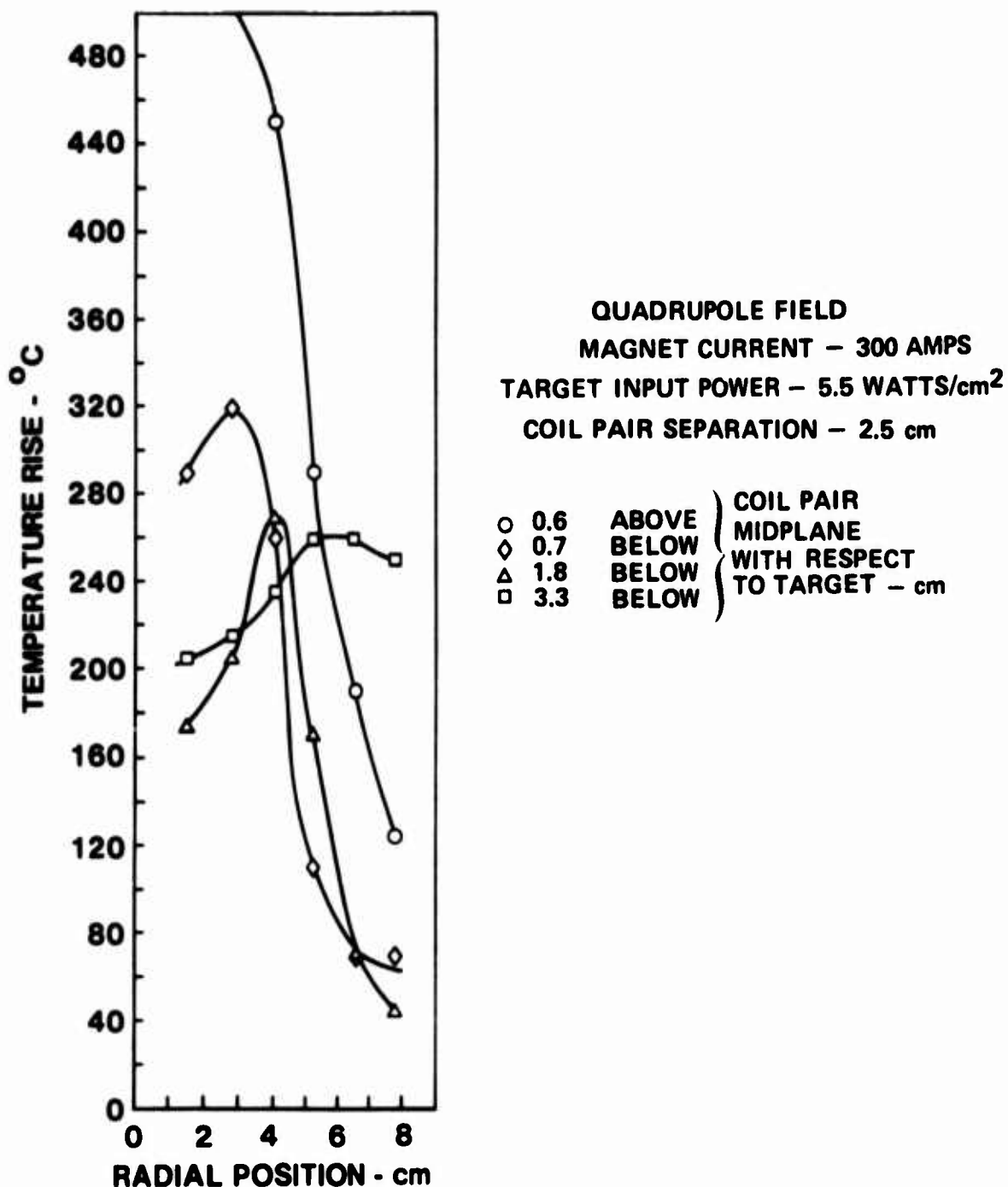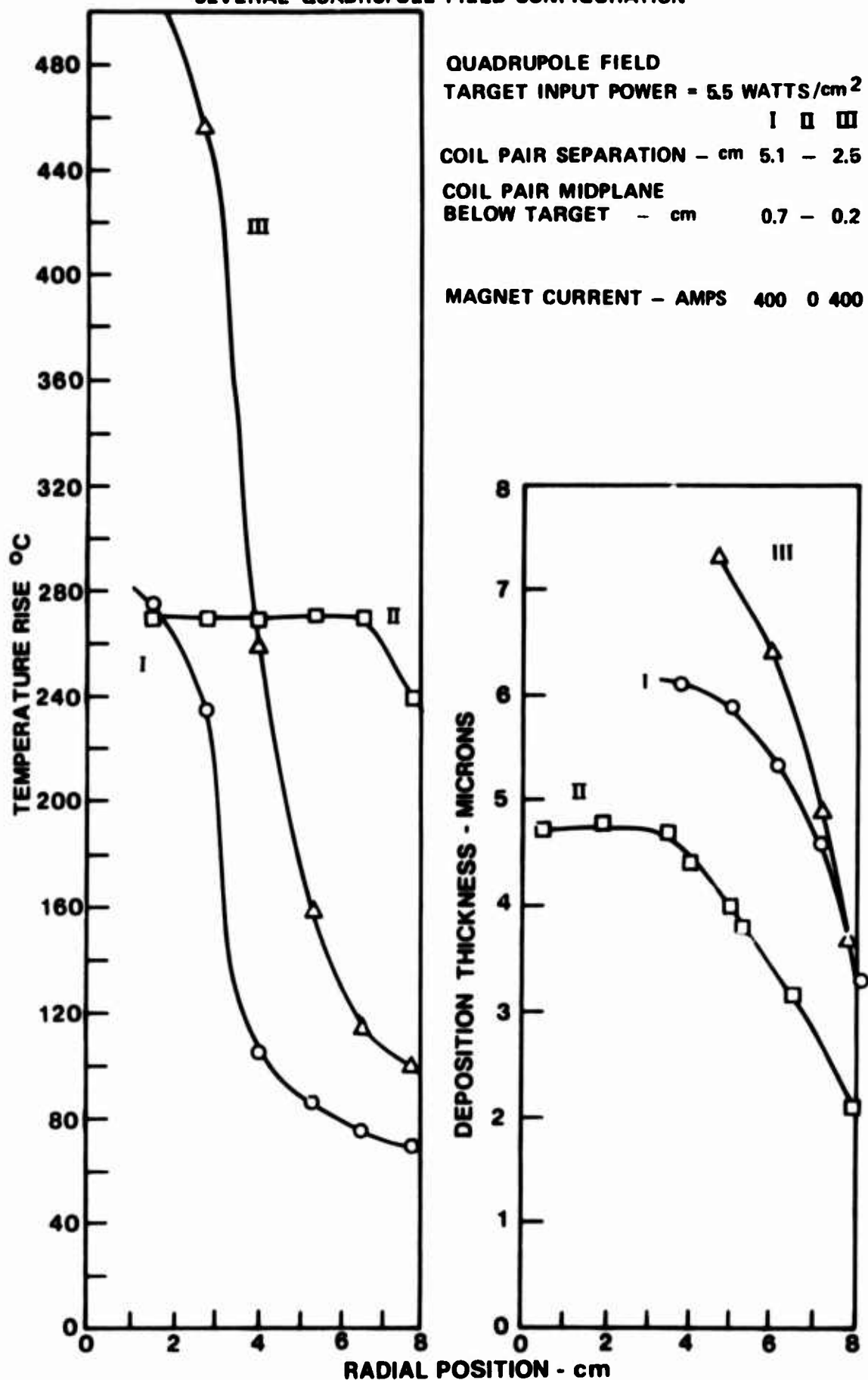
nearly a factor of 2 in the outer 3 cm. This is not too surprising when the deposition profile of the case with no magnetic field is considered, (curve II, Fig. 3-7). For the latter case, nearly the same percentage of rate loss is experienced. For the zero magnetic field, however, the overall rate is less and the temperature is greater at the outer edge than that for the applied quadrupole field Curve III, Fig. 3-7 illustrates yet another example where a further increase in rate is accompanied by a much greater heating effect. This condition was produced by moving the quadrupole field midplane to within 0.2 cm of the target. An increase in deposition rate as the midplane of the quadrupole field is brought in the vicinity of the target cathode dark space is predicted by Kay (Ref. 3-1).

3.2.2 Longitudinal Field

Duplicate experiments were run with the magnetic fields of the coil pair arranged to add. This produced a predominantly axial or longitudinal field with the axis of the field coincident with the central axis of the target and substrate. Figure 3-8 illustrates the effect of varying the magnet coil separation at a mid-plane distance of 0.7 cm below the target plane for a constant current to the coils. The effect is generally to increase the height of the peak temperature with increasing coil separation. However, the temperature near the center does not increase proportionately.

For the case where the magnet separation is kept constant at 2.5 cm and the position of the coil midplane is varied (Fig. 3-9) the peak is seen to move in and out. However, for the case of curve C the temperature near the center is the lowest. There is also a trend toward reducing the temperature gradient in that region as the midplane of the magnetic field is moved toward the midpoint of the target-to-substrate separation distance. Figure 3-10 shows that increasing the magnetic field strength for the condition which produced curve C, Fig. 3-9, has the tendency to further reduce the temperature and temperature gradient in the central region.

Figure 3-11 shows profiles of the temperature and deposition rate for the condition with maximum magnet current available and the configuration which yielded curve C of Fig. 3-9. For comparison, similar data is presented for the zero magnetic field case. Note that these two runs were made at an input rf power to the target of 2.75 watts./cm^2, half of that used for the other runs in these experiments. The deposition rate at the center has not been increased by the use of the axial field over the zero magnetic field case; however, the rise in temperature of the substrate due to the energetic secondary electron bombardment is substantially reduced. On the other hand, the deposition profile with the axial magnetic field has been considerably flattened over that of the quadrupole field

FIG. 3—8

**EFFECT OF MAGNET COIL PAIR SEPARATION DISTANCE ON SUBSTRATE TEMPERATURE
PROFILE FOR A LONGITUDINAL FIELD**

**LONGITUDINAL FIELD
MAGNET CURRENT — 300 AMPS
TARGET INPUT POWER — 5.5 WATTS/cm^2
COIL PAIR MIDPLANE
BELOW TARGET — 0.7 cm**

○ 1.2
◇ 2.5   COIL PAIR
△ 3.8   SEPARATION – cm
□ 5.1

**EFFECT OF MAGNET COIL PAIR MIDPLANE LOCATION ON SUBSTRATE TEMPERATURE
PROFILE FOR A LONGITUDINAL MAGNETIC FIELD CONFIGURATION**

LONGITUDINAL FIELD
MAGNET CURRENT – 300 AMPS
TARGET INPUT POWER – 5.5 WATTS/cm^2
COIL PAIR SEPARATION – 2.5 cm

○ 0.6 ABOVE ⎫
◇ 0.7 BELOW ⎪ COIL PAIR MIDPLANE
△ 1.8 BELOW ⎬ WITH RESPECT TO
□ 3.3 BELOW ⎭ TARGET – cm

N04-143-6

EFFECT OF MAGNET FIELD STRENGTH ON SUBSTRATE TEMPERATURE PROFILE FOR A LONGITUDINAL MAGNETIC FIELD CONFIGURATION

LONGITUDINAL FIELD
TARGET INPUT POWER — 5.5 WATTS/cm^2
COIL PAIR SEPARATION — 2.5 cm
COIL PAIR MIDPLANE BELOW TARGET — 1.8 cm

O 100 ⎫ MAGNET CURRENT
△ 300 ⎬
□ 400 ⎭   AMPS

N04-143-5

FIG. 3-11
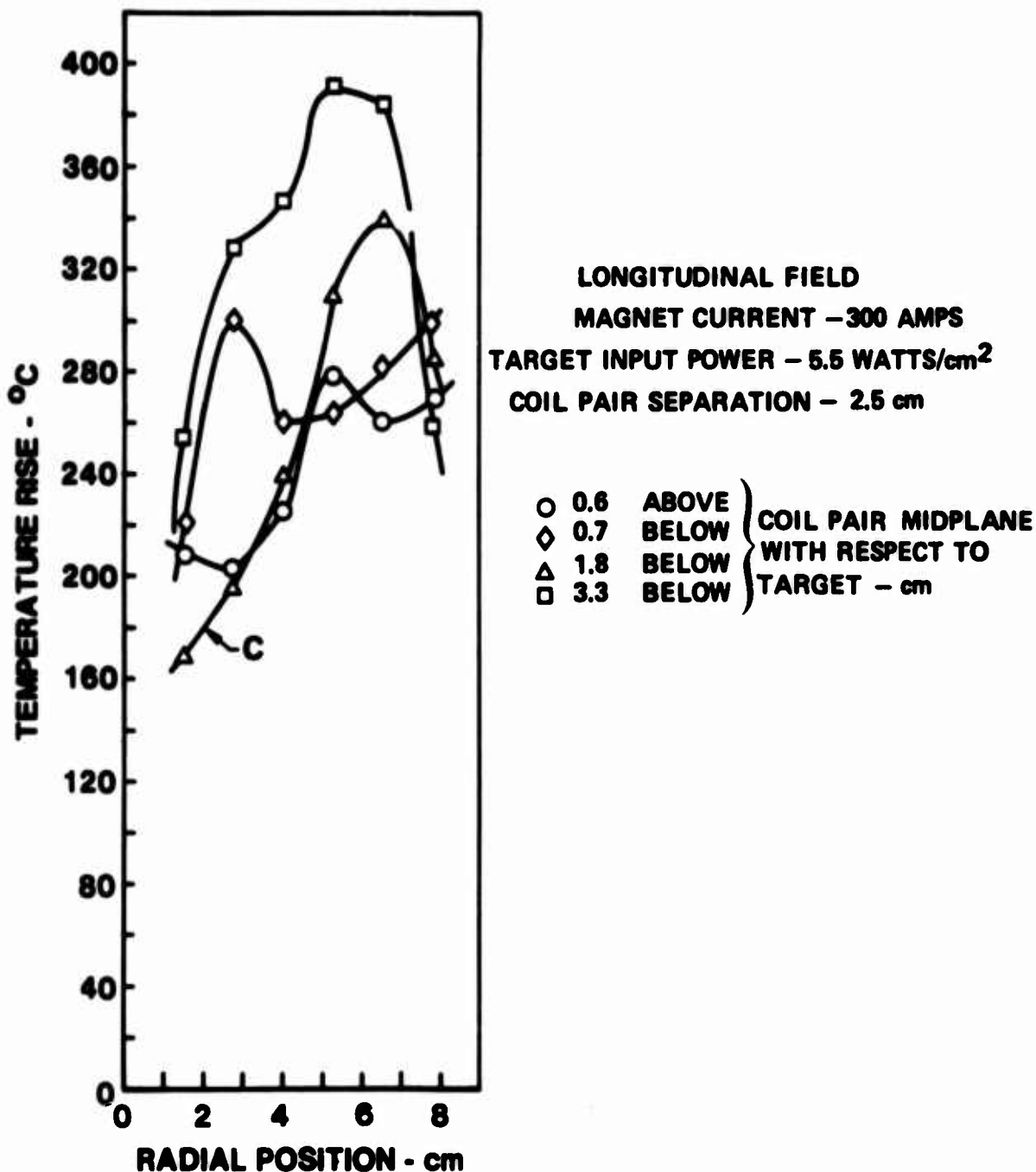
COMPARISON OF DEPOSITION RATE AND SUBSTRATE TEMPERATURE PROFILE FOR A LONGITUDINAL FIELD CONFIGURATION

LONGITUDINAL FIELD
TARGET INPUT POWER — 2.75 WATTS/cm^2

	I	II
COIL PAIR SEPARATION — cm	2.5	–
COIL PAIR MIDPLANE BELOW TARGET — cm	1.8	–
MAGNET CURRENT — AMPS	400	0
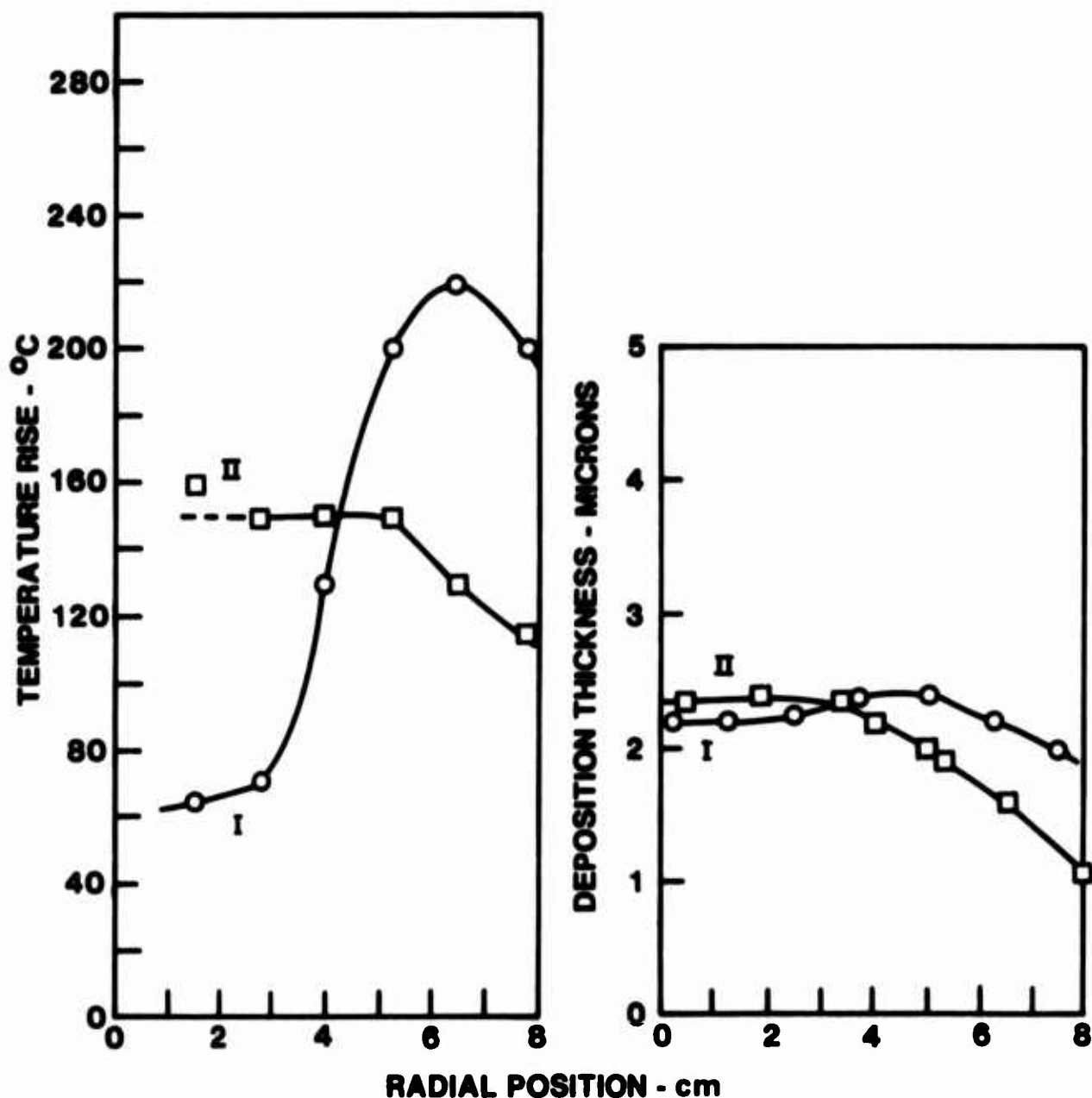
case. The profile is flat to within ± 10% over the entire 15 cm diameter and to within about 2.5% over the central 5 cm.

For the conditions corresponding to curve C of Fig. 3-9, several depositions of ZnO were made on polished single crystal (1T02) oriented sapphire substrates. The substrates were placed at the center of the substrate holder. Figure 3-12 is a comparison photomicrograph of the ZnO coated substrates for two values of the axial magnetic field. The higher magnetic field, which is the condition of curve I, Fig. 3-11, clearly shows a much improved film texture (Fig. 3-12B). From the point of view of growing films for optical wave guiding, the most important aspect of preventing the secondary electrons from interacting with the substrate is their effect on the texture of the film. This is important since the smoother the film is, the less likely it is to loose light from scattering at the surface. Films grown outside of the central 5 cm have a cloudy grainy appearance. The same effect is noted at zero or low magnetic fields for films grown at the center of the substrate holder.

As an application of the knowledge gained with the ZnO sputtering system, a second sputtering system was equipped with a pair of solenoids similar to those described earlier. However, because of space limitations within the chamber, the magnet coils were smaller in diameter and longer. Furthermore, since Fig. 3-9 indicates that the lowest temperatures at the substrate are probably achieved with the coil pair midplane midway between the target and the substrate, the coil separation distance in this second system had to be set at 9.2 cm. Figure 3-13 is a comparison of the film texture of TiO_2 films sputtered onto (0001) oriented single crystal sapphire in this system with the axial magnetic field and without. The improvement in film smoothness for the case with the longitudinal field is clear (Fig. 3-13B)

3.2.3 Discussion

Perhaps some insight can be gained into the understanding of the role that magnetic fields have in affecting the substrate temperature by the following considerations. Kay (Ref. 3-1) has shown that the strength of the radial component of the magnetic field in the vicinity of the cathode dark space has a strong effect on the cathode erosion rate. The reason advanced is that the radial magnetic field causes the electrons to spiral, thereby increasing the probability that they will produce ionization near the dark space. By increasing the local plasma density, more ions are available for sputtering. More ions interacting with the target also increase both the number of secondary electrons emitted as well as the sputtering rate. The result is that if the secondary electron density were measured at the target surface, one would expect it to increase as the magnitude of the radial magnetic field increased.

FIG. 3—12

ELECTRON MICROGRAPH OF ZnO SPUTTERED ON (1Ī02) ORIENTED SAPPHIRE FOR TWO VALUES OF A LONGITUDINAL MAGNETIC FIELD
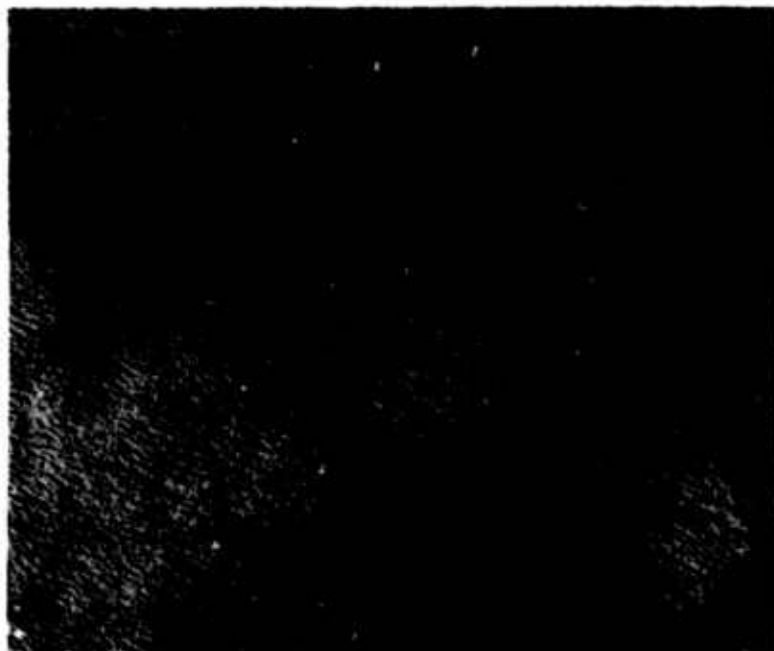
(a) DEPOSITED WITH 45 AMPS IN THE COILS

1µ

(b) DEPOSITED WITH 425 AMPS IN THE COILS

FIG. 3-13

ELECTRON MICROGRAPH OF TiO$_2$ SPUTTERED ON (0001) ORIENTED SAPPHIRE

(a) DEPOSITED WITH NO MAGNETIC FIELD

1 μ
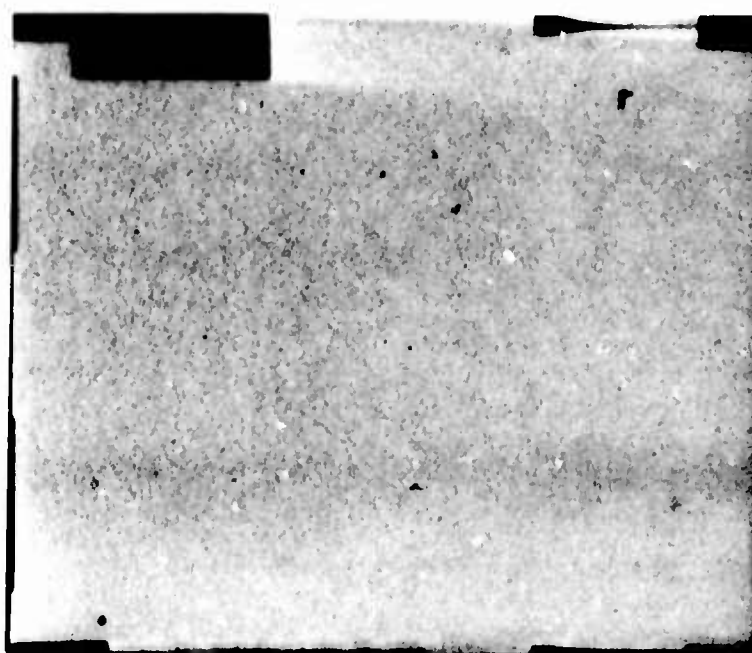
(b) DEPOSITED WITH A STRONG LONGITUDINAL
MAGNETIC FIELD

1 μ

22

Figure 3-14 shows plots of the magnetic field produced by the solenoid pair at a separation distance approximately equal to that used to generate curve C, Fig. 3-9. The left-hand portions of the figure, which show the relative strengths of the axial and radial components of the magnetic field, are drawn to scale and were measured with a directional probe for a constant current input of 200 amps to the coils. From the field plots of Fig. 3-14, one would expect that the secondary electron density at the target surface would generally increase radially outward from the center for nearly any combination of magnetic field and target position, as long as the target and magnetic field centers lay along the same axis. The magnitude of the effect, however, would of course depend on target position and type of field.

The actual sputtering rate at the target is further complicated by the presence of several other competing phenomena associated with the sputtering system. For example, because of scattering, losses of plasma ions are more strongly felt at the outer radius; therefore, one would expect the electron density to peak before reaching the outer edge of the target. Furthermore, it has been shown (Ref. 3-2) that ground shields in the vicinity of the target can have a strong effect on the electric field shape in the dark space. This would also affect the sputtering rate and the path of the secondary electrons at the outer edge of the target. Since the magnet coil cans are connected to ground and are in somewhat close proximity to the target, it is reasonable to expect that their position would affect the electric fields at the target in addition to the perturbation caused by the stationary cathode ground shield (see Fig. 3-2).

As the electrons leave the dark space region and travel toward the substrate, their paths can be further affected by the shape of the magnetic field. In a general way, the electrons will tend to follow the field lines. Therefore, the electron density at the substrate would be further perturbed by the guiding of the electrons along the magnetic lines of force. This would result, for example, in increasing the substrate temperature at the center for the case where the quadrupole field is arranged so that its midplane is near the target. In such an instance, the magnetic field lines converge toward the center as illustrated in Fig. 3-14A. The secondary electrons leaving the target would, therefore, be guided toward the center of the substrate.

It is also possible that some electrons are reflected before reaching the substrate by the mirror effect of the converging quadrupole magnetic fields. For charges particles to be reflected in a magnetic field, the requirement is that (Ref. 3-5)

$$B = B_0/\sin^2 \theta_0$$

where B is the value of the magnetic field where reflection occurs, B_0 is the value of the magnetic field at the point where the particle enters and θ_0 is the angle that the particle makes with B_0.

FIG. 3—14

MAGNETIC FIELD PLOTS FOR 200 AMPS DC CURRENT IN THE COILS

QUADRUPOLE - A

MAGNET COIL

500 GAUSS

500 GAUSS

1 CM

1 CM

MAGNET CURRENT 200A

N04-106-3

LONGITUDINAL - B

MAGNET COIL

N04-106-4

24
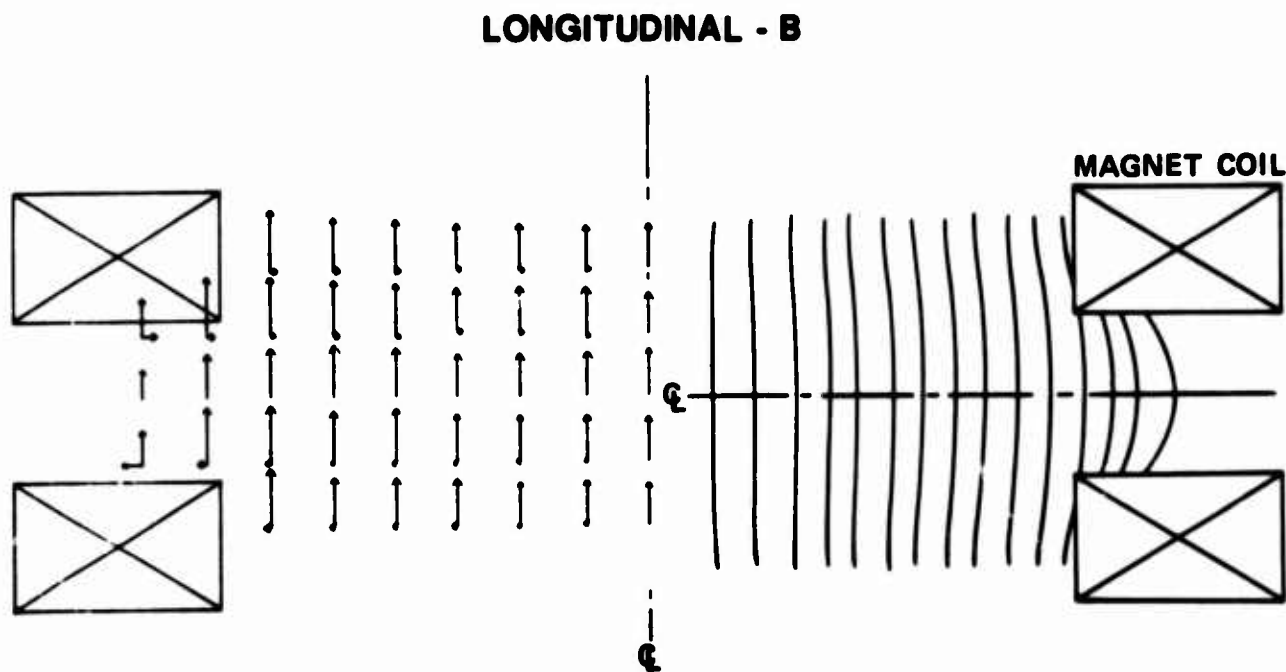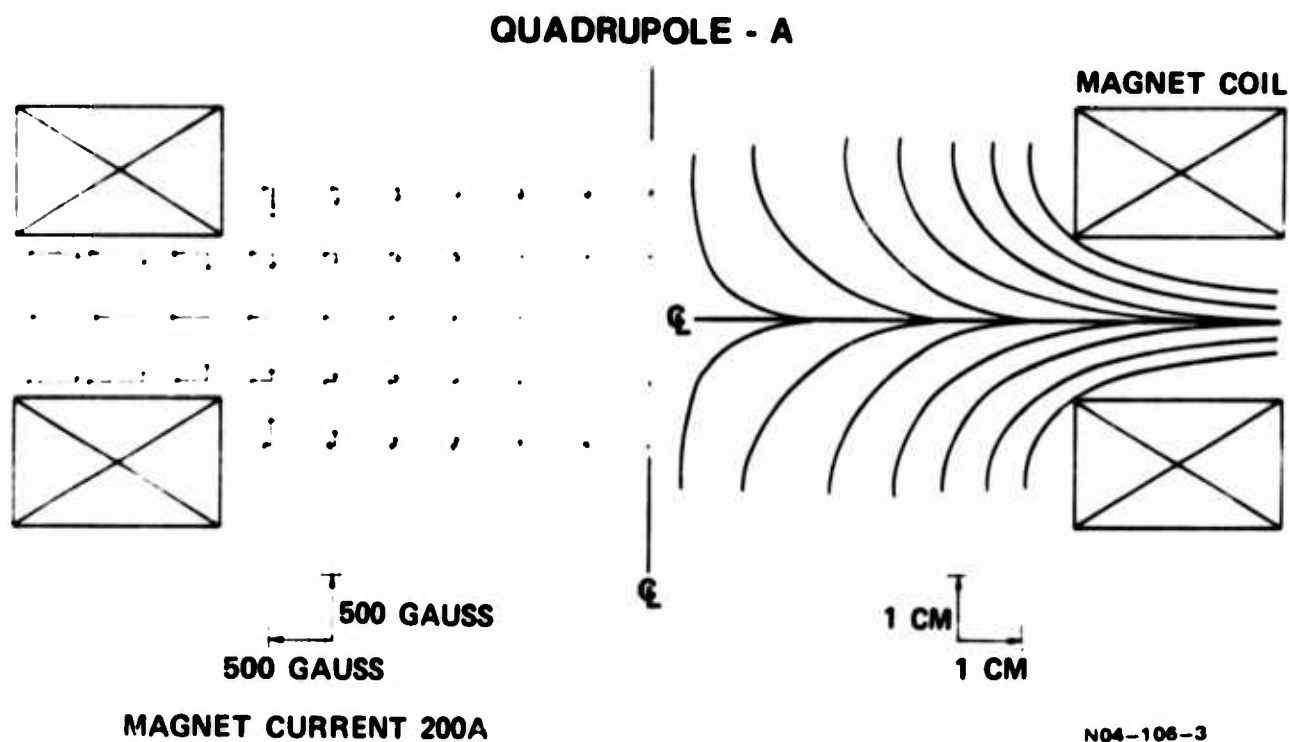
Since this condition is more likely to be satisfied for electrons emitted at the outer radius of the target, this would result in further depressing the temperature at the outer edge of the substrate. Fig. 3-7, curve III is a temperature profile taken with the quadrupole field midplane in the vicinity of the target. The temperature is indeed very high in the center and greatly depressed at the outer radius.

Another consideration which must be taken into account when interpreting the results of these experiments is the fact that the plasma is fundamentally a non-linear element and more often than not exists in a state of rather unstable equilibrium. For these reasons, one should not necessarily expect a smooth transition in operating characteristics in proportion to the "magnitude" of the changes made in the operating conditions. For example, when looking at Fig. 3-8 and Fig. 3-9, it is difficult to see how the temperature profiles plotted there can all follow one from the other as a result of small perturbations to the system. It becomes even more puzzling when comparing these variations with those of Fig. 3-4 and Fig. 3-5. In Fig. 3-4 and Fig. 3-5, the changes in temperature profile seem to follow more logically from the perturbations imposed. The reason for this is probably that the configuration of the quadrupole field is more stable than that of the axial field and that the axial field configuration is much more sensitive to "small" changes. By way of support for this surmise, an experiment was conducted which was able to show in a qualitative way the relative number of secondary electrons reaching the substrate at any time during sputtering. A 17.2 cm diameter quartz plate was covered with a thin coating of zinc sulfide and placed on the substrate holder. When the sputtering system was turned on, the zinc sulfide phosphoresced in proportion to the number of electrons impinging on it. The intensity of the phosphorescence was observed through the system viewing port. The magnet coils were arranged to produce the fields from which the temperature profiles of Fig. 3-10 were taken.

At zero magnetic field the plate was unifromly bright. For the quadrupole field, as the magnet current was increased, a bright ring began to form at the outer radius and gradually moved in. Concurrently, the intensity of the ring decreased. For the axial field case little was observed until the magnet current reached 50 amps. At this point, the phosphor suddenly went dark at the position of the outermost sensor. As the field was increased further, a bright ring began to form at the position of the outer sensor. Between 100 and 200 amps there was noticeable movement of the bright ring. A rapid in and out movement of the ring occurred as the field was changed slowly in the vicinity of 150 amps. Further increases in field strength from 300 to 400 amps served to diminish the intensity within the ring. The rather abrupt changes occurring in the electron impingement profile with small changes in the magnetic field strength are indicative of the plasma switching to slightly different operating modes. That is to say, the spatial and possibly the energy distributions of the charged particles in the plasma are being severely affected at times by the strength of the axial magnetic

field. It is also possible to observe changes in the plasma color and brightness accompanying the rapid movement of the bright phosphorescent ring. Since, in the axial field configuration, indications are that significant changes in the temperature profile can occur for relatively small changes in the field strength, it is not difficult to picture similar or more severe temperature variations occurring when the shape and strength of the field are also changed by the movement of the coils as indicated in Fig. 3-8 and 3-9.

That the configuration of curve C, Fig. 3-9, inhibits substrate heating while providing a rather uniform deposition at the center of the substrate can, therefore, be understood in the light of what has already been discussed. For an axial field arranged so that its midplane is coincident with the target to substrate midpoint, reference to Fig. 3-14 shows that the radial component of the magnetic field at the target only begins to have an appreciable value well away from the center. Therefore, one would expect that for this case, the peak sputtering rate as well as the peak secondary electron emission rate would occur somewhere beyond midway out on the target radius. Because of the shape of the magnetic field, the secondary electrons would not be focused toward the center of the substrate. Meanwhile, the presence of an intense sputtering "ring source" at the position of peak sputtering provides a sufficient contribution to coating the central region of the substrate so that the deposition rate at the center is not seriously depressed (Ref. 3-2).

As a final observation, consider the temperature distribution shown in Fig. 3-3 for the case where the coil pair midplane is 1.8 cm below the target face. These are the same conditions of coil separation and coil midplane location as those which produced curve C of Fig. 3-9 except that the coils were arranged to produce a quadrupole field. There is a strong similarity in these two curves except that the temperature peak is much closer to the center for the quadrupole field case. This is understandable because Fig. 3-14 indicates that when the midplane of the coil pair is approximately midway between the target and the substrate, the strength of the radial component of the quadrupole magnetic field at the target face looks similar to that for the equivalent case with the axial field. However, the radial component near the target face for the quadrupole field case reaches an appreciable strength at a position closer to the center. This would imply that the peak substrate temperature for the quadrupole field case would occur closer to the center than that for the similar axial field case as indeed it does.

3.2.4 Conclusions

From the results of these experiments we can see that a large variety of temperature profiles are possible at the substrate with a given pair of solenoids.

However, in order to minimize temperature and still have a reasonably uniform deposition rate, configurations which minimize the temperature at the center of the substrate holder are more desirable than those which minimize the temperature at the outer edge. From these experiments the configuration which best fulfills this need is that which produced curve C of Fig. 3-9. Because of the complex nature of the plasma and the many perturbations introduced by the presence of the sputtering apparatus, it is difficult to give hard and fast rules as to what will or will not work to achieve the desired results. For the present case it would seem that an axial magnetic field of as great a strength as practical arranged so that the midplane of the field is coincident with the midpoint distance between the target and substrate will produce a reasonably uniform deposition area and the lowest possible substrate heating for a given power input to the target. The principal effect contributing to the achievement of the low substrate heating has been minimizing of substrate bombardment by the secondary electrons. This, in turn, we feel resulted in the smooth film growth obtained.

3.3 Characterization of ZnO Films

The film structure was determined using x-ray diffraction and reflection electron diffraction. Figure 3-15 represents the expected electron diffraction patterns for single crystal zinc oxide films. Figure 3-16 shows typical single crystal reflection electron diffraction patterns obtained for films grown on (0001) and (1$\bar{1}$02) sapphire substrates. The epitaxial relationships between film and substrate are found to be:

$$(0001)ZnO \parallel (0001)Al_2O_3, \ [1\bar{1}02]ZnO \parallel [11\bar{2}0]Al_2O_3$$

$$(11\bar{2}0)ZnO \parallel (1\bar{1}02)Al_2O_3, \ [0001]ZnO \parallel [1\bar{1}0\bar{1}]Al_2O_3$$

3.4 Optimization of Film Growing Parameter

Films were grown on (0001) and (1$\bar{1}$02) oriented polished sapphire substrates for a variety of deposition conditions. Substrates were prepared as described in Appendix I. The deposition conditions which could be controlled were:

      a. substrate temperature
      b. gas pressure
      c. argon/oxygen ratio
      d. rf power input to the target
      e. magnetic field strength

FIG. 3—15

CALCULATED RED PATTERNS FOR ZnO
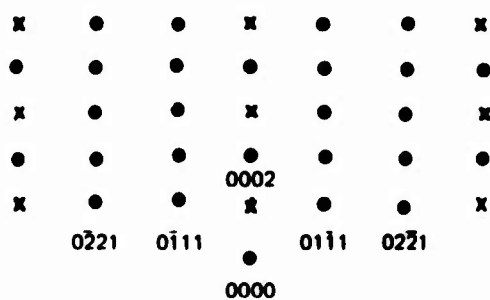
ELECTRON BEAM IN [10$\bar{1}$0] DIRECTION
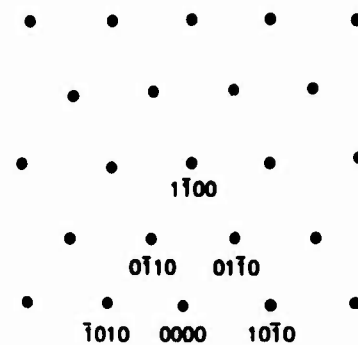
ELECTRON BEAM IN [0001] DIRECTION
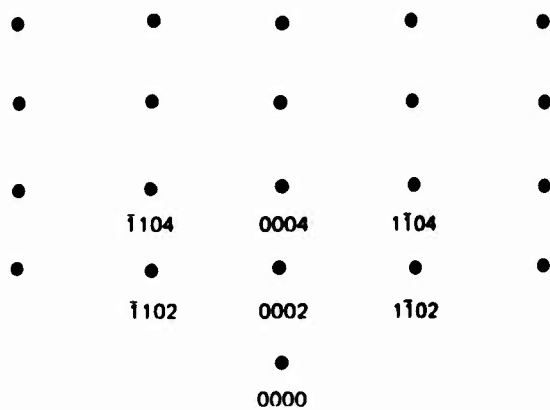
ELECTRON BEAM IN [11$\bar{2}$0] DIRECTION

ELECTRON BEAM IN [11$\bar{2}$0] DIRECTION

FIG. 3-16
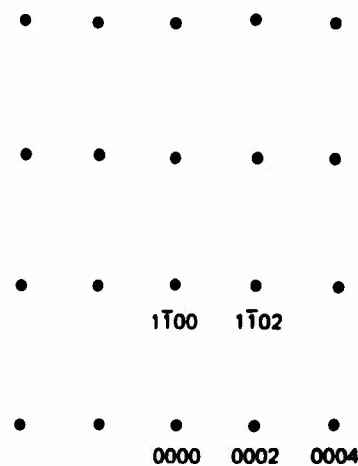
RED PATTERNS FOR ZnO FILMS

(a) RED OF ZnO ON (0001) Al$_2$O$_3$

(b) RED OF ZnO ON (1102) Al$_2$O$_3$
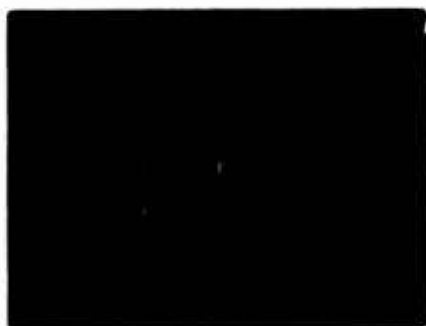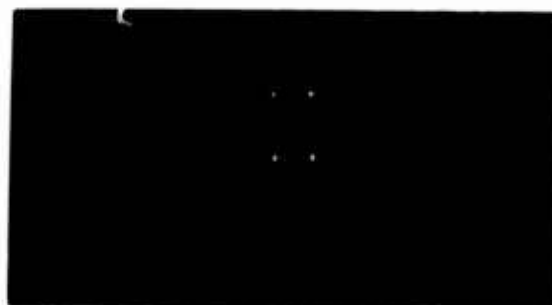
|10T0|

|0001|

|11$\overline{2}$0|

|1120|

Krikorian and Sneed (Ref. 3-4) have established that the three most important parameters which determine epitaxial growth in sputtering for a given material and substrate are the substrate temperature, deposition rate, and background pressure. Rozgonyi and Polito (Ref. 3-5) have investigated the epitaxial growth of sputtered ZnO at a constant pressure of 70mTorr. They found a relationship between substrate temperature and growth rate as predicted by Krikorian and Sneed for ZnO on CdS substrates. However for ZnO an (0001) sapphire, Rozgonyi and Polito found that only a limited region in the temperature-growth rate plane would satisfy the requirements for epitaxial growth. The present investigation has extended the region of the temperature-growth rate plane for ZnO epitaxy on (0001) sapphire for several pressures. Furthermore, substrate temperature-growth rate regions, also for several pressures, have been found for sputtered epitaxial ZnO on (1102) sapphire. Figure 3-17 summarizes the growth conditions for this investigation as well as those of Rozgonyi and Polito.

Total gas pressure and rf power input to the target were used as a means of controlling the deposition rate. For example it was found that the sputtering system rf power supply was not stable enough over long periods of time when operated at output powers of less than about 40 watts. In order to lower the deposition rate and still maintain power supply stability the gas pressure was raised from the more usual total pressure of 10mTorr to a total of 50mTorr. This resulted in a decrease in deposition rate by nearly a factor of ten.

The argon-oxygen gas ratio was maintained at 8:2.

The effect of the magnetic field has been discussed so that once it had been established that a high axial magnetic field produced the smoothest film growth, that condition was maintained throughout the remainder of the investigation.

3.5 Optical Wave Guiding

While it had been established that epitaxial single crystal films of ZnO could be deposited at rates as high as 122Å/min on (0001) orientated sapphire and 100Å/min on (1102) orientated sapphire, it was found that these films were not capable of guiding light of 6328Å wavelength for any appreciable length. Examination of the film surfaces revealed that films grown at elevated temperatures of $800^{\circ}-900^{\circ}C$ exhibited the tendency to grow faceted single crystal nodules on the surface as illustrated in Fig. 3-18. These nodules not only prevented good optical coupling into the film but also served as portals of escape for any light which might get in. It was further observed that these nodules had less of a tendency to grow at the lower substrate temperatures. It was therefore decided to sacrifice some speed in deposition rate, as required at the lower temperatures, in favor of improved as grown surface quality. Since it was found that films grown at

FIG. 3-17

DEPOSITION CONDITIONS FOR SPUTTERED EPITAXIAL ZnO ON SAPPHIRE SUBSTRATES

FIG. 3—18
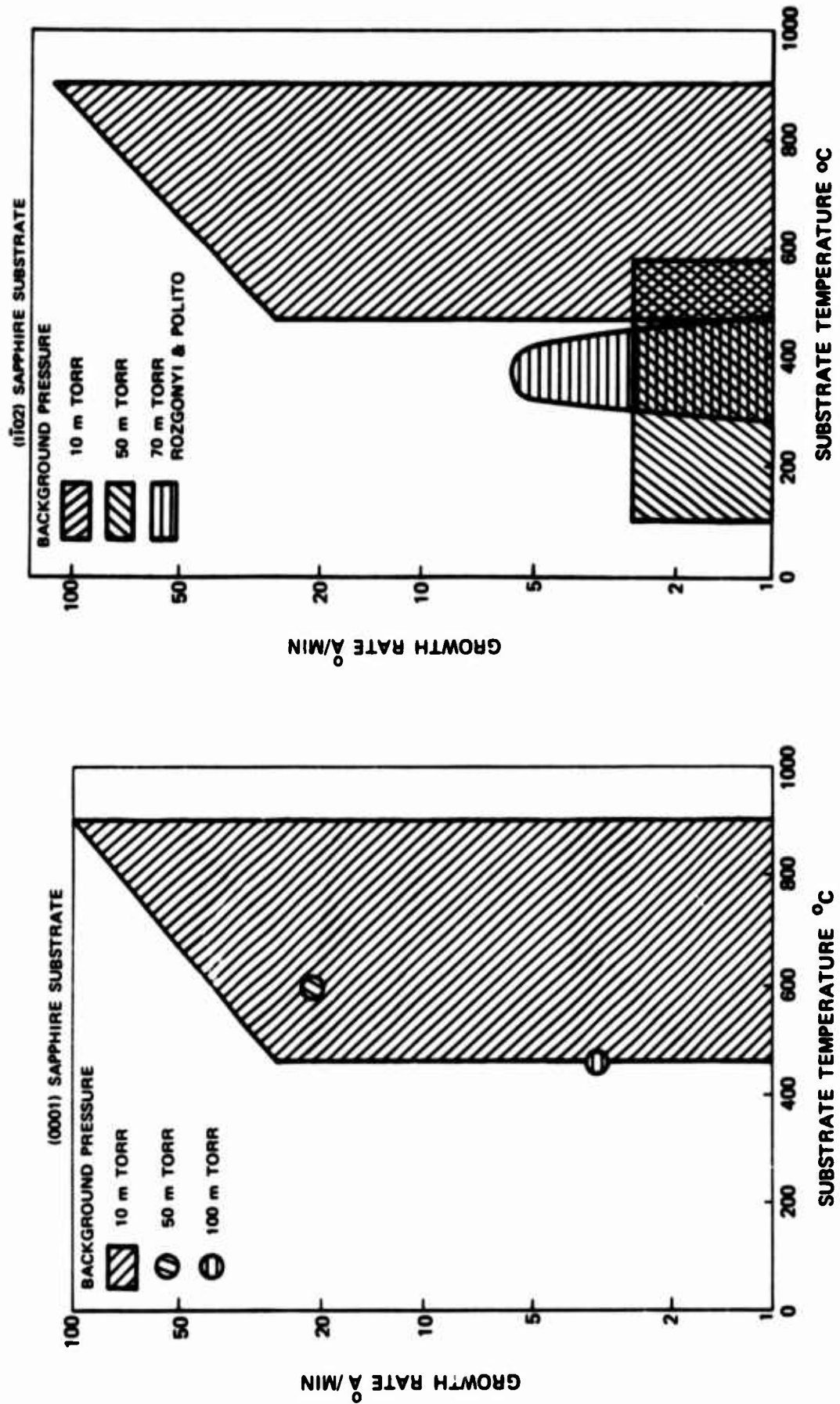
**SINGLE CRYSTAL NODULES OF ZnO ON EPITAXIAL SPUTTERED ZnO FILM AT 800°C
ON (1102) SAPPHIRE SUBSTRATE**

1 μ
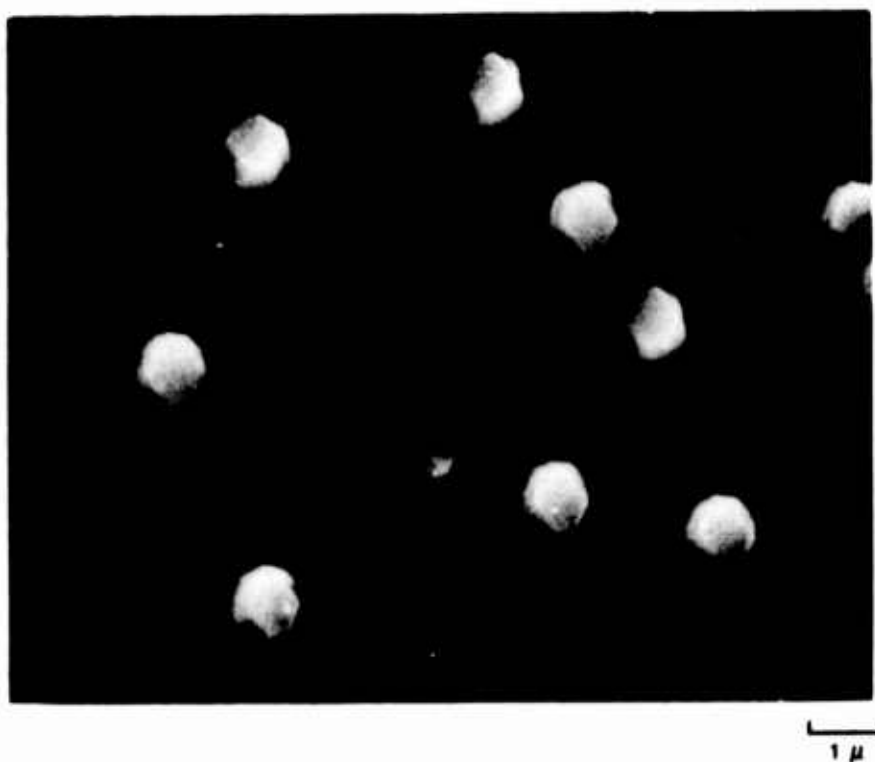
substrate temperatures of 600°C and below were relatively free of faceting, it was decided to investigate this growth region to see if the sputtering process would yield acceptable ZnO light guiding films without the need of post deposition polishing. A second reason which favored growing at a lower temperature was the likelyhood of less mechanical strain being introduced in the film when cooling down to room temperature. In this way it was hoped that the possibility of post deposition annealing could be avoided. Indeed it was found that post deposition annealing at temperatures up to 900°C did nothing to reduce the optical attenuation of these films. Attenuation measurements were made as described in Appendix III. Table 3-I summarizes the more important results of this portion of the investigation. Only samples whose growth conditions yielded films which showed less than about 15db/cm attenuation with .6328μm wavelength light are presented. Note that the films grown at the low rates are much less in thickness so that direct evaluation of the effects of this deposition parameter is difficult.

For the films grown on the (1T02) sapphire, we have listed some samples which are polycrystalline. It is interesting to compare the attenuation measurements of some of these films with the single crystal films. Note that the film of sample 77 in particular exhibits better transmission properties than several other single crystals films. While it is not known exactly why this film should exhibit such desirable properties in spite of its poorer structure, it is felt that the combination of substrate temperature, deposition rate and background gas pressure for this sample resulted in producing a much cleaner film than some other conditions which produced single crystalline but less pure films. Because of this, losses due to impurity absorption could have been reduced in sample 77.

From this portion of the study we found that the best ZnO films for optical waveguiding could be produced using the conditions of sample 82 for the (1T02) sapphire substrates and sample 84 for the (0001) sapphire substrates.

3.6 Surface Acoustic Wave Device Evaluation

The performance of the zinc oxide films grown on (1T02)sapphire substrates was evaluated using an interdigital transducer structure. The film thickness was 1.4μm; therefore, the surface acoustic wave velocity was strongly affected by the sapphire substrate. Transducers were placed to propagate acoustic waves parallel and perpendicular to the c-axis of the zinc oxide (see Fig. 3-19). The minimum untuned two port insertion loss was 43 dB for propagation along the c-axis. Perpendicular to the c-axis the insertion loss was 22dB higher.

The acoustic resonant frequency was determined to be 215MHz.

TABLE 3-I

RESULTS OF FILM ATTENUATION MEASUREMENTS

(1102) SUBSTRATE

SAMPLE	ATTENUATION db/cm	THICKNESS μm	GROWTH TEMPERATURE °C	GROWTH RATE Å/min	BACKGROUND GAS PRESSURE mTorr	STRUCTURE
82	1.9	1.55	465	27.2	10	Single
77	4.3	1.7	465	81	10	Highly Oriented Poly
76	6.4	2.1	525	111	10	Single
88	8.1	0.54	465	3.3	50	Single
78	9.7	2.2	405	122	10	Oriented Poly
90	15.3	0.52	575	3.2	50	Single
79	15.5	1.65	225	122	10	Oriented Poly

(0001) SUBSTRATE

SAMPLE	ATTENUATION db/cm	THICKNESS μm	GROWTH TEMPERATURE °C	GROWTH RATE Å/min	BACKGROUND GAS PRESSURE mTorr	STRUCTURE
84	2	.14	575	2	50	Single
85	4	.19	100	2.6	50	Single
86	7.3	.19	575	.68	50	Single

FIG. 3-19

SURFACE ACOUSTIC WAVE TRANSDUCER PATTERNS ON (11$\bar{2}$0) ZnO

The transducer insertion loss as a function of frequency is shown in Fig. 3-20 for the interdigital transducer pattern aligned to propagate surface acoustic waves along c-axis of the zinc oxide. The piezoelectric coupling coefficient k^2 was measured to be approximately 0.4%.

This is substantially higher than the value of 0.31% (Ref. 3-6) reported for zinc oxide films on sapphire prepared by the close-space transport method. The measured surface acoustic wave velocity was 5100 m/sec. This compares favorably with the calculated value of Lim (Ref. 3-7) for zinc oxide on sapphire for the film thickness to transducer pattern periodicity ratio (.056).

At the time that these measurements were made, the film exhibited a resistivity of better than 10^6 Ω-cm. These were the as grown conditions. This film was then set aside and the measurement of insertion loss repeated at a later date. The film was then found to have an untuned insertion loss of 66db/cm and furthermore the resistivity had dropped to about 10^4 Ω-cm. This experience further points out the necessity of protecting the ZnO film from contact with the atmosphere as pointed out by Hammer et.al. (Ref. 3-8).

3.7 Conclusion

The conclusion is that rf sputtering is a viable technology for growing single crystal ZnO films of sufficient quality for use in integrated optics. Furthermore this process yields a film which does not require lithium diffusion to enhance the resistivity or surface polishing to reduce scattering from surface roughness. By contrast both of these processes are required for ZnO films grown by chemical vapor deposition techniques. The major drawback to the use of ZnO in applications which require it to have a high resistivity such as for electrooptic or acoustic optic devices, is the fact that it reacts quite readily with the atmosphere and becomes less resistive. In order to retain a high resistivity, it would be necessary to passivate the film immediately after growth preferable before the film is even exposed to the atmosphere.

FIG. 3-20

UNTUNED INSERTION LOSS vs FREQUENCY FOR A ZnO FILM ON SAPPHIRE (1102)
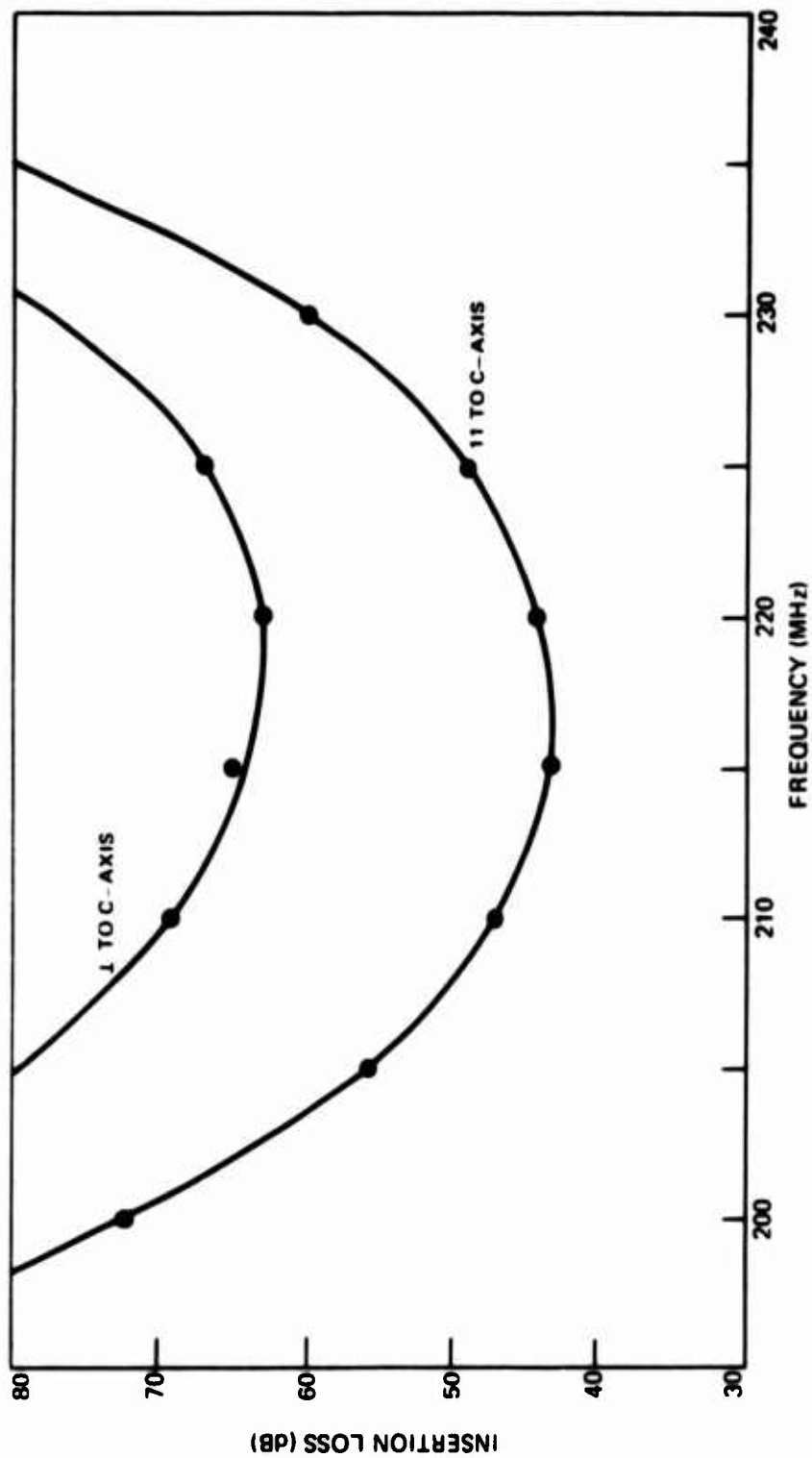
3.8 References

3-1. E. Kay, J. Appl. Phys. $\underline{34}$, 760 (1963).

3-2. G. C. Schwartz, R. E. Jones, and L. I. Maissel, J. Vac. Sci. Technol. $\underline{6}$ 351 (1969).

3-3. See for example Rose and Clark, Plasma and Controlled Fusions, (The MIT Press, Massachusetts Institute of Technology and John Wiley and Sons, Inc., New York (1961) pp. 215 ff.

3-4. E. Krikorian and R. J. Sneed, J. Appl. Phys. $\underline{37}$, 3665 (1966).

3-5. G. A. Rozgony, and W. J. Polito, J. Vac. Sci. Technol. $\underline{6}$, 115 (1969).

3-6. J. H. Collins, P. J. Hagon, and G. R. Pulliam, Ultrasonics $\underline{8}$, 218 (1970).

3-7. T. C. Lim, E. A. Kraut, and B. R. Titman, Appl. Phys. Lett. $\underline{17}$, 34 (1970).

3-8. J. M. Hammer, D. J. Chinnin, and M. T. Duffy, "High Speed Electrooptic Waveguide Grating Modulators," R.C.A. Tech. Report AFAL-TR-73-333, November (1973).

4.0 EPITAXIAL THIN FILMS OF TiO$_2$ AND WO$_3$

The fabrication of an optical waveguide structure requires that the index of refraction of the thin film deposited must be greater than the index of the substrate. For example, high index piezoelectric material such as lithium niobate (n_o = 2.29, n_c = 2.20) can be used as a substrate to fabricate colinear acousto-optic components such as modulators and filters only if the light guiding film has a higher index. Therefore, the need exists fro high index of refraction material for use in integrated optics applications. Two simple oxides which were considered in this regard were TiO$_2$ and WO$_3$.

The rutile modification of titanium dioxide (TiO$_2$) is known to have one of the highest optical indices (n_e = 2.90 || to c axis, n_o = 2.62 ⊥c) among the simple oxides. The preparation of the rutile form of titanium dioxide is complicated by the fact that there exists two other polymorphic forms of the oxide, anatase (2.55, 2.49) and Brookite (2.58, 2.58, 2.74). In many cases, the variation in the measured properties reported on thin film titanium dioxide is due in large measure to the fact that the films deposited are generally comprised of mixed phases of titanium dioxide. Goshtagore and Norieka (Ref. 4-1) have been able to successfully prepare epitaxial films of rutile by chemical vapor deposition utilizing the reaction of titanium tetrochloride and oxygen. We believe that our work represents the first successful effort in obtaining epitaxial single crystal films of rutile by reactive rf sputtering.

Tungsten trioxide has a perovskite like structure. It crystallizes at room temperature in the monoclinic system with lattice parameters a = 7.30, b = 7.53, c = 7.68 and β = 90.9°. It is reported to have one of the highest dielectric constants (∿ 1000) among the simple oxides. The refractive index of WO$_3$ (n_a = 2.703, n_b = 2.376, n_c = 2.283)(Ref. 4-2) makes it a particularly interesting material for fabrication of waveguide structures in combination with high index substrates of piezoelectric lithium niobate.

Initially TiO$_2$ and WO$_3$ films were sputtered onto 7059 glass substrates. Polycrystalline deposits always resulted even at the lowest substrate deposition temperatures (∿ 50°C). Evaluation of the optical waveguiding characteristics of these structures showed that the polycrystalline films exhibited scattering losses in excess of 50dB/cm. Low loss amorphous films could not be deposited as can be done in the case of tantalum pentoxide (Ref. 4-3). These results clearly indicated that epitaxial thin films of TiO$_2$ and WO$_3$ would be required if low loss optical waveguide structures were to be fabricated employing these materials. Therefore, an effort was initiated to explore the feasibility of growth of single crystal films of TiO$_2$ and WO$_3$.

The conditions for epitaxy of TiO$_2$ and WO$_3$ and the structural, electrical and optical properties of the films are presented below.

4.1 Experimental Details For Deposition of TiO_2

Films of rutile were prepared by reactive rf sputtering of a titanium target in oxygen. The titanium target was 99.999% pure and the oxygen was 99.994% pure. The sputtering chamber was of stainless steel, pumped with a conventional oil diffusion pumped and backed with a standard mechanical pump. A liquid nitrogen cooled chevron baffle and a water cooled chevron baffle were located between the chamber and the diffusion pump. All vacuum ports were sealed with viton A "O" rings. The system was evacuated to approximately 2×10^{-6} torr before each run.

A movable shutter was provided between the substrate and the target. The target was sputtered clean for about 10 minutes with the shutter closed. Then, without interrupting the sputtering process, the shutter was opened and deposition began. The sputtering gas was admitted to the chamber through a precision micro-meter valve. Since the system was continuously pumped during deposition, a throttling valve was necessary to keep from overloading the diffusion pump. The inlet and exhaust valves were adjusted to provide a chamber pressure of 15×10^{-3} torr and a diffusion pump foreline pressure of 25×10^{-3} torr. Rated pumping speeds for the diffusion pump at this foreline pressure is about 250 liters per minute. The volume of the sputtering chamber is about 25 liters, so that the sputtering atmosphere was being completely renewed about 10 times per minute.

Substrates were heated by placing them either directly onto a tantalum strip heater or on a thin high purity Al_2O_3 slide which was in direct contact with the heater. The temperature of the heater was monitored with an optical pyrometer at temperatures above $800^{\circ}C$ and with a chromel-alumel thermocouple spot welded to the heater at temperatures below $800^{\circ}C$. Agreement between the two was within $5^{\circ}C$ at $800^{\circ}C$. Above $800^{\circ}C$ the thermocouple weld would not hold due to the deterioration of the heater in the oxygen sputtering environment. At the elevated temperatures strip heater life was limited. The correlation between heater temperature and sapphire substrate temperature was established by measuring the change in length of a c-axis oriented sapphire substrate for a given heater temperature. The substrate temperature was then inferred from values of the linear expansion for sapphire perpendicular to the c-axis. More details of this calibration are presented in Appendix II.

At the outset efforts to achieve epitaxy were directed toward growing rutile on rutile. Rutile substrates oriented with the c-axis normal to the surface. Epitaxy was obtained at a substrate heater temperature of $650^{\circ}C$, an oxygen pressure of 10^{-2} torr and power density of $1.6W/cm^2$. Under similar conditions, heteroepitaxy was not observed for sapphire, spinel or lithium niobate substrates. The preparation of the substrate materials is discussed in Appendix I. The effort to prepare heteroepitaxial deposits of TiO_2 focused initially on sapphire mainly because of the successful results of Goshtagore and Norieka (Ref. 4-1) which were achieved by CVD. Heteroepitaxy of TiO_2 on sapphire by reactive sputtering was first

observed at a substrate temperature of 700°C. Studies were extended to temperatures as high as 1200°C but at the upper heater temperatures, heater life was so severely limited that operation at these temperatures was impractical. The most reproducible results were obtained at a substrate temperature of 850°C. Power densities of 1.2W/cm^2 to 6.4W/cm^2 were explored. For sapphire substrates the best results were obtained at a power input density of 2.4W/cm^2 into the titanium target which corresponds to a deposition rate of 50Å/min. The sputtering ambient was 20mTorr of oxygen. Comparable results were obtained with spinel substrates. The best depositions for TiO_2 on lithium niobate were determined to be a substrate temperature 900°C, power density 6.4W/cm^2 and a chamber pressure of 20μ O_2.

The films which were grown were clear and smooth. Epitaxial layers up to 1μm in thickness were grown. Film uniformity was excellent. Rutile films deposited on silicon substrates had a resistivity of $10^{13}\Omega$-cm. Ellipsometer measurements of rutile films deposited on silicon gave a value of 2.55 for the index of refraction.

4.2 Structural Characterization of TiO_2 Films

The film structure and epitaxial relationships were arrived at by reflection electron diffraction and x-ray diffraction data. Figure 4-1a shows the expected reflection electron diffraction pattern with the electron beam directed along [010] zone axis if the rutile film grows with its c-axis normal to the film plane. The diffraction pattern obtained for an epitaxial film grown on a (001) oriented rutile substrate is shown in Fig. 4-1b.

X-ray diffractometer traces of TiO_2 films grown on ($1\bar{1}02$) oriented sapphire substrates show a single diffraction peak corresponding to a "d" spacing of 2.489Å. This can be interpreted as (101) rutile planes growing parallel to the substrate. In order to analyze the reflection electron diffraction data, diffraction patterns were calculated for the electron beam directed along the [101] and [010] directions with (101) planes parallel to the surface (see Fig. 4-2). This can be readily identified with the experimentally obtained diffraction patterns shown in Fig. 4-3. The angular rotation of the electron beam required to observe the [010] and [101] patterns is 90° and each individual pattern repeats with a period of 180° as expected for a tetragonal structure.

The data for rutile films grown on (0001) sapphire substrates is somewhat more ambiguous to interpret. X-ray diffractometer data indicate that (100) planes of rutile grow parallel to the (0001) planes of sapphire. Figure 4-4 shows reflection electron diffraction data which can be correlated with [010] and]001] directions of rutile. The calculated diffraction patterns are illustrated in Fig. 4-5. Although there is apparent agreement between the measured and calculated results, an examination of the angular dependence of the diffraction patterns

FIG. 4-1

CALCULATED AND EXPERIMENTAL RED PATTERN FOR RUTILE
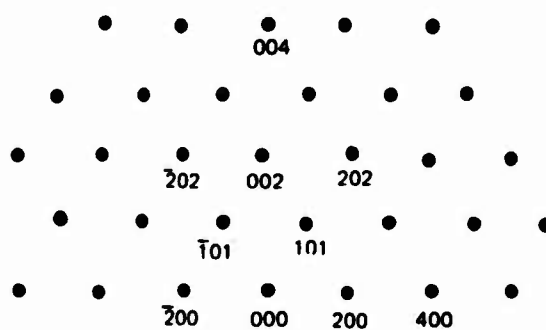
a) CALCULATED RED PATTERN FOR [010] DIRECTION OF RUTILE WITH (001)
PLANES PARALLEL TO FILM SURFACE

b) RED OF TiO_2 ON [001] RUTILE

FIG. 4–2

CALCULATED RED PATTERNS FOR RUTILE FILM
WITH (101) PLANES PARALLEL TO SURFACE
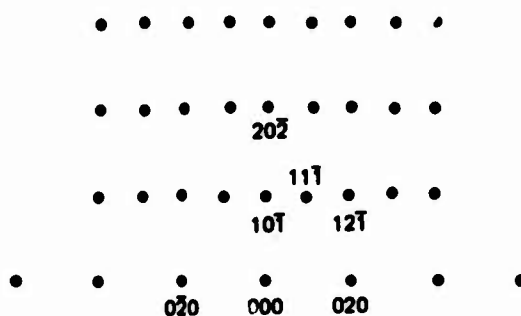
ELECTRON BEAM DIRECTED ALONG [101]

ELECTRON BEAM DIRECTED ALONG [010]

FIG. 4-3
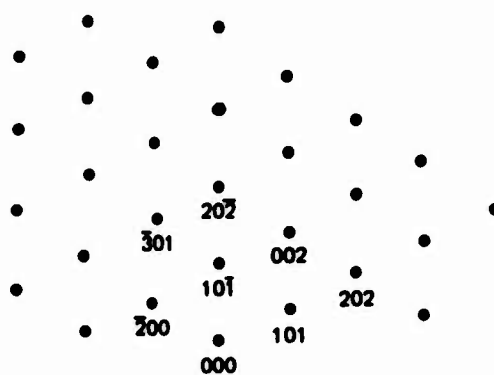
RED OF TiO$_2$ ON (1102) Al$_2$O$_3$

|101|

|010|

FIG. 4-4
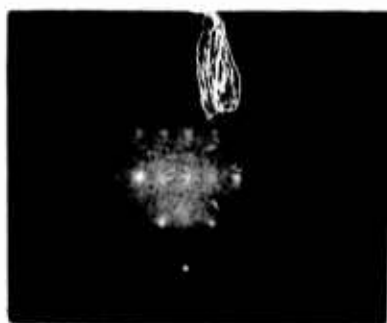
RED OF TiO$_2$, ON (0001) Al$_2$O$_3$

[010]

[001]

CALCULATED RED PATTERN FOR TiO$_2$ FILM
WITH (100) PLANES PARALLEL TO SURFACE
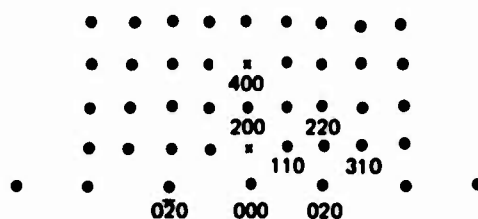
ELECTRON BEAM IN (001) DIRECTION
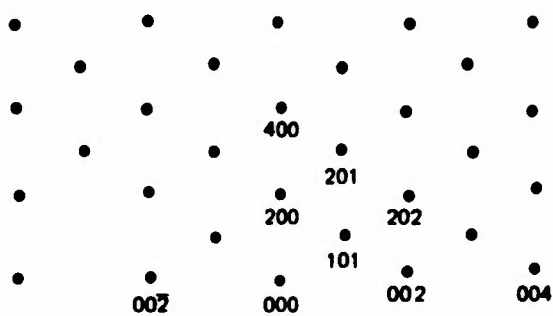
ELECTRON BEAM IN (010) DIRECTION

reveals that the repeat period for the [010] and [001] patterns is 60° rather than 180°. In addition the two patterns alternate with a 30° period rather than 90°. This symmetry cannot be explained on the basis of the tetragonal symmetry of rutile. There is no evidence in the literature that a hexagonal modification of TiO_2 exists. A careful examination of the diffraction patterns reveals that the higher order reciprocal lattice points occur in pairs. A similar effect is observed in the diffraction data for chemical vapor deposited films on (0001) sapphire presented by Goshtogore and Norieka (Ref. 13). Furthermore, (100) rutile planes are identified as growing parallel to (0001) sapphire planes. However, a point of confusion arises with their assessment of the epitaxial relationship between the film and substrate. The reciprocal lattice vectors [001] and [011] of rutile are identified with the [110] direction of sapphire. This appears to be in error and a further comparison of results becomes impossible.

A possible interpretation of our observations is the following. The (0001) plane of sapphire exhibits bi-3-fold symmetry. The atomic arrangement of sapphire in this plane cannot accommodate, in an unambiguous fashion, the atom arrangement of (100) planes of rutile which have two fold symmetry. A reasonably speculation is that three equivalent nucleation sites may occur on the (0001) sapphire which would give rise to an unusual twinned crystal arrangement exhibiting the six-fold symmetry observed.

Rutile films grown on (100) oriented spinel substrates are found to grow with (110) planes parallel to the surface of the substrate. This is borne out by x-ray diffractometer traces which show two diffraction peaks with "d" values of 3.250Å and 1.624Å which correspon' to the interplanar spacing of the (110) and (220) planes respectively. Electrondiffraction data shows the c-axis lying in the plane of the film in agreement with the x-ray data.

X-ray diffractometer data of rutile films grown on YZ cut lithium niobate substrates showed (301) planes of rutile (d = 1.360Å) growing parallel to $(10\bar{1}0)$ planes of lithium niobate. Reflection electron diffraction data is found to be consistant with the x-ray data since one could observe the diffraction pattern for the [010] zone axis oriented with (301) rutile planes parallel to the surface of the film. This is illustrated in Fig. 4-13a. The structure of rutile films deposited on lithium niobate was the poorest in quality in comparison to that obtained for the other substrates and is probably due to the poor lattice match between rutile and lithium niobate.

4.3 Surface Texture and Optical Waveguiding

The surface texture of rutile films first grown on (0001) and $(1\bar{1}02)$ sapphire was relatively rough and resulted in excessive surface scattering losses in the course of optical waveguide studies. The films grown generally were thin and did

not readily lend themselves to polishing. Figures 4-6 and 4-7 show electron micrographs of replicated surfaces of some of the early rutile films grown on (0001) and (1$\bar{1}$02) sapphire substrates. In the course of the deposition parameter studies, an increase in the deposition rate was found to be a very significant parameter in reducing optical loss as it was in the case for aluminum nitride. Deposition rates were increased from 20$\overset{\circ}{A}$/min to 50$\overset{\circ}{A}$/min. The improved surface finish resulting from an increased deposition rate is illustrated in Fig. 4-8. Further improvement in the surface finish was gained by application of 50 gauss longitudinal magnetic field at the substrate. The resulting improvement is shown in Figs. 4-9 and 4-10. The effect of magnetic field on surface finish is covered in detail in section 3.2. Waveguiding has been observed with TiO$_2$ films on both sapphire and lithium niobate substrates. The experimental arrangement is discussed in Appendix III. Typical attenuation figures for waveguide structures of TiO$_2$ on (0001) sapphire and spinel substrates at 0.6328μm is typically $\geq$ 30 dB/cm. The lowest propagation loss, 20 dB/cm, is obtained with rutile on (1$\bar{1}$02) sapphire substrates. The better films grown on LiNbO$_3$ substrates show approximately 28 dB/cm as is illustrated in Fig. 4-11. Values of film index determined from a combination of transmission measurements and waveguiding measurements are 2.55 for TiO$_2$ on LiNbO$_3$ and 2.51 for TiO$_2$ on Al$_2$O$_3$.

4.4 Preparation of WO$_3$ Films

The sputtering system used to grow the TiO$_2$ films was used with no modifications for the tungsten tioxide deposition studies with the exception of the replacement of the titanium target with tungsten. The tungsten target was analyzed to be 99.9% pure and the oxygen gas was analyzed to be 99.994% pure.

A substrate temperature range of 50°C to 1000°C was covered in the deposition studies. Ideally amorphous films of WO$_3$ would suffice for waveguide applications but unfortunately even the films deposited at the lowest substrate temperature were polycrystalline. Consequently efforts were made to grow epitaxial layers of WO$_3$. The best results were obtained at a substrate temperature of 950°C, a power density at the tungsten target of 4.8W/cm^2 and a sputtering chamber pressure of 18mTorr O$_2$.

The films grown had a smooth surface finish, were insulating and had a yellow color. The yellow color results from absorption in the blue since the reported band gap for WO$_3$ is 2.5V(Ref. 4-4).

4.5 Structural Characterization of WO$_3$ Films

The best growth conditions were established by employing reflection electron diffraction. No single domain crystals were grown. Structurally the best results were obtained for films grown on (1$\bar{1}$02) oriented sapphire substrates and the

FIG. 4-6

ELECTRON MICROGRAPH TiO_2 ON ($1\bar{1}02$) Al_2O_3

NO AXIAL FIELD   RF POWER 150 W
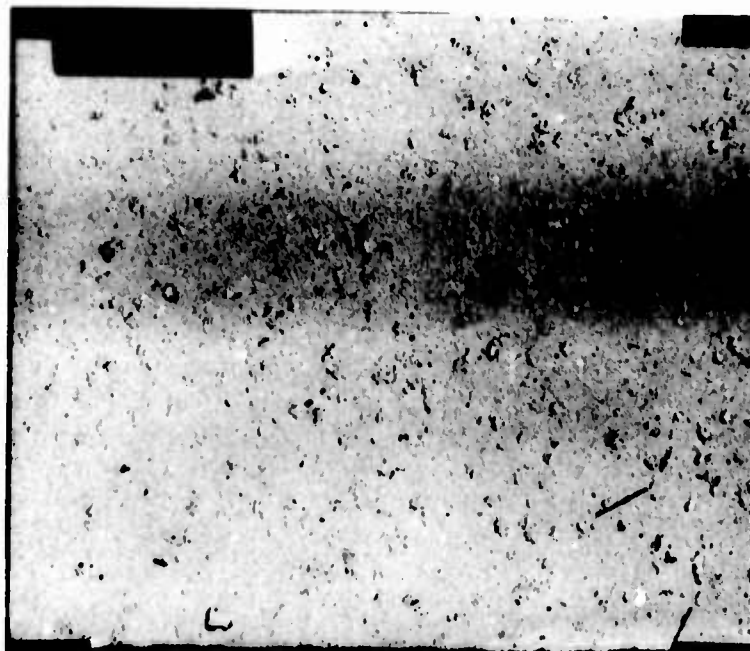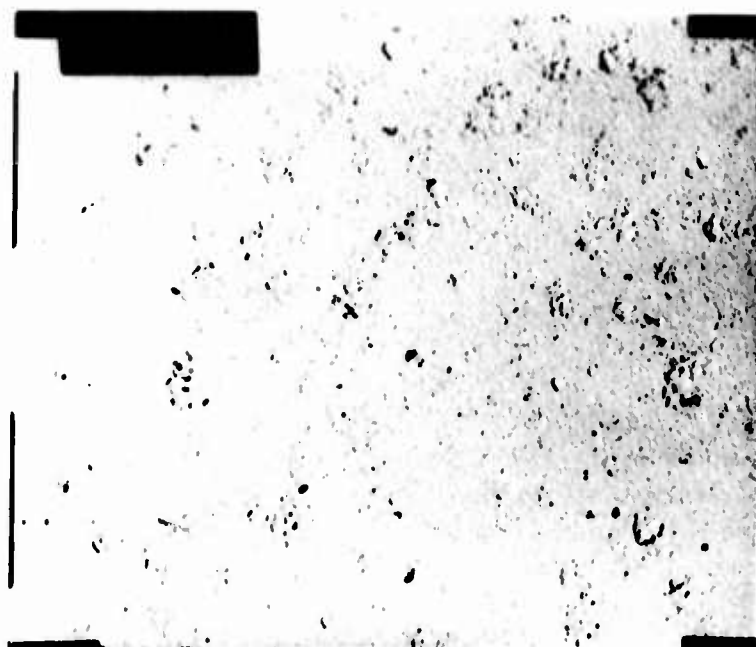
4800X

10,000X

FIG. 4—7

ELECTRON MICROGRAPH OF TiO$_2$ ON (0001) Al$_2$O$_3$

NO AXIAL FIELD   RF POWER 150 W

4800X

10,000X

FIG. 4-8

ELECTRON MICROGRAPH OF TiO_2 ON (0001) Al_2O_3

NO AXIAL FIELD   RF POWER 300W

4800X

10,000X

51

FIG. 4—9
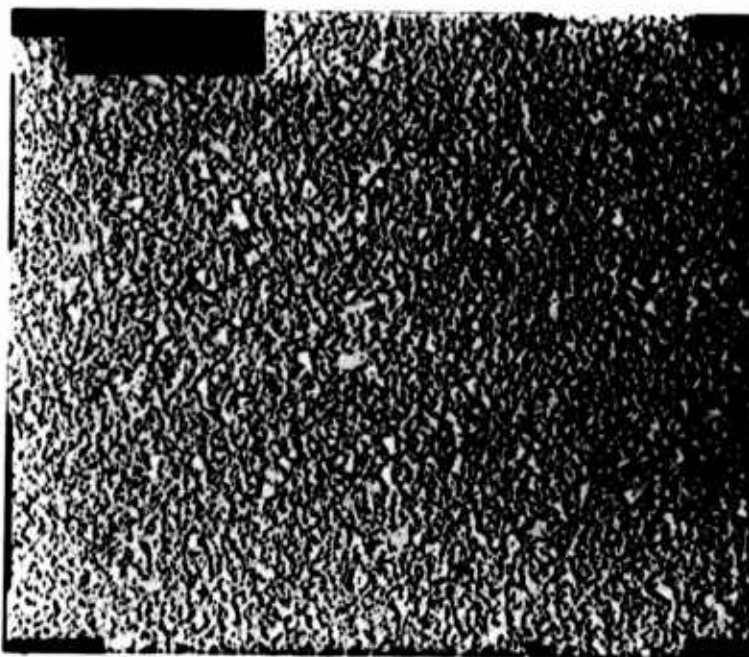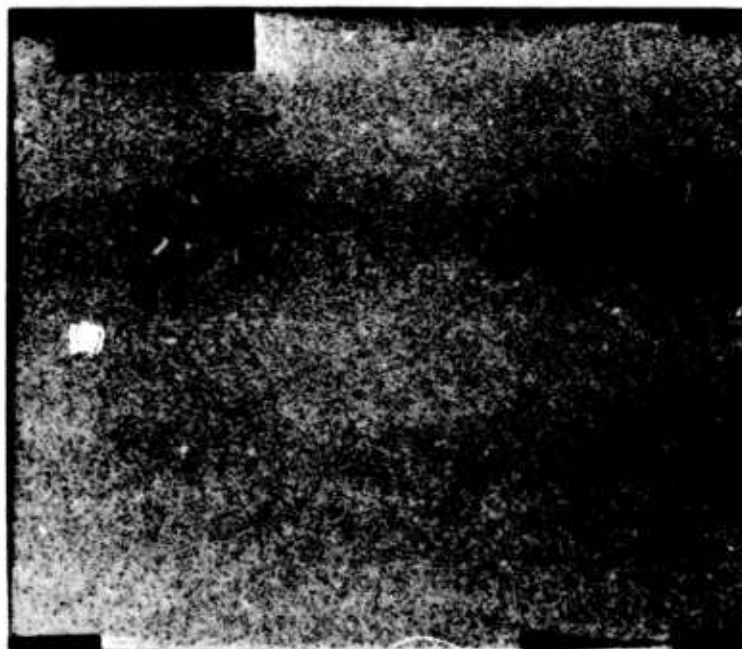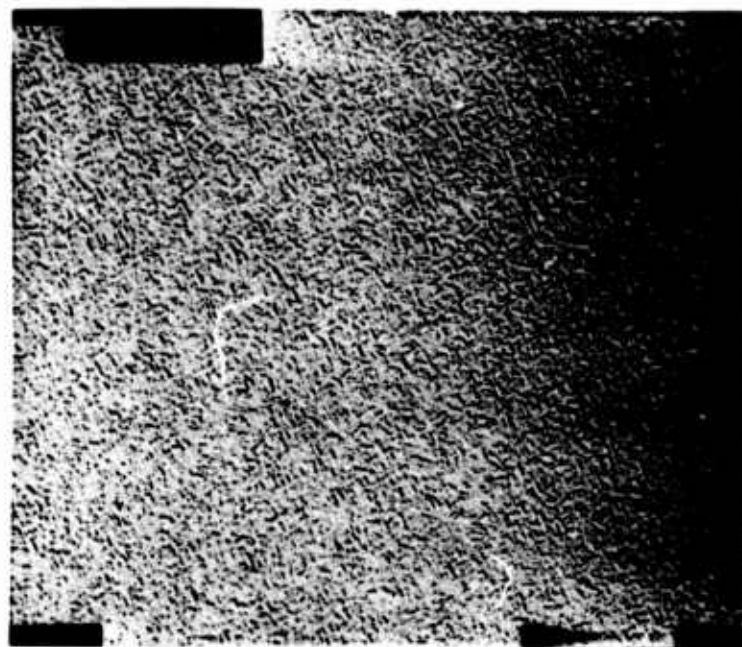
ELECTRON MICROGRAPH OF TiO$_2$ ON (0001) Al$_2$O$_3$

AXIAL FIELD   RF POWER 300 W
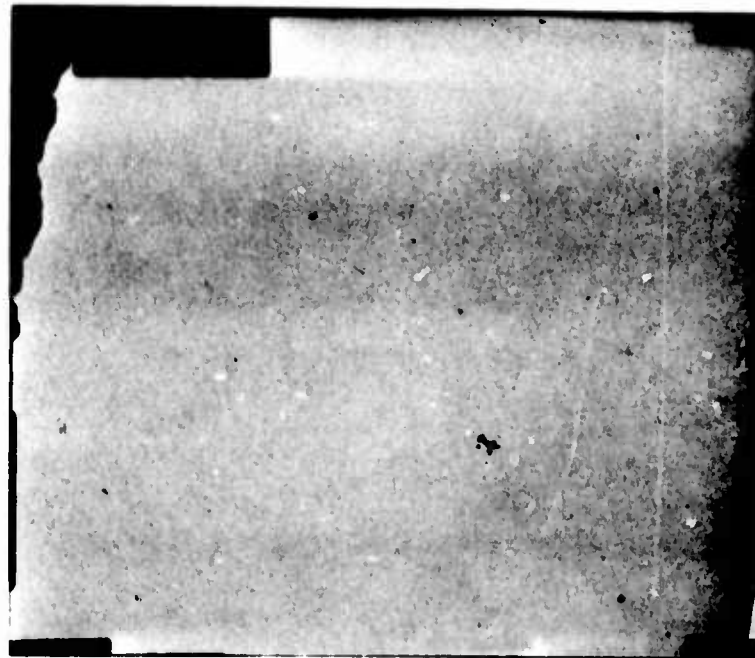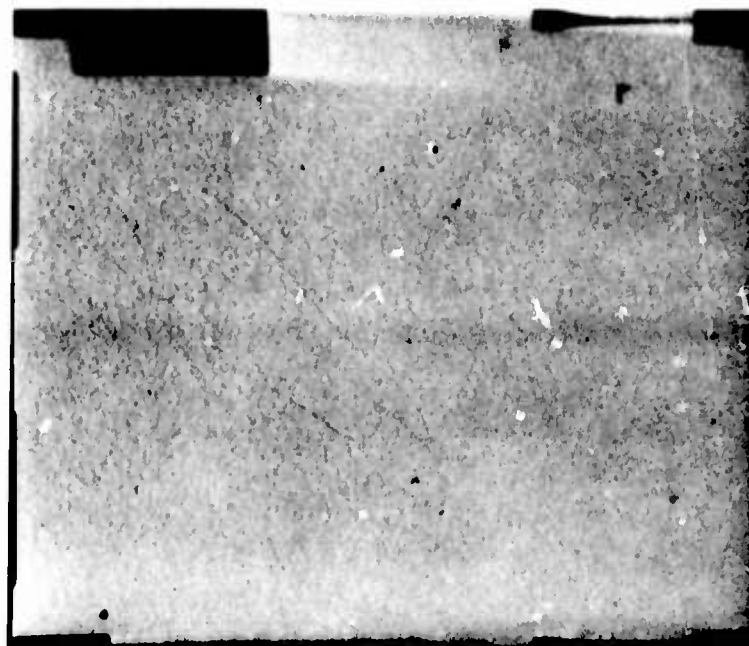
4800X

10,000X

FIG. 4—10

ELECTRON MICROGRAPH OF TiO_2 ON $(1\bar{1}02)$ Al_2O_3

AXIAL FIELD   RF POWER 300 W

4800X
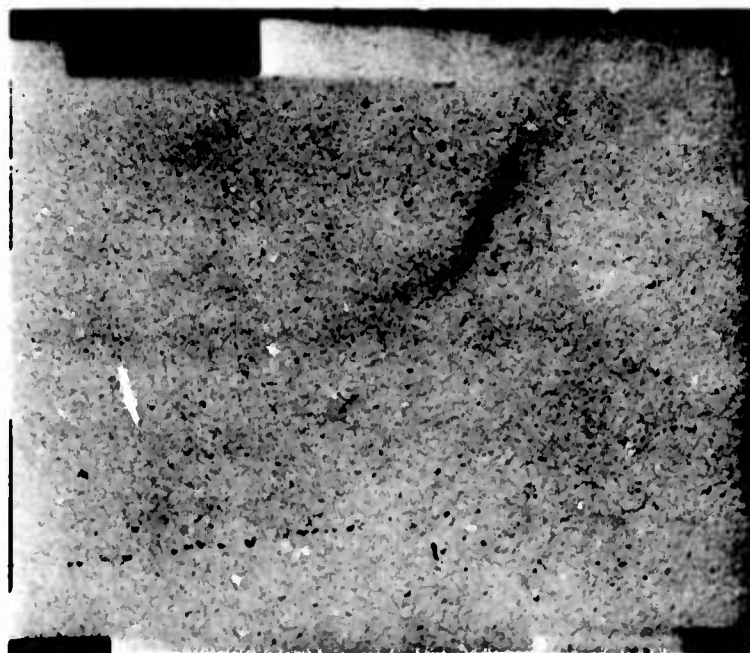
10,000X

SAMPLE NO. 36
TiO_2 ON $LiNbO_3$
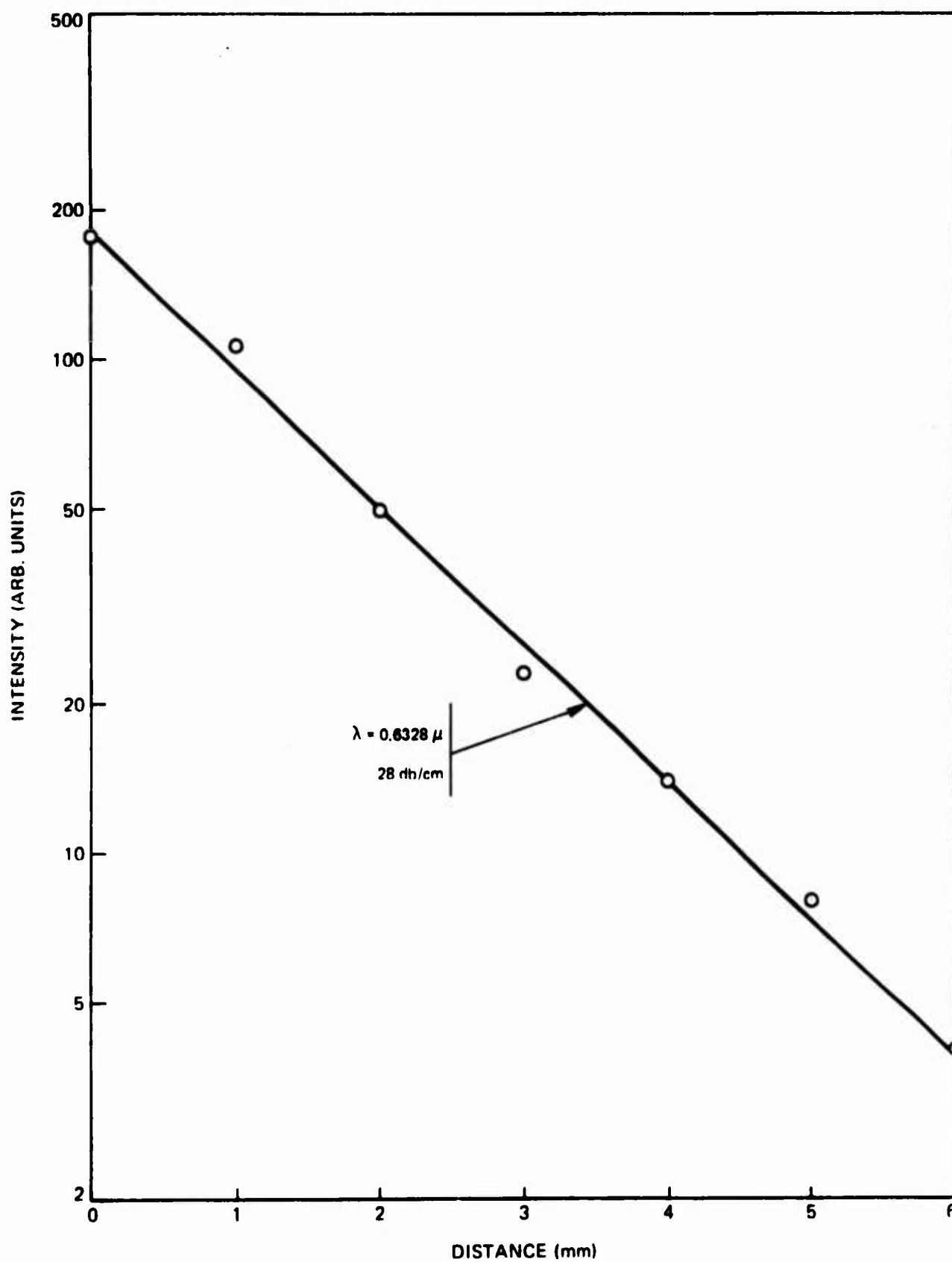
electron diffraction patterns are shown in Fig. 4-12. In all cases evidence of twinning was observed in the diffraction patterns. The twinning in WO_3 arises from domain formation (Ref. 4-5). Tungsten trioxide passes through several phases upon cooling from the growth temperature $950^\circ C$. At temperatures above 740° the crystal structure is tetrogonal. As the crystal is cooled below 740° it becomes orthorhombic and below $330^\circ C$ it passes to the monoclinic phase (Ref. 4-2). In bulk crystals the domains can be removed by an appropriately applied stress (Ref. 4-2). In the thin film heteroepitaxial structures the domain walls are pinned and no way has been found to create a single domain film. The fact that epitaxy does occur is borne out by the orientation dependence of the tungsten trioxide films on the orientation of the substrate and the substrate material on which the film is grown as illustrated below.

Tungsten trioxide films deposited on ($1\bar{1}02$) sapphire and (100) spinel substrates grow with (001) planes parallel to the substrate surface. This is shown by x-ray diffractometer traces which show "d" spacings of $3.820\overset{\circ}{A}$ and $1.916\overset{\circ}{A}$ which corresponds to diffraction from the (001) and (002) planes. The reflection electron diffraction data is shown in Fig. 4-12 for the [110] and [100] zone axes.

Tungsten trioxide films grown on (111) spinel and (0001) sapphire grow with (221) planes parallel to the substrate surface. The x-ray diffractometer trace shows a single line with $d = 2.180$ which corresponds to the interplanar spacing of the (221) planes of WO_3.

Tungsten trioxide grown on YZ cut lithium niobate grown with (111) planes parallel to the ($10\bar{1}0$) planes of lithium niobate. The x-ray diffractometer run shows two diffraction peaks with "d" spacings of $3.11\overset{\circ}{A}$ and $1.555\overset{\circ}{A}$ which corresponds to the (111) and (222) planes of tungsten trioxide. Fig. 4-13b shows the electron diffraction pattern for the [110] zone axis which is expected to occur in the plane of (111) oriented films of WO_3.

4.6 Optical Evaluation of WO_3 Films

Optical waveguide studies showed that the scattering loss of the WO_3 films was excessive on the various substrates that the films were deposited. Scattering is due primarily to domain formation in the WO_3 films. The refractive index anisotropy ($\Delta n = 0.42$) is extremely large and can give rise to excessive scattering. This feature makes tungsten trioxide unattractive for integrated optics applications.

4.7 Conclusions

The work reported constitutes, to our knowledge, the first successful effort in applying reactive rf sputtering for the epitaxial growth of the high refractive

FIG. 4-12

REFLECTION ELECTRON DIFFRACTION PATTERNS FOR WO$_3$ ON (1$\bar{1}$02) SAPPHIRE
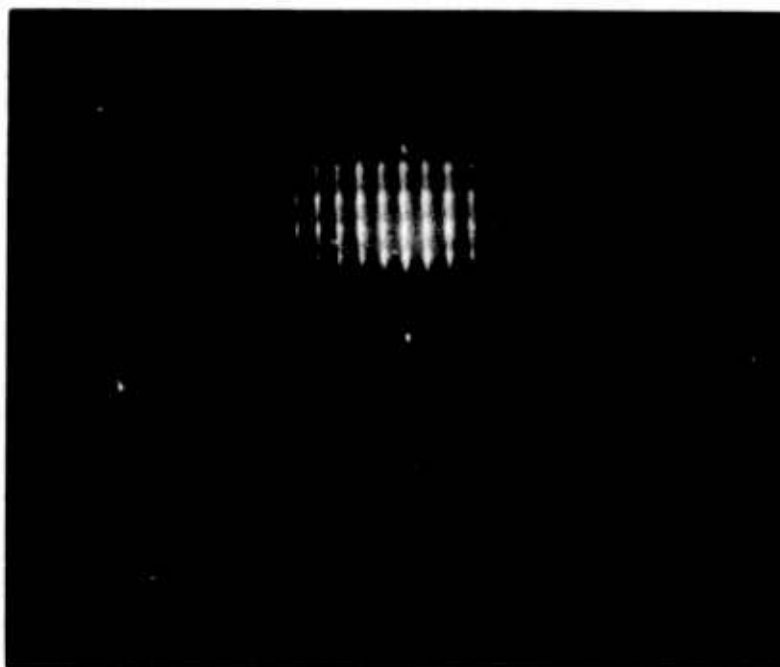
ELECTRON BEAM DIRECTED ALONG [110]
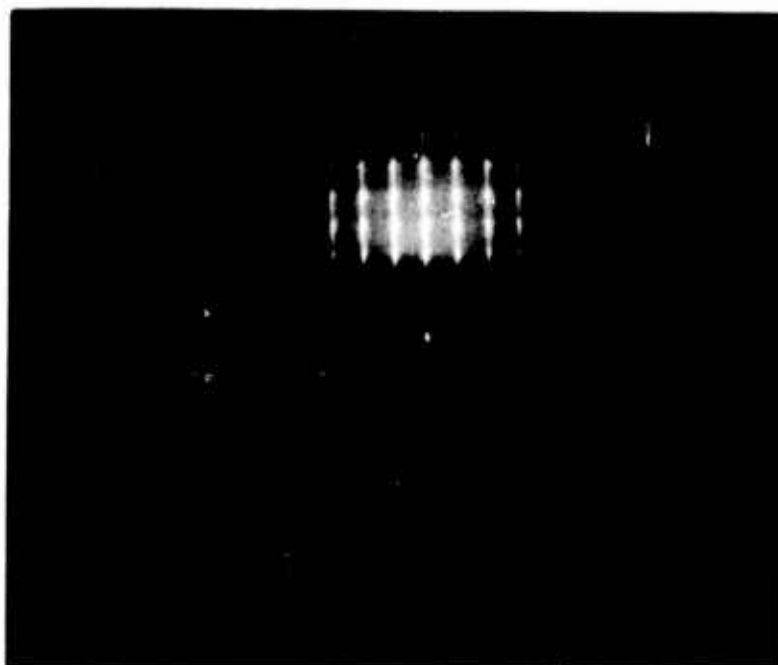
ELECTRON BEAM DIRECTED ALONG [100]

N05-240-2

FIG. 4—13

RED OF TiO$_2$ + WO$_3$ ON LiNbO$_3$

a) TiO$_2$ [010] ZONE AXIS

b) WO$_3$ [1$\bar{1}$0] ZONE AXIS

N12—159—1
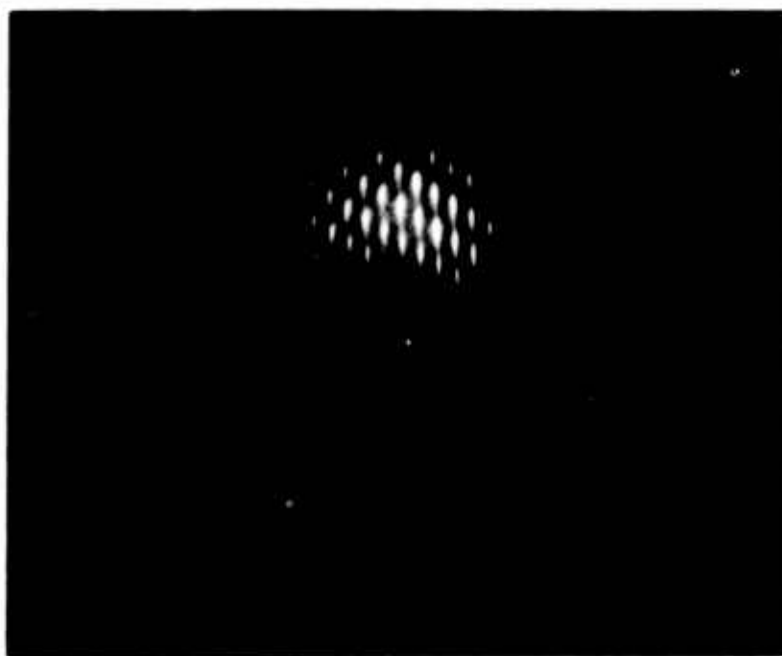
index materials - rutile and tungsten trioxide. Reactive sputtering has been demonstrated to be an effective and a less complex process for producing epitaxial deposits of these materials than chemical vapor deposition. The structural quality of the films produced is largely dictated by how close the lattice parameter match is between film and substrate and also their relative thermal coefficients of expansion. The best structural deposits of rutile were obtained with homo-epitaxial growth of rutile on rutile. The best hetroepitaxial growth of rutile was obtained on (1Ī02) oriented sapphire substrates. Although the optical wave-guide results obtained are the first of their kind for rutile, the lowest propagation losses measured, ∿ 20dB/cm, indicate that the heteroepitaxial combinations explored with rutile do not appear to be useful for integrated optics applications. The scattering losses appear to be too high. The scattering appears to be due to strain and compensating structural disorder in the films in an attempt to accomodate the mismatch in lattice parameters between film and substrate.

Epitaxial films of tungsten trioxide in waveguide structures exhibit excessive scattering loss due to domain formation and this precludes the application of tungsten trioxide for optical waveguide structures.

4.8 References

4-1. R. N. Goshtagore and A. J. Norieka, J. Electrochem. Soc. 117, 1310 (1970).

4-2. S. Sawada and G. C. Danielson, Phys. Rev., 113, 1008 (1959).

4-3. P. K. Tien, Appl. Opt., 10, 2395 (1971).

4-4. S. Sawada, J. Phys. Soc. Jap., 11, 1237 (1956).

4-5. S. Sawada and G. C. Danielson, Phys. Rev., 113, 1005 (1959).

5.0 GROWTH OF ALUMINUM NITRIDE AND GALLIUM NITRIDE
FILMS BY REACTIVE SPUTTERING

5.1 Aluminum Nitride

Aluminum nitride is one of the more refractory materials of the III-V semi-conductor group. It has a decomposition temperature in excess of 2400°C. The band gap of AlN is 6.2eV (Ref. 5-1) and it crystallizes in the hexagonal wurtzite structure with unit cell dimensions of a_o = 3.111Å and c_a = 4.980Å. Its high chemical stability and hardness makes it an attractive material for device applications.

The fabrication of aluminum nitride films has been of continuing interest in many laboratories because of the potential usefulness of these films in a variety of solid state device applications. (Ref. 5-2,3,4). In particular the preparation of single-crystal films of aluminum nitride and silicon on a common sapphire substrate presents the attractive possibility of integrating acoustic, optic and microelectronic processing functions on a single monolithic substrate. In the past, aluminum nitride films have been fabricated in several different ways. Wauk and Windslow (Ref. 5-2) used thermal evaporation of aluminum in nitrogen and ammonia gas to produce polycrystalline films suitable for microwave delay line use. Chemical vapor deposition (CVD) was employed by Manasevit and Simpson (Ref. 5-5) and Duffy et.al. (Ref. 5-6) to fabricate single-crystal films for surface acoustic wave applications. Norieka et.al. (Ref. 5-7) presented electrical and optical data on polycrystalline films prepared by dc reactive sputtering in argon-nitrogen mixtures. Rutz et.al. (Ref. 5-4) reported that polycrystalline switchable memory resistor could be fabricated by rf sputtering in nitrogen. This work was reported when we were well into our research program.

The objective of this study was to explore the feasibility of using reactive rf sputtering for the preparation of epitaxial films of aluminum nitride on selected single crystal substrates which would be useful for integrated optics and surface acoustic wave technology, and to compare the relative merits of nitrogen and ammonia ambients for the synthesis and growth of nitrides by reactive sputter-ing. The work reported here represents the first extensive work on sputtering in ammonia ambients. At the outset of the program, substrate deposition temperatures were limited to a range of 50°C to 700°C. The limitation was imposed by the substrate heater design. It was found that films grown in this temperature range were polycrystalline. One interesting feature of the study was a surprising orientation dependence on the composition of the sputtering gas ambient. Structural, optical and electrical characteristics of the polycrystalline films are presented below.

In order to establish the conditions for epitaxial growth of AlN, higher substrate temperatures were required. This led to the use of molybdenum or

tantalum strip heaters. The conditions determined for epitaxial growth of aluminum nitride on single crystal substrates of sapphire, spinel and silicon carbide are described. In addition, data on the structural, piezoelectric and optical properties of the epitaxial films are presented.

5.2 Reactive Sputtering System

The sputtering chamber is constructed of stainless steel and all feedthroughs are sealed with crushed copper gaskets so that the system is bakeable to 300°C without degradation of seals or contamination by them. Sputtering pressure is measured by Varian Millitorr ion gauges. Two magnet coils which have been welded into stainless steel cases are mounted internal to the chamber to provide an axial field between the target and substrate. The magnets enhance as well as confine the rf plasma. Adjustment of field strength influences substrate heating and uniformity of the deposition. The chamber is evacuated by a Welsh 3103 turbo-molecular pump which is capable of pumping of 250 L/sec in the millitorr range. Use of the turbomolecular pump in place of conventional oil diffusion pump eliminates the "backstreaming" of hydrocarbons which could result in contamination of the substrate when the system is operated at high temperatures. The system used in the program for epitaxial deposition of aluminum nitride and gallium nitride is shown in Fig. 5-1.

5.3 Deposition of Reactively Sputtered AlN 50-700°C

Aluminum nitride was synthesized by reactive rf sputtering of aluminum in either ammonia or nitrogen ambients. The reactive gases had an assayed purity of 99.999% or better. The target was 99.999% aluminum. Films were deposited on single crystal substrates of (0001) Al_2O_3, ($1\bar{1}02$) Al_2O_3, (110) $MgAl_2O_4$, (111) $MgAl_2O_3$, (0001) SiC and (100) silicon. Fused silica and 7059 Corning glass substrates were also used.

A typical sputtering run was as follows: .

(1) The sputtering system was evacuated to 10^{-6} torr or less. Substrates were heated to 700°C during evacuation and then cooled to the deposition temperature required.

(2) The reactive gas was introduced to the desired pressure and the rf discharge started while the substrates were protected with a shutter during sputter cleaning of the target. The target was sputter cleaned at a power density of 4.4 watts/cm^2 for one-half hour. This removes approximately 0.5μ of material from the target before film deposition is started.

RF SPUTTERING SYSTEM

FIG. 5-1

RF SPUTTERING SYSTEM
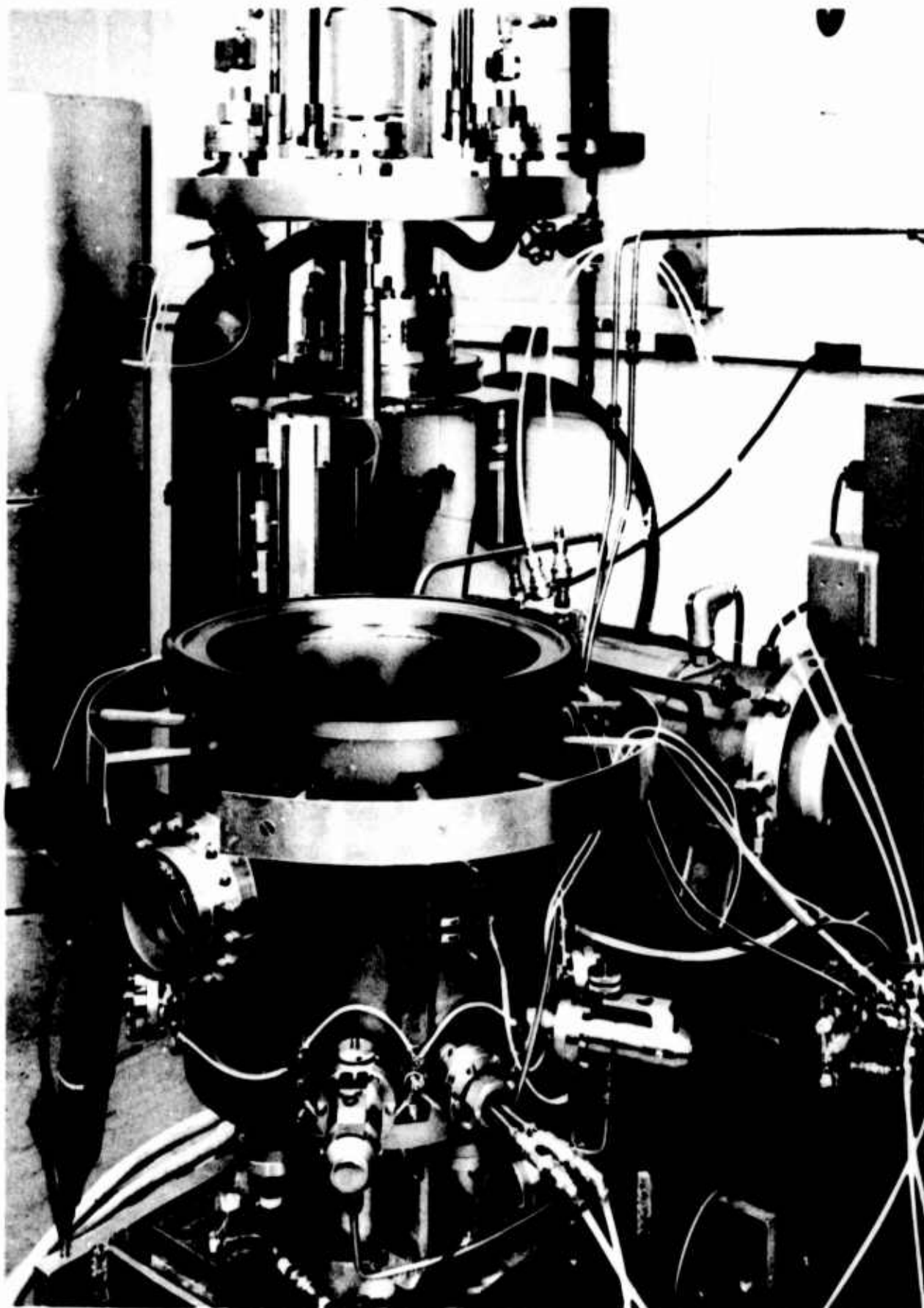
(3) With the shutter removed the sputtering of the films was started. Rf power density was varied between 0.16 watts to 4.4 watts/cm^2. This corresponded to a range of AlN deposition rates between 1-60Å/min. Films deposited ranged between 1000Å and 18μ in thickness.

5.3.1 Film Structure

Films which were deposited even at the lowest substrate temperature (50°C) were polycrystalline. All films exhibited the hexagonal wurtzite structure of aluminum nitride. A marked difference in structural ordering was observed between films grown in nitrogen and ammonia ambients. Nitrogen sputtered films tend to grow with (00.ℓ) and (h0.ℓ) planes parallel to the film surface, whereas films grown in ammonia tend to grow with the c-axis in the plane of the film. The degree of ordering increases with increasing substrate temperature. This is illustrated in Figs. 5-2 through 5-5 for films deposited at substrate temperatures ranging between 200-700°C. Films sputtered in ammonia exhibits a higher degree of ordering at comparable substrate temperatures then those sputtered in N$_2$. To our knowledge this is the first evidence for a preferential structural ordering which is influenced by the composition of the reactive gas. Foster (Ref. 5-8) has observed that hydrocarbon contamination tend to yield films with the c-axis in the plane of the film.

Noreika (Ref. 5-7) deposited AlN films by dc reactive sputtering in a nitrogen-argon ambient at a substrate temperature of 900°C and produced films with a highly preferred fiber texture with (0001) planes parallel to the substrate surface. Fig. 5-5, shows the variations in orientation and texturing for polycrystalline films of AlN deposited at selected temperatures and reactive ambients. The diffraction patterns were obtained with a Read thin film camera using Cu-Kα radiation with a fixed beam-to-film angle of 29.5°. Clearly the ordering is most pronounced for films sputtered in ammonia as a illustrated in Figs. 5-5 and 5-6d.

The reason for the orientation dependence AlN films on the reactive ambient is not certain but may be related to the relative reactivities of NH$_3$ and N$_2$. The more highly reactive ammonia could result in the formation of AlN on the aluminum target and result is the direct sputtering of AlN. Nitrogen being less reactive could result in the formation of aluminum nitride at the substrate. The yellow cast of films grown in nitrogen tend to support this surmise.since the yellow coloring is attributed to nitrogen deficient films.

5.3.2 Optical Characteristics of Polycrystalline Aluminum Nitride

Films sputtered in nitrogen were amber to brown in color and showed an absorption edge shifted to lower frequencies. Similar results were reported by

FIG. 5-2

DIFFRACTOMETER TRACES OF AlN FILMS REACTIVELY SPUTTERED IN NH₃ AT 200° C ON (0001) AND (10$\bar{1}$2) Al₂O₃ SUBSTRATES.

63

FIG. 5-3
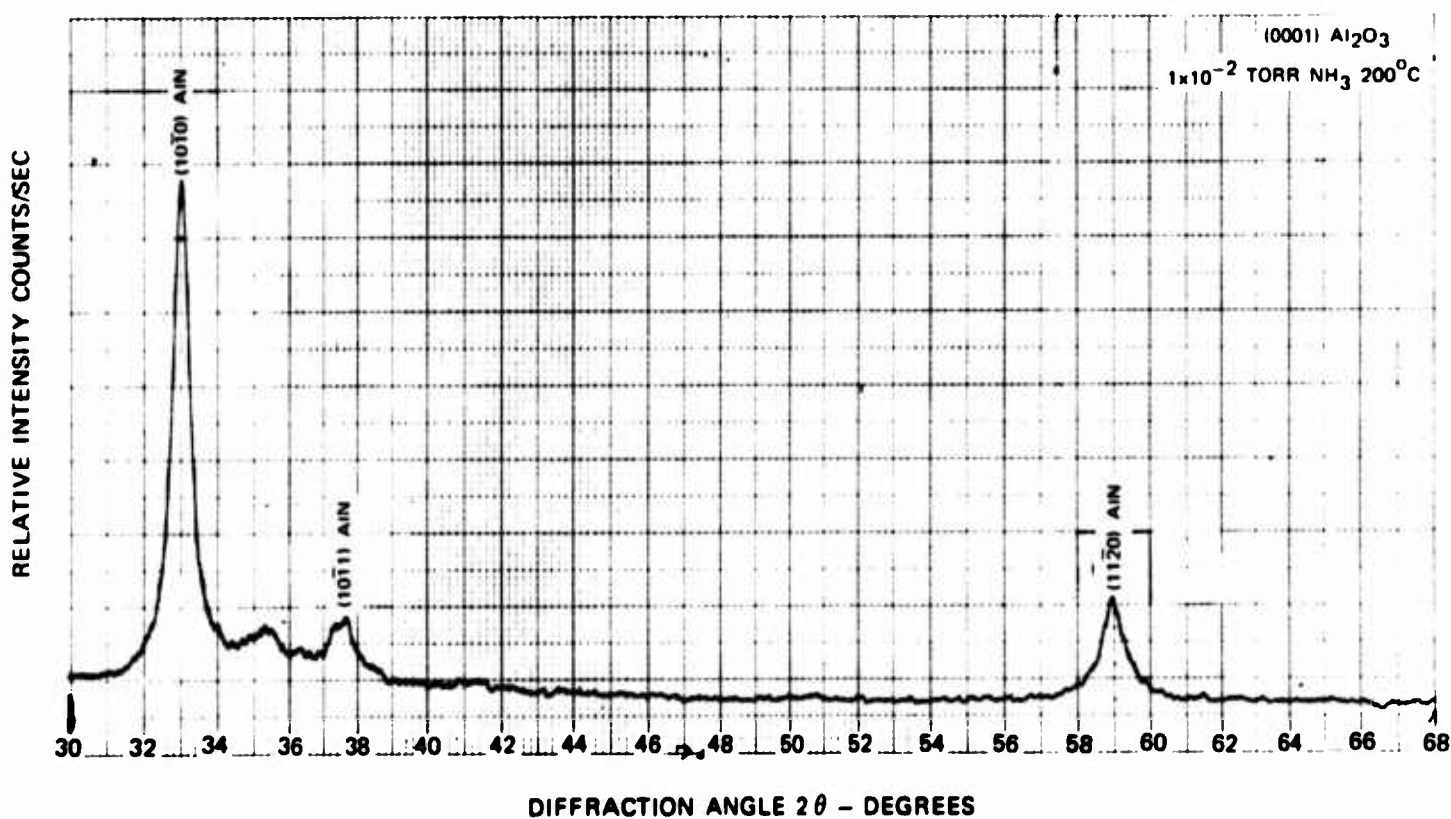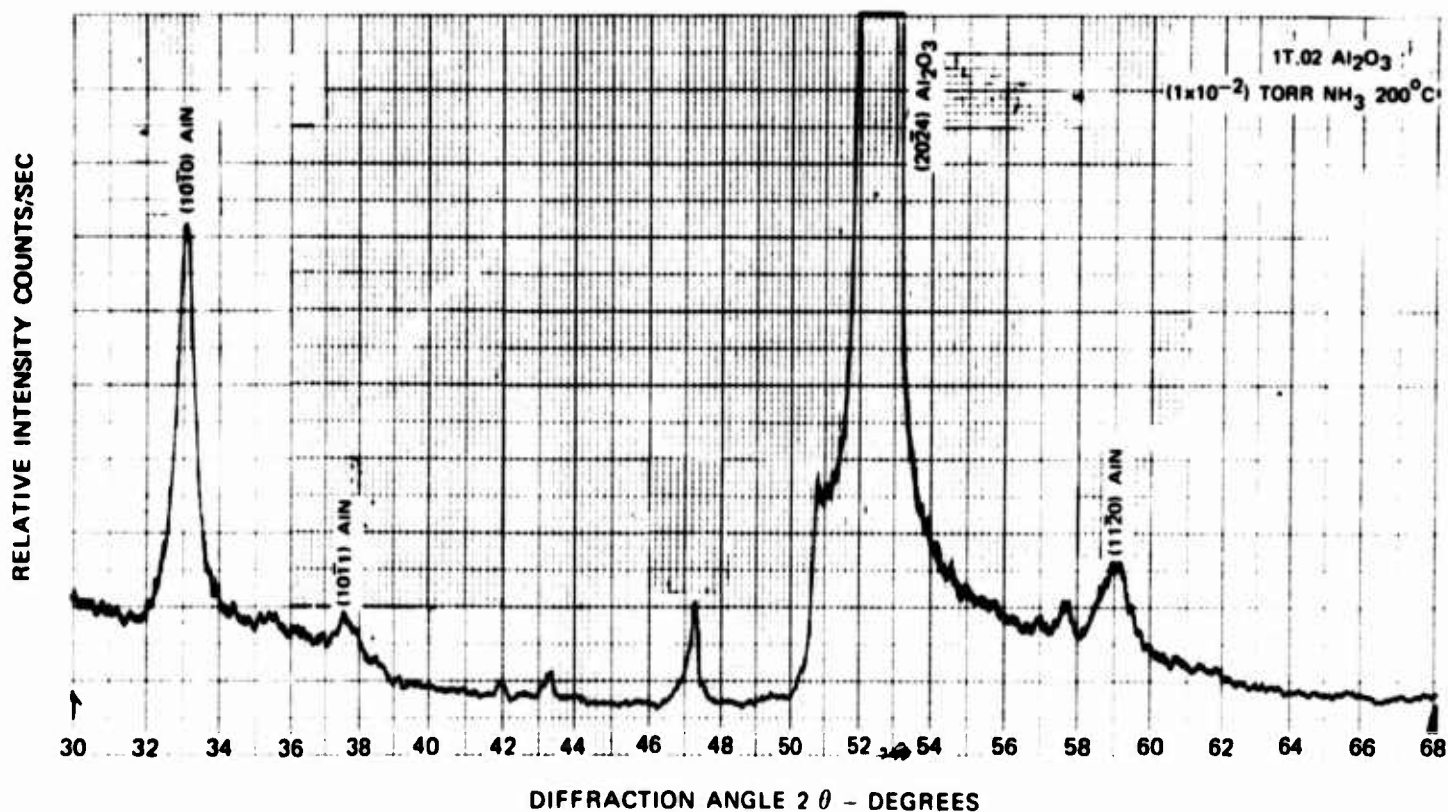
DIFFRACTOMETER TRACES OF AlN FILMS REACTIVELY SPUTTERED IN N$_2$ AT 700°C ON (000$\bar{1}$)

AND (10$\bar{1}$2) Al$_2$O$_3$ SUBSTRATES
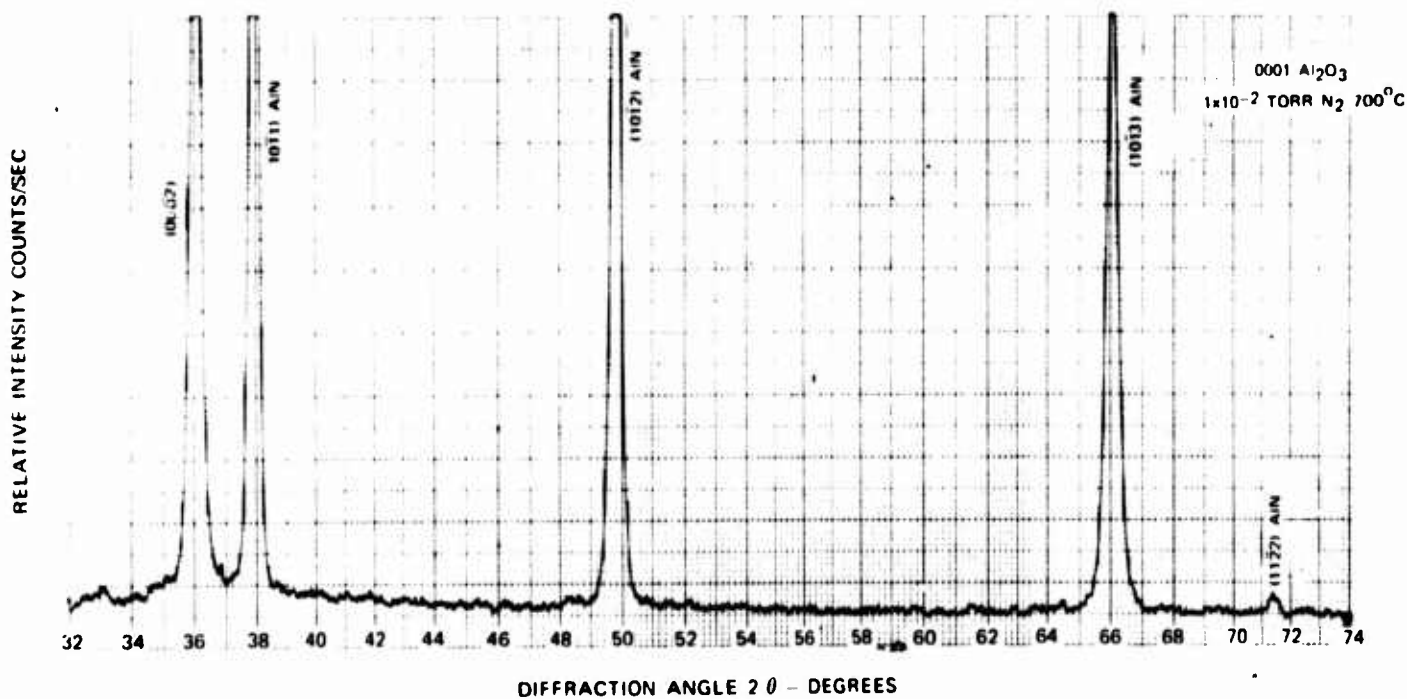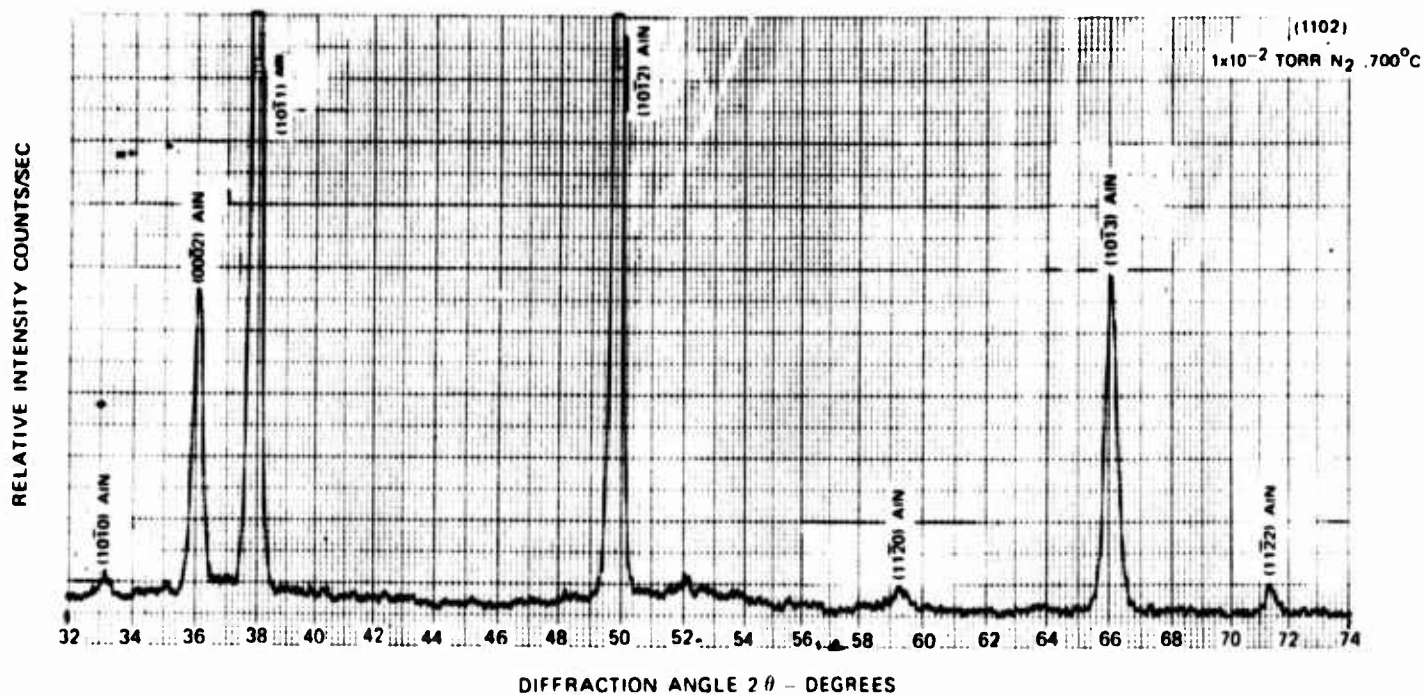
FIG. 5-4

DIFFRACTOMETER TRACES OF AIN FILMS REACTIVELY SPUTTERED IN 5 X 10^{-3} TORR NH$_3$ AT 700 °C ON (0001) AND (10$\bar{1}$2) Al$_2$O$_3$ SUBSTRATES.
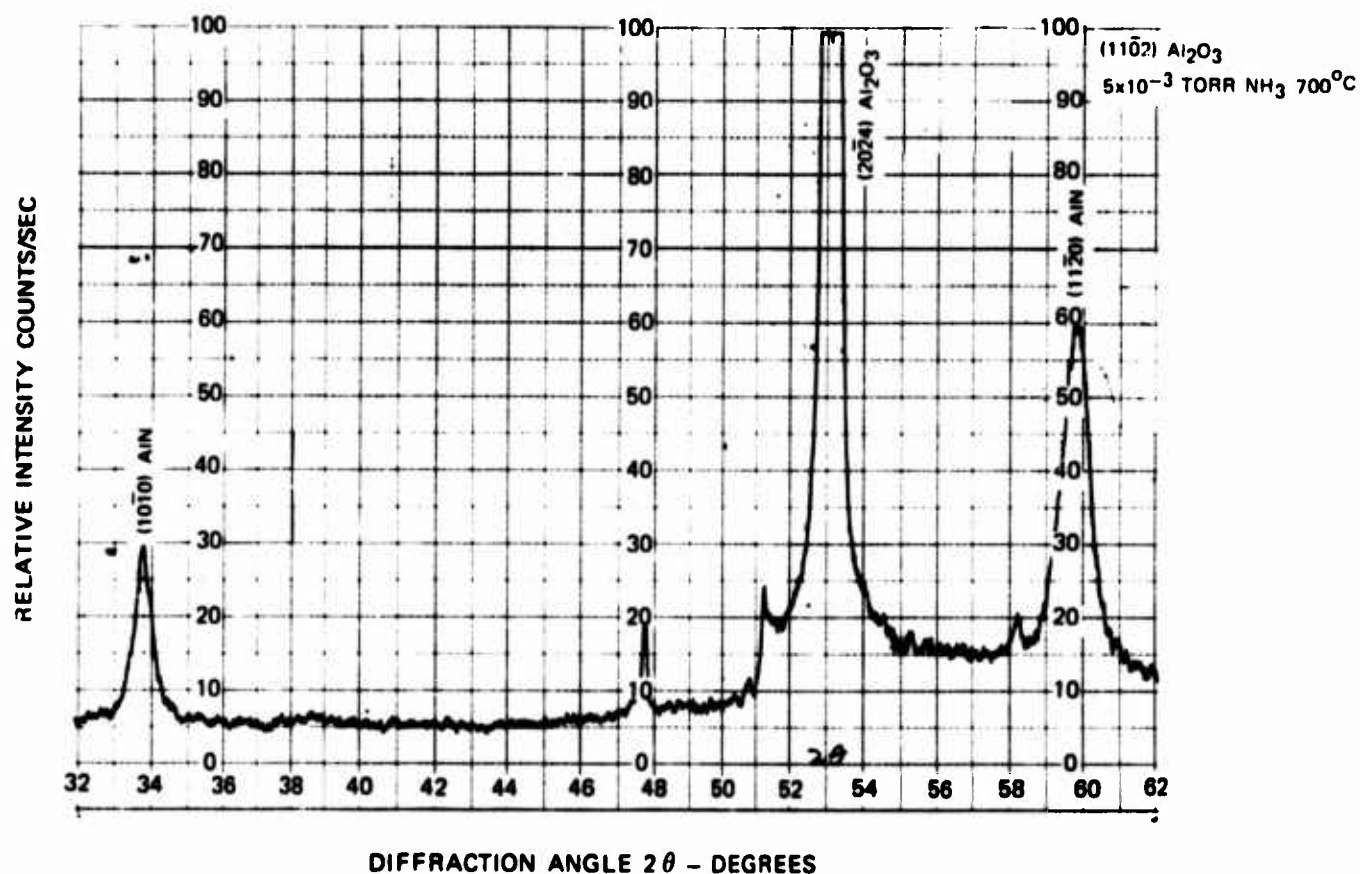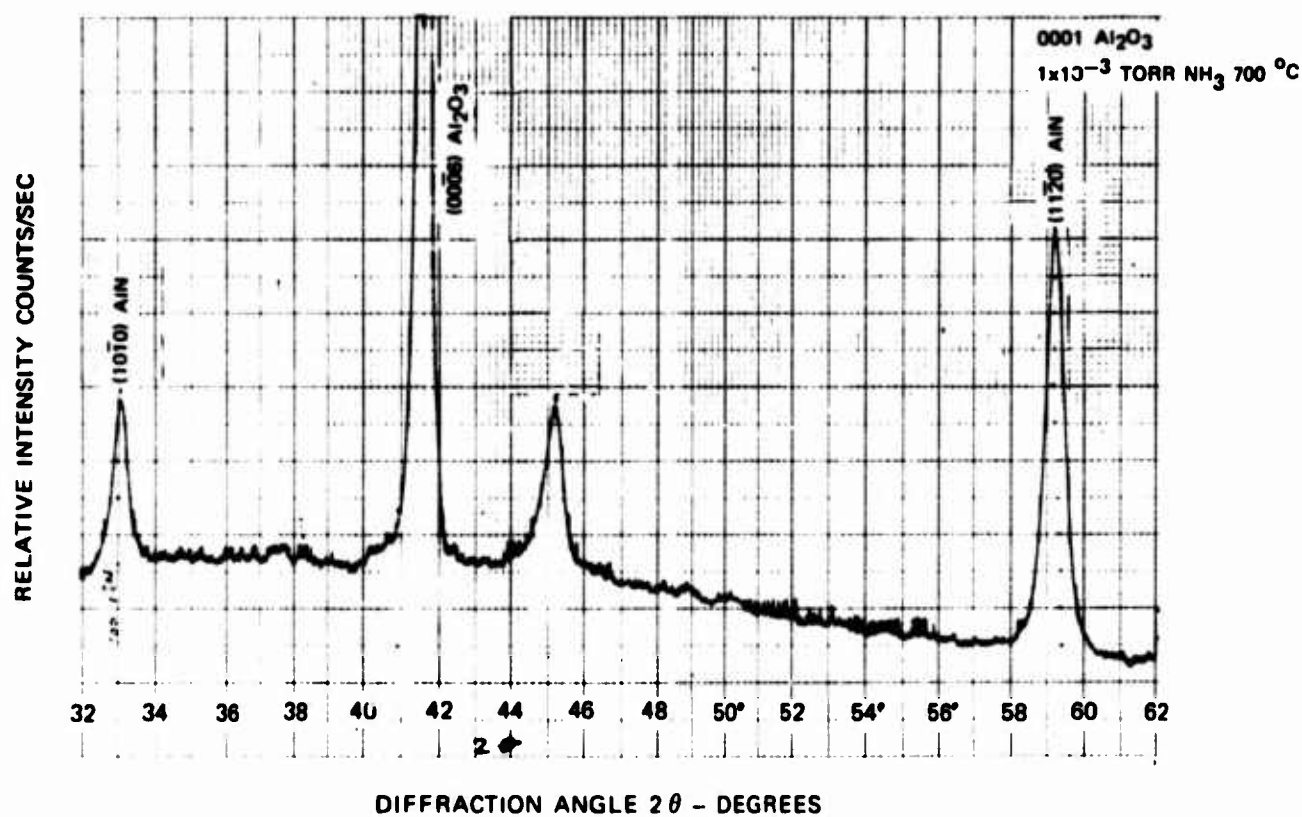
DIFFRACTION ANGLE 2θ – DEGREES

DIFFRACTION ANGLE 2θ – DEGREES

65

FIG. 5-5

DIFFRACTOMETER TRACES OF AIN FILMS REACTIVELY SPUTTERED IN 7 X 10^{-2} TORR NH_3 AT 700 °C ON (00$\bar{0}$1) AND (10$\bar{1}$2) Al_2O_3 SUBSTRATES.

DIFFRACTION ANGLE 2θ – DEGREES

DIFFRACTION ANGLE 2θ – DEGREES

FIG. 5-6
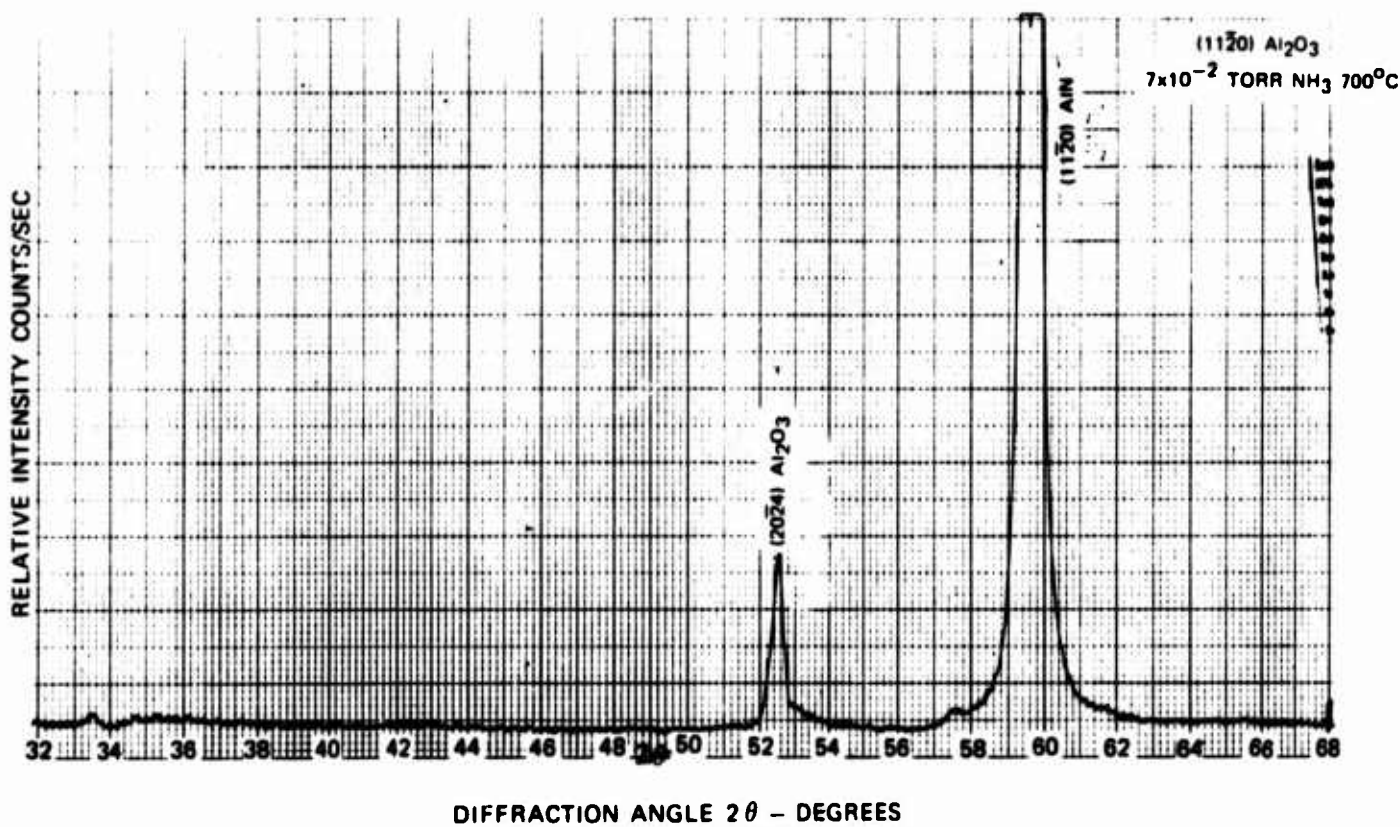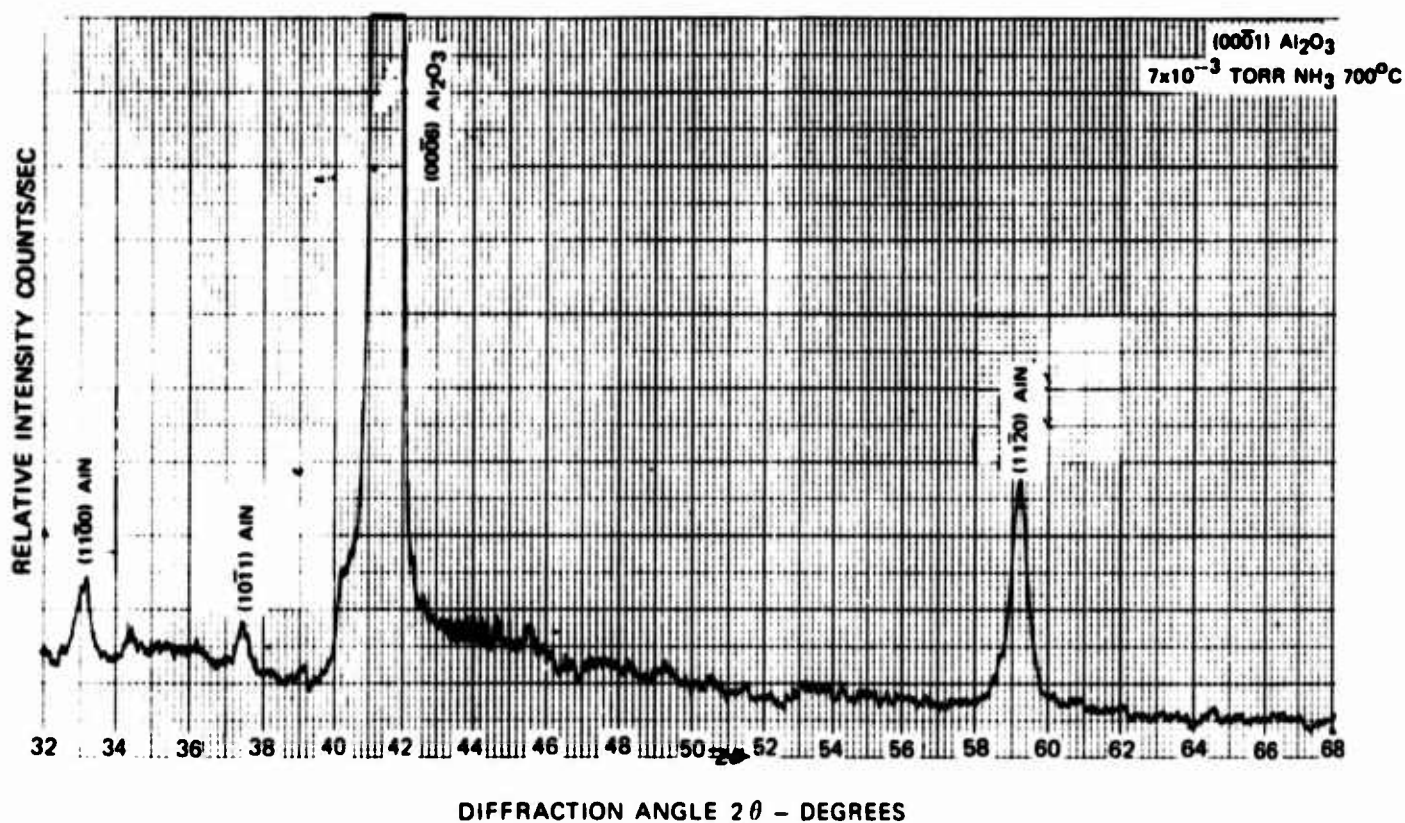
X—RAY DIFFRACTION DATA FOR REACTIVELY SPUTTERED ALUMINUM NITRIDE
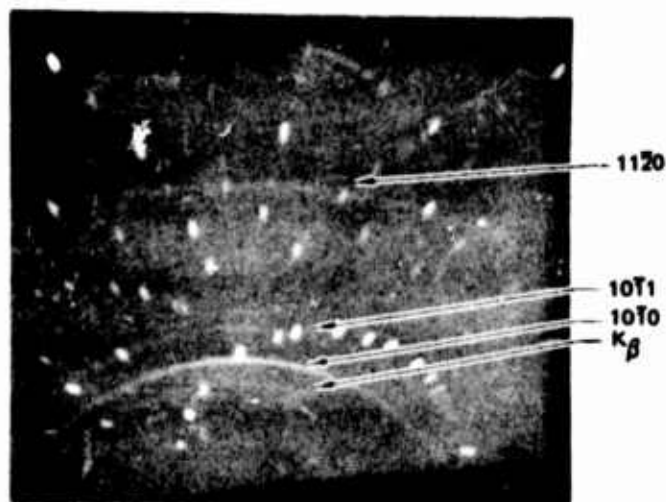
(a) 1x10^{-2} TORR NH$_3$ (0001) Al$_2$O$_3$ SUBSTRATE 200°C DECOMPOSITION TEMP.
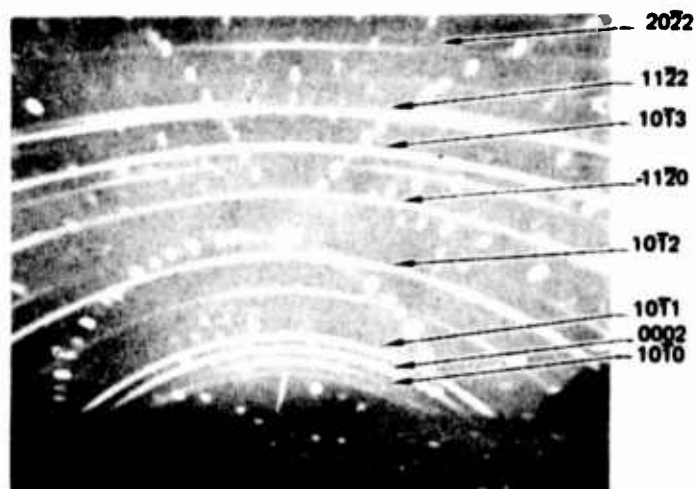
(b) 1x10^{-2} TORR N$_2$ (1$\bar{1}$02) Al$_2$O$_3$ SUBSTRATE 700°C DEPOSITION TEMP
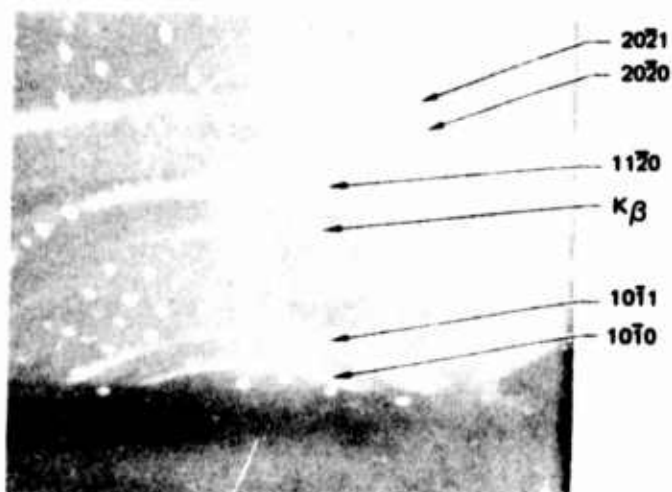
(c) 5x10^{-3} TORR NH$_3$ (1$\bar{1}$02) Al$_2$O$_3$ SUBSTRATE 700°C DEPOSITION TEMP.
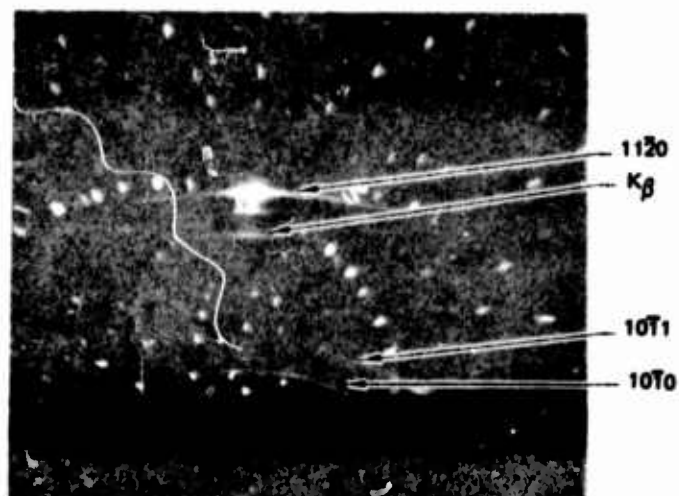
(d) 7 X 10^{-2} TORR NH$_3$ (1$\bar{1}$02) Al$_2$O$_3$ SUBSTRATE 700° DEPOSITION TEMP.

Noreika (Ref. 5-7) for films sputtered at $900^{\circ}C$ in an argon-nitrogen mixture (85×10^{-3} torr Ar, N_2 partial pressure 5×10^{-3} torr). The band edge shift was attributed to a probable nitrogen deficiency and a built in surplus of argon due to the relatively high-pressure argon ambient. An anneal of these films in N_2 at $900^{\circ}C$ for 2 hours produced a band edge shift to values reported for bulk single crystals (5.9eV). Our samples sputtered at 1×10^{-2} torr N_2 and a substrate temperature of $700^{\circ}C$ and annealed for a comparable period did not yield as dramatic a shift of the band edge to shorter wavelengths. This is probably indicative of the reduced reactivity of the nitrogen at the lower substrate temperature. Films sputtered in ammonia and deposited at a substrate temperature as low as $50^{\circ}C$ were colorless and exhibited the band edge absorption of stoichiometric material. This clearly points up the superiority of ammonia for the synthesis of stoichiometric AlN films. The polycrystalline films of aluminum nitride exhibited a high degree of scattering and are unattractive for optical waveguide applications. This is to be contrasted with sputtered films of Ta_2O_5 which can be deposited in the amorphous phase (Ref. 5-9) and can be used to fabricate low loss optical waveguide structures.

5.3.3 Electrical Evaluation

Resistivity measurements were made on AlN deposited on silicon. The resistivity of the films generally ran $10^{12} \Omega$-cm or greater. Piezoelectric properties of the films were evaluated in the surface acoustic wave delay line configuration and were found to exhibit coupling coefficients which were less than .001%. These results indicate that polycrystalline films of aluminum nitride deposited at relatively low temperatures are far less piezoelectrically active than polycrystalline films of zinc oxide.

5.4 Epitaxial Deposition of Aluminum Nitride

The high temperature capability of the sputtering system had to be extended in order to satisfy the conditions for epitaxial growth of aluminum nitride. A strip heater was incorporated into the sputtering system which permitted achieving substrate deposition temperatures approaching $1800^{\circ}C$. Molydenum and tantalum heaters produced a blackening of the substrates at the elevated temperatures. Sapphire liners inserted between the substrates and the heater eliminated the problem. Aluminum coated molydenum heaters from RD Mathis Company were used in the final configuration and were found quite acceptable.

The substrates were located 2 inches from the aluminum target. This rather large separation was required to minimize heating and warping of the shutters

which were required for sputter cleaning. Excessive heating would result in spalling and peeling of material from the shutters. This particulate matter would then comtaminate the substrates and result in the growth of polycrystalline films.

A calibration proceedure was worked out to determine the true temperature of the transparent substrates which were held in place on the heater assembly by their own weight. The substrate heater temperature was determined by means of an optical pyrometer and the corresponding sample temperature was arrived at by measuring its thermal expansion. Plots were made of the substrate heater temperature versus sample temperature which permitted conversion of optical pyrometer readings of the substrate heater to actual substrate temperature. More complete details of the measurement are discussed in Appendix II.

Prior to film deposition a new substrate heater is prepared for use in the following manner. The vacuum chamber is pumped down to 10^{-6}torr and the heater is raised to 1200°C and outgassed till the background pressure drops back to 10^{-6}torr. Subsequently, the heater temperature is raised to 1800°C for five minutes and then dropped back to 1400°C, and a coating of aluminum nitride is deposited on the substrate heater.

After a heater is broken in, a typical run sequence consists of (1) evacuating the sputtering chamber to 10^{-6}torr with the heater adjusted to operating temperature, (2) admission of the reactive gas into the chamber and adjustment to operating pressure (typically 2 x 10^{-2}torr), (3) readjustment of the heater to the required deposition temperature, and (4) sputter cleaning of the aluminum target for five minutes at a power density of 40W/in^2. With the completion of this sequence the system is ready for film deposition. The sputtering target is 99.999% pure aluminum and the reactive gases have an assayed purity of 99.999% or better.

Epitaxy was achieved with either nitrogen or ammonia as the reactive gas. Epitaxial films up to 4μm in thickness were grown. Ammonia was found to the preferred reactive ambient since epitaxy could be achieved at a considerably lower substrate temperature. This is a particularly important aspect regarding heater lifetime for deposition of thicker films. The films grown with ammonia are smooth, clear and insulating. The elevated temperature (1400°C) required for eqitaxial growth of AlN in nitrogen produced films which had a rough surface texture. Consequently the remaining efforts for preparation of single crystal films of aluminum nitride were limited to ammonia as the reactive ambient.

Heteroepitaxial deposits of aluminum nitride were prepared on (0001) and (1$\bar{1}$02) oriented sapphire substrates, (111) and (110) $MgAl_2O_4$ and (0001) SiC. The best conditions determined for epitaxial deposition of aluminum nitride are tabulated below

Reactive Ambient – 2 x 10^{-2} torr NH_3
Substrate Temperature – 1250°C

Substrate Target Separation - 2 inches
Power Density and Deposition Rate - $4W/cm^2$, $50\overset{\circ}{A}$/min. for ($1\bar{1}20$) oriented AlN
                                  - $7.9/cm^2$, $100\overset{\circ}{A}$/min for (0001) oriented AlN
Axial Magnetic Field

For completeness the epitaxial conditions determined for films deposited in a nitrogen ambient are:

Reactive Ambient - 6×10^{-2} torr N_2
Substrate Temperature - $1400^{\circ}C$
Power Density and Deposition Rate - $2W/cm^2$, $20\overset{\circ}{A}$/min
                                  for ($1\bar{1}02$) and (0001) oriented AlN

Epitaxy has been observed at substrate temperatures as low as $1050^{\circ}C$ but the reproducibility is erratic. Consistent results are obtained at the somewhat higher substrate temperature quoted ($1250^{\circ}C$). The maximum rf power which could be coupled into the system was 1000W. This corresponds to a power density of $7.9W/cm^2$ at the aluminum target. The maximum deposition rate achievable at this power density was $100\overset{\circ}{A}$/min. Epitaxial films of (0001) oriented AlN could be obtained at this rate but no data could be obtained for the maximum growth rate attainable for this orientation due to rf power limitations. A deposition rate of $50\overset{\circ}{A}$/min could not be exceeded during growth of ($1\bar{1}20$) oriented AlN without the formation of poly-crystalline films.

5.4.1 Structural Characterization of AlN Films

Reflection electron diffraction and x-ray diffraction were employed to determine the structure and epitaxial relationships of the film to the substrate. Figure 5-7 shows the calculated reflection electron diffraction pattern expected for the electron beam aligned with the $[10\bar{1}0]$ and $[1\bar{1}20]$ directions. The patterns correspond to AlN grown with (0001) planes parallel to the surface of the film. As the electron beam is rotated in the plane of the film, each pattern shoudl exhibit a repeat period of 60° and the two patterns shoudl alternate every 30°. Figure 5-8 shows the reflection electron diffraction patterns obtained for AlN grown on (0001) oriented aluminum oxide. Under rotation, the angular dependence of the diffraction patterns was found to vary as described above. In the diffraction experiments the electron beam is incident at a grazing angle and illuminates the full length of the film. Traversal of the sample over its full width in a direction orthogonal to the beam produced no variation in the diffraction pattern indicating that the film was indeed single. Diffractometer traces exhibited a single diffraction peak corresponding to a "d" spacing of $2.490\overset{\circ}{A}$. This value coincides with the spacing expected for (0002) planes of aluminum nitride. Epitaxial growth of (0001) AlN films was also obtained on (0001) silicon carbide and (111) magnesium aluminum spinel substrates.

CALCULATED RED PATTERN FOR AIN OR GaN

ELECTRON BEAM IN [10$\bar{1}$0] DIRECTION

ELECTRON BEAM IN [11$\bar{2}$0] DIRECTION

71

FIG. 5-8
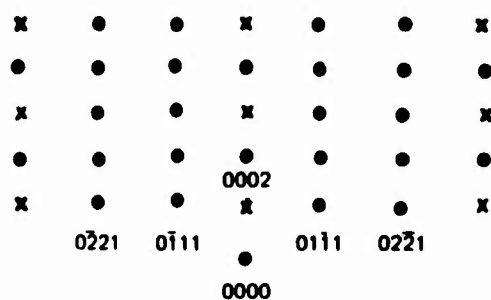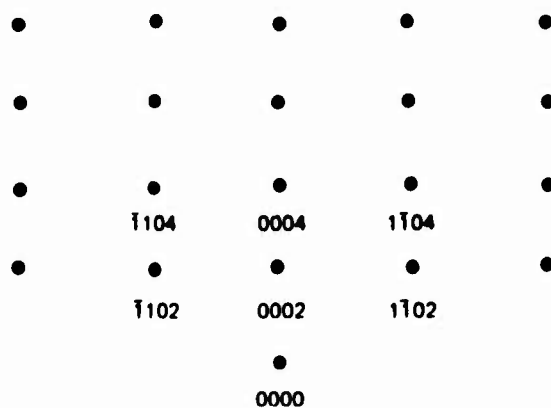
RED OF AIN ON (0001) Al$_2$O$_3$

ELECTRON BEAM ALONG [10$\bar{1}$0]
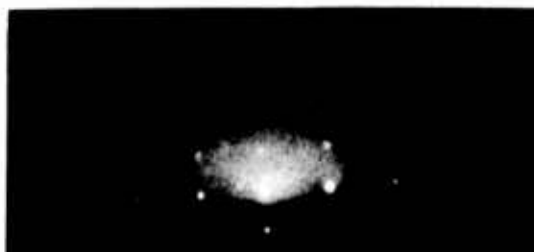
ELECTRON BEAM ALONG [11$\bar{2}$0]

Figure 5-9 depicts the expected diffraction patterns with the electron beam directed along the [0001] and [1120] zone axes for AlN with (1120) planes parallel to the surface of the film. Figure 5-10 shows the actual reflection electron diffraction pattern obtained for AlN grown on (1102) oriented aluminum oxide substrates. The [0001] and [1120] patterns alternate every 90° for a rotation of the beam in the plane of the film. The periodic behavior exhibits the proper symmetry. Diffractometer traces showed a single peak corresponding to a "d" spacing of 1.557Å which is that expected for (1120) planes of AlN. Yim, et.al. (Ref. 5-1) have reported that two other orientations were observed for single crystal AlN layers grown on (1102) sapphire, (3035) and (1127) AlN. These results were obtained by chemical vapor deposition. In our work only the (1120) orientation of AlN was obtained on (1102) sapphire substrates. Epitaxy was also obtained on (110) magnesium aluminum substrates with AlN (1120) planes growing parallel to the film surface.

The single crystal films grown were generally clear and transparent but on occasion films with a hazy appearance were produced. Optical transmission measurements indicated that the optical cutoff in the ultraviolet occurred near 2000Å corresponding to a band gap of approximately 6.2ev in agreement with the work of Yim, et.al. (Ref. 5-1).

The surface quality of the films grown by sputtering is generally superior to that obtained by chemical vapor deposition. It has been reported that surface acoustic wave devices fabricated with AlN films thicker than 1.6μ, which were grown by chemical vapor deposition, require mechanical polishing to remove the surface irregularities before definition of interdigital transducers can take place (Refs. 5-3,10). Figures 5-11 and 5-12 are electron micrographs of replicated surfaces of 2.5 micron thick aluminum nitride films grown on (0001) and (1102) sapphire substrates.

5.4.2 Surface Acoustic Wave Device Evaluation of AlN Films

Surface acoustic wave delay lines were fabricated to evaluate the piezoelectric characteristics of the films grown by sputtering. To date the only published data on surface acoustic wave devices fabricated with AlN on sapphire is the work at North American-Autonetics. Their data is confined to AlN on (1102) sapphire substrates with the c-axis of the AlN lying in the plane of the film.

The data presented in our earlier progress report was the first useful data for AlN grown on (0001) oriented sapphire (c-axis ⊥ to the film plane). The advantage of this orientation for delay line construction is that the anisotropy (and delay line beam steering) is low in the (0001) plane, whereas with the c-axis in the plane of the film, the interdigital transducers must be aligned to propagate surface acoustic waves along the c-axis of the AlN.

CALCULATED RED PATTERN FOR AIN OR GaN

ELECTRON BEAM IN [0001] DIRECTION

ELECTRON BEAM IN [11$\bar{2}$0] DIRECTION

FIG. 5—10
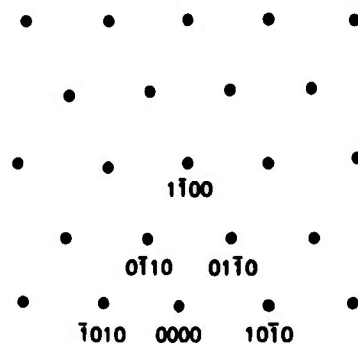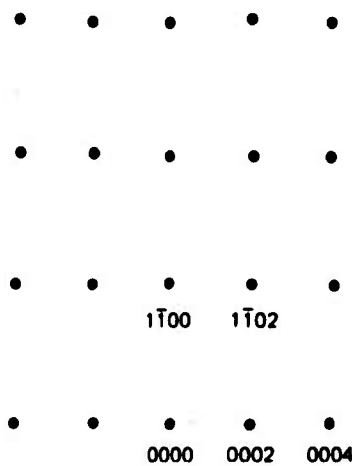
RED OF AIN ON (1$\bar{1}$02) Al$_2$O$_3$

(0001)

[11$\bar{2}$0]

FIG. 5-11
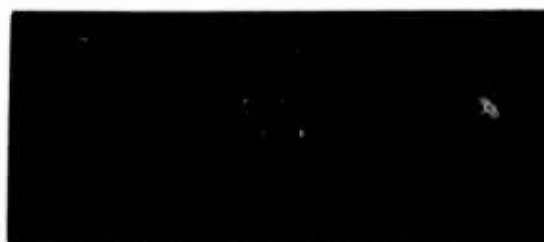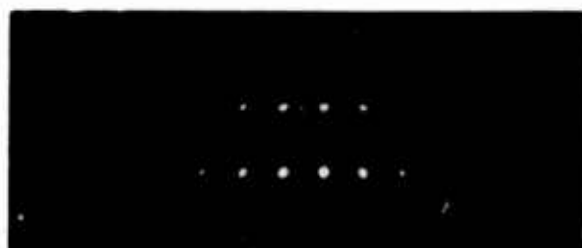
ELECTRON MICROGRAPH OF AIN ON (0001) Al$_2$O$_3$

6777

2μ

6778

1μ

FIG. 5-12
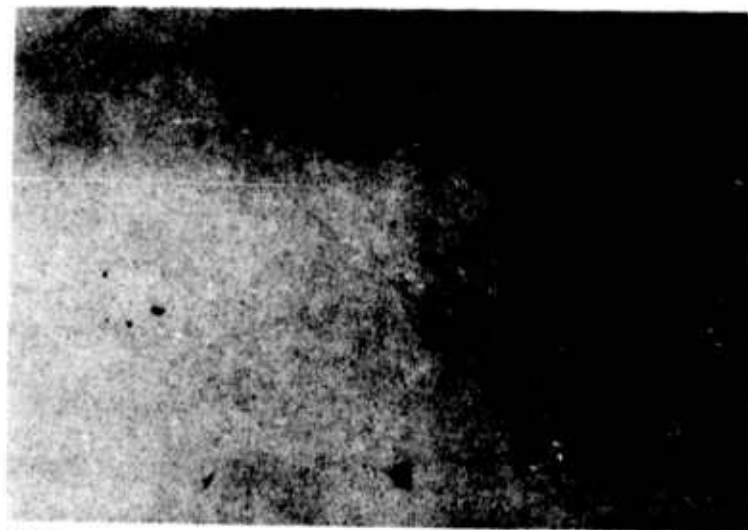
ELECTRON MICROGRAPH OF AIN ON (1$\bar{1}$02) Al$_2$O$_3$

6780

2μ

6781

1μ
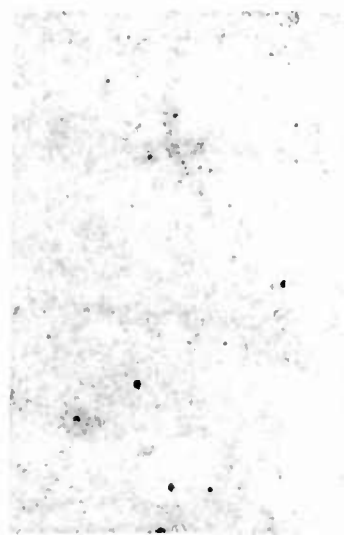
The surface acoustic wave data presented below is for a 2 micron thick single crystal aluminum nitride film grown on a (0001) sapphire substrate. Interdigital (ID) transducers were photolithographically fabricated with the following specifications:

Pattern Spacing   - 5.1mm
Number ID Fingers - 21
Finger Length   - 1mm
ID Periodicity   - 25μm
Metallization   - 0.15μm aluminum

The surface acoustic wave transducer configuration is illustrated in Fig. 5-13, and Fig. 5-14 shows a plot of the input impedance versus frequency for the two transducers. The nearly identical response for the two transducers is indicative of the uniformity of film thickness. Transducer insertion loss as a function of frequency is shown in Fig. 5-15. The two port insertion loss was lowered from 68dB to 37dB at 216MHz by series tuning with miniature inductors. In fact, the insertion loss would have been much lower, at least as low as 25dB, if our transducer pattern had had low spurious shunt capacitance. A pulse delay time for the above structure was measured to be 90ns with a propagation loss of 1.5dB for the path. Ths pulse echo response is shown in Fig. 5-16. The aluminum nitride dielectric loss Q was estimated to be 10, the dielectric constant approximately 10 and the resistivity greater than $10^5 \Omega$-cm. The surface acoustic wave velocity was determined to be 5500 m/s. The effective piezo coupling constant (k^2) was determined to be .08%. This compares very favorably with the value of .09% obtained at Autonetics (Ref. 5-11) for the same film thickness to transducer pattern periodicity utilized here.

Measurements were made on five other AlN delay lines with film thickness in the range 0.8-3μ and transducer periodicity ranging from 10 to 25μm yielded values of k^2 in the range 0.05=0.2% for film-devices fabricated on (0001) sapphire and somewhat less on (1T02) sapphire. In compansion, data reported by Duffy et.al. (Ref. 5-6) for CVD films fabricated on (0001) sapphire gave values of k^2 too small to be measured. However, CVD films on (1T02)oriented sapphire have given values in the range 0.05-0.6% (Ref. 5-11,12). Figure 5-17 shows the untuned and series inductor tuned insertion loss versus frequency curves for a 0.9μ film device on (0001) sapphire. The coupling for this device was $K^2 = 0.2°/o$, and the acoustic phase velocity obtained from the transducer periodicity ($\Lambda = 12.5$μm) and apparent synchronism frequency ($f_c \simeq 442$MHz) was 5500 m/sec. The puslse echo delay between the 0.4 in spaced tranduces was 1.8μsec.

The results of the surface acoustic wave evaluations of the piezoelectric properties of AlN are very encouraging since this material was prepared by a technique which has not had the years of process development put into the chemical vapor deposition techniques for preparation of aluminum nitride films.

FIG. 5-13

INTERDIGITAL TRANSDUCER

FIG. 5-14
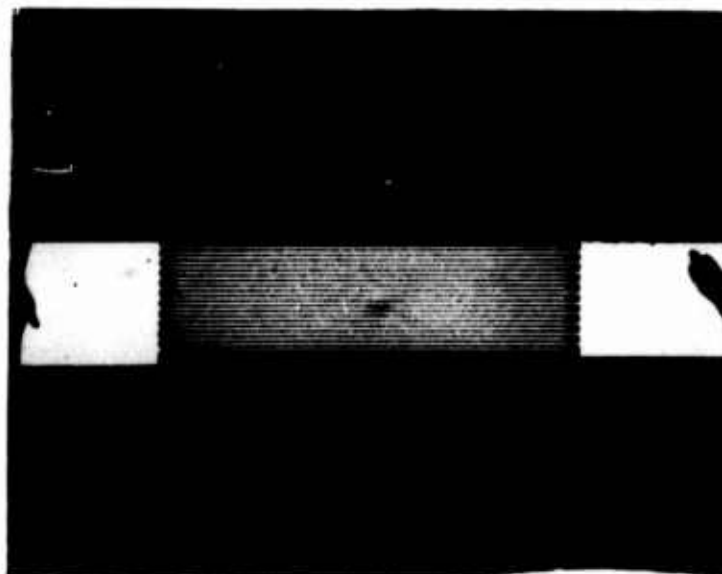
INPUT IMPEDANCE VS FREQUENCY FOR AIN—103
(SHOWS NEARLY IDENTICAL RESPONSE FOR THE TWO TRANSDUCERS)

PORT 1

PORT 2

FIG. 5-15
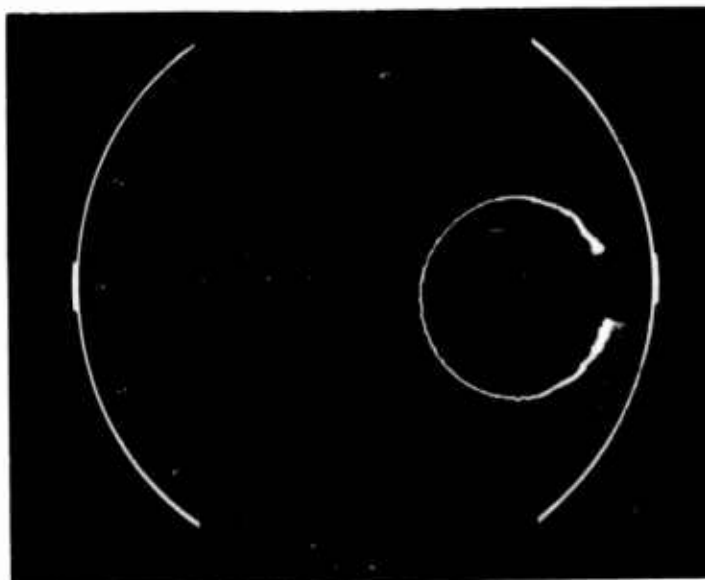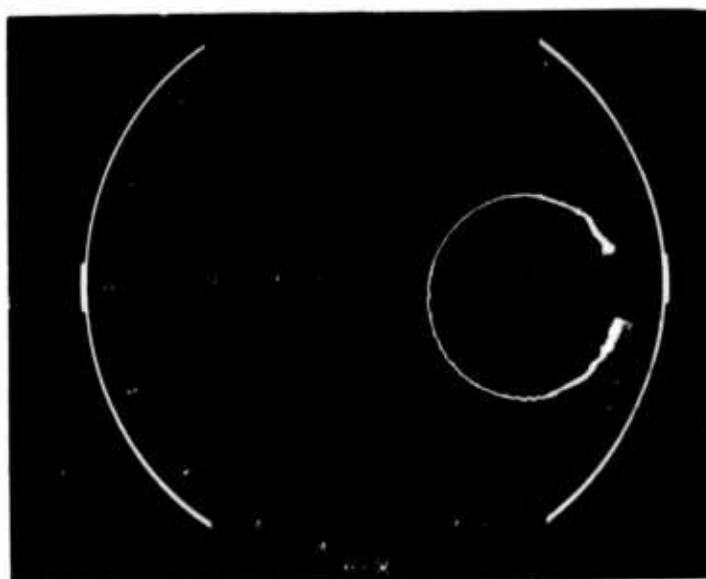
TRANSDUCER INSERTION LOSS VS FREQUENCY FOR AIN ON (0001) SAPPHIRE

FIG. 5-16
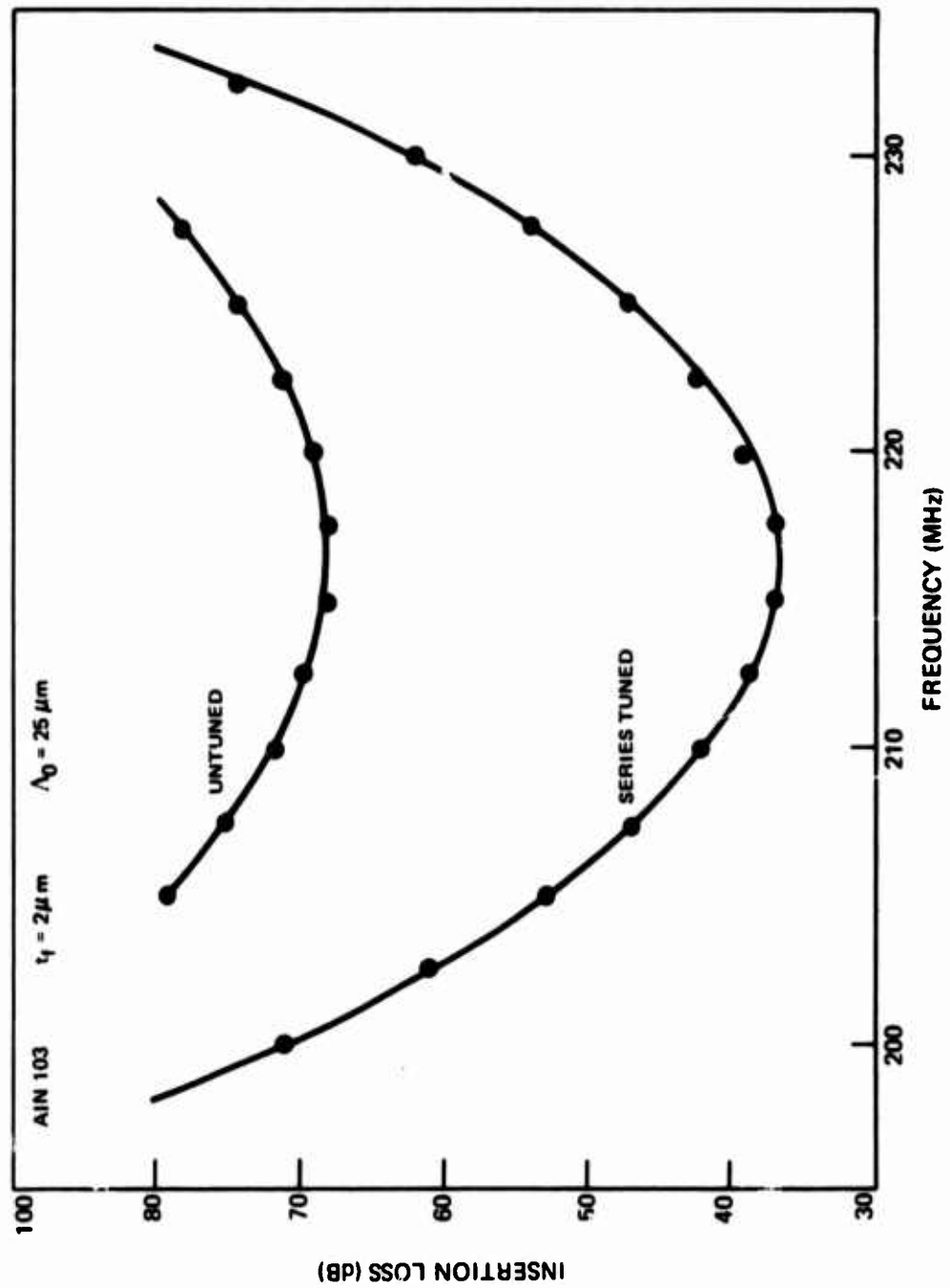
PULSE ECHO RESPONSE OF AIN-103
(f = 216 MHz, IL = 37 dB, BW = 10 MHz)

FIG. 5-17
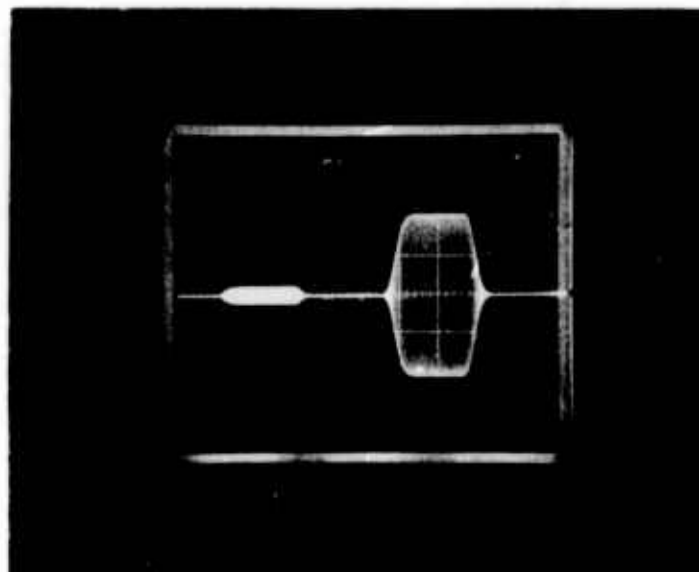
INSERTION LOSS VERSUS FREQUENCY CURVES FOR A 0.9 μm ALUMINUM NITRIDE FILM ON (0001) SAPPHIRE DELAY LINE.
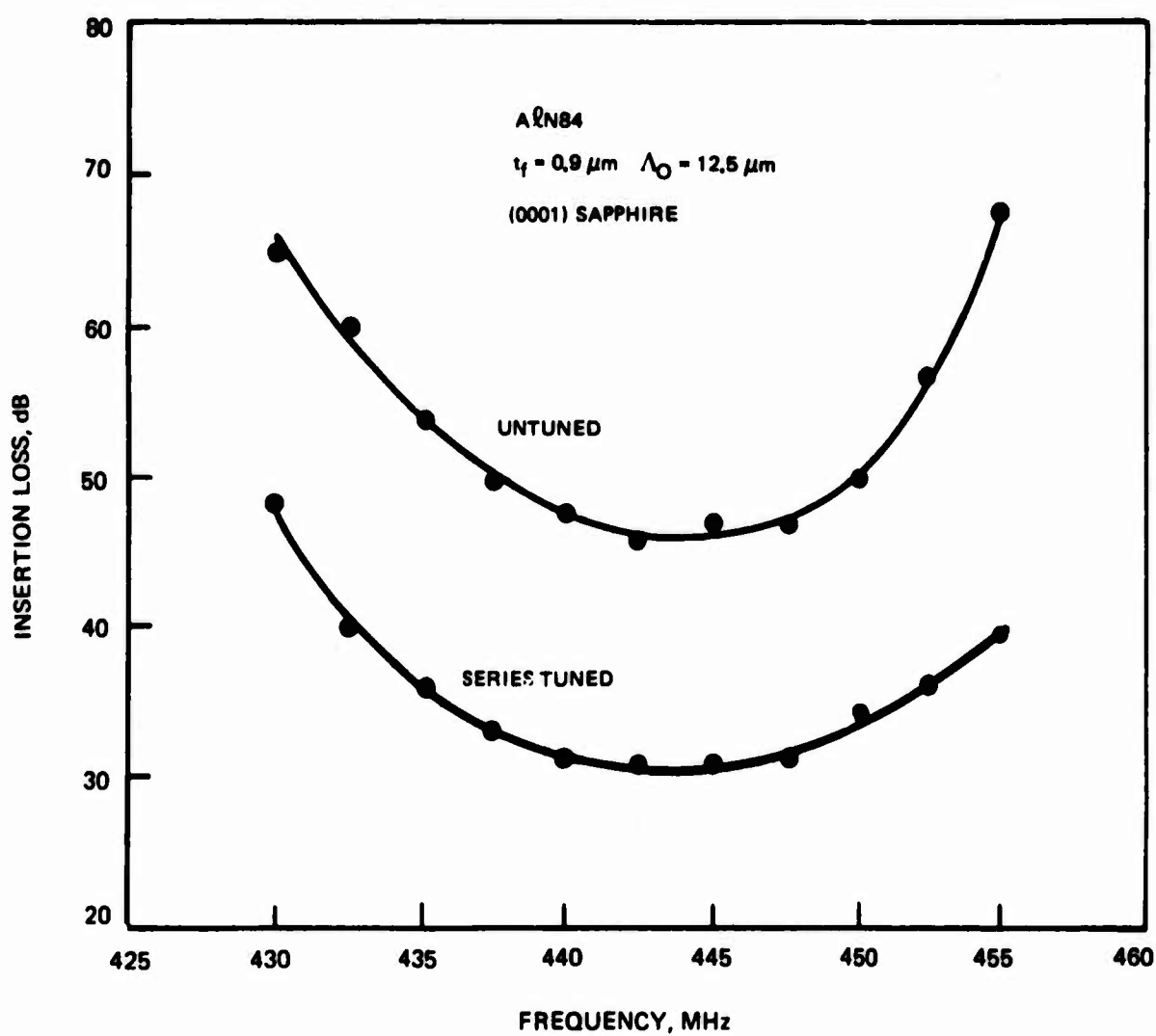
5.4.3 Optical Waveguiding

The experimental arrangement for the optical waveguide evaluation of the heteroepitaxial structures of AlN is described in Appendix III. Very high optical loss ($\geq$ 50dB/cm) is observed in (1120] AlN films grown on (1102) sapphire substrates. Parametric variations of substrate temperature, sputtering pressure and deposition rate produced no detectable reduction in propogation loss. The high optical loss is apparently due to a high level of stress (Ref. 5-6) in the films. This arises from the large differences in thermal coefficients of expansion between aluminum nitride and aluminum oxide (Ref. 5-13). An added complication may be that a mosaic block structure exists in the (1120] oriented AlN films. Manesevitz et.al. (Ref. 5-14), in structural studies of AlN grown by the metalorganic CVD process, obtained structural data which implies the existance of a mosaic-block type of structure with a block size of probably $\leq$ 1µm. This would account for the high optical waveguide losses observed in the (1120) oriented films.

Somewhat better results were obtained with (0001) oriented films of AlN. The lowest propagation loss which was obtainable with (0001) oriented films was in the vicinity of 30dB/cm at a wavelength of 0.6328µm and 15dB/cm at 1.06µm. Figure 5-18 is a plot of scattered light intensity versus distance along the guided beam for AlN sample No. 119, which is typical of the better films which were grown. The index of refraction for the (0001) oriented AlN films was determined to be 2.15 at 0.6328µm. The lowest loss films were obtained at the highest growth rate ($\sim$ 100Å/min.) attainable with the sputtering system employed. The elevated temperature at which AlN films are grown makes stress generated by a mismatch in thermal coefficients of expansion unavoidable. Attempts to reduce loss by annealing met with no success. The lower scattering loss exhibited by (0001) oriented films probably can be attributed to better film structure since any stress developed in the film would tend to be uniform because the thermal coefficient of expansion is isotropic in the plane of the film. Stresses generated in (1120) oriented AlN the film would tend to be non-uniform since the thermal coefficient of expansion is very anisotropic in the plane of the film and this stress anisotropy would generate a non-uniform strain distribution resulting in a higher loss film. Epitaxial films of zinc oxide, which are isomorphous in structure with AlN, grow at a considerably lower substrate, temperature (600°C) and exhibit very low scattering losses. These results tend to lend evidence to the fact that the major contribution to scattering losses in AlN films is due to strain.

FIG. 5-18

SAMPLE NO. 119

AlN ON Al$_2$O$_3$ (0001)
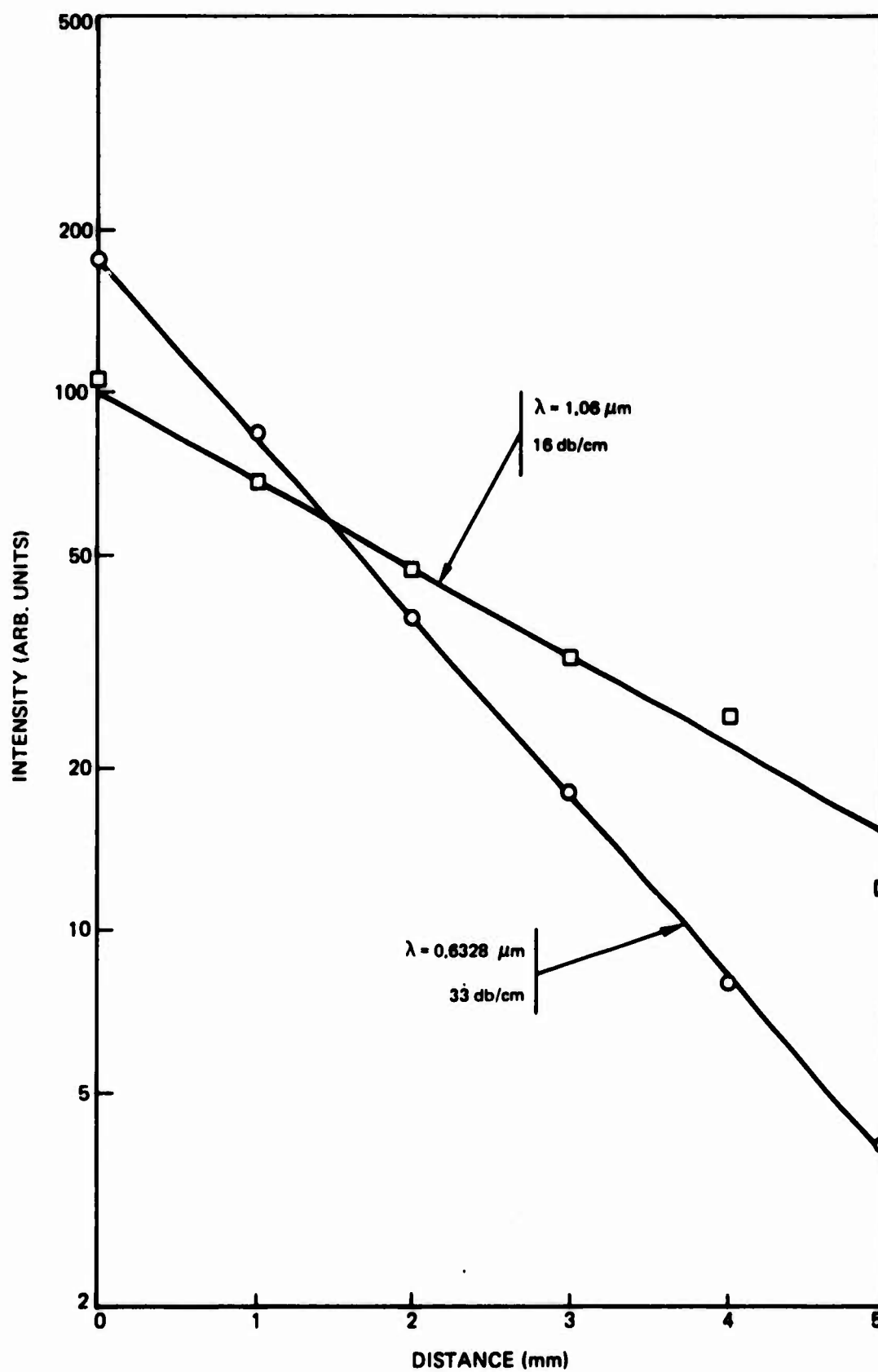
5.5 Epitaxy of Gallium Nitride By Reactive Sputtering

5.5.1 Introduction

Single crystal films of gallium nitride have been prepared by reactive sputtering of gallium in an ammonia ambient. To our knowledge the work described constitutes the first successful effort to grow single crystal films of gallium nitride by this technique. Epitaxy has been achieved on (111) oriented substrates of magnesium aluminum spinel (0001) and (1T02) oriented sapphire substrates an (0001) substrates of SiC.

Gallium nitride crystallizes in the hexagonal wurtzite structure with unit-cell dimensions $a_o = 3.180\overset{o}{A}$ and $c_o = 5,166\overset{o}{A}$. It is isomorphous in structure to aluminum nitride and is piezoelectric. Gallium nitride has a direct bandgap of 3.5eV (Ref. 5-15) and, potentially, junction light emitting diodes in the ultraviolet and the blue can be fabricated from it. A disadvantage to material prepared by chemical vapor deposition is that it yields n-type material with a carrier concentration of $\sim 10^{19}/cm^3$, (Ref. 5-15). Semi-insulating films of gallium nitride can be produced by compensation with zinc during growth. The motivation for growth of gallium nitride by reactive sputtering is to determine if a different method of preparation would result in films with a considerably lower electron concentration. If successful, this would provide the basis for preparation of p-type material required for the fabrication of junction light emitting diodes in the ultraviolet and blue or a solid state laser in the ultraviolet.

5.5.2 Experimental Arrangement

The sputtering of gallium metal presents special problems in the design of the sputtering cathode. Gallium is liquid at 30^oC and oxidizes readily. Several design permutations were gone through before a satisfactory cathode configuration was arrived at. The first configuration employed a molybdenum dish cathode to contain the gallium, and the substrate heater assembly was suspended above the cathode. A number of difficulties were encountered with this arrangement. Flaking of material from the substrate heater resulted in contamination of the gallium. The substrate clamping system resulted in non-uniform film deposition. Therefore, the system was modified to conform to the more conventional sputtering geometry with the cathode suspended above the substrate heater. An alcohol and dry ice mixture was used as a coolant to maintain the gallium in solid form even though substrate heater temperatures employed ranged as high as 1100^oC in the course of the experiments. This arrangement was significantly better but when any restrictions to flow of the coolant developed or the coolant pump failed gallium would be dumped into the system. This presented a serious clean up problem. The final configuration settled on for the cathode employed a thin molydbenum disk which was

coated with a layer of gallium. A failure with the cooling system would not result in a gallium spill since the surface tension was sufficient to contain the gallium. The sputtering system used in the AlN studies was also used for the gallium nitride work.

5.5.3 Epitaxial Thin Film Deposition

The preparation of the substrates prior to deposition is described in Appendix I. The sputtering rate for gallium was extremely high and the rf power density had to be limited to values below $1.6W/cm^2$ in order to prevent deposition of metal rich films. Reactive ambients of nitrogen, nitrogen-ammonia mixtures and ammonia were studied. The best results were obtained with a reactive ambient of ammonia gas. Epitaxial films of gallium nitride were grown on (0001) and (1$\bar{1}$02) sapphire, (111) $MgAl_2O_4$ and (0001) SiC. The sputtering conditions which yielded the best results are:

Reactive Ambient - 20mtorr NH_3
Substrate Temperature - 900°C
Power Density - $0.8W/cm^2$
Deposition Rate - 40Å/min

A deposition rate up to 80Å/min could achieved and still produce single crystal film growth of (0001) oriented gallium nitride. A deposition rate of 40Å/min could not be exceeded in growth of (1$\bar{1}$20) oriented gallium nitride. A similar dependence of growth rate with orientation was observed with aluminum nitride.

5.5.4 Evaluation of Gallium Nitride Films

Electron diffraction and x-ray diffraction were employed to evaluate the structure of the gallium nitride films. Figure 5-19 shows electron diffraction patterns for selected zone axes for epitaxial gallium nitride grown on (1$\bar{1}$02) sapphire. Rotation of the electron beam in the plane of the film results in a periodic variation of the diffraction patterns characteristic of (1$\bar{1}$20) planes of growing parallel to the substrate. The epitaxial relationship between film and substrate is same as that for AlN. Figure 5-20 illustrates the typical electron diffraction patterns observed for (0001) oriented films of GaN which were grown on (0001) sapphire, (111) $MgAl_2O_4$ and (0001) SiC substrates.

The films which are grown are clear and insulating. The insulating character appears to be due primarily to the high defect density of the films which is

FIG. 5-19

RED OF GaN ON (1102) Al$_2$O$_3$

[0001]
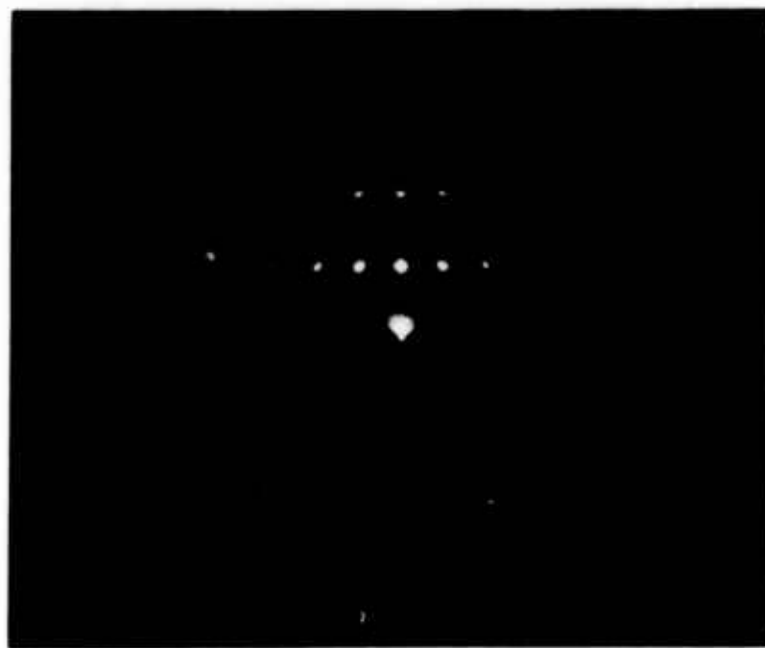
[11$\bar{2}$0]

FIG. 5 — 20

RED OF GaN ON (0001) SiC
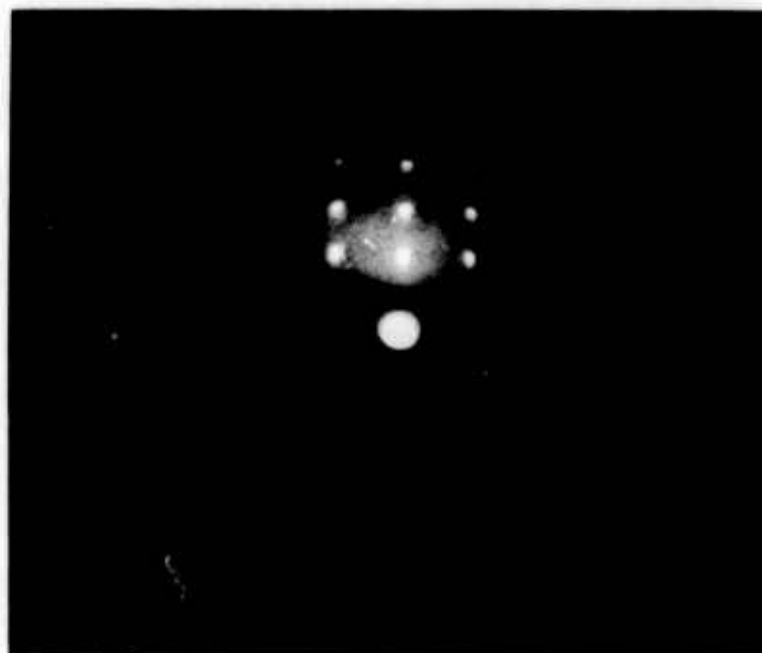
[11$\bar{2}$0]
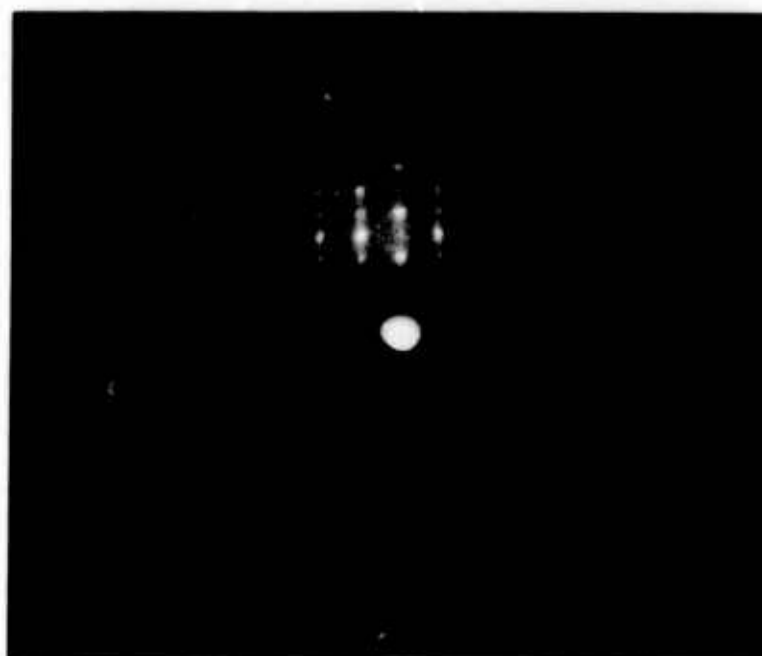
[10$\bar{1}$0]

apparent from the broadening of the diffraction spots which may be indicative of
a mosaic-block type structure in the films. Optical waveguide evaluation of the
heteroepitaxial structures of gallium nitride grown on sapphire and spinel showed
very high loss. The high loss is probably attributable to a high residual stress
level in the films which may result from a poor lattice match and/or differences
in thermal coefficients of expansion between the film and substrate. The structure
of the films was found to show some improvement with each improvement to the
cathode geometry but doping studies were not initiated because the defect density
of the films could not be reduced sufficiently before the termination of the contract.

5.6 Conclusions

Reactive sputtering has proven itself as a viable technique for the synthesis
and growth refractory compounds such as aluminum nitride and gallium nitride. The
development of the sputtering deposition process is not as complex as that
required for growth by chemical vapor deposition techniques. Reactive sputtering
of the nitride in an ammonia ambient has been shown to be preferred over sputtering
in nitrogen.

Although the deposition rate by sputtering is less than that obtained by
chemical vapor deposition techniques, this is more than offset by the uniformity
of film thickness over large areas and the superior surface finish obtained by
sputtering.

The surface acoustic wave evaluation of aluminum nitride has been very
encouraging. The first useful data on the piezoelectric coupling coefficient for
(0001) oriented AlN films has been generated. Although the coupling coefficient
is expected to be smaller for this orientation, the measured value $K^2 = 0.2\%$ is
comparable to the best reported value ($K^2 = 0.6\%$) for ($11\bar{2}0$) oriented films grown
by CVD. Surface acoustic wave transducers can be applied directly to as grown
surfaces of films prepared by sputtering whereas films prepared by CVD require
mechanical polishing. Our results point up the fact that preparation of AlN films
by reactive sputtering deserves serious consideration for fabrication of surface
acoustic wave devices for future signal processing applications. A particulary
encouraging consideration is that growth of aluminum nitride by reactive sputtering
has been under study for slightly more than a year whereas the process development
for growth by chemical vapor deposition has been continuing for more than three years.

The results obtained with optical waveguide evaluations of aluminum nitride
heteroepitaxial structures has not been as ecnouraging. Optical waveguide loss
has been reduced to 30dB/cm at 0.6328μm and 15dB/cm at 1.06μm but these figures are
to high for useful device applications in integrated optics. Residual film stress
appears to be the limiting factor preventing the further reduction of optical wave-
guiding losses. This stems from the large differences in thermal coefficients of
expansion between the film and substrate.

The preparation of gallium nitride by reactive sputtering presented itself as a more difficult problem. This was due to the fact that gallium metal is liquid at $30^{\circ}C$ and is readily oxidized. The structure of films grown was improved with successive improvements to the sputtering cathode. Insulating films were grown but the defect density was still high. Optical waveguiding losses were very high and can be attributed to the relatively poor structure of the films. This may be due in part to a high residual stress level in the films. It appears that further improvement could be achieved in film quality with added effort. It would be of interest to continue the growth studies to determine if p-type gallium nitride could be prepared by reactive sputtering.

5.7 References

5-1 Y. M. Yim, E. J. Stofko, P. J. Zanucchi, J. I. Pankove, M. Ettenbury and S. L. Gilbert, J. Appl. Phys., 44, 292 (1972).

5-2 M. T. Wauk and D. K. Winslow, Appl. Phys. Lett. 13, 286 (1968).

5-3 J. H. Collins, P. J. Hagon and G. R. Pulliam, Ultrasonics, 8, 218 (1970).

5-4 R. F. Rutz, E. P. Harris, and J. J. Cuomo, IBM J. Res. Develop. 17, 61 (1973).

5-5 H. M. Manasevit, F. M. Erdmann and W. I. Simpson, J. Electrochem. Soc. 118 1864 (1971).

5-6 M. T. Duffy, C. C. Wang, G. D. O'Clock, Jr., S. H. McFarlane, III, and P. J. Zanzucchi, J. Electron. Mater. 2, 359 (1973).

5-7 A. J. Norieka, M. H. Francombe, and S. A. Zeitman, J. Vac. Sci. Technol. 6, 194 (1969).

5-8 N. F. Foster, J. Vac. Sci. Technol. 6, 111 (1969).

5-9 P. K. Tien, Appl. Opt., 10, 2395 (1971).

5-10 P. J. Hagon and L. Dyal, Proc. 1972 Ultrasonics Symposium, p. 274 (1972).

5-11 P. J. Hagon and L. Dyal, Proc. 1972 Ultrasonics Symposium p. 247 (1972).

5-12 G. D. O'Clock, Jr. and M. T. Duffy, Appl. Phys. Lett., 23, 55 (1973).

5-13 Y. M. Yim and R. J. Paff, J. Appl. Phys., 45, 1456 (1974).

5-14 H. M. Manasevit, J. E. Cofer, F. A. Pizzarello, R. P. Ruth, Air Force
Materials Lab. Report AFML-TR-73-295.

5-15 J. I. Pankov, H. P. Maruska and J. E. Berkheiser, Appl. Phys. Lett. $\underline{17}$,
197 (1970).

6.0 GROWTH OF GaAs EPITAXIAL FILMS

6.1 Introduction

GaAs and its ternary alloys, especially $Ga_{1-x}Al_xAs$, find wide application in integrated optics as both active and passive elements. These include lasers, light emitting diodes, modulators, and waveguides. Sputtering provides a promising alternative in the fabrication of these devices.

Previous investigations in the evaporation of GaAs have generally yielded high-resistivity and very low-mobility films (Ref. 6-1 to 6-4) as compared to that obtainable from vapor and liquid phase epitaxy. Sputtering has also yielded films with $\rho \sim 10^2$ to 10^5 ohm-cm (Ref. 6-5), but single crystal epitaxial growth was obtained at considerably lower temperatures than that possible by conventional techniques. Since argon was used as the sputtering gas, and since arsenic is considerably more volatile than gallium, it is quite possible that arsenic deficiency existed and may have been responsible for the poor electrical characteristics of the films. In order to realize the inherent advantages of sputtering, UARL proposed the sputtering of GaAs with arsenic vapor and therefore compensate for its likely deficiency in previous results with evaporated and argon-sputtered films of GaAs.

6.2 Experimental Details

6.2.1 Arsenic Sputtering System

Since arsenic has a low vapor pressure at room temperature, a special sputtering system had to be designed so that the whole chamber could operate at elevated temperatures. To obtain a pressure of arsenic in the millitorr range, the system had to be heated to 250°C to 300°C to prevent undue condensation of the arsenic on the internal surfaces. The chamber is constructed of stainless steel, and all feed-throughs are sealed with crushed copper gaskets so that the system can be heated to 300°C without degradation of or contamination by organic seals. Arsenic pressure is measured by a Varian Millitorr ion gauge. Substrate temperature is controlled by heaters which are welded on to a stainless steel mounting block. Figures 6-1 and 6-2 show the chamber with and without the heat shroud, and a schematic diagram of the system is shown in Fig. 6-3.

Conventional oil diffusion pumped systems suffer from the continual admission of hydrocarbons from the diffusion pump, however exquisitely designed the baffle between the chamber and diffusion pump may be. Once it is pumped to the desired pressure, a chamber may be sealed and a stagnant process used for sputtering. This has the disadvantage of permitting contaminants desorbed from the chamber walls by the glow discharge to have ample time for diffusion to the substrate. A continuously pumped sputtering chamber is, thus, desirable. The chamber is therefore evacuated

FIG. 6-1

ARSENIC SPUTTERING SYSTEM

RL-72-380-D

FIG. 6-2
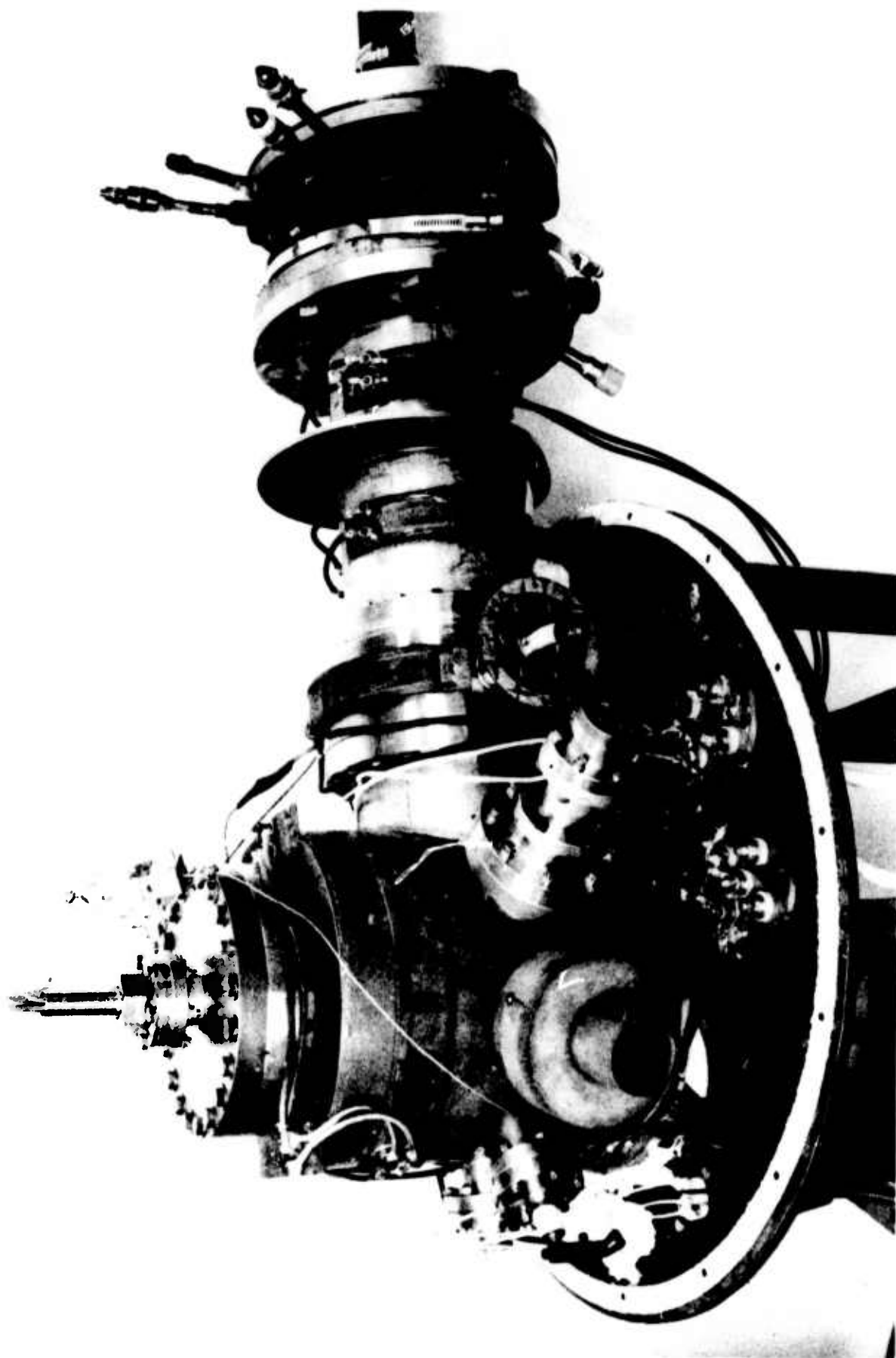
ARSENIC SPUTTERING SYSTEM WITH HEAT SHROUD

RL-72-380-A

FIG. 6-3

SCHEMATIC OF GaAs SPUTTERING SYSTEM

b)

a)
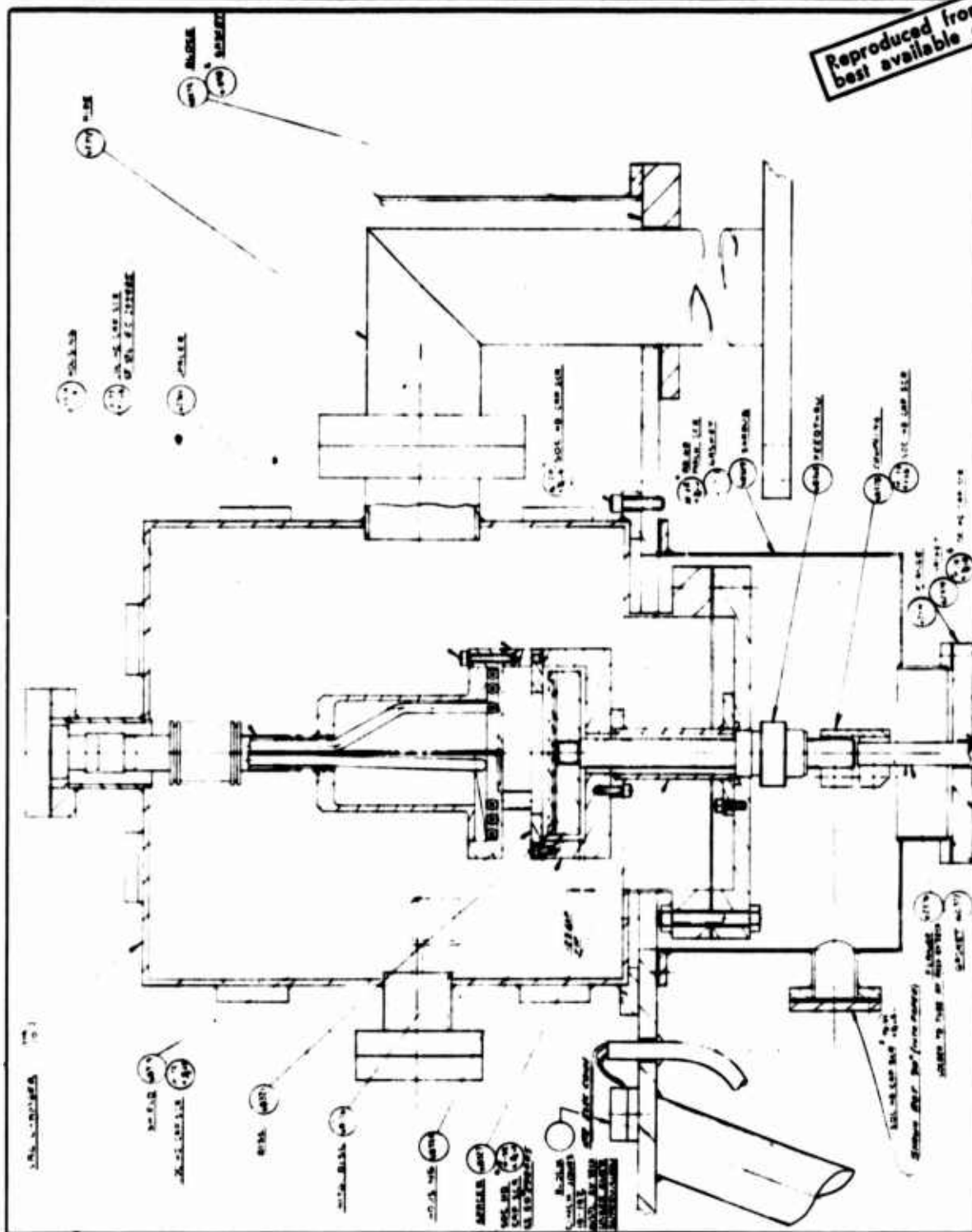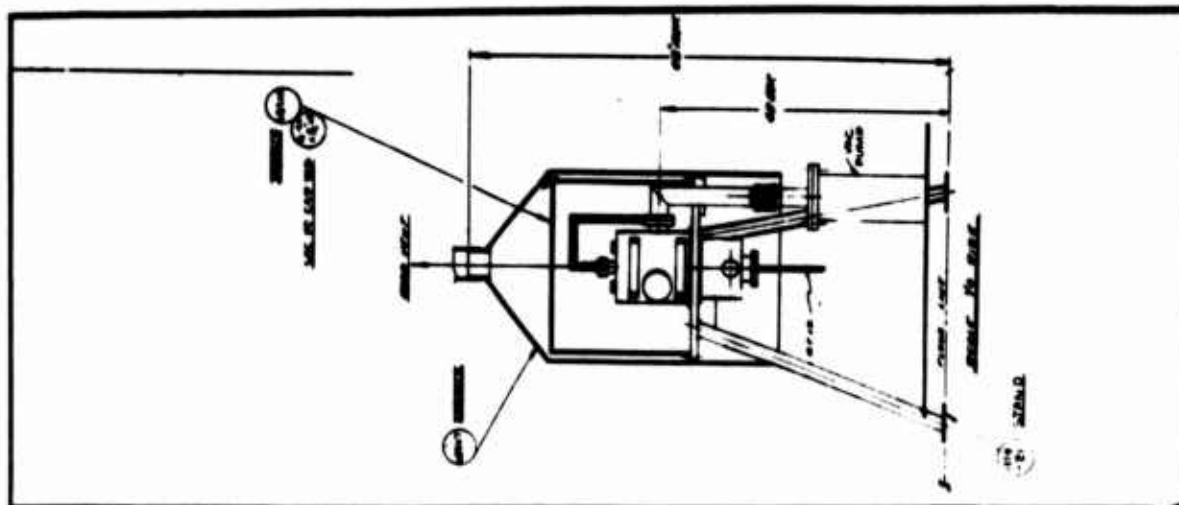
by a Welsh 3101 turbomolecular pump which is capable of a pumping speed of 250 L/sec in the millitorr range. Thus, "backstreaming" hydrocarbons are completely eliminated and a high rate flushing action can be maintained.

Since it was found necessary in the early stages of GaAs sputtering that both a shutter and sputter cleaning capability were necessary to achieve epitaxy, these features were installed. Figure 6-4 shows the details of the electrode assembly. The gallium target is liquid at the 250°C to 300°C chamber temperature and must be held in a saucer shaped electrode. Because of its low reactivity with gallium, molybdenum was chosen as the material from which the electrode was fabricated. A grounded ring was placed over the electrode edge to shield it from sputtering. Only the gallium is then permitted to be exposed to the plasma.

To maintain a constant arsenic pressure, a controller was designed which has an output proportional to the difference between the ion gauge voltage and a preset voltage. This output regulates an S.C.R. circuit which supplies current to a pair of crucibles in the chamber (see Fig. 6-5). Aluminum oxide coated tungsten wire crucibles are used to prevent the arsenic from reacting with the hot wire. Since arsenic condensation would take place in the turbine pump, two liquid nitrogen traps are placed between the chamber and the pump. It is this baffle which actually pumps the arsenic. A flap type valve is located inside the heated shroud just before the baffle to provide control of the arsenic consumption.

6.2.2 Experimental Procedures for GaAs Epitaxial Growth

The starting materials used in the III-V sputtering growths were all high purity*. Substrate material was in-house grown via the horizontal Bridgman technique, and was silicon doped to be n-type ($n \sim 0.6 - 4 \times 10^{18}$ cm^{-3}) or Cr-doped semi-insulating ($\rho \sim 10^7 - 10^8$ ohm-cm). Boules were cut to yield (100) oriented wafers, which were lapped and chemi-mechanically polished in sulfuric-peroxide or sodium hypochlorite etches. Prior to mounting of the substrate wafers, they were cleaned using the following steps: (1) degreasing in Kern decontam, (2) rinsing in distilled water and propanol prior to boiling in trichlorethylene, (3) propanol and distilled water rinses followed by 10 minutes in warm 4:1 = HCl:H$_2$O to remove any oxides and (4) final rinsing in distilled water and alcohol. All reagents were electronic grade. After the cleaning and mounting procedures, As, which had been purchased in sealed evacuated containers, was loaded into the arsenic crucible. The system was sealed with a new copper gasket and pumped to $< 2 \times 10^{-6}$ torr with the liquid nitrogen traps filled. At this point, current was supplied to the substrate and tank heaters; three hours were required to equilibrate to temperature during which time the system

---

* Ga - 99.9999% pure, Alusuisse
  As - 99.999% pure, Cominco
  Al - 99.999% pure, Atomergic
  Sb - 99.9999% pure, Cominco

FIG. 6-4

SCHEMATIC OF ELECTRODE CONFIGURATION

SUBSTRATE HEATER

INSULATOR

MASK

MOVABLE SHUTTER

AND ARM

SAPPHIRE PLATE

S.S. PLATE

GaAs SUBSTRATE

Ga ELECTRODE

MOLYBDENUM DISH

ELECTRODE
GROUND SHIELD

FIG. 6-5
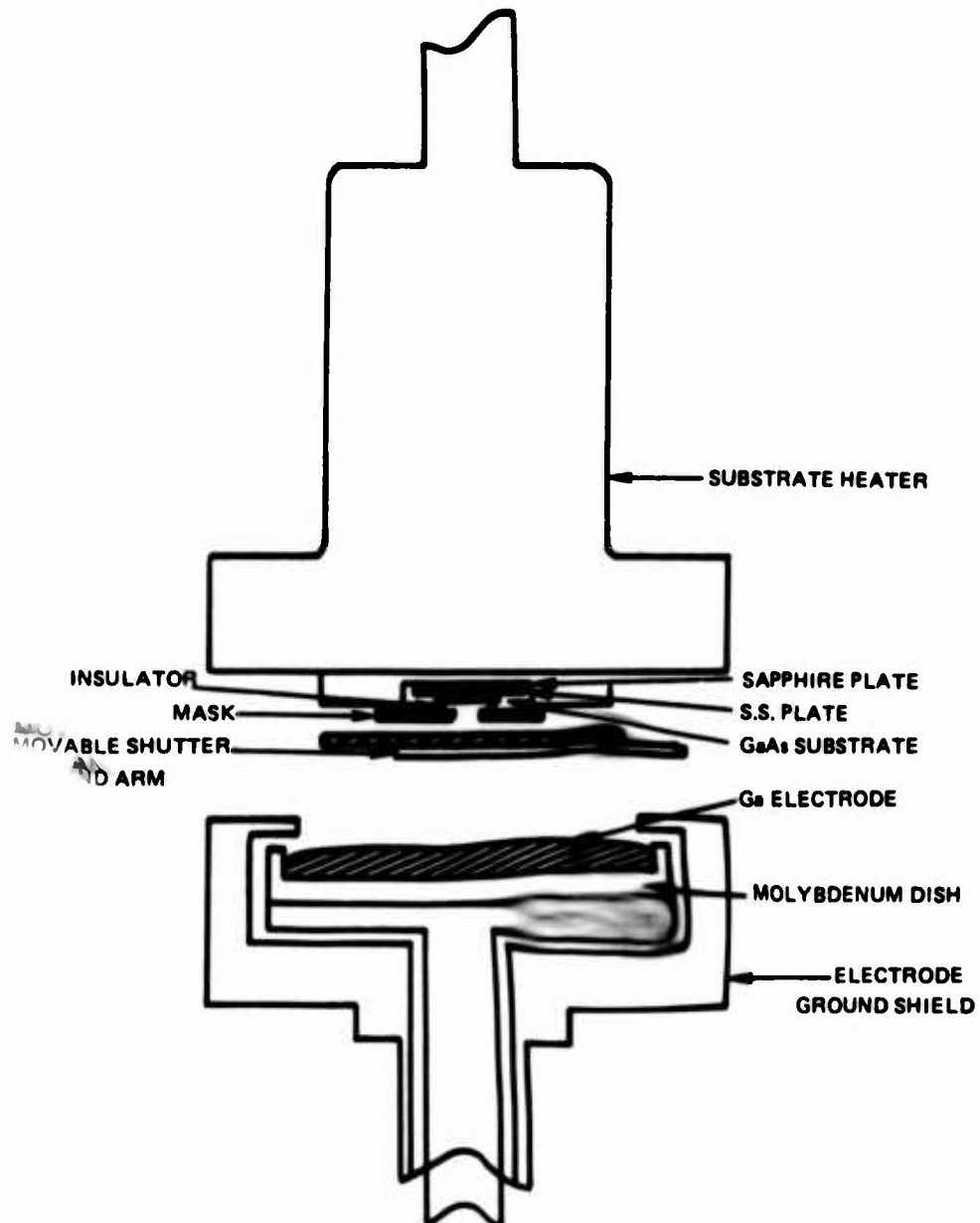
ARSENIC GAS CONTROL SYSTEM

TURBOMOLECULAR PUMP

OVEN

SPUTTERING CHAMBER

DOUBLE LN$_2$ TRAP (As PUMP)

As PUMP CONTROL

ION GUAGE

OVEN

HEATED CRUCIBLE CONTAINING As

STRIP CHART RECORDER

ION GAUGE CONTROL UNIT

CRUCIBLE HEATER CONTROL

ARBITRARY SET POINT

N12-24-3

99
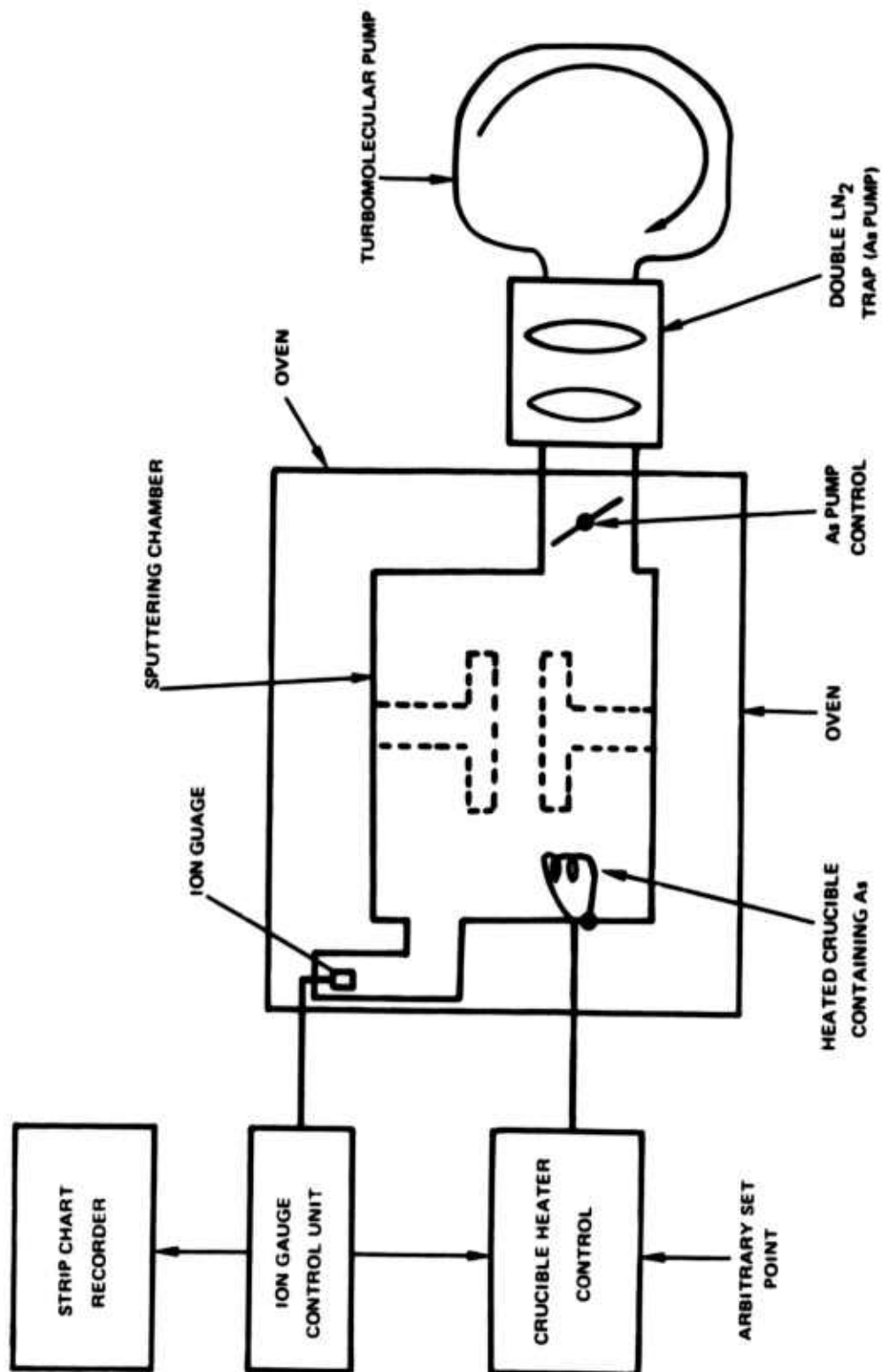
was continually pumped via the turbopump. The arsenic pressure control was set to a desired value, and when this was reached, the target was sputter cleaned with the shutter closed for 15 to 25 minutes at 350 to 500 watts (4-inch diameter target). The substrate was then sputter cleaned (rms voltage of $\sim$ 150 Volts) for ten minutes with the shutter open. After this, the shutter was closed, the plasma stabilized at a desired power setting, and growth commenced when the shutter was again opened. At the end of the growth run, all heaters were turned off, the arsenic pump control valve was fully opened, and while keeping the liquid nitrogen traps filled, the system cooled to room temperature overnight. After removal of a sample, its IR reflectance interference pattern was recorded on a Perkin-Elmer Type 621 infrared spectrophotometer in order to measure the film's thickness.

6.3 Verification of GaAs Synthesis by Reactive Sputtering

Initial depositions yielded polycrystalline material which had to be proven to be GaAs. X-ray diffraction, electron microprobe analyses, and infrared spectroscopy were used in this verification.

6.3.1 X-Ray Diffraction

A Phillips X-ray Diffractometer with a copper target was used in this investigation. The target was excited by 40 Kev electrons, and a nickel filter was inserted into the X-ray beam. An X-ray diffraction scan of a single-crystal gallium arsenide substrate is shown in Fig. 6-6a. The substrate is oriented with a (100) face parallel with the surface, and therefore, large peaks due to the (200) and (400) planes are recorded. Figure 6-6b is a diffractometer scan of a sputtered film on another (100) oriented gallium arsenide substrate. The large (200) and (400) peaks are principally due to the substrate, but all the other peaks result from the polycrystalline film indexed to be gallium arsenide. No other materials or phases were observed.

6.3.2 Electron Microprobe Analysis

Using a Norelco electron probe, two polycrystalline samples were quantitatively analyzed and were found to be stoichiometric to within 0.5 to 1% which is the accuracy of the method.

The samples were also microprobe analyzed for impurities. Specific analysis was made for those materials used in the vacuum system, that is, Fe, Ni, Cr, Cu, Si, and O. These elements were not observed down to the sensitivity of the measurement which is about 0.1 weight percent. A full spectral check was made for all the other detectable elements, but this measurement did not reveal any other impurities.

FIG. 6-6

X – RAY DIFFRACTION SCANS
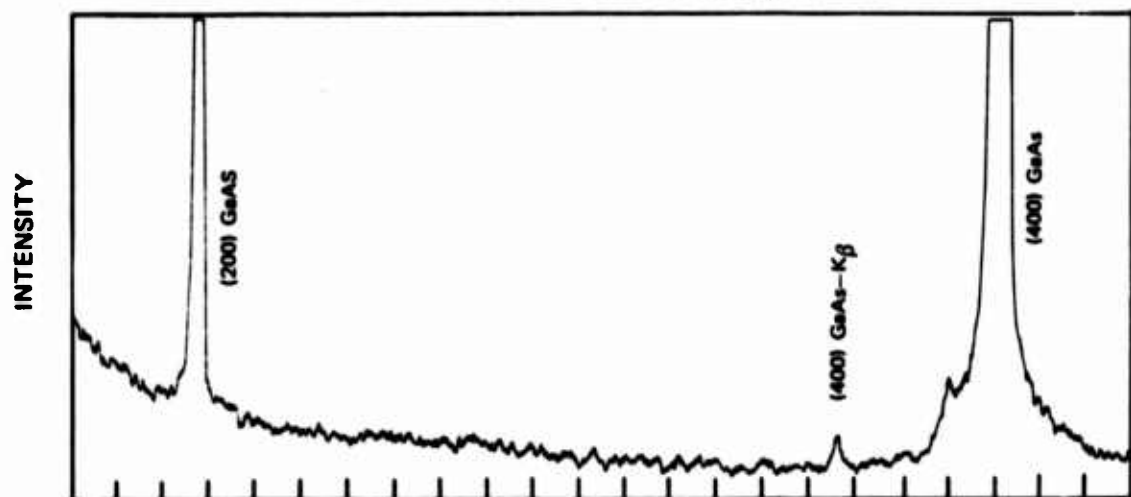
a. (100) GaAs SUBSTRATE
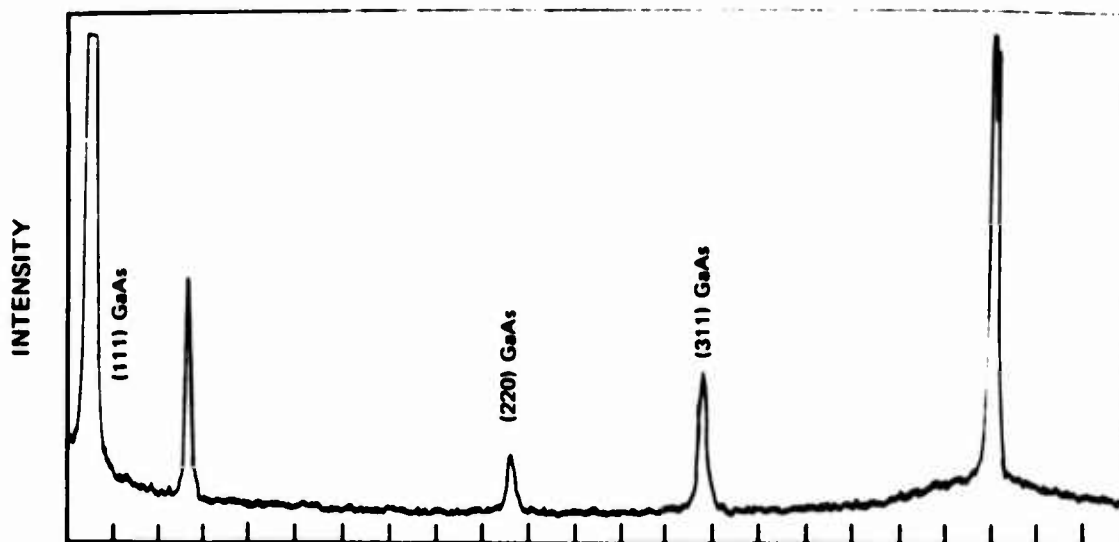
b. POLYCRYSTALLINE GaAs FILM

c. EPITAXIAL GaAs

DIFFRACTION ANGLE, 2θ DEG
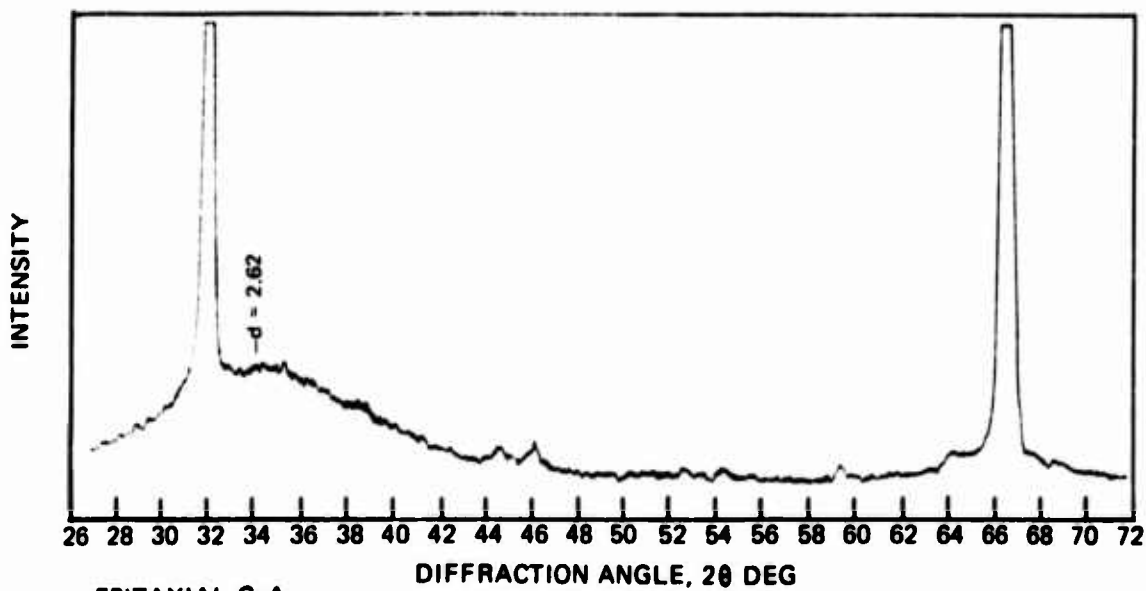
6.3.3 Infrared Spectrographic Analysis

A Perkin-Elmer Type 621 infrared spectrophotometer fitted for reflectance measurements was employed in this phase of the investigation.

The reststrahlen peak was used to identify the presence of GaAs deposited on a silicon substrate. The silicon substrate was chosen since there is no change in its reflectivity in the 30- to 40-μm range. An almost identical reflectance peak was found for the GaAs film as is seen for bulk chromium-doped semi-insulating GaAs (compare Figs. 6-7a and 6-7b).

Early films grown on GaAs substrates gave rise to very large interference fringes, a typical example of which is seen in Fig. 6-7c. This could only happen if there was a large difference in the index of refraction between the film and substrate, or if an interfacial layer, with a different index, existed between the GaAs substrate and the film. Examination of Fig. 6-7c also reveals a periodic amplitude variation with wavelength which suggests the presence of a second film.

6.4 Verification of the Presence of an Interfacial Layer

Two techniques were employed to determine if such a layer existed. First, a substrate was mounted in cross section, lightly etched and replicated. The replica was then observed in an electron microscope. The photomicrograph in Fig. 6-8 clearly shows an interface layer between the substrate and the GaAs deposit. Second, another sample was etched slowly down from the surface until the interface layer was revealed. A photograph of this layer is shown in Fig. 6-9, where the interface layer has folded over. Another sample of the interface layer was floated off this GaAs substrate and placed on a silicon wafer. Electron microprobe analysis of this film indicated only gallium and oxygen; therefore, the interfacial layer is most probably Ga_2O_3.

Contamination of the gallium target by oxygen and water vapor occurs when the vacuum system is opened. The films discussed above were deposited directly from such a contaminated target; consequently, the interface layer of gallium oxide is formed as the oxidized target surface is sputtered. When all the oxide is sputtered from the target, a distinct gallium arsenide layer is deposited on the oxide layer as can be seen in Fig. 6-8 and as verified by X-ray diffraction (Fig. 6-6b).

6.5 Techniques to Eliminate the Interfacial Layer

The preceeding experiments have determined the existence of an oxide layer on the substrate. This layer was the cause of polycrystalline growth and must be eliminated to enable epitaxial growth.

FIG. 6-7

IR REFLECTANCE SPECTROGRAPHS
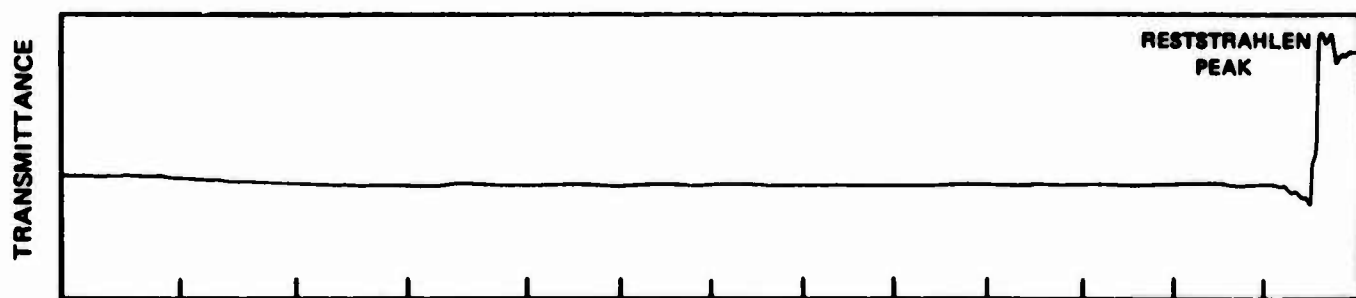
a. BULK CHROMIUM–DOPED GaAs
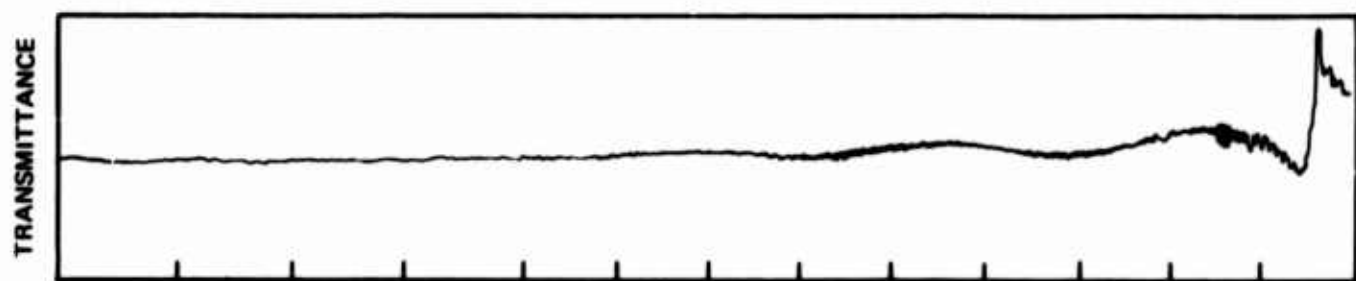
b. GaAs FILM ON SILICON

c. GaAs FILM ON GaAs

FIG. 6-8
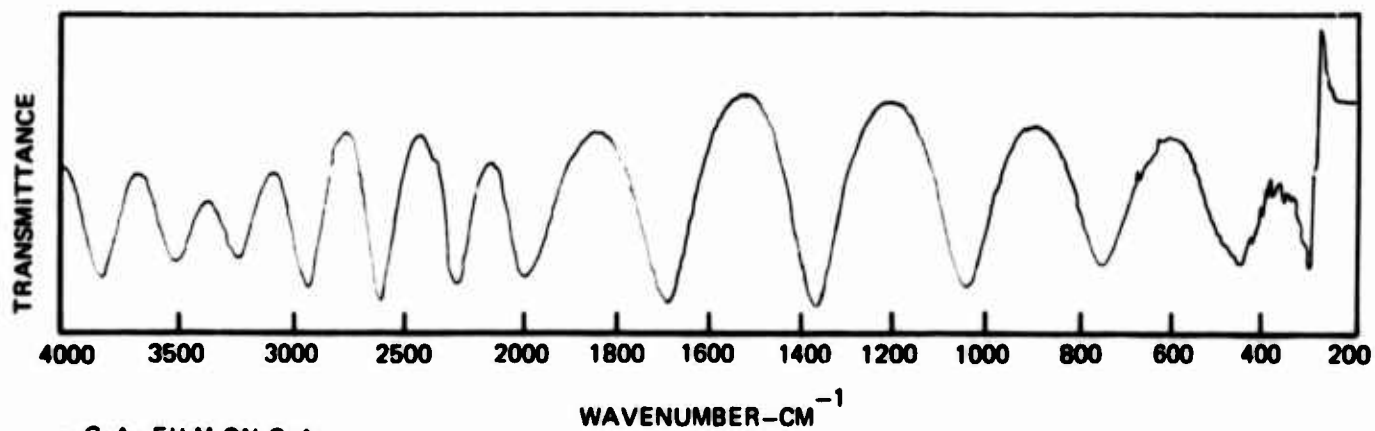
ELECTRON PHOTOMICROGRAPH OF GALLIUM ARSENIDE AND SPUTTERED LAYERS
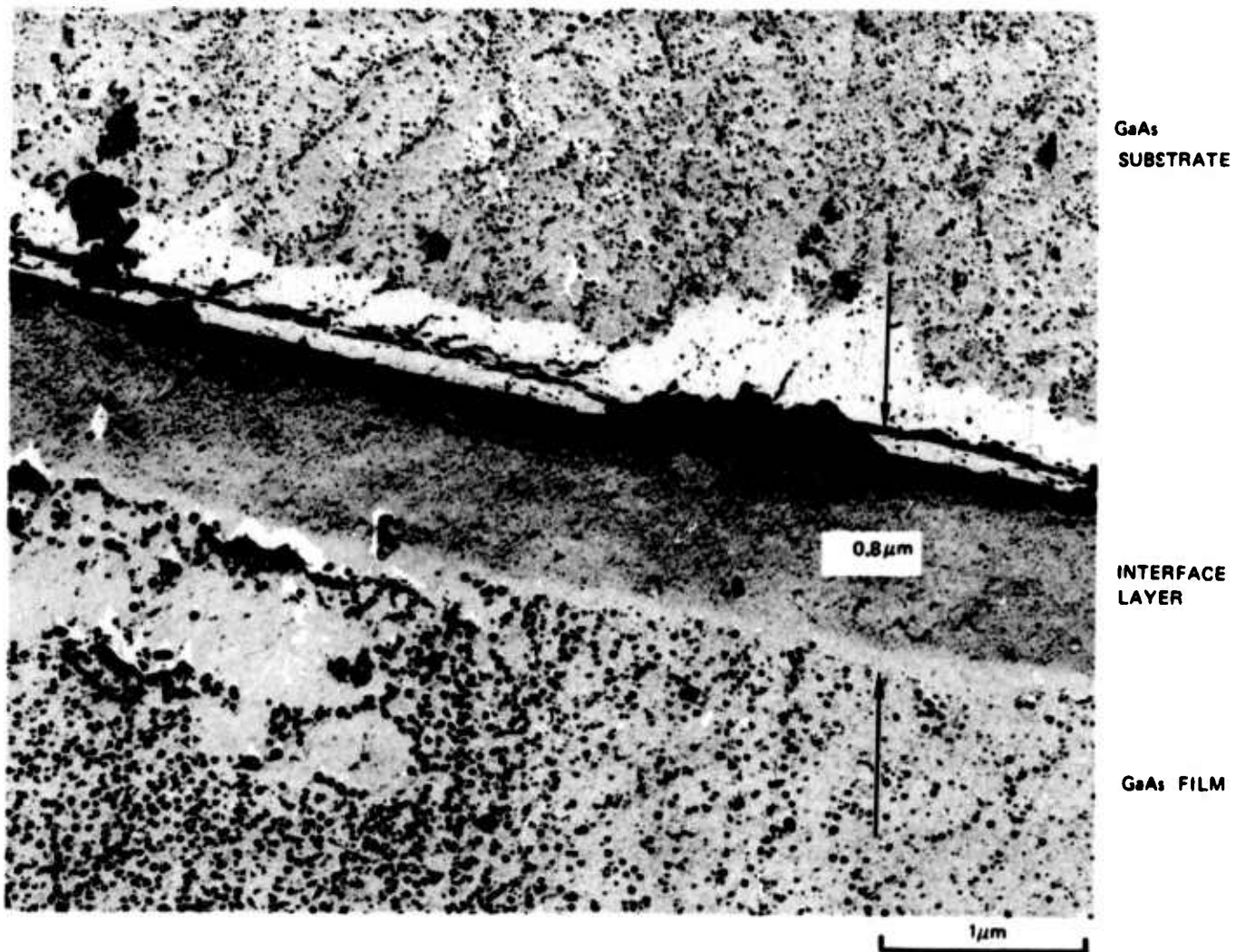
OPTICAL PHOTOMICROGRAPH OF THE TOP VIEW OF THE INTERFACE LAYER
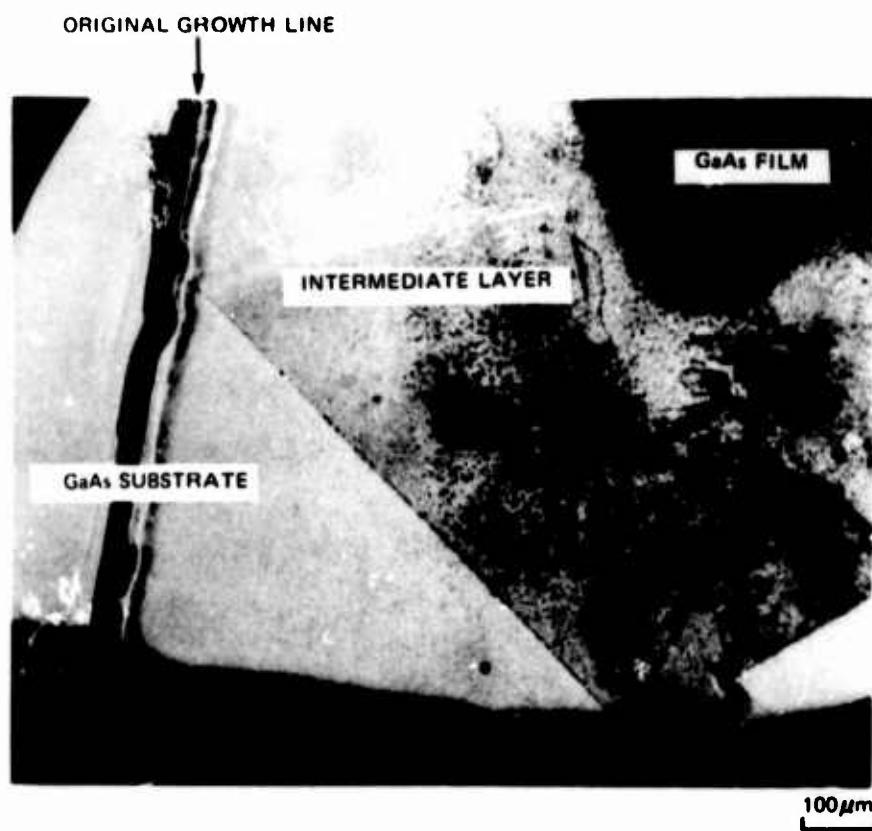
Two procedures have been employed which together have solved the problem of the interface layer. First, the gallium target is sputter cleaned with a shutter positioned in front of the substrate. This removes the gallium oxide from the target surface. Secondly, the shutter is opened and the substrate is sputter cleaned to remove any contamination that might have occurred during system bake-out and target cleaning. The use of these procedures enabled the deposition of an epitaxial film which is described in the next section.

6.6 Characterization of Initial Epitaxial Films of GaAs

6.6.1 Depositon Parameters

The first epitaxial GaAs film (Ga-17) was sputtered using the following deposition parameters:

1. Gallium target sputter cleaning - 15 W/cm^2 for 15 min.
2. Substrate rf sputter cleaning - 220 V (rms) for 12 min.
3. Film deposition - 3.7 W/cm^2 for 82 min.
4. Substrate temperature - 375°C.
5. Deposition rate - 280 Å/min (2.2 Å/min/watt)
6. Arsenic pressure - 20 to 25 mtorr
7. Substrate - Cr-doped GaAs oriented in the (100) direction.

To our knowledge, this is the first time that single crystal epitaxial GaAs has been sputtered in an arsenic ambient.

6.6.2 Reflection Electron Diffraction (RED)

Each of the samples was mounted on a pedestal using silver paint. The edges of the substrate were also covered with paint to prevent diffraction off the substrate. The (110) pattern from the film can be seen in Fig. 6-10. The computed "d" spacing is proper for gallium arsenide, and the orientation of the patterns with respect to the substrate cleavage planes is correct. Kikuchi lines, which indicate a high degree of order, are present for all orientations of the film with the electron beam. No evidence of polycrystalline rings, amorphous halos or twinning can be observed.

These RED results strongly indicate that the film surface is single crystal gallium arsenide which is epitaxially grown on the substrate.

FIG. 6-10

RED OF EPITAXIAL GaAs GROWN ON (100) GaAs SUBSTRATE

ELECTRON BEAM ALONG [110]

6.6.3 X-Ray Diffraction

The X-ray scan shown in Fig. 6-6c for the epitaxial sample has very large (200) and (400) peaks due to both the substrate and the film. There are also very weak GaAs lines associated with (311) and (220) planes parallel to the sample surface. This indicates polycrystalline growth somewhere in the film. Together with the RED results it is presently believed that the polycrystallinity arises due to initial growth on dirt particles. The X-ray diffraction scan also has an unexplained broad peak around a "d" spacing of 2.62 Å.

6.6.4 Microscopic Examination of an Epitaxial Layer

Figure 6-11 shows a cleaved cross-section of a sputtered epitaxial film of thickness 7.5 μm on a Cr-doped substrate. In the as-grown picture there is no indication of an interface separating the film from the substrate. Upon etching in 1:1:1 = HNO_3:HF:H_2O, the substrate-layer interface is clearly shown since etch rates either at the boundary or between the film and substrate do vary.

6.6.5 Initial Resistivity and Hall Measurements

The conductivity was determined for our first single crystal film Ga-17 grown on a chromium-doped GaAs semi-insulating substrate over the temperature range -100°C to 130°C. Due to the high impedance of the sample ($\sim 10^8$ ohms) dc measurements were made using a Keithley electrometer. Sample preparation involved defining a Hall mesa by etching through the film. Tin contacts were alloyed to the epitaxial layer, but this process also makes contact to the substrate. The resistivity of the chromium-doped gallium arsenide is $\sim 10^7$ to 10^8 ohm-cm at room temperature and decreases rapidly with increasing temperature, $\rho \sim \exp(\Delta E/kT)$ where $\Delta E \sim 0.57$ eV (Ref. 6-6) in our temperature interval of measurement. Resistivity measurements made on our epitaxial layer and substrate above room temperature (see Fig. 6-12) show an activation energy (0.63 eV) characteristic of the substrate and not the film. At lower temperatures, the substrate becomes more insulating and properly isolates the film to give meaningful film resistivity data. At room temperature the film resistivity is 9.3×10^3 ohm-cm and exhibits a resistivity variation with temperature of exp (0.085 ev/kT). If the reasonable assumption is made that the carrier mobility does not change appreciably over this temperature interval, this temperature dependence can be due to a structural defect (Ref. 6-7) or to an impurity, e.g., copper (Ref. 6-8) or manganese (Ref. 6-9). If levels deeper than 0.1 ev below the conduction band are present, these of course, would be masked by the shorting-out effect of the substrate at higher temperatures.

No reliable Hall data could be extracted from the first single crystal film. If one calculates the Hall mobility and carrier concentration from our results at room temperature and assigns these values to the epitaxial layer, the results are as follows: free electron density, n = 7×10^{13} cm^{-3} and Hall mobility,

FIG. 6-11

CROSS SECTION OF SPUTTERED GaAs FILM ON GaAs SUBSTRATE (Ga20)
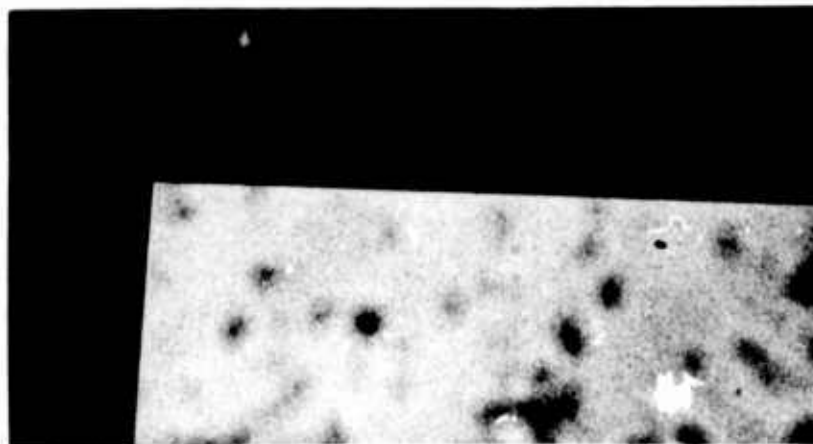
AS-GROWN (CLEAVED)

ETCHED

FIG. 6—12
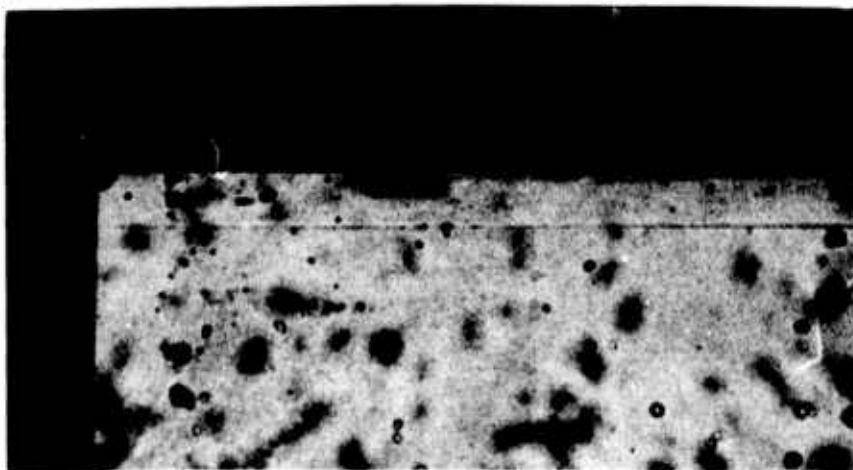
RESISTANCE VS. INVERSE TEMPERATURE FOR EPITAXIAL GaAs
ON SEMI-INSULATING SUBSTRATE
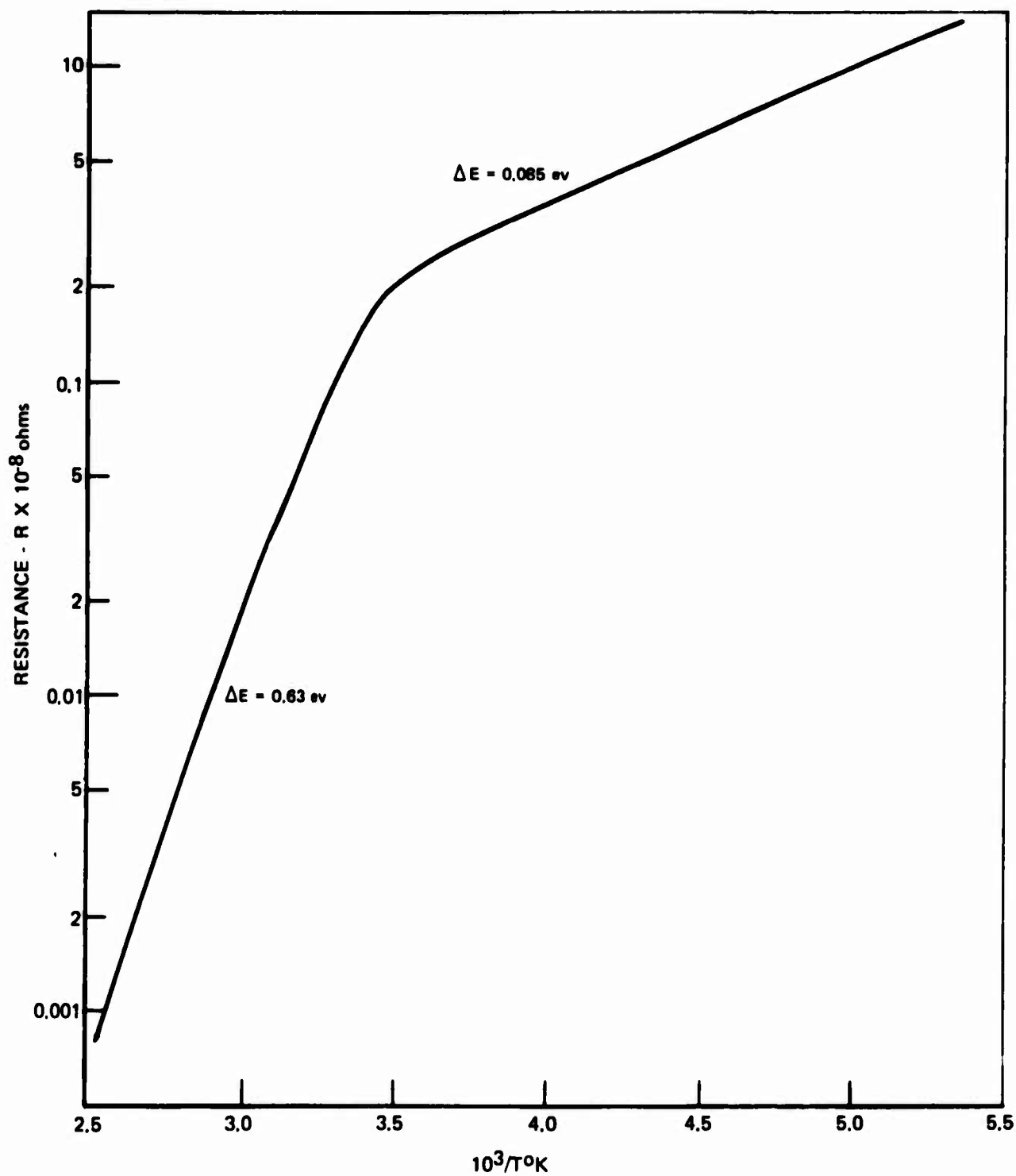
μ_H = 9.7 cm^2/V-sec. Since typical Hall measurements for the Cr-doped substrate material indicate a net n-type conductivity with Hall mobilities $\sim$ 100-600 cm^2/V-sec, significant contributions from the substrate to the measured Hall voltages will exist if the Hall mobility of a fairly resistive film is below that of the semi-insulating substrate. This is believed to be the situation here. Furthermore, a Hall mobility of 9.7 cm^2/V-sec for electrons does not make sense in GaAs. However, it is possible that the epitaxial film is p-type and has a Hall mobility less than commonly observed room temperature values of $\sim$ 400 cm^2/V-sec for pure material. The measured Hall voltage will then consist of a negative contribution from the substrate and a positive contribution from the film and not give a meaningful result if assigned to the film.

There are two possible reasons for the observed properties of the first epitaxial GaAs film. The most ambiguous results are the high resistivity ($\sim$ 10^4 ohm-cm) and the apparent low n-type mobility ($\sim$ 10 cm^2/V-sec). These imply a free carrier density of 7 x 10^{13} cm^{-3}. On the other hand, a mobility of 10 cm^2/V-sec implies an ionized impurity concentration greater than 10^{20} cm^{-3}. This indicates an extremely high level of compensation. The question then is whether these compensating species are principally impurities or arsenic and/or gallium vacancies. Electron microprobe analysis indicates impurity levels less than 10^{19} cm^{-3}. One might, therefore, conclude that the compensation is due to vacancies rather than impurities. Since the present mobility measurements are in doubt due to the canceling effect of the substrate in the net measured Hall voltage, it is impossible to draw any hard conclusions from this sample. On the other hand, the influence of the substrate on the measurements could be eliminated if GaAs is grown on an insulating substrate, e.g., sapphire, so that unambiguous mobility measurements can be made. This will be described in Section 6.7.2.

6.6.6 Sputter-Ion Spectroscopy of a GaAs Film*

In order to further identify the cause of the anomalously low carrier mobility in the sputtered GaAs films, sputter-ion mass spectrographic analysis was employed. Depending on the particular impurity under analysis, concentrations as low as 20 ppb can be detected. As mentioned in Section 6.6.5, the cause of the low mobility in the GaAs films could be due to scattering by structural imperfections or to a large concentration ($\sim \leq$ 10^{20} cm^{-3}) of impurities. Since the electron microprobe technique initially used for impurity analysis could only detect high 10^{19} cm^{-3} concentrations, it obviously could not be used to detect the presence of several impurities whose concentrations add up to $\sim$ 10^{20} cm^{-3}. Table 6-I shows the results of the sputter ion analysis of sample Ga-23. Impurity determinations are listed for depths of 4.7 μm and 14 μm below the original film surface. If the concentrations of the non-III-V elements are added their total concentrations at these depths are 0.7 x 10^{18} cm^{-3}

---

*Analysis performed by F. G. Satkiewicz of GCA Corporation, Boston, Massachusetts.

Table 6-I

Mass Spectrographic Analysis of a Gallium Arsenide Film
(Sample Ga-23)

Species	ppm, atomic	
	4.7 μm depth*	14 μm depth*
B		~ 1
C	3	3
O	5	6
Na	0.4	1.4
Mg	~ 0.2	1.4
Al	8	17
Si	1	1.2
Cl		0.4
K	0.2	0.06
Ca		2.2
Ti	0.02	0.14
V	2.2	0.6
Cr	0.8	0.9
Mn	~ 2	1
Fe	~ 1	1.4
N:	N.D. **	~ 2
Co		~ 0.4
Cu	N.D. **	
Mo	~ 1	3.6
In	600	650

*Depth from film surface
**N.D. - not detected

FIG. 6-13

SPUTTER-ION MASS SPECTRUM OF A GaAs FILM
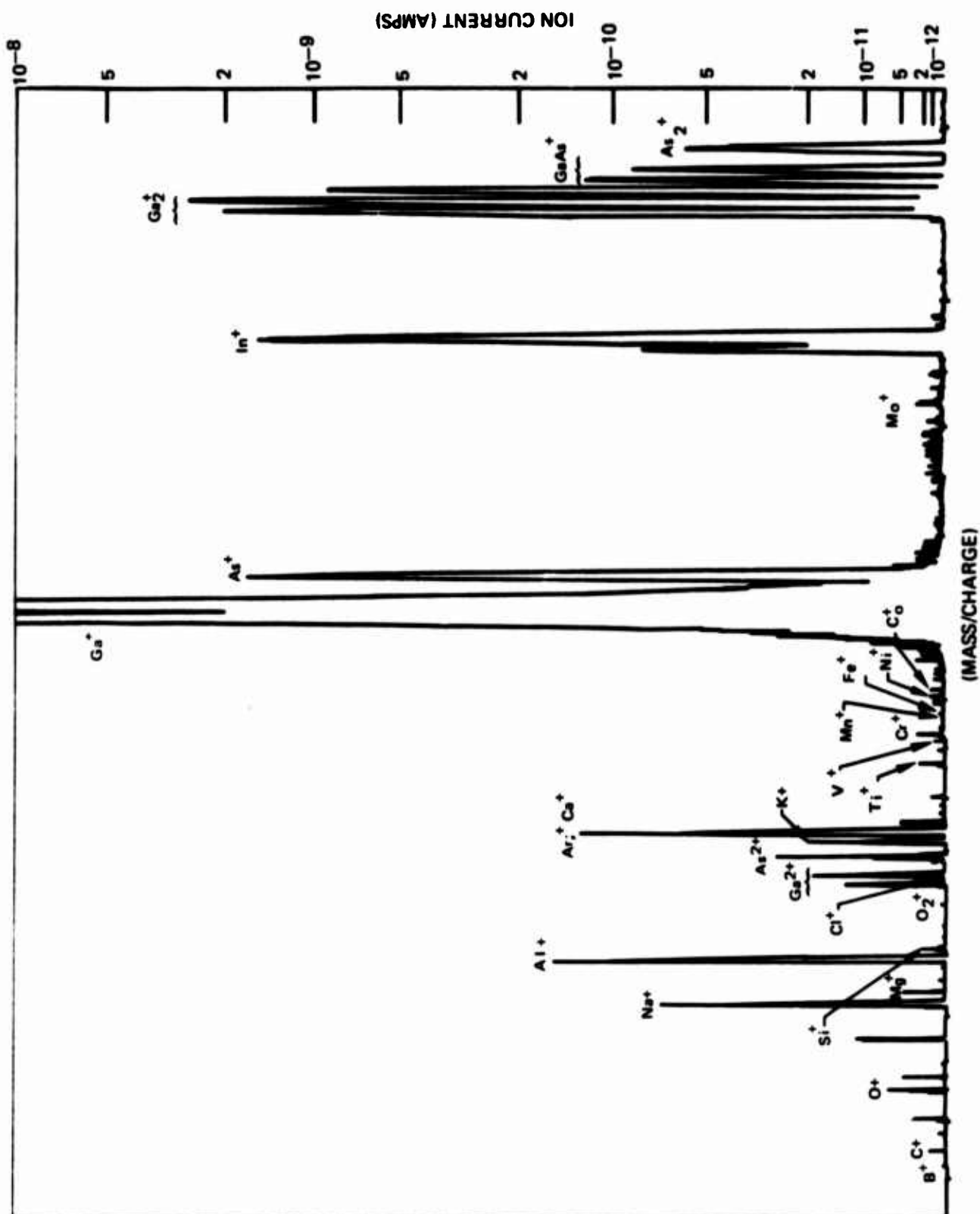
and 1.1×10^{18} cm^{-3}, respectively. The presence of impurities at these levels could not account for the low measured mobilities. Since the spectral line of the Ga^{69} positive ion partially interferes with the appearance of the copper line, the sensitivity of the analysis is limited to 2 ppm ($\sim 10^{17}$ cm^{-3}) for this impurity. Copper contamination had been a concern since copper gasketing is employed in the sputtering chamber. The rather large concentration of indium in the films cannot be traced to any component in the vacuum chamber. Spectrographic examination of the gallium target did reveal the presence of 24 ppm of indium. A separate analysis of the original gallium material showed less than 10 ppm indium; therefore, its presence must be due to an accidental contamination. Since indium and aluminum are group III elements, these will enter the lattice substitutionally and be electrically inactive. The possibility of strong alloy scattering from such a low concentration of these elements is highly unlikely.

The spectrum in Fig. 6-13 also reveals interesting facts about the nature of the argon-sputtered GaAs species. It is found that GaAs primarily dissociates on sputtering to give As$^+$, As$_2{}^+$, As^{+2}, Ga$^+$, Ga$_2{}^+$, and Ga^{2+}. In addition, a much lower concentration of associated species like GaAs$^+$ exist in the plasma. Since the Ga target in the GaAs sputtering system is exposed to arsenic at elevated temperatures, a film of GaAs is formed on the Ga surface. Under normal sputtering conditions it is this film that supplies the Ga species. It is expected that the distribution of the various species when sputtering with As is similar to that found in the case of sputter-ion spectroscopy.

6.7 Effect of Deposition Parameters on Sputtered GaAs

The deposition parameters that are readily controlled are: substrate temperature, deposition rate, sputtering gas and pressure, bias sputtering and choice of substrate material and it's orientation. The nature of the deposited film is in part controlled by the substrate temperature in that amorphous, polycrystalline or single crystal films can be formed. In addition, since it was shown by sputter-ion mass spectrometry in Section 6.6.6 that the major sputtered species are Ga and As, a chemical recomination to form GaAs must occur on the substrate. Therefore, the substrate temperature influences the kinetics of this reaction. Depending on the deposition rate at a given temperature amorphous, polycrystalline or single crystal films can be formed. A high rate tends to produce the more disordered forms; however, under certain circumstances (e.g., in the case of a volatile constituent) a low rate might enhance vacancy formation. Also, the concentration of impurities incorporated from the gas phase will be lowered by a high growth rate. The pressure of the sputtering gas affects the energy of the sputtered species via collisions with the ambient gas. Given any level of contamination in the sputtering gas a decrease in pressure will result in a larger concentration of impurities in the deposited film. In the case of GaAs the concentration ratio of arriving species can be controlled by varying the As pressure in the system. This is necessary in order to accommodate

the large difference in the sticking coefficient of the two elements. Sputtering at As pressures below that at which a plasma can be maintained can be accomplished by adding an inert gas. Choice of inert sputtering gas controls the deposition rate since sputtering is a momentum transfer process, and therefore, the rate goes as the square root of the molecular weight. Bias sputtering can affect film properties by removing weakly bonded impurities or hot atoms in metastable positions (similar to annealing). At higher bias-sputtering energies, however, radiation damage can be introduced into the film.

In order to characterize the effect of variations in the above deposition parameters, RED, resistivity and Hall effect measurements were employed. Combined resistivity and Hall effect measurements lead to a value for the carrier mobility which is commonly used as an integrity factor for single crystal GaAs. The Hall mobility provides a measure of the ionized impurity content and is affected by the presence of structural defects on a microscale. Carrier concentrations derived from Hall measurements permit the calculation of the free carrier depression of the optical index and extent of free carrier absorption. In addition to these more routine measurements, a determination of the stoichiometry of two GaAs films grown under different experimental conditions was made using the electron microprobe; these results are described below.

6.7.1 Electron Microprobe Determination of GaAs Stoichiometry

Since it appears that impurity scattering is not a reasonable explanation for the low observed carrier mobilities, a method to determine the presence of structural defects is required. Nonstoichiometry is a clear indication of structural defects. The electron microprobe can determine the composition of major constituents of a thin film to about 0.3%. This would be equivalent to a defect density $\sim 6 \times 10^{19} \text{cm}^{-3}$.

For accurate analysis using the microprobe a standard is measured along with the unkown film. The standards used for this application are Bridgman, Cr-doped, semi-insulating, single crystal GaAs. A convenient way to prepare the standard-film pair on one substrate is to partially mask the substrate during GaAs film deposition. The standard and film can then be measured in alternate fashion. To improve the accuracy of the determination, the sample and standard are alternately measured ten times for each element. Two films along with separate standards were evaluated, and the consistency between standards was also corroborated by comparing one standard with respect to the other. The standards were assumed to be stoichiometric GaAs.

Table 6-II summarizes the results for these samples. The films were prepared using different growth conditions to determine whether changes in stoichiometry would result. Changes were made in substrate temperature, growth rate, and sputtering gas (see Table 6-III). Sample Ga-27, prepared at 330°C clearly indicates a deficiency in Ga and an excess in arsenic. The higher temperature (490°C) sample is

TABLE 6-II

DETERMINATION OF STOICHIOMETRY BY ELECTRON MICROPROBE ANALYSIS

MEAN CHEMICAL COMPOSITIONS AND TWO SIGMA LIMITS BASED ON 10 ANALYSES

STANDARD

ELEMENT	WEIGHT PERCENT	STOICHIOMETRY
Ga	48.21	$Ga_{1.00 \pm 0.01} As_{1.00 \pm 0.01}$
As	51.79	

SAMPLE 41

ELEMENT	WEIGHT PERCENT	STOICHIOMETRY
Ga	48.18	$Ga_{0.999 \pm 0.008} As_{1.003 \pm 0.008}$
As	51.93	

SAMPLE 27

ELEMENT	WEIGHT PERCENT	STOICHIOMETRY
Ga	46.80	$Ga_{0.970 \pm 0.006} As_{1.027 \pm 0.006}$
As	53.25	

**

**

Table 6·III

Deposition Conditions and Electrical Properties of GaAs Films

Growth Run	Substrate Temp. (C°)	Deposition Rate Å/min (Å/min-watt)	Sputtering Pressure (μm)	ρ (ohm-cm)	Observed Mobility $cm^2 V^{-1} sec^{-1}$
(100) Cr-Doped GaAs Substrates					
17	375	280 (2.2)	20-25-As	9×10^3	< 10
20	375	1070 (4.3)	25-30-As	$> 2 \times 10^5$	< 20
21	375	130 (2.4)	25-As	---	--
22A	450	190 (3.4)	21-As	$> 2 \times 10^5$	--
23	375	1460 (3.0)	25-As	---	--
25	330	50 (1.0)	30-40-As	157	7.5
27	330	85 (1.3)	~ 40-As	54	1.3
32	555	230 (3.0)	< ~ 15-As	$> 3 \times 10^4$	--
35	565	270 (1.9)	0.3-As, 60-Ar	$> 3 \times 10^4$	--
39 [22V]*	495	45	~ 10-As, 15-20-Ar	$> 3 \times 10^4$	--
41 [50V]*	490	330	~ 5-As, 2-Ar	$> 2 \times 10^4$	--
43 [67V]*	460	160	~ 5-As, ~ 10-Ar	$> 2 \times 10^4$	--
44 [61V]*	490	75	~ 3-As, ~ 10-Ar	$> 2 \times 10^4$	--
45 [79V]*	490	90	~ 10-As, ~ 7-Ar	$> 2 \times 10^4$	--
46	490	50 (1.0)	< 0.1-As, 7-Ar	---	--

*Bias sputtering runs, applied rms voltage in brackets

			Sapphire Substrates		
20 (0001)	375	1070	25-30-As	---	--
21 (0001)	375	130	25-As	8.8×10^3	< 1
21 (1$\bar{1}$02)	375	130	25-As	---	--
27 (0001)	330	95 (1.5)	~ 40-As	48	< 0.2

117

Table 6-IV

Deposition Conditions and Electrical Properties of GaAs Films (Continued) and GaAlAs Films

Growth Run	Substrate Temp. (°C)	Deposition Rate Å/min (Å/min-watt)	Sputtering Pressure (μm of As)	ρ ohm-cm
47**	445	525(2.1)	40	-
48**	445	950(3.1)	30	-
51**	450	190	∿20	-
60	450	420(1.6)	∿20	>1 x 10^5
61	380	215(.71)	25	-
64	375	295(1.1)	30	>3 x 10^4
65	375	200(.8)	20-30	-
66	535	420(1.6)	30	>2 x 10^4
67	475	480(1.9)	35	-
68	475	475(2.3)	30	-
69	475	650(2.7)	35	>1 x 10^6
71	525	610(2.7)	35	-
75	500	575(3.2)	30-35	-
GaAlAs:				
72	510	465(2.1)	35	
73*	500	410(2.0)	35	>1 x 10^5
76	500	370(2.2)	40	-

* Polycrystalline
** InSb contaminated - 0.3 atom % In
                         0.8 atom % Sb

stoichiometric to within the accuracy of the technique. The importance of these measurements is that high concentrations of structural defects do exist in the sputtered GaAs films, and their density is sensitive to process parameters. It is most probable that structural defects below the detection limits do exist even in the higher temperature sample; these defects could be responsible for the low Hall mobility. Clearly then, this technique, although useful for demonstrating nonstoichiometry is not practical for optimizing the deposition process parameters as one approaches stoichiometry. From Table 6-II it can also be seen that the Ga deficiency is equal to the As excess for sample Ga-27. This would imply that Ga-vacancy-As-interstitial pairs are present.

6.7.2 Deposition Conditions and Electrical Data on Sputtered GaAs

Since the number of process parameter combinations is so large, it was necessary to limit the investigation to extreme and mean values. Tables 6-III and 6-IV are a compilation of the deposition parameters and electrical results on GaAs films. RED measurements indicate that all but one of the films deposited on GaAs substrates were single crystal; the polycrystallinity observed in Ga-23 is probably due to the high deposition rate. The films grown on sapphire, however, were polycrystalline. A good RED pattern of a GaAs film grown on GaAs was shown in Fig. 6-10. Films produced have predominantly high resistivities and low Hall mobilities, and the obtaining of accurate electrical data was a problem for films grown on GaAs. To ascertain a more accurate Hall mobility for GaAs, films were grown on sapphire. Even though these latter films are polycrystalline, their measured mobilities are too low ($\mu < 1$ cm^2 V^{-1} sec^{-1}) to be accounted for on the basis of grain boundary scattering and are, therefore, typical of the sputtered films. In the cases where the Hall voltage was definitely measured, a net n-type conductivity was indicated. The interesting effect of the substrate on obtaining accurate Hall data is exemplified by comparing films obtained from growth run 27. Although both films had almost identical resistivities, their calculated carrier mobilities differ by almost two orders of magnitude or more. The other values of mobility recorded in the table for the epitaxial films are therefore also too high. Depending on thickness and resistivity, accurate resistivity values greater than 2×10^4 to 1×10^6 ohm-cm were not obtained due to shunting of current into the substrate. Using the electrical data for Ga-21 and Ga-27, a minimum carrier density can be associated with the measured resistivity and maximum possible Hall mobility. For the more insulating film, the number of carriers has to be greater than 4×10^{14} cm^{-3}. In the case of Ga-27, the carrier density is greater than 8×10^{17} cm^{-3}. Since the electron microprobe results on Ga-27 (Table 6-II) show a large deviation from stoichiometry, the increased carriers are probably generated from the lattice defects present. Assuming one conduction electron for each Ga-As defect, then 6×10^{20} electrons/cc are possible. Films grown at high temperatures have low carrier concentrations as evidenced by Schottky barrier measurements on Ga-66 and Ga-69. Both of these layers were depleted through the entire film thickness, 10.0 μm and

12.7 μm, respectively. This indicates maximum free-carrier densities of 10^{13} cm^{-3} for the high-temperature samples. In order to ascertain the effect of annealing on the electrical properties of the sputtered films, Ga-60 was divided into two samples, one destined for electrical measurements directly and the other annealed at 700°C for 35 minutes and then measured. The result was that the same lower limit in resistivity could be assigned to both samples.

Limitations on the accuracy of the above electrical data mask most trends with variation in the process parameters. Unless a fortuitous choice in the process parameters is made, optimization of these parameters for GaAs is impossible using electrical characterization techniques. Analyses for nonstoichiometry in two of these films indicate that a film grown at a high substrate temperature is closer to stoichiometry than one grown at low temperature. This is also the direction towards higher resistivity where the electrical measurements become meaningless. In Section 6.8 growth results on a III-V semiconductor (InSb) with the same lattice structure as GaAs are presented. InSb is known to evaporate to give high carrier mobility and low resistivity films (Ref. 6-9). It was hoped that by varying the process parameters for growth of InSb, information would be gained from electrical data which could be extrapolated to the GaAs system.

Some trends in the data of Tables 6-III and 6-IV are discernable.

(1) Higher substrate temperatures yield higher resistivities and higher growth rates for the same incident flux.

(2) Bias sputtering using 22V to 79V did not lower the resistivity compared to one (Ga 22) grown without bias.

(3) Changing the Ga/As ratio by a factor of 50 at temperatures near 560°C did not yield measurable changes in the resistivity.

(4) Using argon as the sputtering gas decreases the sputtering rate (as expected).

(5) Variations in the specific sputtering rate (Å/min-w) also indicate that a chemical reaction occurs on the substrate. The increased reaction rate more than compensates for any decrease in the sticking coefficient of As.

From the above results, including the microprobe analysis for stoichiometry, it appears that growths at higher temperatures are preferred. It was felt that experience with InSb system would suggest the direction towards optimization of the GaAs system.

6.8 Sputtered Indium Antimonide Films

Thin films of InSb with high carrier mobility were first produced by Günther (Ref. 6-10) by evaporating In and Sb by the method of three temperatures. Since this material can readily be deposited in thin film form having near bulk-like electrical properties and having the highest reported Hall mobility of all the III-V compounds, the effect of changes in sputtering parameters on the electrical properties can readily be measured. The crystal structures of GaAs and InSb are the same, and therefore, they should have many of the same structural problems on being sputtered. Any trends in the measured electrical data observed in the sputtering of InSb can then be extrapolated to GaAs. Obviously, this approach is valid only if defects exist in sufficient quantity to affect the electrical properties in InSb, and their formation is similar to that in GaAs.

An InSb target was fabricated by melting a boule of InSb in a carbon mold. The carbon mold was inductively heated in vacuum. The InSb target was attached to the electrode in the sputtering chamber. An excess of antimony was obtained in two ways: (1) by heating Sb in a crucible as was the case with As, and (2) by placing Sb directly onto the InSb target. Since the sticking coefficient of the sublimed Sb on the chamber walls is high, the vapor does not go through the elbow and reach the ionization gauge. As a result of this, measurement and control of the antimony vapor pressure with an ion gauge (as is possible for arsenic) is not possible. Argon was, therefore, chosen as the sputtering gas for InSb.

Single crystal films of InSb were deposited on both InSb and GaAs substrates. This was verified by RED as shown in Figs. 6-14, 6-15, 6-16, and 6-17. Polycrystalline films of InSb were also grown on AlN, sapphire and spinel. Deposition conditions for these films are given in Table 6-V. All the deposited InSb films exhibit low resistivity and high mobility compared to the GaAs films, and their electrical properties are easily measured when grown on semi-insulating GaAs substrates. The electrical properties of the InSb films are shown in Table 6-VI. All films exhibit n-type condictivity at room and liquid nitrogen temperatures, and most show a slight decrease in carrier concentration at low temperature. The observed carrier concentrations are much too low to limit the mobilities via impurity scattering to the measured values. If impurity scattering were dominant, $\sim 2 \times 10^{19}$ cm^{-3} would be required to give these values. Compensation by impurities to levels of $\sim 10^{17}$ cm^{-3}, although possible, is highly unlikely to occur in such a reproducible fashion in all the InSb samples. Therefore, the combination of the low mobility and low carrier concentration leads to the conclusion that some type of systematic structural defect exists in sputtered InSb at the 10^{19} cm^{-3} levels.

Substrate temperature, the method of providing excess Sb, and to a lesser extent, deposition rate, were the growth parameters initially varied. Argon pressure was maintained essentially constant during these runs. The method of introducing

FIG. 6—14

RED OF (111) InSb—BEAM ALONG [$\bar{2}$11]

InSb SUBSTRATE PRIOR TO GROWTH

SPUTTERED InSb FILM ON InSb

FIG. 6-15
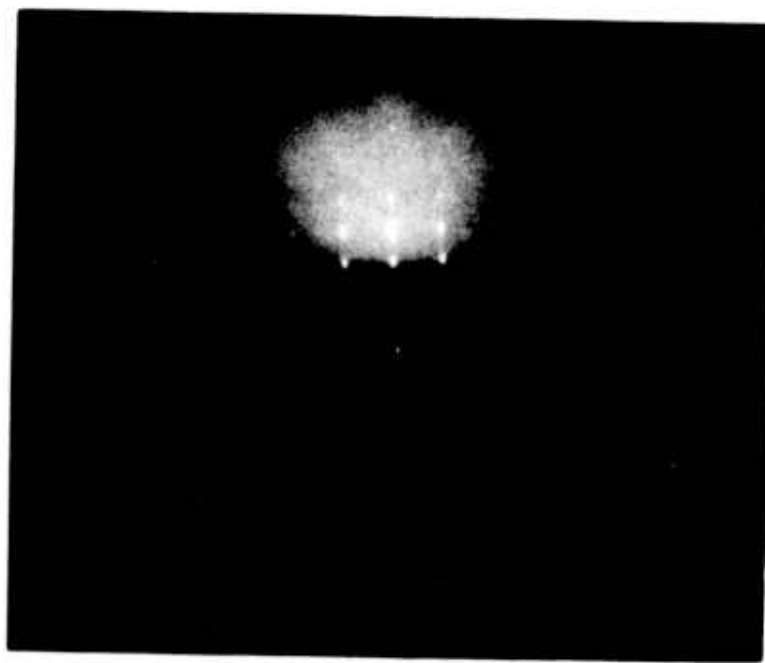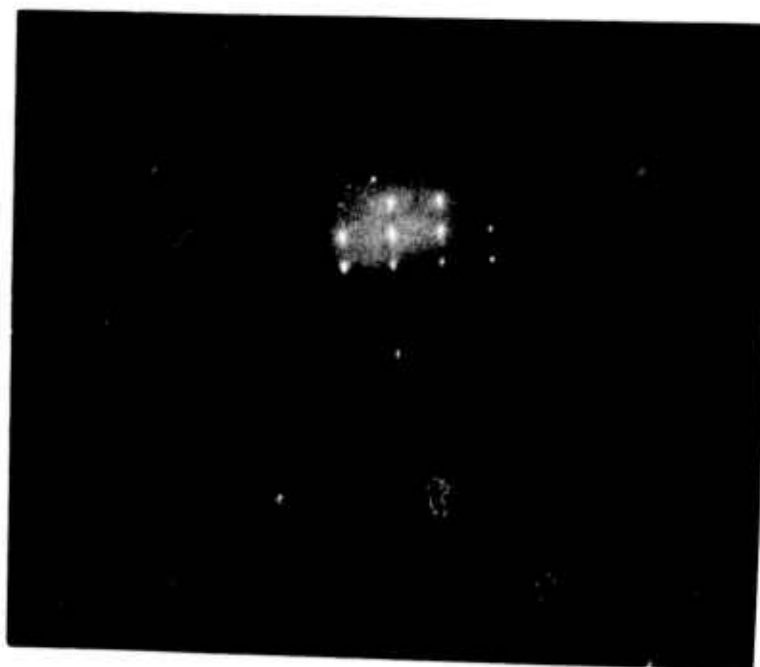
RED OF (111) InSb—BEAM ALONG [1$\bar{1}$0]
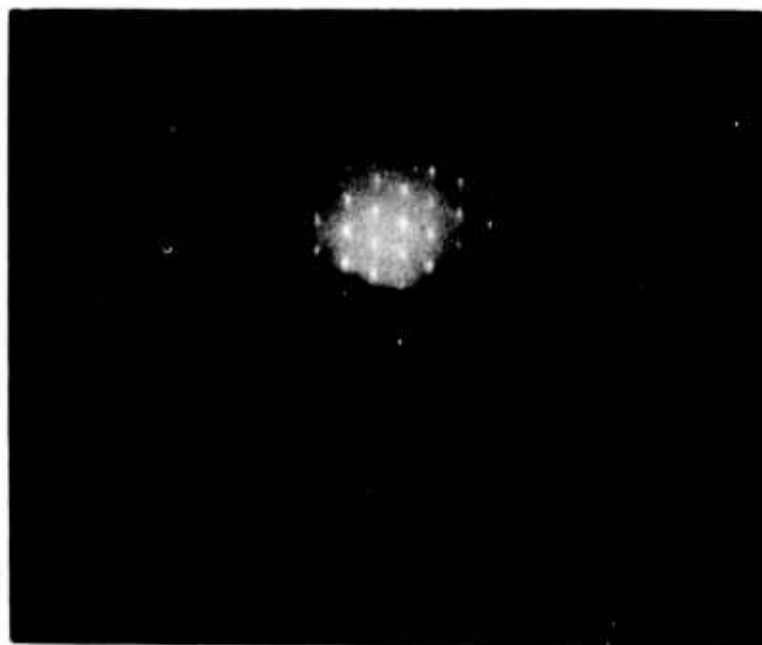
InSb SUBSTRATE PRIOR TO GROWTH

SPUTTERED InSb FILM ON InSb

FIG. 6—16

RED OF InSb ON (100) GaAs—BEAM ALONG [100]
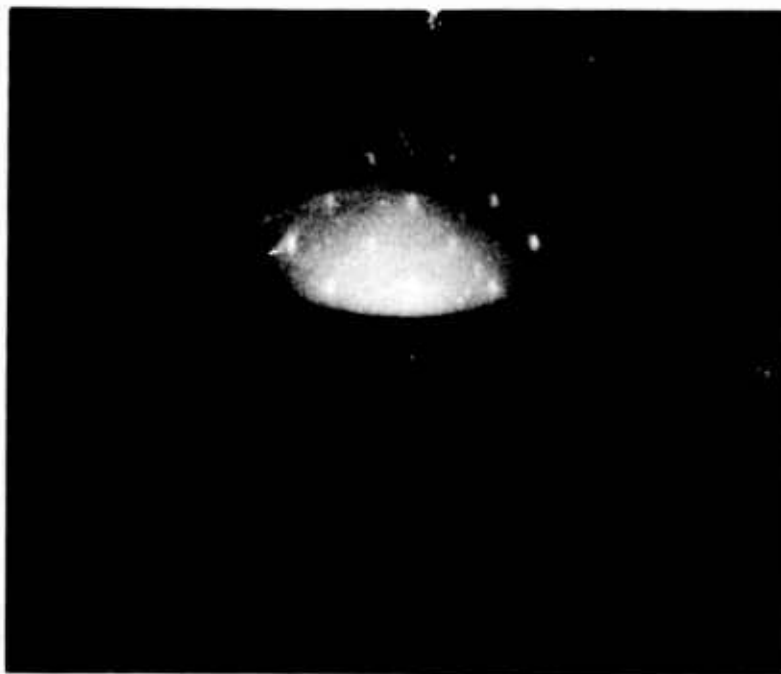
GaAs SUBSTRATE PRIOR TO GROWTH

SPUTTERED InSb FILM ON GaAs

FIG. 6-17
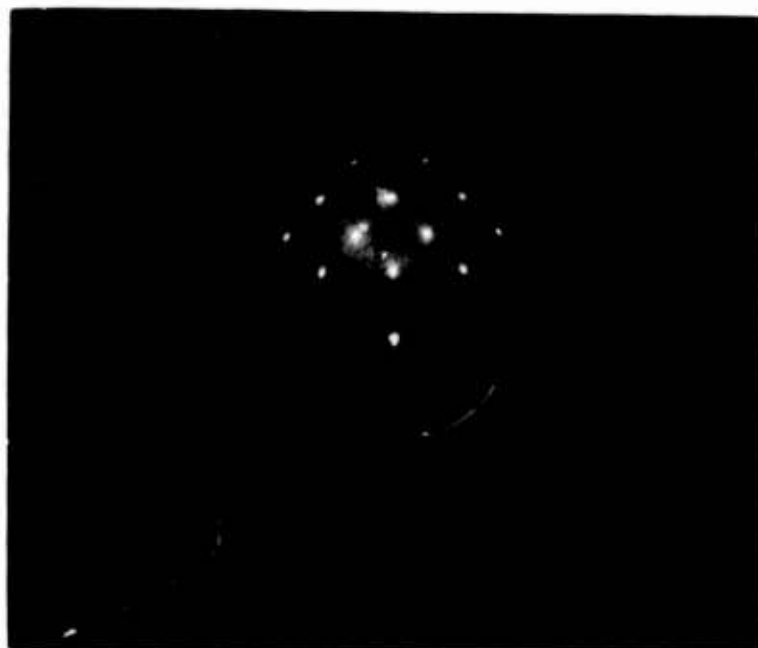
RED OF InSb ON (100) GaAs—BEAM ALONG [110]
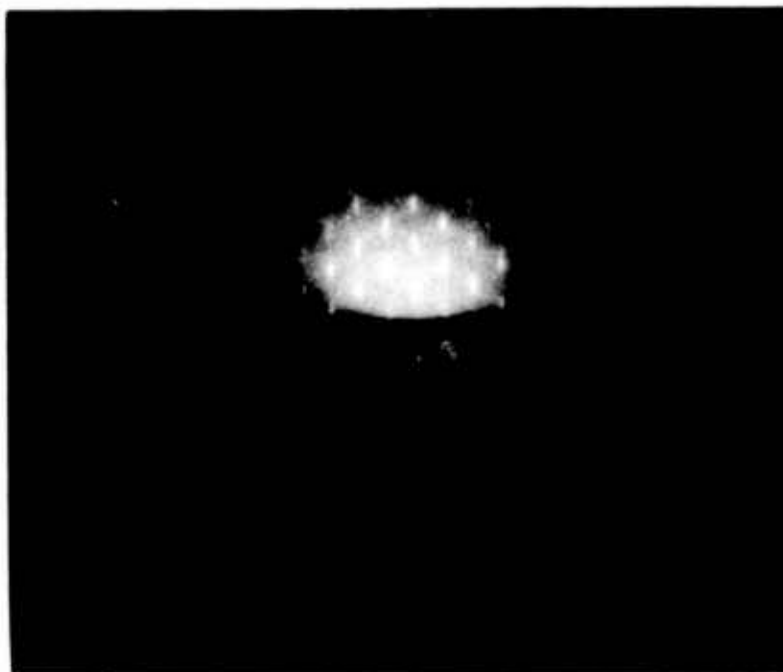
GaAs SUBSTRATE PRIOR TO GROWTH
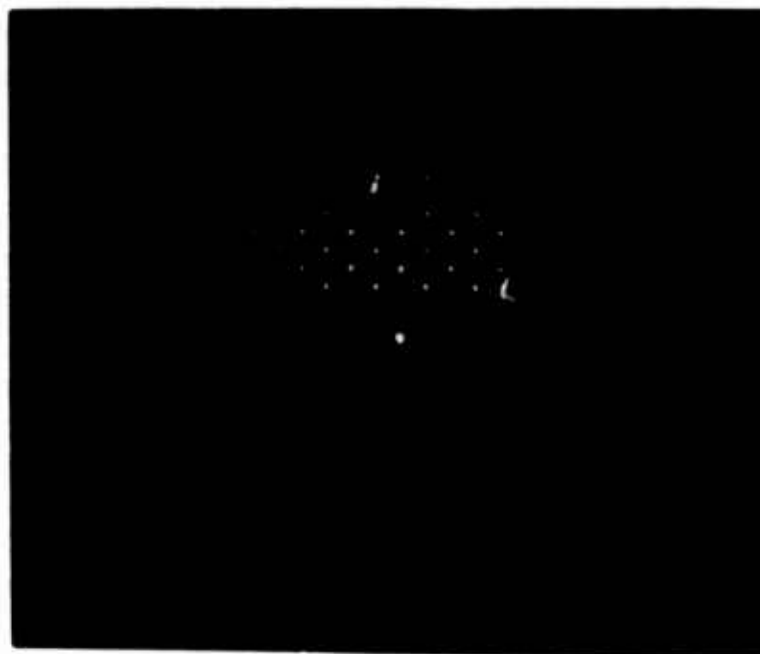
SPUTTERED InSb FILM ON GaAs

Table 6-V

Deposition Parameters for InSb Films

Run #	Substrate Temp. (°C)	Deposition Rate Å/min (Å/min-w)	Sputtering Pressure (µm of Ar)
1-C-(111) Spinel *	415	621 (4.2)	14
1-C-(1Ī02) Sapphire *	415	590 (4.0)	14
2-C	375	435 (5.0)	30
4-C	435	55 (2.5)	23
5-C-AlN *	465	220 (4.5)	16
6-C	375	320 (3.7)	28
7-0	375	450 (5.4)	25
8-S	375	340 (3.9)	23
9-S	375	320(3.7)	29
11-S	375	2120 (5.4)	32
12-S-*	375	2750 (3.4)	27
13-S-*	375	-	28
14-S-*	375	-	33
15-C	375	1293 (3.2)	42
16-C	375	2730 (4.6)	33
21-C-*	375	442 (4.9)	32
22-C-*	375	1700 (4.3)	30

C - Sb supplied by heated crucible, sputter InSb
0 - No extra Sb source, sputter InSb
S - Sb pieces placed on InSb target to provide excess Sb
* - Polycrystalline

Table 6-VI

Electrical Properties of InSb Films

Run #	Room Temperature Electrical Properties			77°K Electrical Properties		
	ρ(ohm-cm)	n(e$^-$/cc x 10^{17})	μ(cm^2 V^{-1} sec^{-1})	ρ	n	μ
1-C-Al$_2$O$_3$*	6.8 x 10^{-3}	2.1	4340	1.2 x 10^{-2}	----	----
2-C	2.4 x 10^{-3}	4.2	6340	3.0 x 10^{-3}	3.4	6130
4-C	6.5 x 10^{-3}	2.8	3980	8.5 x 10^{-3}	2.4	3120
5-C-AlN*	1.9 x 10^{-2}	0.40	8240	3.7 x 10^{-1}	0.32	530
6-C	7.1 x 10^{-3}	1.7	5200	1.6 x 10^{-2}	0.79	4910
7-O	1.8 x 10^{-2}	1.6	2175	2.8 x 10^{-2}	0.34	6440
8-S	3.1 x 10^{-3}	4.5	4420	3.5 x 10^{-3}	3.9	4580
9-S	5.3 x 10^{-3}	4.1	2875	6.9 x 10^{-3}	3.0	2960
11-S	3.5 x 10^{-2}	0.21	8420	4.1	~.05	~300
12-S-*	4.1 x 10^{-2}	~0.5	~3200	2.8 x 10^{-1}	~0.2	~1300
15-C	1.2 x 10^{-2}	1.7	3150	4.7 x 10^{-2}	0.57	2330
16-C	1.3 x 10^{-2}	1.4	3450	5.4 x 10^{-2}	0.51	2290

* Polycrystalline

antimony is an important parameter since the sputtering chamber cannot be heated high enough to permit Sb to reach the shielded ionization gauge, and therefore, the partial pressure of Sb at the substrate is unknown. Judging from deposition of Sb on the chamber surfaces and the loss of Sb from the crucible, a finite excess of Sb must have existed for runs 1 through 6 and 15 through 22. This must also have been the case for runs 8 to 14 in which the excess Sb was sputtered from the target. Comparing the rest of the electrical results to run 7, in which no excess Sb was present, it is clear from the low room temperature Hall mobility of this sample that an excess of Sb is an important requirement. Except for this, there does not seem to be any systematic correlation of resistivity and Hall data with either the method of introducing excess Sb or the deposition parameters of Table 6-V. Together with the poor room-temperature electrical results of sample 7, these inconsistencies must have been due to our inability to control the Sb vapor pressure in the chamber and the subsequent variations in Sb vapor pressure that result. The observed specific sputtering rates at a growth temperature of 375°C as seen in Table 6-V are not very different than those observed at higher temperatures; therefore, any increase in specific deposition rate with temperature (as was the case for GaAs growth) cannot be concluded from this data.

To summarize, the electrical results on epitaxially sputtered InSb lead to the conclusion that defects are limiting the carrier Hall mobility as in sputtered GaAs. The majority carrier at room and liquid nitrogen temperatures is the electron. Due to the inability to control the Sb vapor pressure in the chamber and the fact that lack of excess Sb during sputtering yielded a film with poor electrical characteristics, correlation of InSb electrical data with growth conditions and subsequent application to the growth of GaAs were not possible. Rather than proceeding into a study of rf sputtering of indium arsenide (this can be evaporated in thin film form and have reasonably high carrier mobility) and applying these results to GaAs, work again commenced on growing GaAs and eventually $Ga_{1-x}Al_xAs$ in order to produce layers suitable for waveguide evaluation. In order to place the InSb work into a chronological framework, the InSb sputtering runs were done between GaAs runs 46 and 47. The GaAs runs listed in Table 6-IV were done after the InSb work.

6.9 Sputtered $Ga_{1-x}Al_xAs$ Films

The incorporation of aluminum as a substitute for gallium in GaAs brings about two important changes in the optical properties of the host GaAs lattice which are relevant to integrated optics applications. As the atomic fraction of Al(x) increases, the index of refraction decreases and the forbidden energy gap increases. Since (1) AlAs is completely miscible with GaAs in the solid state and (2) the crystal structures and cell constants are essentially identical (a_o(GaAs) = 5.6535 Å and a_o(AlAs) = 5.661 Å, Ref. 6-11), sequential single-crystal heteroepitaxial growth

of layers with varying x is possible without large interfacial problems (e.g., strain and dislocations). With proper sequencing of the $Ga_{1-x}Al_xAs$ layers, confinement of a near-infrared beam, whether generated internally (laser or light emitting diode) or externally (waveguide application), in one of the layers is possible due to the dependence of the index of refraction on x. In addition, increasing the energy gap with Al introduction extends the useful range of application of this system closer to the visible region of the spectrum.

Since sputtered $Ga_{1-x}Al_xAs$ must be shown to operate as a waveguide before it can ever be considered for active applications, growth of aluminum containing GaAs layers was attempted. The only practical way of introducing aluminum into the GaAs sputtering system is to add aluminum to the target. The solubility limit of aluminum in gallium at the target temperature ($\sim 275°C$) is approximately 25 atomic percent (Ref. 6-12). If one assumes equal incorporation of both of these elements into the film during sputtering, then x = 0.25 would be the highest obtainable value. Due to this lack in flexibility in not being able to obtain higher aluminum concentrations, e.g., $x\sim0.4$, using a uniform target and rather than redesigning the sputtering system to encorporate a target heater, a second method was chosen. Since a GaAs crust forms on the gallium during sputtering in the arsenic atmosphere, separation of Al from the Ga melt is possible. By placing small pieces of 1/16 inch diameter aluminum wire (which would form an AlAs skin in the As atmosphere) on the GaAs skin and distributing these at random, a greater degree of flexibility would be gained in introducing aluminum into the GaAs films. This method, however, does have one disadvantage in that the target is not uniform; however, being able to change the percentage of aluminum exposed to the plasma at will is a definite advantage, particularly since the sticking coefficient of gallium versus aluminum was not known.

The deposition conditions used in the sputtering of the mixed GaAs-AlAs target are shown in Table 6-IV. High growth temperatures were chosen to avoid the possibility of excess arsenic encorporation into the films as had been the case for Ga-27. For runs Ga-72 and Ga-73, about one half of the exposed area of the target was initially covered with aluminum and about 1/3 was covered for Ga-76. The sputtered layers grown in runs Ga-72 and Ga-76 were single crystal; an RED of the Ga-76 layer (which had been grown on a sputtered film from Ga-72) is shown in Fig. 6-18. The films from Ga-73, however, were polycrystalline. Since the same target was used for Ga-72 and Ga-73, this result probably arose from inadequate sputter cleaning of the AlAs, which had been exposed to the atmosphere between these runs. The affinity of AlAs for water is well known. For purposes of growing a single crystal film of different composition, a new target was created by first growing GaAs (Ga-75) to form the GaAs skin on the gallium and then adding aluminum to the target prior to growth run, Ga-76. Optical microscopic cross sections of the layers from runs Ga-76 and Ga-73 are shown in Fig. 6-19. The top photograph shows two layers, one from Ga-72 (t = 5.5 μm) and one from Ga-76 (t = 4.4 μm), after cleavage. The fact that layers here can be differentiated without enhancement through selective etching

RED OF EPITAXIAL $Ga_{0.60}Al_{0.40}As$ GROWN ON EPITAXIAL $Ga_{0.39}Al_{0.61}As$
ON A (100) GaAs SUBSTRATE

ELECTRON BEAM ALONG (110)

FIG. 6-19

CROSS SECTIONS OF SPUTTERED Ga$_{1-x}$Al$_x$ AS FILMS
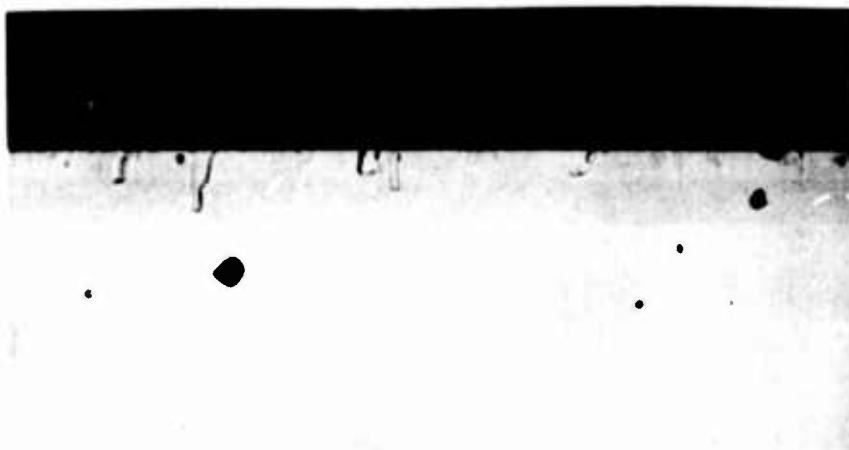
(a) SINGLE CRYSTAL FILMS OF Ga$_{0.60}$Al$_{0.40}$As AND Ga$_{0.39}$Al$_{0.61}$As ON
n$^+$- GaAs SUBSTRATE (Ga76 ON Ga72)

(b) POLYCRYSTALLINE Ga$_{0.39}$Al$_{0.61}$As ON Cr-DOPED GaAs SUBSTRATE
(Ga73)

N12-76-2

is due to the higher aluminum content of the Ga-72 layer (e.g., change in reflectivity). As a comparison to the single crystal films, the 6.0-μm thick polycrystalline layer from Ga-73 is also shown in Fig. 6-19.

The aluminum content of these layers can be obtained directly through electron microprobing or through inference from the position of the infrared reststrahlen bands from the room temperature reflectivity curves. As the aluminum concentration increases in $Ga_{1-x}Al_xAs$, a new reststrahlen band appears and is shifted to shorter wavelength in a gradual fashion (Ref. 6-13). By recording the wavelength of the short-wavelength reflectivity minimum, the alloy composition can be determined. Results from such plots together with electron microprobe results give x = 0.61 for Ga-72 and Ga-73 and x = 0.40 for Ga-76. These aluminum concentrations are close to what was expected on the basis of the percentage of the target area which was occupied by AlAs; therefore, the ratio of the sticking coefficients of Ga and Al is approximately unity.

6.10 Optical Waveguide Considerations and Results

The typical sputtered films used for optical evaluation in this section were all grown under conditions to yield high-resistivity films ($\rho > 10^4 - 10^5$ ohm-cm) of low carrier mobility ($\mu_H < \sim 1 cm^2/V\text{-sec}$). These properties would rule out application of this material for light emitters, but it is possible that a modulator operating at 1.06 μm could be constructed. Prior to modulation, the necessary waveguide properties must be examined.

The types of waveguide structures investigated are shown in Fig. 6-20. In structures 20a and 20b, the GaAs layer should have the highest index and is the waveguiding medium. One side of each of these waveguides is bounded by n^+-GaAs and $Ga_{0.39}Al_{0.61}As$, respectively, while air forms the other boundary in both cases. The $Ga_{0.60}Al_{0.40}As$ film in structure 20c is the waveguiding medium. The indices of each of the layers at 1.059 μm are also shown in Fig. 6-20. The assigned indices for semi-insulating GaAs or $Ga_{1-x}Al_xAs$ were calculated using the relation

$$n = \left(A + \frac{0.97501}{\lambda^2 - C} - D\lambda^2\right)^{1/2} \tag{6-1}$$

where λ = 1.059 μm and parameters A through D are a function of the aluminum concentration (see Ref. 6-14). Using this relation, the index of refraction of insulating GaAs is 3.473 at 1.06 μm. The index of refraction of n^+-GaAs is depressed from this value due to free carrier effects and can be calculated from

FIG. 6– 20

SPUTTERED $Ga_{1-x}Al_x$ AS WAVEGUIDE STRUCTURES

a)

n = 1	AIR
n ~ 3.47¹	GaAs FILM
n = 3.468	GaAs n⁺ – SUBSTRATE (SI DOPED – 2.8x10¹⁸cm⁻³)

b)

5.7 μm   2.3 μm

n ~ 1	AIR
n ~ 3.47	GaAs FILM
n = 3.17	$Ga_{0.39}Al_{0.61}$ As FILM
	GaAs n⁺ – SUBSTRATE

c)

5.5 μm   4.4 μm

	AIR
n = 3.27	$Ga_{0.60}Al_{0.40}$ As FILM
n = 3.17	$Ga_{0.39}Al_{0.61}$ As FILM
	GaAs n⁺ – SUBSTRATE
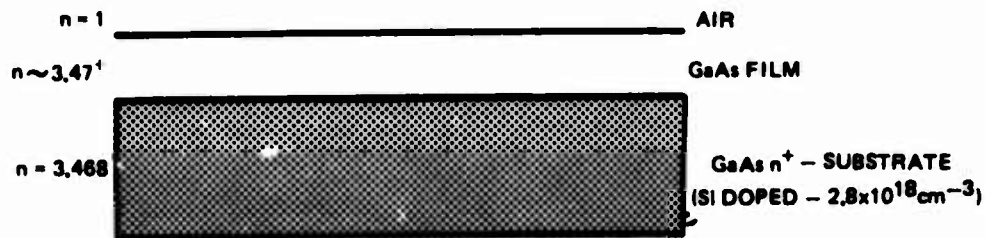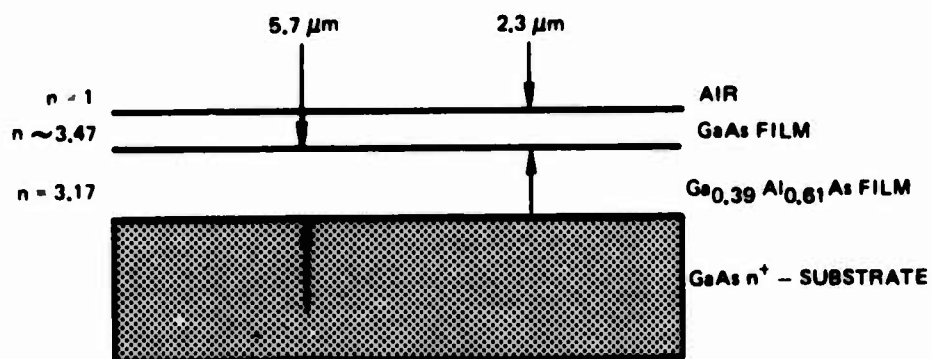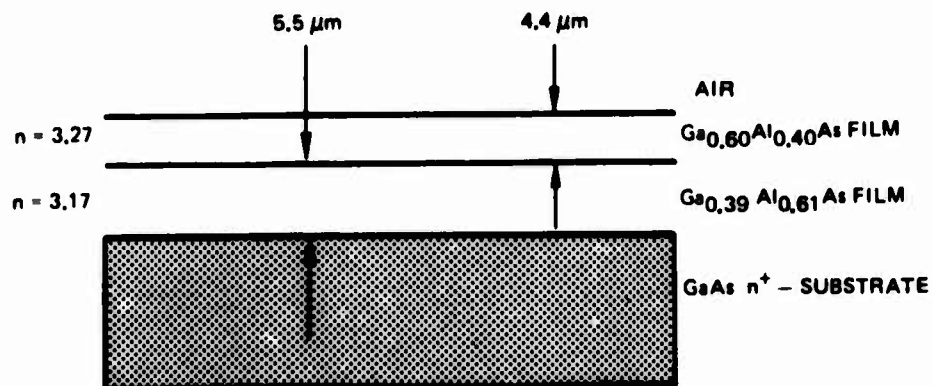
$$\Delta n = - \frac{e^2/2m^* \epsilon_0 \omega^2}{\left(n_1^2 - \frac{N_s e^2}{m^* \epsilon_0 \omega^2} \right)^{1/2}} \quad \Delta N \qquad (6\text{-}2)$$

where n, e, m^*, ω, and N are the index of refraction, electronic charge, effective mass, operating frequency, and electron density, respectively. The calculated difference in index for GaAs at 1.059 μm for an N_s (substrate) of 2.8×10^{18} cm^{-3} is 5.3×10^{-3}. In order to verify that an index difference of this magnitude exists between the sputtered film and a substrate of this carrier density, the interference fringes that exist between 3 and 10 μm wavelengths were recorded. By measuring the change in the reflectivity at the interference extrema and dividing by the value of the mean reflectivity at this wavelength, and extrapolating to 1.06 μm, a value of 3.5×10^{-3} was found for the index difference. This is a direct measure of the index difference and does not require measurement of the absolute value of the indices to four significant places. However, this technique does not reveal the sign of the index difference, so that the film index could be lower than the substrate. In such a case, waveguiding would not occur in the GaAs film shown in Fig. 20a. Assuming the film has the higher index, the lower value of the index difference compared to that calculated from free carrier depression may be due to nonstoichiometry which will result in a decrease in the dipole concentration.

An important design consideration for optical waveguides is the determination of the film thickness that will propagate at least a zero-order mode. This thickness is a function of the difference in the index of refraction between the substrate and the film. Figure 6-21 shows the minimum film thickness required for a zero-order mode between GaAs and an n$^+$-GaAs substrate as a function of the index difference. This curve was calculated for 1.059 μm radiation (Ref. 6-15) since that wavelength is in the range where a GaAs-based integrated optics technology would operate and is convenient for attenuation measurements using a Nd:YAG laser. From this plot it can be seen that a GaAs film at least 2 μm thick is required.

Another important design consideration is attenuation of the guided wave caused by losses due to the n$^+$ substrate. Using the analysis for the loss due to an absorbing reflector (Ref. 6-16), the waveguiding film loss shown in Fig. 6-22 was calculated as a function of the index difference between the n$^+$ substrate and the film at 1.059 μm for several film thicknesses and for two substrate absorption coefficients. The absorption coefficient of GaAs depends on free carrier density and wavelength. Using substrates of known carrier concentration, the bulk absorption coefficient, α_s, was determined to lie between 20 cm^{-1} and 40 cm^{-1} using the optical data in Ref. 6-17 . For substrate absorption losses less than 10 dB/cm,

FIG. 6 – 21

MINIMUM FILM THICKNESS REQUIRED TO SUPPORT m = 0 MODE VS. INDEX DIFFERENCE BETWEEN FILM AND SUBSTRATE
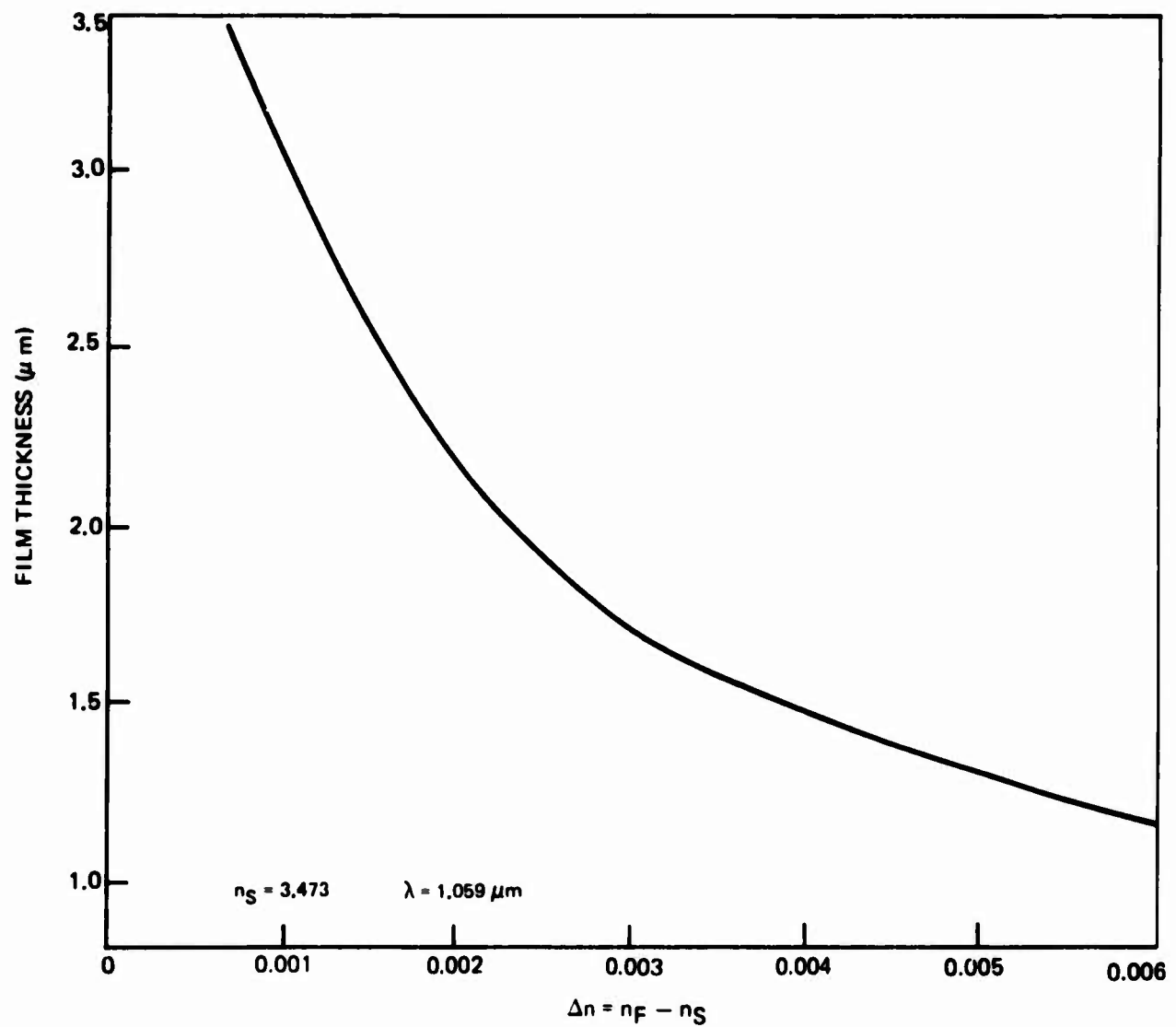
FIG. 6-22

CALCULATED TE$_0$ MODE FILM LOSS AT 1.069 μm DUE TO n$^+$–GaAs SUBSTRATE

N12–76–1

136
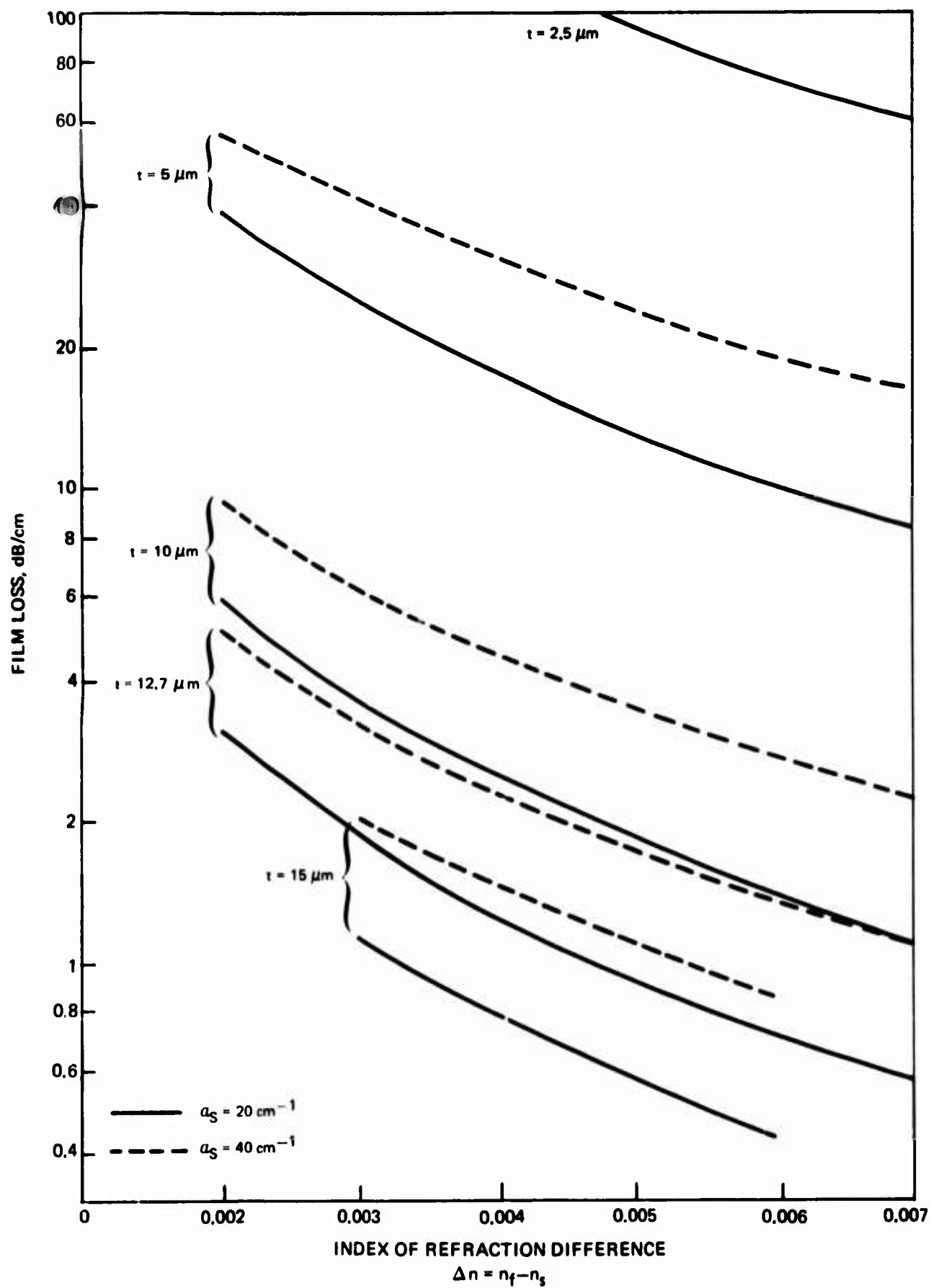
a film thickness greater than 7 μm would be required for an index difference of
0.0053 (see Fig. 6-22).

The common approaches to coupling light into thin film waveguides are via
prisms, gratings and focusing the light onto a cleaved edge of the device (Ref. 6-18).
At 1.06 μm the availability of transparent prism materials with an index greater
than GaAs is very limited. Intrinsic GaAs, however, is a possible candidate.
Boron phosphide does have the required optical properties but is not readily available
as an optical component. In addition, the chances of GaAs cracking under stress
applied through prism coupling is high. Due to these prism problems, the grating
and edge coupling techniques were employed. Coupling via a grating is the most
effective technique for waveguide coupling, but submicron grating spacings are
required at 1.06 μm. Input and output gratings (d ~ 0.7 μm) for coupling the
1.06 μm light were fabricated using the interference of two beams split off from a
one-watt argon-ion laser onto films which had previously been coated with photoresist
(Shipley Type PZ-130). Gratings were also fabricated on amorphous tantalum
pentoxide films on 7059 glass and were demonstrated to couple properly using a
He-Ne laser. Edge coupling using a cleaved surface perpendicular to the (100)
substrate plane was performed by focusing a Nd:YAG laser beam (1.059 μm) onto the
cleaved edge of the film and substrate with a 25 cm focal length lens. Provision
was made for rotating the plane of the film with respect to the beam. A "snooperscope"
was used to observe any 1.059 μm radiation that might be scattered from a guided
mode in the sample. To reduce the incident angular range for substrate mode
propagation, the back side of the substrates was left in a matte condition. In most
cases, this restricted our observation of film modes to orders greater than $m = 0$
since the presence of substrate modes at low angles overwhelms the weaker film mode.
Verification that edge coupling can be obtained was provided by observing waveguiding
in a 10.7 μm thick film that had been deposited through vapor phase epitaxy onto
an n^+-GaAs substrate ($n^+ = 2.7 \times 10^{18}$ cm^{-3}). The optical bench used in this experi-
ment is shown in the appendix.

Initial waveguiding experiments were performed using grating coupling into the
GaAs waveguide structure shown in Fig. 6-20a. Both grating coupling to a 29-μm
and 4-μm thick sputtered film and edge coupling to a 12.7-μm film were attempted.
Substrate modes were easily observed in these experiments. These were characterized
by a broad angle of acceptance at low incident angles. No sharp film modes could be
detected. In general, the lack of waveguiding could be due to high scattering
losses, high absorption losses in the film, or too low an index for the film compared
to the substrate. Since no light was observed to be scattering out of the film near
the edge of the couplers, high scattering losses are ruled out. At this point, it
was impossible to differentiate between the other two loss mechanisms. In order to
resolve this question, a $Ga_{0.39}Al_{0.61}As$ film was interspaced between the GaAs film
and n^+-substrate (Fig. 20b). This arrangement insures that the waveguiding GaAs
layer is surrounded by lower-index material; therefore, the predominant loss
mechanism should be absorption by the film. The allowed modes for this structure are

indicated in the family of curves at the top of Fig. 6-23. The zero-order mode, if present, could not be seen due to substrate mode interference. Modes m = 1 through m = 3 should be visible but were not. Therefore, it must be concluded that absorption is large in the sputtered GaAs film. Modes m = 4 and m = 5 cannot be excited by edge coupling using these guides due to the high index of refraction of GaAs.

Unless band tailing is extremely severe, one would expect a decrease in absorption at 1.059 μm if the band edge is moved away in energy as would be the case when one adds aluminum to GaAs. To investigate this possibility, the structure shown in Fig. 20c was fabricated. The composition of the waveguide film obtained shifts the bandgap from 1.40 ev in GaAs to 1.9 ev (Ref. 6-19) in $Ga_{0.60}Al_{0.40}As$. In order to confine the light within this film, a lower-index film is required between the substrate and waveguide film. This was obtained by first sputtering $Ga_{0.39}Al_{0.61}As$ onto the substrate. If high absorption does not occur in this device, then the modes shown in the bottom family of curves in Fig. 6-23 should be observable. Modes m = 0 to m = 2 could not be seen due to substrate mode propagation and interference. The other modes were not detected. The high absorption in both the GaAs and its aluminum alloy, together with the structural defects indicated from the GaAs electrical results, suggests that severe band tailing exists in the sputtered films.

6.11 Conclusions

Reactive sputtering using sublimed arsenic as the sputtering gas inside a heated vacuum chamber is a safe and practical technique for synthesizing GaAs. The basic process of using a sublimed solid as the reactive sputtering gas can also be extended to the phosphides, antimonides, sulfides, selenides, and tellurides. In the sputtering of GaAs, not only have single crystal and polycrystalline layers been formed, but these have been uniformly deposited at temperatures far lower than is possible using conventional techniques. The controlled growth of single crystal alloys of $Ga_{1-x}Al_xAs$ at low temperatures has also been demonstrated, and there is no reason to believe that other mixed III-V and II-VI compounds could also be formed in this manner. One of the objectives of this program was to determine whether a highly reactive material such as arsenic could be used with conventional vacuum-chamber construction materials at elevated temperatures without severe contamination of the growing films. Mass spectrographic analysis of a GaAs film has shown that the total impurity concentration assignable to the materials of construction is only 7ppm (3×10^{17} cm^{-3}). This is a fortunate result in that it should permit growth of reasonably pure GaAs films.

FILM THICKNESS VERSUS β/K FOR TE MODES IN $Ga_{1-x}Al_xAs$ WAVEGUIDE STRUCTURES AT 1.059 μm
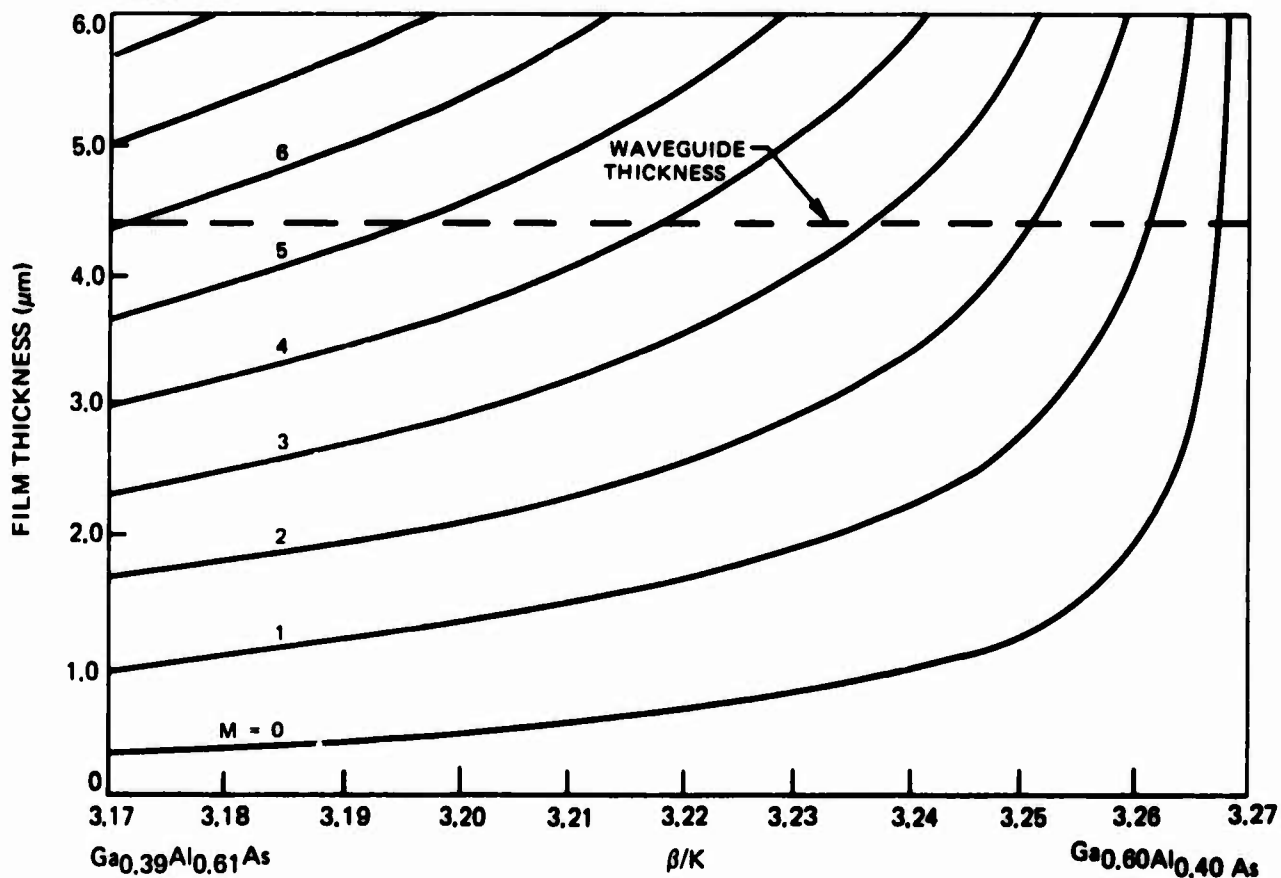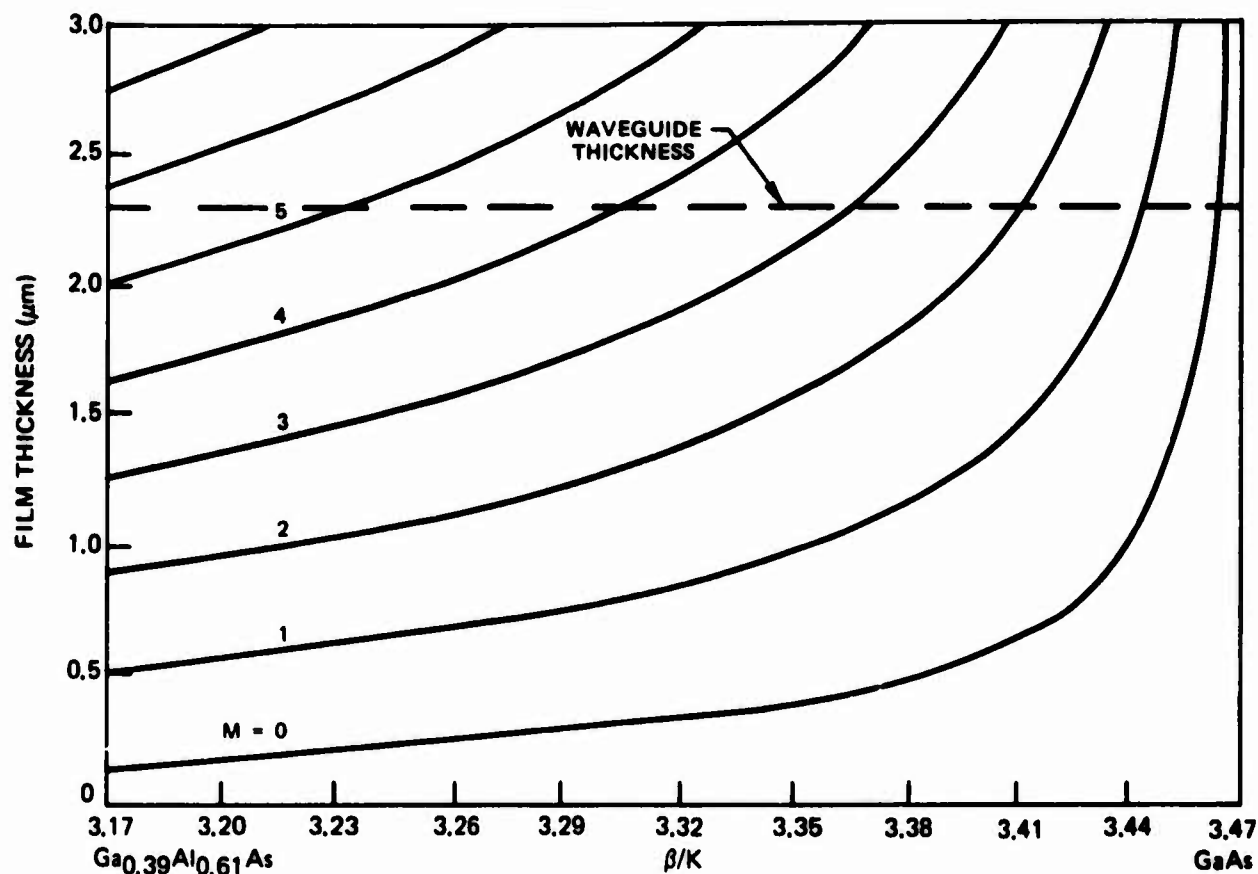
Sputtered GaAs films grown between 330°C and 565°C show inordinately low carrier Hall mobilities due to lattice defects. Independent evidence for this conclusion arises from the measured nonstoichiometry and low impurity concentrations in these films as well as high absorption at 1.059 μm even in $Ga_{1-x}Al_xAs$. When the sputtering parameters for GaAs are correlated with the film characteristics, several trends appear to exist. Substrate temperature affects the film stoichiometry and determines the film growth rate for a given flux of sputtered GaAs. Higher substrate temperatures tend to result in higher growth rates and produce more-stoichiometric and higher resistivity films. It is concluded that elevated temperatures enhance the removal of arsenic from metastable sites or prevent arsenic from occupying these sites. Since the film growth rate is increased at higher substrate temperatures, the reaction rate of the gallium atoms with the growing surface must be enhanced. The observation that the gallium deficiency and arsenic excess are equal for the low temperature runs indicates that the two defects exist as pairs. The pair defect could consist of a gallium vacancy and arsenic interstial. The energetics of the growth process will control which defect is initially formed. This defect would be present in a meta-stable state and be responsible for the formation of the other. The possibility of an arsenic atom occupying a gallium site and so account for the nonstoichiometry is energetically less likely. Although less in concentration, defects like this must exist in the GaAs samples prepared up to the maximum operating temperature of the apparatus. In a similar vane it has been observed here by electron microprobe analysis that argon entrapment in argon-sputtered metal films can occur and can be greatly reduced by increasing the substrate temperature.

Films of GaAs, whether evaporated or sputtered in argon, have electrical characteristics that are probably due to an arsenic deficiency. Films prepared by reactive sputtering in arsenic have the opposite problem in that they contain excess arsenic. Deviations from stoichiometry from an excess to a deficiency of arsenic can therefore result from the choice of the sputtering gas. Since excess arsenic incorporation is reduced at elevated temperatures, a substrate heater could be designed to operate in an arsenic ambient at temperatures higher than what is possible with the present apparatus in order to reduce the excess arsenic in the films to an acceptable level. In order to utilize the advantages of sputtering, such a course of action should be pursued.

6.12 References

6-1 M. R. Farukhi and E. J. Charlson, Journal of Applied Physics 40, 5361 (1969).

6-2 K. Takahashi, Journal of Vacuum Science and Technology 9, 502 (1972).

6-3 D. Hua Hu and E. J. Charlson, Journal of Vacuum Science and Technology 9, 1443 (1972).

6-4 J. L. Kenty, Journal of Electronic Materials 2, 239 (1973).

6-5 G. V. Bunton and M. Day, Thin Solid Films 10, 11 (1972).

6-6 T. Inoue and M. Ohyama, Solid State Communications 8, 1309 (1970).

6-7 C. S. Fuller, K. B. Wolfstirn, and H. W. Allison, Applied Physics Letters 4, 48 (1964).

6-8 C. S Fuller and J. M. Whelan, Journal of Physics and Chemistry of Solids 6, 173 (1958).

6-9 L. J. Vieland, Journal of Applied Physics 33, 2007 (1962).

6-10 K. G. Günther, Zeit. Naturforschung 13a, 1081 (1958); K. G. Günther and H. Fuller, Zeit. Naturforschung 16a, 279 (1961).

6-11 H. H. Wieder, Journal of Vacuum Science and Technology 8, 210 (1971).

6-12 M. Hansen, Constitution of Binary Alloys (McGraw Hill, New York, 1958) p. 96.

6-13 M. Ilegems and G. L. Pearson, Physical Review 1B, 1576 (1970).

6-14 J. T. Boyd, IEEE Journal of Quantum Electronics QE-8, 788 (1972).

6-15 P. K. Tien, Applied Optics 10, 2395 (1971).

6-16 M. Born and E. Wolf, Principles of Optics (Pergamon, Oxford, 1965) p. 627.

6-17 M. G. Mil'vidskii, V. B. Osvenskii, E. P. Rashevskaya, and T. G. Yugova, Soviet Physics (Solid State) 7, 2784 (1966).

6-18 J. C. Tracy, W. Wiegman, R. A. Logan, and F. K. Reinhart, Applied Physics Letters 22, 511 (1973).

6-19 C. A. Mead and W. G. Spitzer, Physical Review Letters 11, 358 (1963).

6.12 References

6-1 M. R. Farukhi and E. J. Charlson, Journal of Applied Physics 40, 5361 (1969).

6-2 K. Takahashi, Journal of Vacuum Science and Technology 9, 502 (1972).

6-3 D. Hua Hu and E. J. Charlson, Journal of Vacuum Science and Technology 9, 1443 (1972).

6-4 J. L. Kenty, Journal of Electronic Materials 2, 239 (1973).

6-5 G. V. Bunton and M. Day, Thin Solid Films 10, 11 (1972).

6-6 T. Inoue and M. Ohyama, Solid State Communications 8, 1309 (1970).

6-7 C. S. Fuller, K. B. Wolfstirn, and H. W. Allison, Applied Physics Letters 4, 48 (1964).

6-8 C. S Fuller and J. M. Whelan, Journal of Physics and Chemistry of Solids 6, 173 (1958).

6-9 L. J. Vieland, Journal of Applied Physics 33, 2007 (1962).

6-10 K. G. Günther, Zeit. Naturforschung 13a, 1081 (1958); K. G. Günther and H. Fuller, Zeit. Naturforschung 16a, 279 (1961).

6-11 H. H. Wieder, Journal of Vacuum Science and Technology 8, 210 (1971).

6-12 M. Hansen, Constitution of Binary Alloys (McGraw Hill, New York, 1958) p. 96.

6-13 M. Ilegems and G. L. Pearson, Physical Review 1B, 1576 (1970).

6-14 J. T. Boyd, IEEE Journal of Quantum Electronics QE-8, 788 (1972).

6-15 P. K. Tien, Applied Optics 10, 2395 (1971).

6-16 M. Born and E. Wolf, Principles of Optics (Pergamon, Oxford, 1965) p. 627.

6-17 M. G. Mil'vidskii, V. B. Osvenskii, E. P. Rashevskaya, and T. G. Yugova, Soviet Physics (Solid State) 7, 2784 (1966).

6-18 J. C. Tracy, W. Wiegman, R. A. Logan, and F. K. Reinhart, Applied Physics Letters 22, 511 (1973).

6-19 C. A. Mead and W. G. Spitzer, Physical Review Letters 11, 358 (1963).

6.12 References

6-1 M. R. Farukhi and E. J. Charlson, Journal of Applied Physics 40, 5361 (1969).

6-2 K. Takahashi, Journal of Vacuum Science and Technology 9, 502 (1972).

6-3 D. Hua Hu and E. J. Charlson, Journal of Vacuum Science and Technology 9, 1443 (1972).

6-4 J. L. Kenty, Journal of Electronic Materials 2, 239 (1973).

6-5 G. V. Bunton and M. Day, Thin Solid Films 10, 11 (1972).

6-6 T. Inoue and M. Ohyama, Solid State Communications 8, 1309 (1970).

6-7 C. S. Fuller, K. B. Wolfstirn, and H. W. Allison, Applied Physics Letters 4, 48 (1964).

6-8 C. S Fuller and J. M. Whelan, Journal of Physics and Chemistry of Solids 6, 173 (1958).

6-9 L. J. Vieland, Journal of Applied Physics 33, 2007 (1962).

6-10 K. G. Günther, Zeit. Naturforschung 13a, 1081 (1958); K. G. Günther and H. Fuller, Zeit. Naturforschung 16a, 279 (1961).

6-11 H. H. Wieder, Journal of Vacuum Science and Technology 8, 210 (1971).

6-12 M. Hansen, Constitution of Binary Alloys (McGraw Hill, New York, 1958) p. 96.

6-13 M. Ilegems and G. L. Pearson, Physical Review 1B, 1576 (1970).

6-14 J. T. Boyd, IEEE Journal of Quantum Electronics QE-8, 788 (1972).

6-15 P. K. Tien, Applied Optics 10, 2395 (1971).

6-16 M. Born and E. Wolf, Principles of Optics (Pergamon, Oxford, 1965) p. 627.

6-17 M. G. Mil'vidskii, V. B. Osvenskii, E. P. Rashevskaya, and T. G. Yugova, Soviet Physics (Solid State) 7, 2784 (1966).

6-18 J. C. Tracy, W. Wiegman, R. A. Logan, and F. K. Reinhart, Applied Physics Letters 22, 511 (1973).

6-19 C. A. Mead and W. G. Spitzer, Physical Review Letters 11, 358 (1963).

7.0 GROWTH OF (ULTRAPHOSPHATE) LASER MATERIALS

7.1 Introduction

A totally integrated optical technology must include elements that produce gain. Lasers meet these requirements, and for this application should be fabricated in thin-film form. One technique for achieving this goal is to optically pump a thin-film laser material with a light emitting diode (LED) such as GaAs or its mixed alloys. In particular, GaAs-type LEDs can be used to pump the 8000 Å to 9000 Å absorption bands of the neodymium ion, which is properly spaced in a host lattice like yttrium aluminum garnet (YAG). The solubility of neodymium in the garnet lattice is one-to-two percent. This limits the gain per unit length of the laser and requires large geometries. To be compatible with integrated optics, materials exhibiting much higher gain are required. Laser action has recently been demonstrated in 35-micron-long platelets of neodymium ultraphosphate (NdP_5O_{14}) (Ref. 7-1). Dimensions of this magnitude are ideally suited for integrated optics applications. This material has also lased, but with increased threshold, in the amorphous state. This is an important fact since the heteroepitaxy of single crystal NdP_5O_{14} via sputtering would probably require temperatures above $800^\circ C$. These high temperatures would not be compatible with a GaAs-based technology. Furthermore, due to the orthorhombic crystal structure of NdP_5O_{14}, epitaxial growth on the zinc-blend GaAs structure is unlikely. At elevated temperatures the sticking coefficient of Nd, P, and O will vary and give rise to stoichiometry problems. In light of the above, a low temperature deposition of an amorphous film of NdP_5O_{14} would more likely yield a thin film laser.

7.2 Growth of Ultraphosphate Bulk Crystals

Bulk crystals are required in order to (1) provide target material and (2) establish a reference value of the fluorescence lifetime to which measured values of the film can be compared. In addition to neodymium ultraphosphate, compositions of the form, $Nd_{1-x}M_xP_5O_{14}$, where M = La, Dy, and Y were also grown. The substitution of these elements for Nd is known to affect the fluorescence lifetime of the crystal (Ref. 7-2).

The rare-earth 4f ultraphosphates were prepared by heating the transition metal oxide (99.9% to 99.99% pure) with phosphoric acid (electronic grade) to about $500^\circ C$ to $700^\circ C$ in an Au or PdAu crucible under a dry oxygen flow. In the process, water is preferentially lost to form higher phosphoric acids, and a transition metal ultraphosphate, MP_5O_{14}, is eventually crystallized out of solution. As a part of the heating schedule (before raising the crucible to high temperatures) the reactants are held at $\sim 250^\circ C$ to $300^\circ C$ to ensure dissolution of the oxide. Table 7-I summarizes the growth conditions for the MP_5O_{14} runs. In all cases the amount of phosphoric

TABLE 7-I

Summary of Growth Conditions for Bulk MP_5O_{14}

Run No. *	Reagents **	$\dfrac{\text{Moles } H_3PO_4}{\text{Moles } M_2O_3}$	Composition	Temp (°C)	Time (hrs)	Lifetime τ (µsec)
2M	Nd_2O_3-MC	11.8	NdP_5O_{14}	500	20	
3M	Nd_2O_3-MC	10.9	NdP_5O_{14}	500	20	
4M	Nd_2O_3-MC	10.9	NdP_5O_{14}	500	20	80-100
5M	Nd_2O_3-MC	11.0	NdP_5O_{14}	475	20	
6M	Nd_2O_3-MC	130	NdP_5O_{14}	550	140	55-120
7M	Nd_2O_3-MC La_2O_3-BR	127	$Nd_{0.50}La_{0.50}P_5O_{14}$	550	140	160
8M	Nd_2O_3-MC Dy_2O_3-BR	135	$Nd_{0.99}Dy_{0.01}P_5O_{14}$	600 +(725)	70 +($\sim$1)	20-22
9M	Nd_2O_3-MC	22	NdP_5O_{14}	575	190	--
10M	Nd_2O_3-MC La_2O_3-BR	19	$Nd_{0.50}La_{0.50}P_5O_{14}$	625	96	190
11M	Nd_2O_3-MC La_2O_3-Br	28	$Nd_{0.50}La_{0.50}P_5O_{14}$	625	96	--
12M	Nd_2O_3-M La_2O_3-M	30	$Nd_{.50}La_{0.50}P_5O_{14}$	575	168	200
13M	La_2O_3-M	28	LaP_5O_{14}	625	150	--
14M	Nd_2O_3-M La_2O_3-M	21	$Nd_{0.25}La_{0.75}P_5O_{14}$	625	280	--
15M	Nd_2O_3-M La_2O_3-M	123	$Nd_{0.50}La_{0.50}P_5O_{14}$	625	280	80
17M	Nd_2O_3-M Y_2O_3-M	104	$Nd_{0.99}Y_{0.01}P_5O_{14}$	625	168	80

* Runs 2M to 5M – use Pd-Au crucible
   Runs 6M to 17M – use Au crucible

** All runs employ electronic grade phosphoric acid
   Reagent Code: MC – Michigan Chemical Corporation – 99.9% pure
                     BR – Bernard Ring – 99.9% pure
                     M – Molybdenum Corp. of America – 99.99% pure

acid initially present is greater than that required to form the ultraphosphate. In order to form only the composition MP_5O_{14}, the ratio (moles H_3PO_4)/(moles M_2O_3) must be equal to 10. The numbers in the third column, then, are an indication of the excess phosphoric acid initially present in the crucible. In the more dilute solutions, the crystals tended to be larger and more perfect (as expected) whereas smaller crystallites were produced in the more concentrated solutions. Growth out of concentrated solution was necessary in order to synthesize sufficient material to fabricate a target in a minimum number of growth runs. A minimum of fifty grams of ultraphosphate was necessary to cover a 4-inch diameter target, whereas ~ 150 grams was necessary for a pressed target. The growth runs were terminated when no visible vapors from further decomposition of the polyphosphoric acid could be seen coming out of the crucible. After removal from the crucible, the ultraphosphates were digested in hot water to remove any unreacted species of phosphoric acid. Lifetime measurements, which will be described in Section 7.4.2 and compared to the literature values, are listed in the last column of Table 7-I. Variations in the growth conditions summarized in this table did not significantly affect the measured lifetimes for either NdP_5O_{14} or $Nd_{0.5}La_{0.5}P_5O_{14}$.

Identification of NdP_5O_{14} was accomplished through X-ray powder diffraction using copper $K\alpha$ radiation and a Debye camera. This material is orthorhombic with cell constants, 12.95, 8.73, and 8.93 for the a, b, and c axes, respectively, and is reported to belong to the space group P_{mna} (Ref. 7-3). Since no ASTM card is available for this compound, the observed diffraction lines were compared with those calculated from the unit-cell parameters taking into account space group extinctions. Using this information all the "d" spacings of the 38 observed lines between 2θ values of $19°$ and $82°$ could be assigned Miller indices. Table 7-II lists the overall good agreement between observed "d" spacings with "d" spacings calculated from possible (hkl) reflections for NdP_5O_{14}. Slight disagreement in the unit cell parameters has been reported in a more recent paper (Ref. 7-4); however, these small differences do not obfuscate the above identification of neodymium ultraphosphate.

7.3 Growth of Ultraphosphate Films

Sputtering of NdP_5O_{14} was performed in an 18" oil-diffusion-pumped vacuum chamber. Provision was made for sputter cleaning of the target material by introducing a movable shutter into the vacuum system. Powdered target material prepared from bulk crystals mentioned in the last section was used throughout this investigation.

During sputtering of bulk NdP_5O_{14}, both polycrystalline and amorphous films can be grown. Since polycrystalline films of this material are useless for waveguide application due to the extremely high scattering caused by the crystallites, studies were made to characterize the deposition parameters for formation of the amorphous

Table 7-II

Powder X-Ray Diffraction Data for NdP_5O_{14}

Line	I/I_o (eyeball)	"d" (obs)	Possible (hkl)	"d" (cal)
1	40	4.462	002	4.465
2	15	4.304	020	4.365
3	20	3.763	112	3.800
4	100	3.651	202	3.676
5	20	3.613	220	3.619
6	10	3.346	212	3.388
7	`~`?	3.227	400	3.238
8	10	3.106	022	3.121
9	10	3.013	122	3.034
10	100	2.895	030	2.910
11	10	2.806	013	2.817
12	20	2.603	402	2.621
13	10	2.518	322	2.529
14	10	2.436	023	2.459
15	10	2.405	511	2.392
16	20	2.246	004	2.233
17	10	2.168	600	2.158
18	20	2.132	204	2.111
19	5	1.947	503	1.954
20	100	1.937	620	1.935
21	10	1.908	341	1.903
22	10	1.871	242	1.877
23	5	1.802	440	1.810
24	100	1.785	622	1.775
25	10	1.753	050	1.746
26	5	1.679	442	1.677
27	5	1.637	052	1.626
28	5	1.573	524	1.577
29	5	1.538	640	1.535
30	5	1.526	614	1.528
31	10	1.461	060	1.455
32	10	1.384	062	1.383
33	20	1.325	036	1.325
34	10	1.301	163	1.301
35	15	1.243	070	1.247
36	50	1.203	072	1.201
37	20	1.185	536	1.180
38	10	1.167	037	1.168

phase. As a result of the initial experiments, it was found that the amorphous phase could only be grown over a narrow temperature range. At higher temperatures polycrystalline films were formed while at lower temperatures decomposition products condensed as a viscous liquid on the substrate. It was also ascertained that a partial pressure of oxygen was required during sputtering to prevent the formation of brown oxygen-deficient films. To insure the highest degree of oxidation of the films, a pure oxygen plasma was employed. Good amorphous films were obtained at a pressure of 30 millitorr. Figure 7-1 shows RED patterns of a sample deposited near the upper transition temperature and had both cloudy and transparent areas which were sputtered during one growth run onto 7059 glass. The diffuse halos of the amorphous (transparent) area are to be compared with the additional ring patterns generated by the clouded polycrystalline area. Since there are inherent difficulties in making uniform thermal contact to insulating glass substrates, an alternative approach is to thermally float the substrate in the plasma and adjust the substrate temperature by changing the applied rf power. With such an arrangement, good amorphous films were deposited with a sputtering power of 125 watts. Even though this results in a low deposition rate, it was adequate to prepare samples for optical evaluation. During these growths, measured substrate temperatures were approximately 200°C. Since the substrate temperature is such an important factor in depositing optically good films, an experiment was designed to accurately determine the temperature range for amorphous growth; this is described in the following section.

7.3.1 Determination of the Temperature Range for Amorphous Growth of NdUP

Three major constraints were imposed on the design of the needed experimental apparatus. In the first place, accurate measurement of the substrate temperature is required. This excludes the use of thermally insulating substrates and mandates the use of metallic substrates with strategically located thermocouples. Secondly, the substrate surface must be similar to the glass substrates used to fabricate the samples used for optical evaluation. The reason for this is that the substrate surface plays an important role at the onset of crystal nucleation. Such a surface was obtained by sputtering a 0.2 μm layer of amorphous quartz onto a polished metallic substrate. Finally, since it had already been established that the temperature range for amorphous growth is narrow, a large number of depositions at closely incremented temperatures would be required to avoid overlooking the small temperature window. Alternatively, a single substrate with a temperature gradient established between 150°C and 300°C will contain the proper temperature for amorphous growth somewhere along its length. This latter technique was chosen to economize on the number of required growth runs.

In the present apparatus, both ends of the substrate (shown in Fig. 7-2) are maintained at the same temperature. A symmetric temperature gradient was established by passing an ac current through the bar. This was done in order to observe a symmetric growth pattern and therefore increase the confidence factor of the run
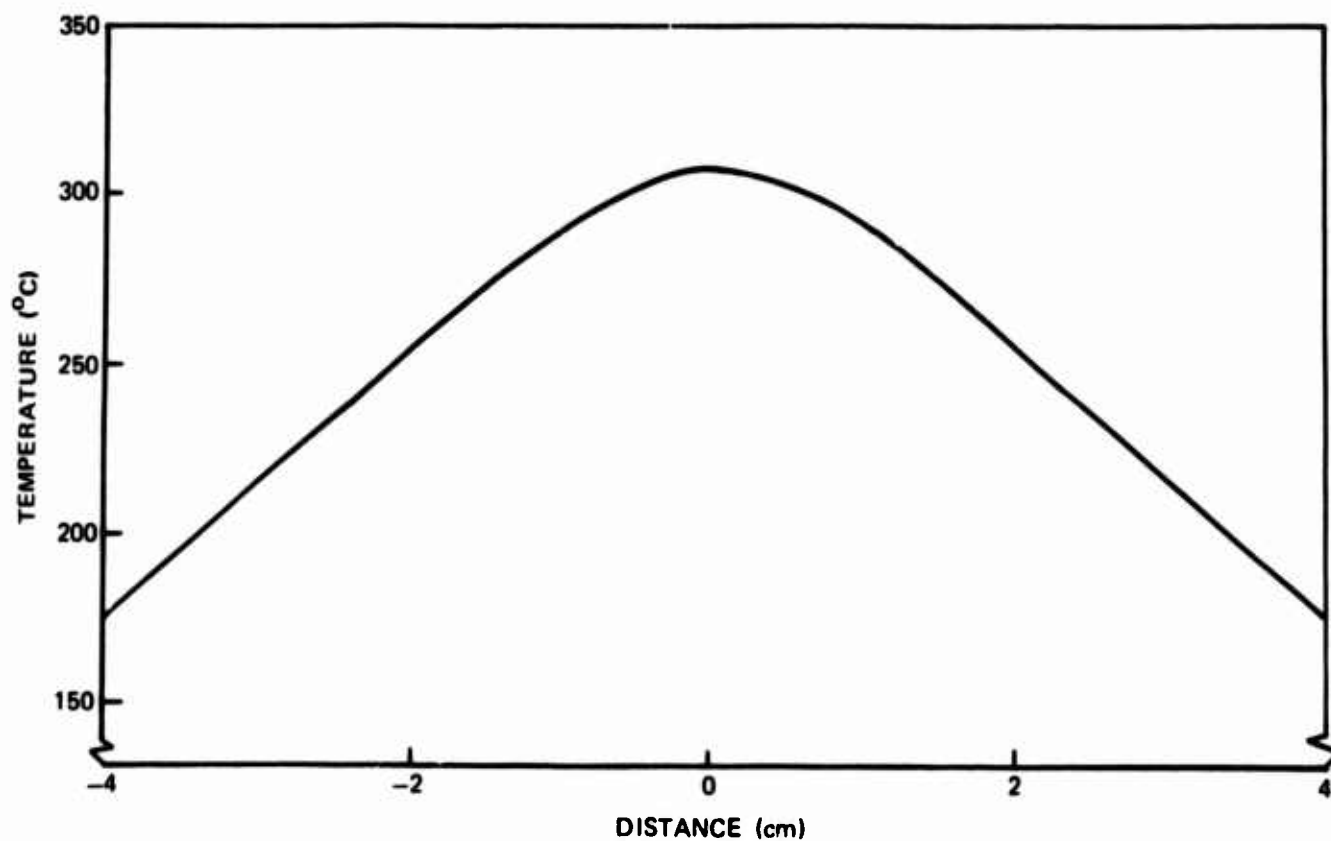
FIG. 7–1

RED OF SPUTTERED NEODYMIUM ULTRAPHOSPHATE (#6)

CLOUDY AREA

TRANSPARENT AREA

N04–181–4

FIG. 7-2

DETAILS OF TEMPERATURE GRADIENT BAR
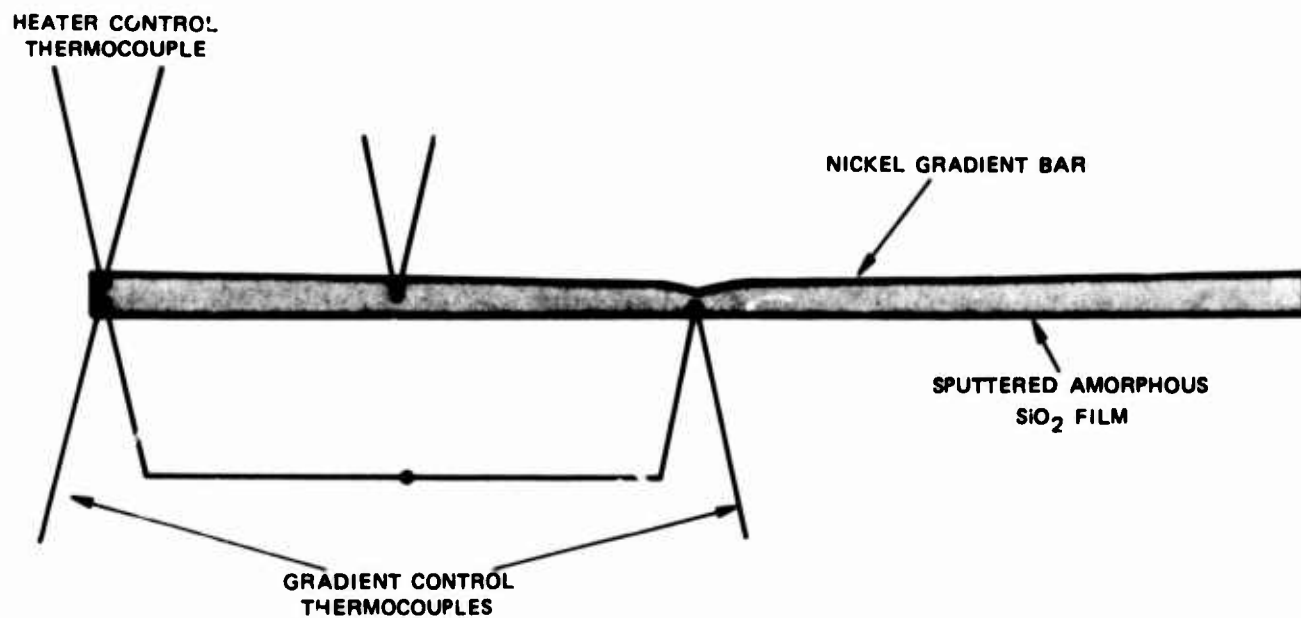
over the case of simply maintaining the ends of the substrate at two temperature levels. Ohmically heating a uniform bar of cross-sectional area A with a current I results in a quadratic dependence of temperature on position (x). The sputtering process itself can be an added source of heat for the substrate, and for a given power the amount of added heat is proportional to the exposed area. This flux of heat also results in a quadratic dependence of temperature on x for a uniform bar. In order to reduce the expected x^2 dependence, the bar thickness, t, was tailored slightly as a function of position so that $t = t_0 + .05x^2$. The ends of the bar were maintained at a given temperature by cartridge heaters brazed into a copper block (see Fig. 7-3). Due to possible arcing inside the heater when the lead end of the heater is pumped down, O-ring couplings which connect to atmosphere via leak-tight tubes were placed over the heater ends. This precaution was necessary since heater failure did occur during testing of the apparatus when the lead ends of the heater were inside the vacuum system. In order to reduce the time constant of the system and avoid excessive drift, the heaters were connected to a water-cooled heat exchanger by a copper gradient bar. Proportional controllers were used to power both the heaters and the gradient current through the bar. Thermocouples at the end and center, connected differentially, controlled the gradient current, and another thermocouple at the end controlled the heater power. One experimental temperature profile across the substrate bar is shown in Fig. 7-2. Nickel was chosen as the material of construction for the substrate since (1) the electrical and thermal conductivities give the desired gradient with practical heater power and bar current, and (2) nickel is relatively inert in the oxidizing ambient.

The above experimental apparatus revealed four temperature dependent growth morphologies. For temperatures below $150^{\circ}C$, a yellow viscous liquid was deposited; this is probably a form of phosphoric acid. Between $150^{\circ}C$ and $190^{\circ}C$ there exists a mixed phase composed of microscopic droplets of phosphoric-acid-like material in an amorphous matrix. The range of interest, i.e., a clear transparent deposit, exists between $190^{\circ}C$ and $250^{\circ}C$. Above this range, a polycrystalline film is produced which scatters light very effectively. These results were obtained under the following deposition conditions: (1) target-to-substrate separation, 4 cm, (2) sputtering power, 125 watts, (3) target diameter, 4 inches, and (4) oxygen pressure, 30 millitorr.

7.3.2 Stoichiometry of Sputtered Ultraphosphate Films

Although the sputtered films will be referred to in this report as ultra-phosphate films, their analyzed phosphorous-to-neodymium atomic ratios are less than the value 5 as in the ultraphosphate. This is illustrated by the electron microprobe results in Table 7-III for various Nd ultraphosphate films. For purposes of this analysis, a single crystal of NdP_5O_{14} selected from growth run #6M was used as reference. Counts were taken in an alternate fashion between the standard and each of the three sputtered films, and this was repeated ten times for each element (neodymium and phosphorous). Oxygen was determined by difference since the

FIG. 7-3

APPARATUS FOR DETERMINATION OF THE TEMPERATURE RANGE FOR AMORPHOUS GROWTH OF NdUP.

SHUTTER CONTROL

O-RING COUPLING OVER HEATER END

END HEATER WIRES

THERMOCOUPLES

WATER COOLED HEAT EXCHANGER

GRADIENT BAR SUBSTRATE

END HEATER

WATER INLET AND OUTLET TUBES

OXYGEN INLET

ELECTRODE FOR AC CURRENT TO BAR

MILLITORR GAUGE

N12-46-2
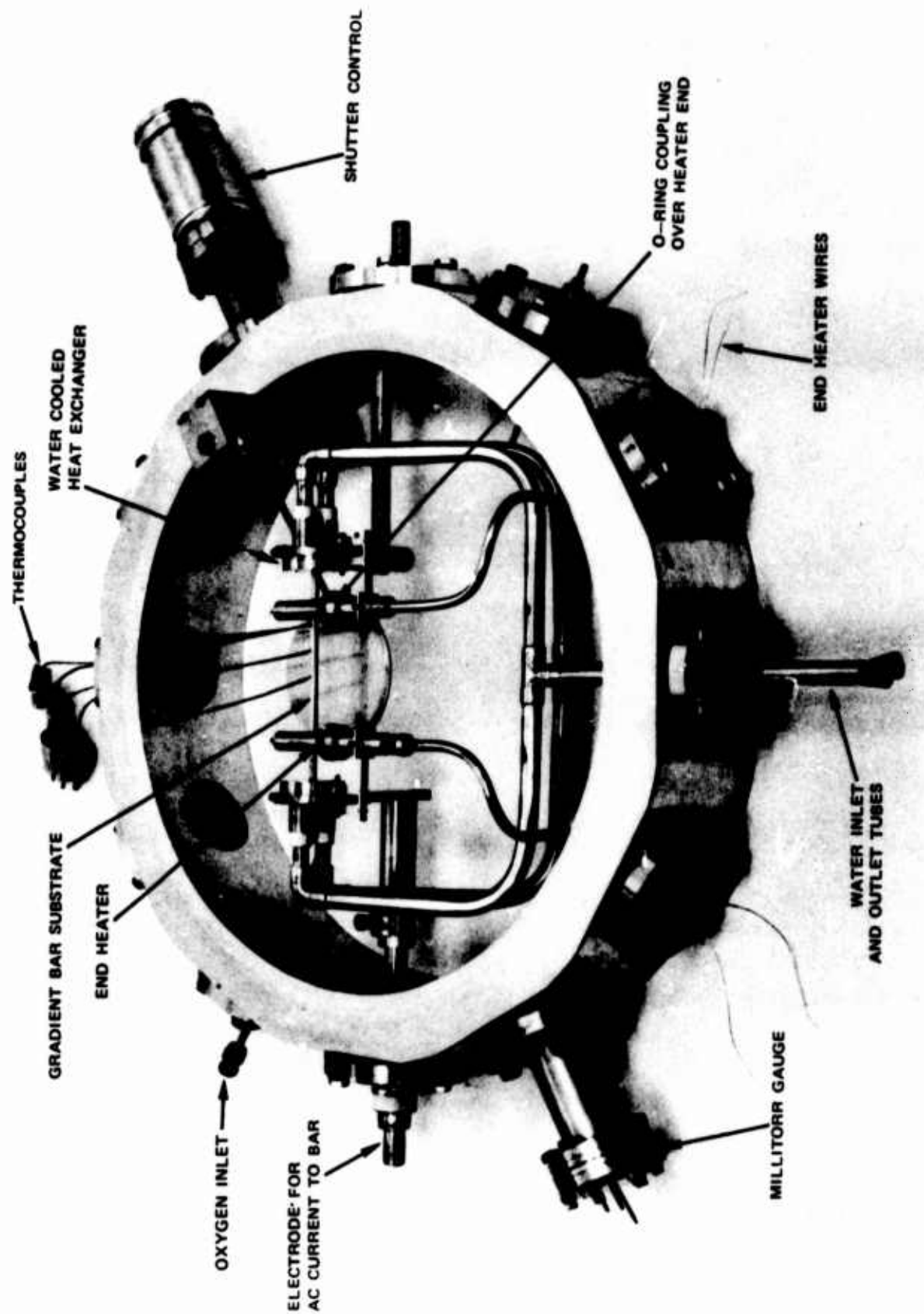
TABLE 7-III
DETERMINATION OF FILM STOICHIOMETRY BY ELECTRON MICROPROBE ANALYSIS

MEAN CHEMICAL COMPOSITIONS AND TWO SIGMA LIMITS BASED ON TEN ANALYSES

ATOMIC PERCENT

	STANDARD	NdUP # 2	NdUP # 7	NdUP # 14
Nd	5	6.69 ± 0.17	7.14 ± 0.37	6.36 ± 0.54
P	25	22.35 ± 0.48	19.56 ± 1.74	18.41 ± 1.32
O	70	70.96 ± 0.64 *	73.30 ± 2.08 *	75.23 ± 1.76 *

ATOMIC PERCENT

	STANDARD	NdLa UP # 15
Nd	2.5	4.89 ± 0.11
La	2.5	4.95 ± 0.12
P	25	22.10 ± 0.68
O	70	68.06 ± 0.77 *

* DETERMINED BY DIFFERENCE

151

neodymium line interferes with the K-α oxygen line. In addition, general analyses
showed the absence of other atomic constituents (to within five-tenths of a percent).
The particular results show that the NdUP films are neodymium rich and phosphorous
deficient and the atom ratio, P/Nd, varies between 2.8 and 3.3. That the P/Nd
ratio is low is expected on the basis of the greater volatility and the generally
lower sticking coefficients of phosphorous compounds compared to neodymium. This
suggests that the amorphous films should be sputtered at as low a temperature as
possible consistent with formation of the amorphous phase, i.e., approximately
200°C. This would have the added advantage of reducing interfacial stresses which
may develop between the sputtered film and substrate as the sample is cooled to
room temperature after growth. An alternative route to raising the phosphorous
content in the film would be to add phosphorous or phosphorous pentoxide to the
NdP_5O_{14} target. This would raise the partial pressure of phosphorous containing
species in the plasma and ultimately in the deposited film. It is not clear,
however, whether phosphorous deficiency will have a deleterious effect on the optical
properties of the films. Other variables which may be more important in affecting
laser performace are absolute neodymium concentration (self-quenching), stress, and
certain impurities. It has been demonstrated in the literature (Ref. 7-2) and in
this report that lanthanum substitution in neodymium ultraphosphate bulk material
improves the fluorescence lifetime by reducing self-quenching between neodymium
ions. Since the composition, $Nd_{0.5}La_{0.5}P_5O_{14}$ has been suggested as an optimum one,
material was selected from growth run #10M to be used as target material for
sputtering of an ultraphosphate film containing neodymium and lanthanum. The electron
microprobe results are shown in Table 7-III. The phosphorous content is similar to
the NdUP layers but the measured high neodymium and lanthanum concentrations cannot
be explained. A consistent factor is the close agreement in the Nd and La concentra-
tions in the film. This indicates that the sticking coefficients for these elements
are nearly the same and that their relative compositions in the film can be varied
by suitable adjustment of their compositions in the target.

7.4 Optical Characterization of the Ultraphosphates

Important material properties for laser application are (1) low loss at the
lasing wavelength due either to absorption or scattering, (2) long fluorescence
lifetime, which is affected by stress, impurities, and fluorescence quenching due
to cross relaxation between active ions, and (3) optimization of the active ion
concentration in order to balance gain versus heat dissipation.

The subject of this section will be a discussion of the experimental techniques
and results of absorption and fluorescence lifetime measurements of bulk and thin
film ultraphosphate samples. An upper limit on the scattering losses in the
sputtered films has also been established.

7.4.1 Optical Absorption

A Cary spectrometer was used to obtain the absorption spectra of the ultra-phosphate samples shown in Fig. 7-4. As can be readily seen, no major absorption occurs in the region of 1.05 μm, and the neodymium pump bands are located in the same regions as the bulk crystals. At the Ar-ion laser wavelength of 0.5145 μm, the film has an absorption coefficient of $\alpha = -22$ cm^{-1}. This wavelength has successfully been used to pump the neodymium ion. All of the absorption measurements of bulk and film ultraphosphate materials have the same absorption spectra.

7.4.2 Fluorescence Lifetime

The fluorescence lifetime was determined by pumping an ultraphosphate sample with a 1.5 μsec pulse at 0.5850 μm wavelength from a Rhodamine-6G dye laser. The experimental set up is summarized in Fig. 7-5. About 100 millijoules of power pass through a KG-3 IR absorbing filter and onto either the sputtered film, a single crystal, or a collection of small bulk crystals sandwiched inside on O-ring between two glass slides. Both the visible laser light and that generated as photoluminescent radiation strike an optical filtering network consisting of a bandpass interference filter and two visible absorbing filters placed in front of the detector. The bandpass filter allows a peak transmission at 1.062 μm of 75%, and this falls by 50% at 165 Å on either side of this wavelength. Thus, the most intense room temperature fluorescence line at 1.051 μm (Ref. 7-3) will pass with minor attenuation. Additional visible cut-off filters attenuate infrared light above 0.8 μm. Behind the filter stack is an S-1 photomultiplier detector operated at room temperature. The signal is displayed on an oscilloscope which has been triggered by the laser pulse using a silicon photocell. The overall resolution limit of the detection system is ~ 2 μsec. Figures 7-6 to 7-8 are photographs of the fluorescence decay for selected bulk and thin-film ultraphosphates. Figure 7-9 shows plots illustrating the method used for obtaining the fluorescence lifetime from these photographs. In all cases, good exponential behavior with time is observed. A summary of all the lifetime measurements of bulk and sputtered film samples along with literature values for bulk material is shown in Table 7-IV.

Fluorescence lifetime (τ) is a critical parameter for laser materials in that the population density at the lasing threshold (N_T) of the upper state is directly proportional to this quantity, that is

$$N_T = \frac{P_T \tau}{h\nu V} , \qquad \text{(Eq. 7-1)}$$

where P_T is the threshold pump power and V is volume of the pumped region. In addition, τ is related to the line width ($\Delta\nu$) by

FIG. 7-4

ABSORPTION SPECTRA OF SPUTTERED AND BULK NEODYMIUM ULTRAPHOSPHATE

FIG. 7-5
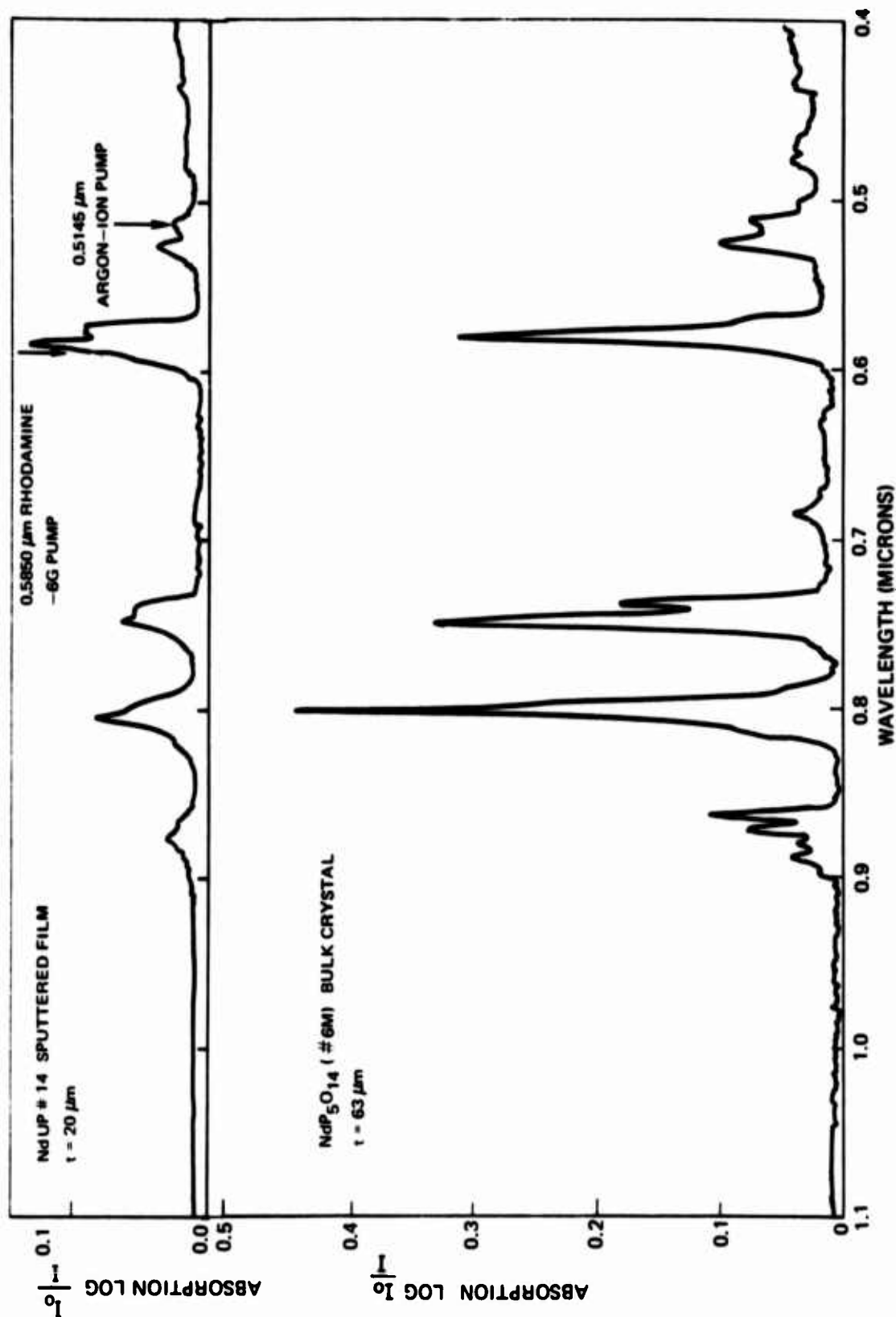
EXPERIMENTAL SET UP USED FOR FLUORESCENCE LIFETIME MEASUREMENTS
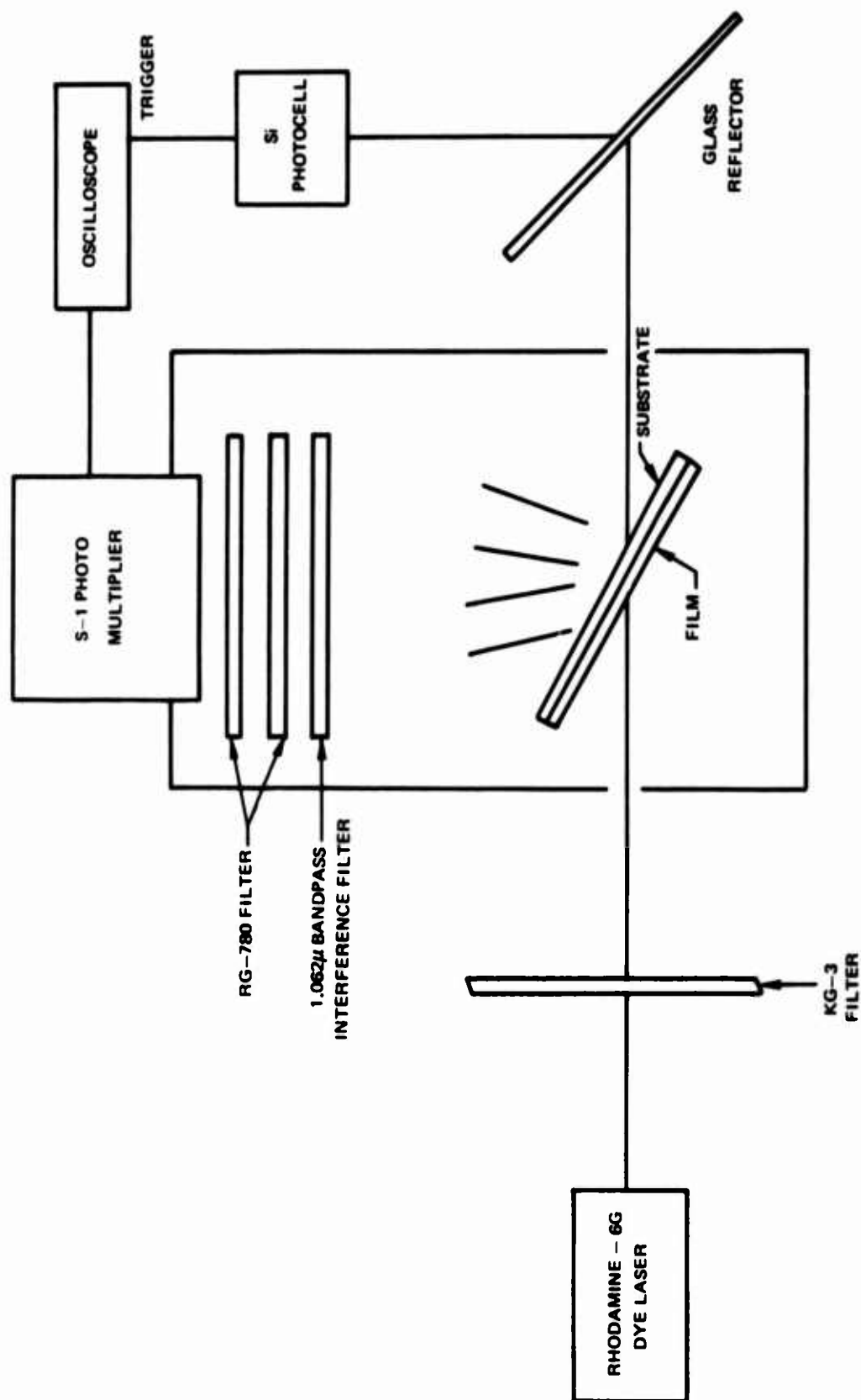
INFRARED FLUORESCENCE DECAY CURVES FOR BULK NEODYMIUM ULTRAPHOSPHATE (6M) AND NEODYMIUM LANTHANUM ULTRAPHOSPHATE (10M)

NdUP (τ = 96 μsec)

TIME (MICROSECONDS)

NdLaUP (τ = 190 μsec)

TIME (MICROSECONDS)

N04-181-3

FIG. 7–7
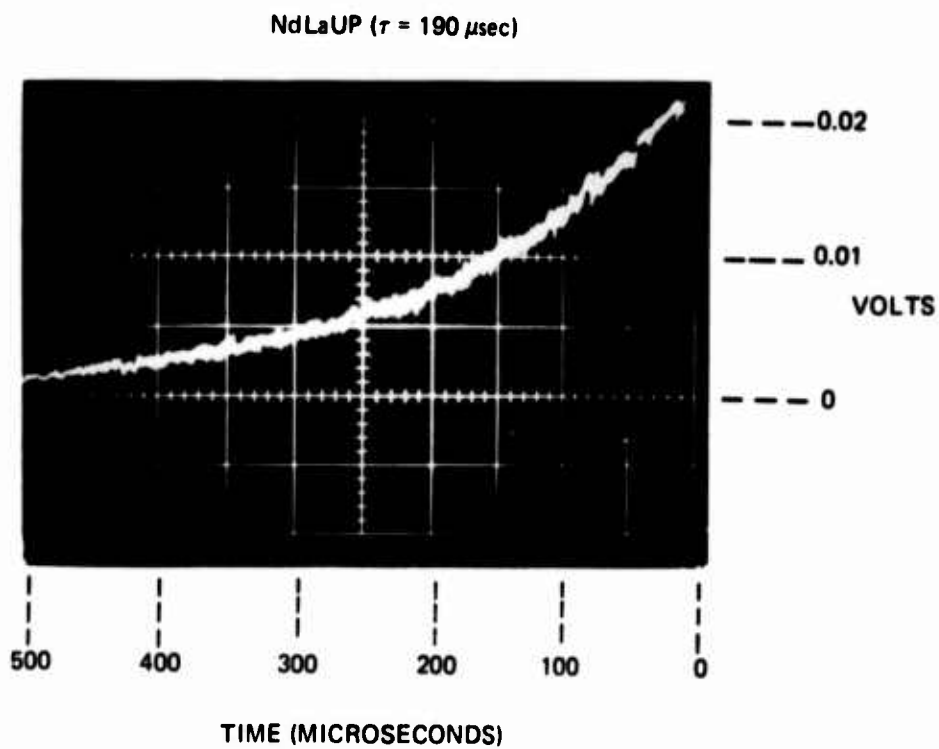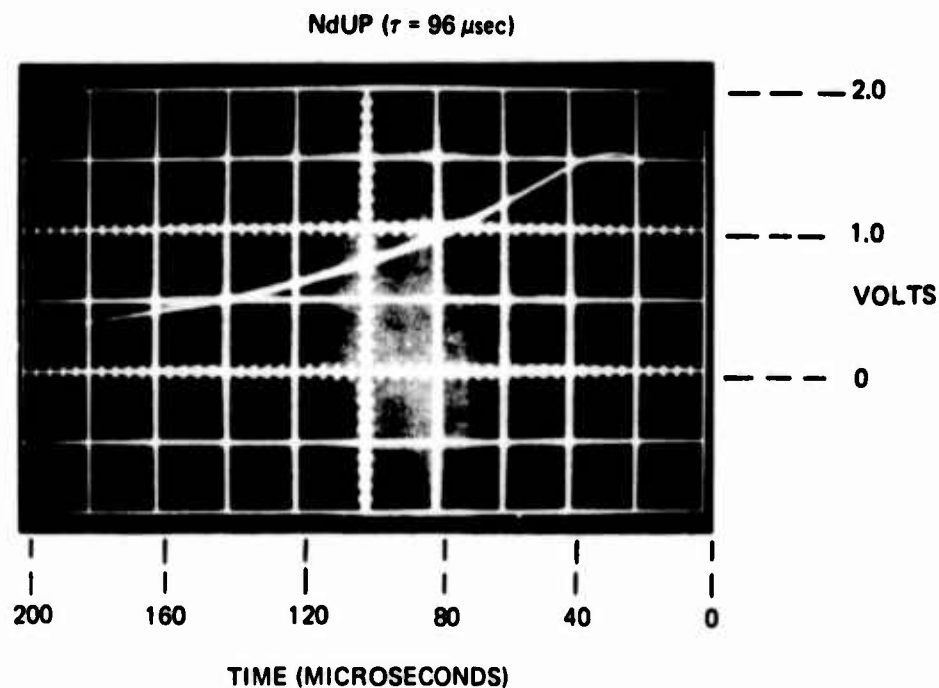
**INFRARED FLUORESCENCE DECAY CURVE FOR SPUTTERED THIN FILM
NEODYMIUM ULTRAPHOSPHATE GLASS (#14)**

$\tau = 8.3 \, \mu \, \text{sec}$

FIG. 7–8
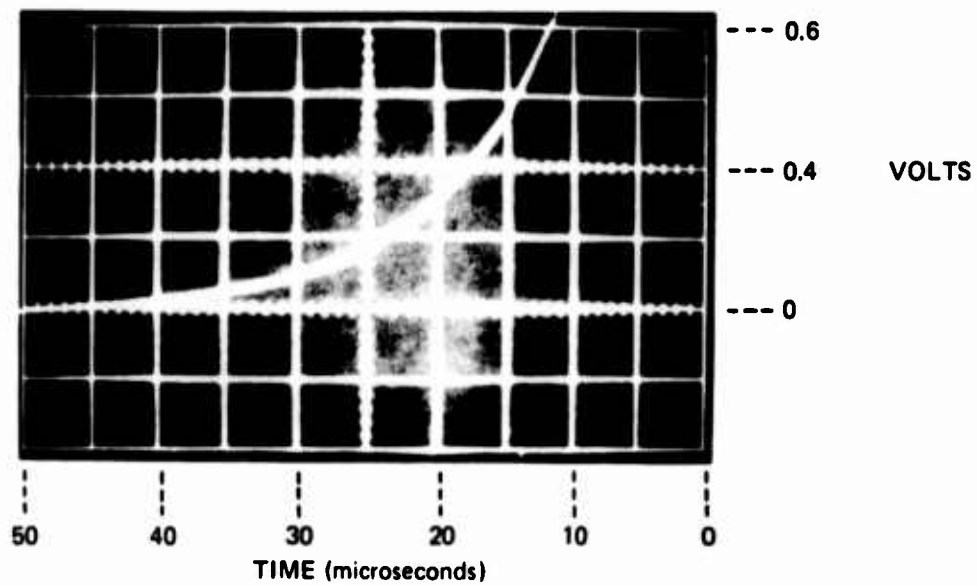
INFRARED FLUORESCENCE DECAY CURVE FOR SPUTTERED THIN FILM
NEODYMIUM–LANTHANUM ULTRAPHOSPHATE GLASS (#15)

$\tau = 16.3\ \mu\text{sec}$

TIME (MICROSECONDS)

FIG. 7-9
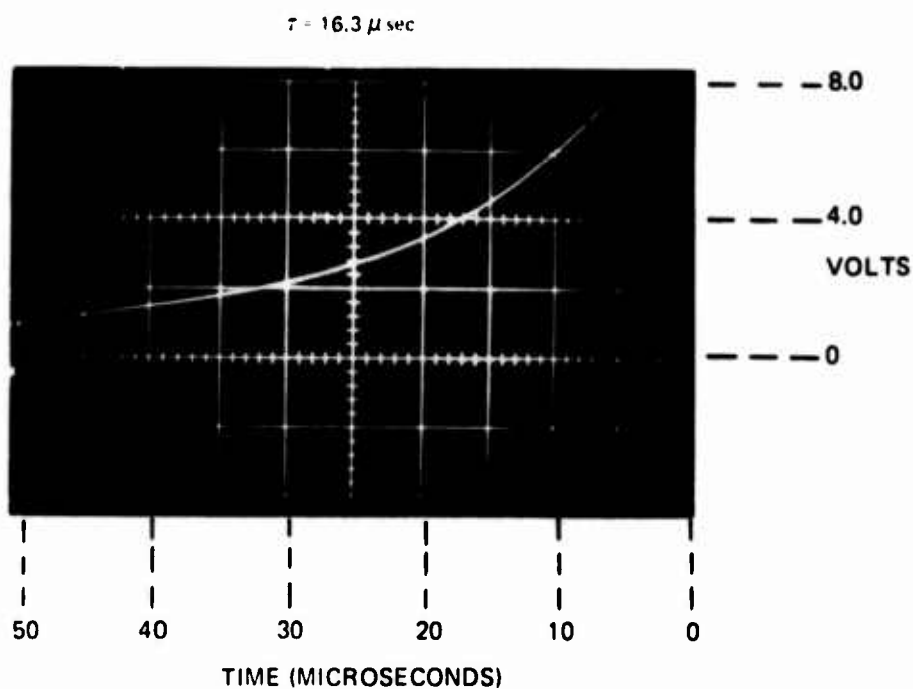
FLUORESCENCE LIFETIME DETERMINATION FOR NdUP #14 AND NdLaUP #15 SPUTTERED FILMS

$$I(t) = I_o e^{-\frac{t}{\tau}}$$

NdUP
$\tau = 8.3$ μsec

NdLaUP
$\tau = 16.8$ μsec

TIME (MICROSECONDS)

INTENSITY
(NORMALIZED)
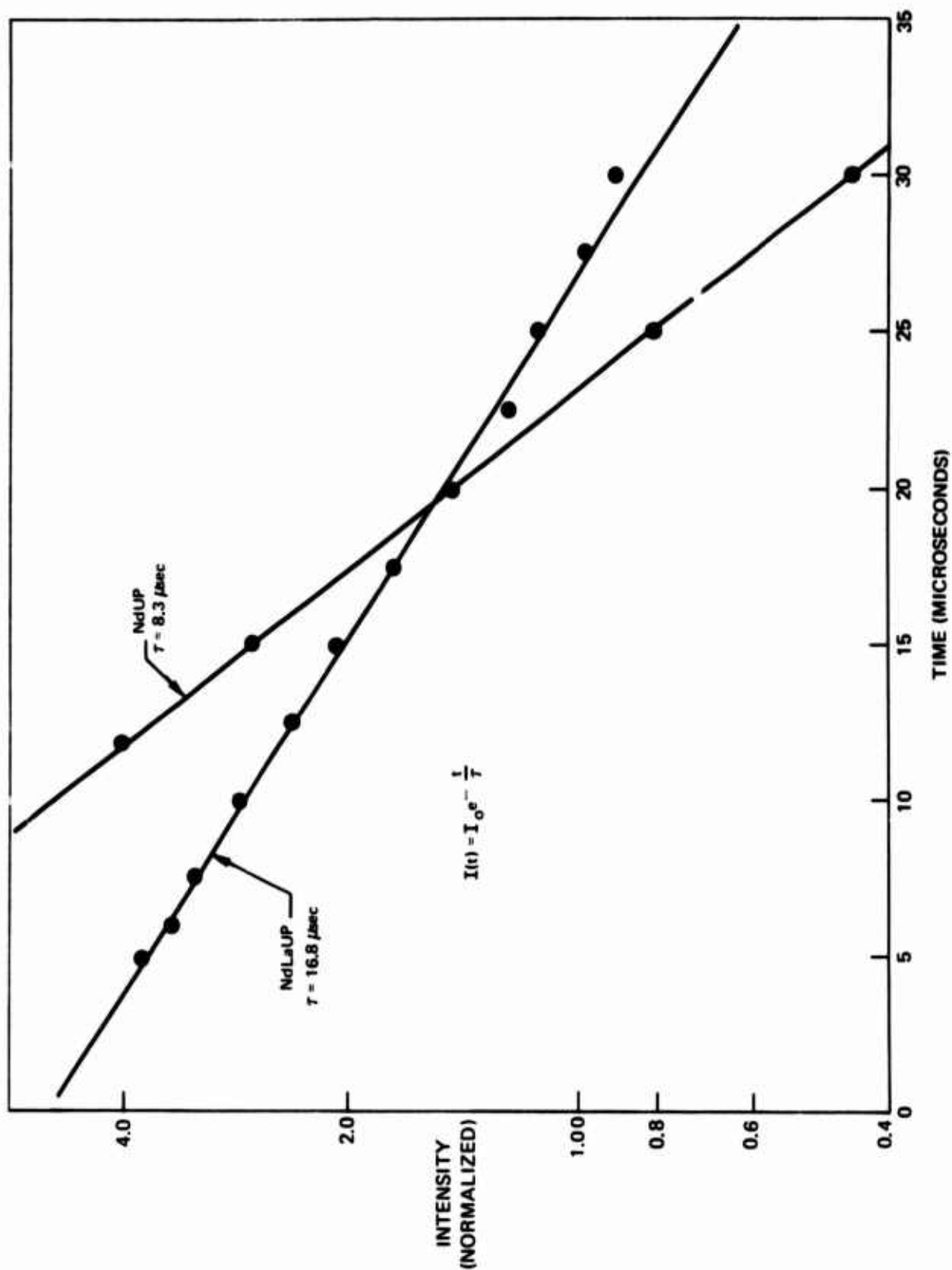
TABLE 7-IV

Summary of Fluorescence Lifetime for Ultraphosphate Samples

	Fluorescence Lifetime (μsec)		
	Bulk UP		Sputtered Film
Composition	Literature Values	UARL	
NdUP	66**	55-120	8
$Nd_{0.5}La_{0.5}UP$	30-200**	80-200	16
$Nd_{0.99}Dy_{0.01}UP$	24*	20-22	-

*   Reference 7-5
** Reference 7-2

$$\tau = \frac{\lambda^2}{8\pi^2 n^2 \Delta\nu\delta_o} ,$$

(Eι. 7-2)

where n is the index of refraction, λ the wavelength, and δ_o the emission cross-section. The linewidth of a particular transistion is controlled by perturbations of the local fields at the site of the active ion. These perturbations are caused by variations of the positions of the atoms surrounding the active ion. Factors which influence interatomic spacings are stress, temperature, and structural imperfections. In the amorphous highly disordered state, each atom sees a slightly different environment, and each active ion, therefore, has a distinct set of split energy levels. Increasing stress, temperature, or transforming from the crystalline to the amorphous state will decrease the fluorescence lifetime. In addition, cross-relaxation processes, which are a function of the interneodymium distance, result in a decrease in the fluorescence lifetime as the neodymium concentration increases. Certain impurities that have energy levels within the lasing levels will permit fast transitions to the ground state (impurity quenching), thus also shortening the fluorescence lifetime. Other impurities just serve to dilute the active ions but do not participate in the lasing process.

The measured lifetime results illustrate the general principles mentioned in the last paragraph. The literature values show the increase in lifetime with lanthanum addition which decreases the probability for cross relaxation. That dilution is possible with lanthanum is due to the facts that lanthanum is completely miscible with neodymium (nearly the same ionic radii and causing little stress) and lanthanum has no atomic levels appearing between the $^4F_{3/2}$ and $^4I_{11/2}$ neodymium fluorescence levels. Dysprosium, on the other hand, has several levels within the fluorescence bands of the neodymium ion and impurity quenching results. It has been reported in the literature (Ref. 7-2 and 7-5) that varying growth conditions (e.g., temperature and presence of impurities) affect the resultant lifetimes. This is suggested to be the reason for the wide variation in lifetimes reported for bulk $Nd_{0.5}La_{0.5}UP$ and is probably responsible for our generally higher lifetime results for bulk NdP_5O_{14} and $Nd_{0.5}La_{0.5}P_5O_{14}$. Crystal stress may also be a factor here.

With regard to the sputtered films, a decrease in fluorescence lifetime can be attributed to any or all of the following factors: (1) disorder due to the amorphous phase, (2) self-quenching due to the increased neodymium atom concentrations compared to the bulk, and (3) intrinsic stress due to the deposition process or induced stress due to mismatch of the expansion coefficients between the film and substrate. It is impossible at this time to ascertain which of these processes is the predominant one. Even though the neodymium ion is located in an amorphous structure, which may be responsible here for the short lifetime, values as high as 700 μsec have been measured for bulk Nd^{3+} in a rubidium lime silicate glass (Ref. 7-6).

Self-quenching seems to be operative when comparing the measured lifetimes of the NdUP and NdLaUP films because a decrease in neodymium concentration from 6.3% (NdUP #14) to 4.89% (NdLaUP #15) resulted in an increase in the lifetime by a factor of two. If self-quenching is a factor in the amorphous films, it is reasonable to expect at least a factor of two increase in the lifetime for the amorphous films if the neodymium concentration is halved to 2.5 atom percent - this is known to be the case for the bulk material. As discussed before, changes in the constitution of the target can be made to affect this change in the film's neodymium concentration. The third factor, stress, is evident in sputtered films greater than about seven microns in thickness. The stress manifests itself as cracks which when analyzed under an optical microscope or Talysurf are accompanied by raised areas which, in one case, NdLaUP #15, were about 200 Å high and 50 microns wide. Depositions on quartz and pyrex showed considerably more crazing compared to the 7059 glass. This indicates that the mechanism of mechanical failure is the thermal mismatch with the substrate.

7.4.3 Waveguide Attenuation in Sputtered NdUP Films

Our amorphous ultraphosphate films have optical attenuation due to scattering well below 1 dB/cm. Attenuation of 1 dB/cm caused by scattering can readily be seen as a bright streak in a thin film waveguide; however, the light scattered out of the ultraphosphate films is so small that it can barely be seen by the naked eye, indicating a scattering loss of well-below 1 dB/cm. A few surface and volume irregularities do result in occasional bright points of light but these do not constitute an appreciable loss mechanism nor do they characterize the scattering from the continuum of the film. A quantitative measurement of the losses has not been made since the methods of measuring scattering losses described in the appendix are not suitable for films with losses below $\sim$ 1 dB/cm.

In order to place an upper limit on the absorption losses near the laser wavelength (1.06 μm), a waveguide with input and output prism couplers was employed and is shown schematically in Fig. 7-10. The high-index prisms were bonded to the waveguide with an organic glue (aroclor) having an index of refraction between the prism and the ultraphosphate film. A Nd:YAG laser was used to produce beam A, and the intensities of this beam and all the reflected beams, as well as the coupled output beam, were measured. Assuming that there is a 100% coupling efficiency at both the input and output prisms, then all of the light that cannot be accounted for can be attributed to absorption in the waveguide. Since some scattered light is lost in the prisms, it is impossible to account for all of the lost light. Therefore, this measurement only places an upper limit of 1.25 dB/cm on the film absorption.

The above results indicate that a thin film laser should be possible using sputtered NdUP. Both scattering and absorption losses are low ($< \sim$ 1 dB/cm) at the laser wavelength, the absorption in the pump band is large, and the lifetimes (especially for the lanthanum alloy films) are long enough to at least allow pulsed operation.

FIG. 7-10

SCHEMATIC OF WAVEGUIDE ASSEMBLY USED TO DETERMINE OUTPUT EFFICIENCY AND MAXIMUM FILM LOSS
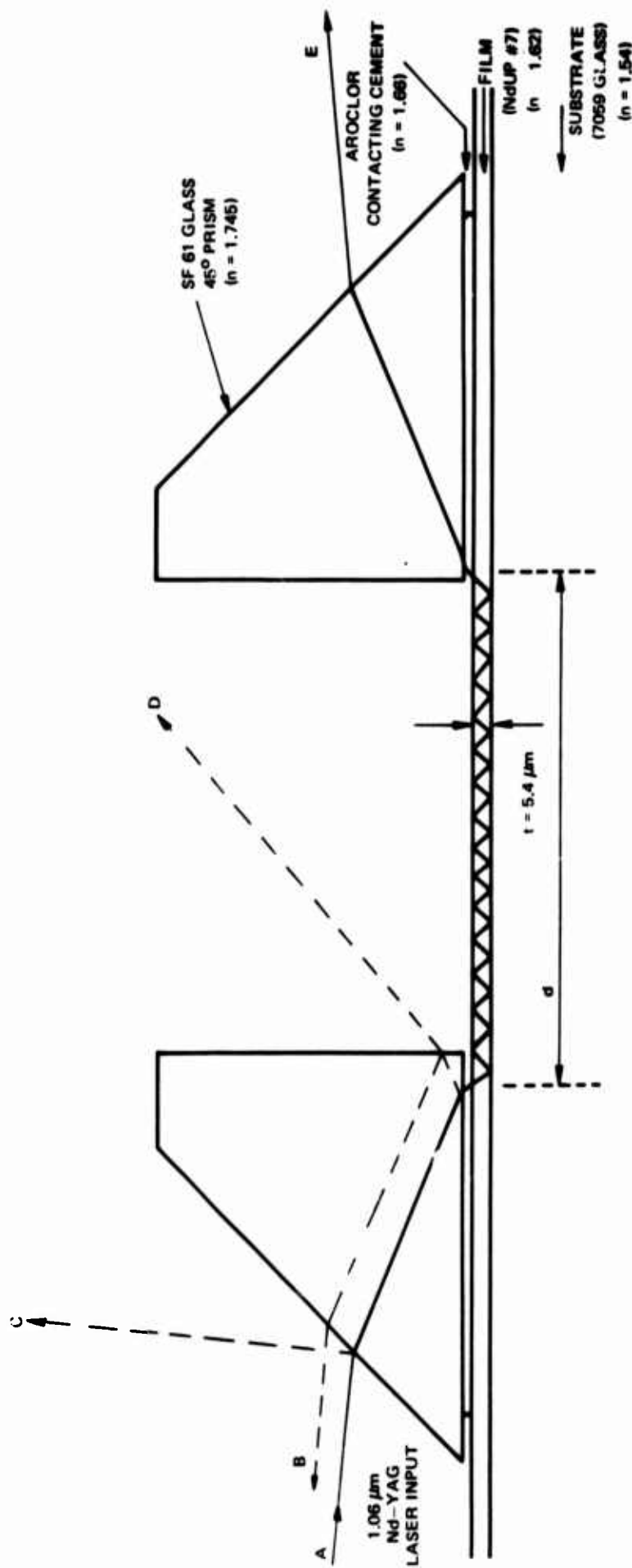
INTENSITY MEASUREMENTS AT 1.06 μm						UNMEASURED LIGHT INTENSITY $A-(B+C+D+E)$	d(cm)	OUTPUT EFFICIENCY $\frac{100(E)}{A}$	MAX FILM LOSS (dB/cm)
A	B	C	D	E					
850	40	64	490	72		184	2.1	8.5%	2.6
800	30	62	350	110		248	4.1	13.7%	1.25

N04-198-1

163

7.5 Ultraphosphate Laser Experiments

7.5.1 Introduction

The final objective of thin-film sputtering research into growth of the ultraphosphate materials is to produce a thin-film laser which can be pumped in the plane of the film by a light emitting diode. Although film loss, lifetime, and absorption measurements on the ultraphosphate glass are encouraging, it still must be demonstrated that laser action is possible. In order to accomplish this, losses due to the cavity and laser material must be low. Before any valid conclusions can be made concerning the laser potential of the sputtered NdUP films, the same cavity used for film testing should be capable of supporting laser action in the bulk crystals. Two lasers, available to us, that could be used to effectively pump NdUP were a one-watt argon-ion and a pulsed rhodamine - 6G dye laser. The argon-ion laser could be used with prism coupling to introduce sufficient energy into a sputtered film but this is not feasible with small bulk crystallites. Direct pumping of the bulk crystals can result in sufficient absorption whereas this is not the case with the film. On the other hand, the dye laser has sufficient power to excite both crystal platelets and films. For the above reasons, an unambiguous interpretation of the results is possible using the method of direct pumping with the dye laser.

7.5.2 Experimental Details and Results

A schematic diagram of the experimental apparatus used in the laser experiments is shown in Fig. 7-11. A flash-lamp pumped rhodamine-6G dye laser was focused onto the NdUP sample through one of the cavity mirrors. The pulse had a duration of 2 microseconds and could deliver approximately 75 mw per pulse to the crystal after mirror and lens losses were taken into account. Beam divergence was about 10 milliradians and the beam diameter at the crystal calculated from the divergence was about 10 mil. The cavity mirrors each had a radius of curvature of 4 cm; their optical transmission at 1.05 μm and 0.5850 μm was 1.5% and 80%, respectively. The sample was mounted in the center of these mirrors, which were separated by 7.8 cm. A collecting lens directed the emerging radiation to an S-1 photomultiplier detector via a filterpack consisting of a visible cut-off filter and a 1.06 μm band-pass interference filter ($\sim$ 50% transmittance at 1.051 μm). The signals were displayed on one channel of a Tetronix Type 555 dual-beam oscilloscope. The oscilloscope was triggered off the pump beam using a silicon photodiode.

The large number of randomly nucleated crystals grown in runs 6M, 15M, and 17M were examined under low power magnification, and initial candidates for lasing were chosen on the basis of low optical distortion. These platelets (20 μm to 50 μm thick) were then subjected to examination under higher magnification ($\sim$ 200X), and the final samples for testing were selected on the same basis. In spite of the demonstrated performance of the type of cavity design described above for unpolished 35 μm thick platelets (Ref. 7-1), no laser action was observed for our crystals.

FIG. 7-11

SCHEMATIC DIAGRAM OF LASER TEST APPARATUS
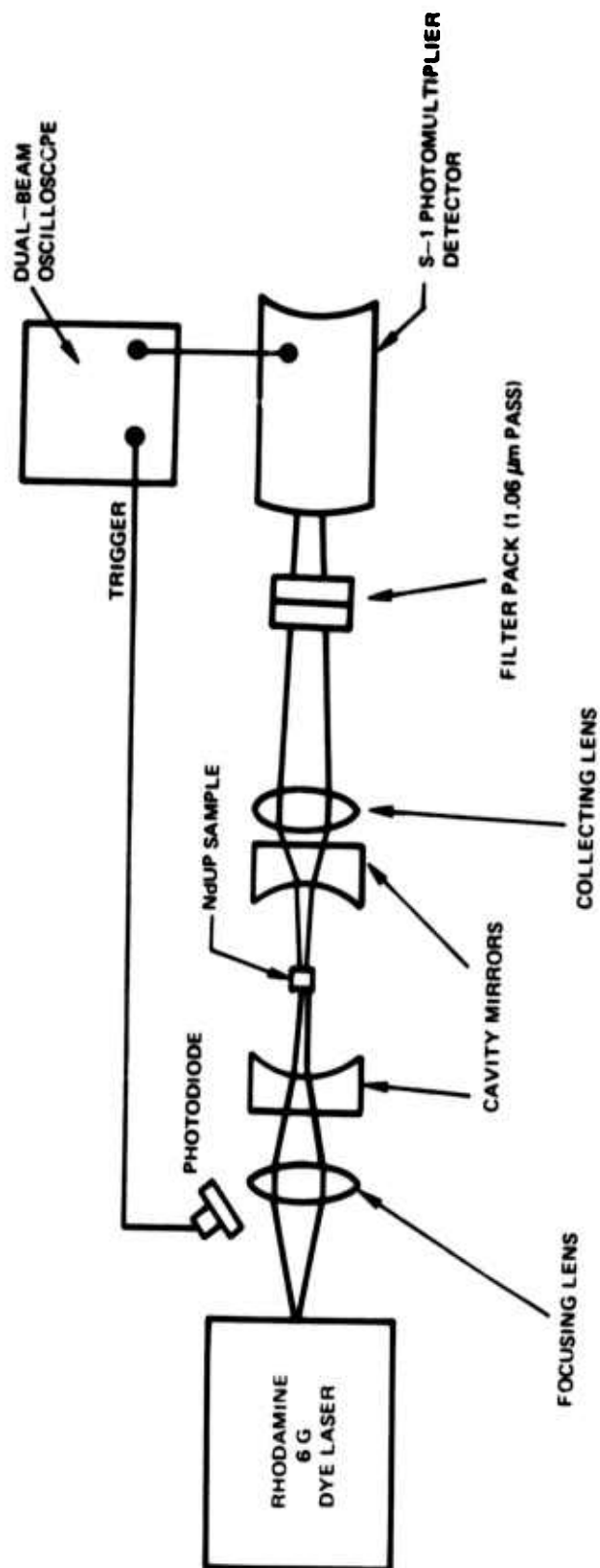
It, therefore, must be concluded that these crystals did not have sufficient optical quality associated either with the surface or bulk to enable them to lase. Although the successful operation of our cavity with bulk crystals is necessary before any definitive conclusions can be made with regard to the sputtered films, attempts were also made to observe laser action in the films. The thinnest ultraphosphate crystals reported to have lased were 35 μm thick (Ref. 7-1). Since this thickness provides sufficient gain to lase, the films should also be at least this thick. However, in attempting to grow thick films, it was found that crazing occurred above 7 μm due to thermal mismatch with the substrate. This cracking decreases the optical quality of the sputtered films, so that a trade-off exists between optical quality and film thickness. A 5.4 μm thick film (NdUP #7) did not lase in our cavity, and this is probably due to the low saturated gain arising from the short pump length of material. Thicker crazed films, NdUP #14 (t = 20 μm) and NdLaUP (t = 14 μm), also did not lase. This must be due in large part to the poor optical quality arising from the cracks. Thicker films may be required to produce sufficient gain for the films to lase; however, the optical quality must be improved by finding a more suitable substrate. Thick films are only required for the present optical evaluation; much thinner films could be used for a waveguide laser. Depositions on quartz and pyrex showed considerably more crazing compared to the 7059 glass. This indicates that the mechanism of mechanical failure is the thermal mismatch with the substrate.

7.6 Conclusions

Amorphous films sputtered from a NdP_5O_{14} target exhibit low optical attenuation (less than 1 dB/cm) at 1.059 μm. Absorption in the neodymium pump bands is high, and the fluorescence lifetime appears long enough to at least allow pulsed laser operation. Lifetimes have been increased in the sputtered films through neodymium dilution using lanthanum. These sputtered films have all the basic properties required of a thin-film laser material. Ultimately, these films could be coupled with a light emitting diode to produce a useful integrated optics technology.

7.7 References

7-1 H. P. Weber, T. C. Damen, H. G. Danielmeyer, and B. C. Tofield, Applied Physics Letters 22, 534 (1973).

7-2 H. P. Weber, B. C. Tofield, and T. C. Damen, Topical Meeting on Integrated Optics, Paper MB8-1, New Orleans, 1974.

7-3 H. G. Danielmeyer and H. P. Weber, Journal of Quantum Electronics QE-8, 805 (1972).

7-4 K. R Albrand, R. Attig, J. Fenner, J. P. Jeser, and D. Mootz, Materials Research Bulletin 9, 129 (1974).

7-5 H. G. Danielmeyer, J P. Jeser, E. Schonherr, and W. Stetter, Journal of Crystal Growth (1974) to be published.

7-6 R D. Mauer, Proceedings of the Symposium on Optical Lasers (New York, Polytechnic Press), Vol. XIII, 435 (1963).

8.0 SPUTTERED STRONTIUM TITANATE FILMS

8.1 Introduction

At room temperature $SrTiO_3$ crystallizes in the simple cubic perovskite structure and exhibits a dielectric constant of about 300 (Ref. 8-1). Pennebaker has reported on the properties of sputtered $SrTiO_3$ films on metal substrates (Ref. 8-2). A particularly interesting combination for study is $SrTiO_3$ deposited on silicon. This configuration holds potential for the fabrication of high transconductance insulated gate field effect transistors and charge storage memory transistors.

The charge storage memory is a variable threshold field effect transistor with the gate insulator consisting of a dual dielectric layer. When a bias of sufficient magnitude is applied across the dual insulator structure to cause charge transport charges are trapped at sites in the vicinity of the interface of the two insulators. The presence or absence of charge at these traps close to the surface of the semi-conductor has a direct influence on the surface potential of the semiconductor, and hence the threshold voltage of the transistor. The relative thickness of the two insulators determines to a large extent the mechanisms for current transport, and the write and erase speed of the device. Strontium titanate in combination with SiO_2 will permit high fields to be developed across the SiO_2 layer at a considerably lower voltage than for comparable layer structures employing Si_3N_4-SiO_2 or Al_2O_3-SiO_2 (Ref. 8-3,4) and hence lead to considerably lower threshold voltages for switching memory states. See Fig. 8-1 for a comparison of switching voltages for several insulator combinations. MIS (Metal-Insulator-Semiconductor) capacitors with dual insulator gate structures comprised of 1000Å $SrTiO_3$-20Å SiO_2 were fabricated and studied with regard to charge storage characteristics. Insulated gate field effect transistors with the above gate structure were fabricated and evaluated.

8.2 Preparation of MIS Capacitors and Transistors

MIS capacitors were fabricated on 7-10 ohm-cm (100) n-type silicon wafers. The silicon substrates were degreased, stripped of oxide, rinsed in deionized water and spun dry. They were then placed in the vacuum chamber which was evacuated and baked out. The system was then allowed to cool to room temperature and an equilibrium pressure in the low 10^{-8} to 10^{-9} torr was reached.

Substrate temperature was then raised to $600^\circ C$ and 10 microns of ultrapure argon is introduced into the system. The silicon wafers were then sputter cleaned to remove any contamination which may have occurred during the baking of the chamber or which may have been left as residue from the cleaning process. This high tempera-ture sputter cleaning does not degrade the silicon surface as was believed by many workers in the field. MIS transistors made by this technique have high transcon-

FIG. 8-1

COMPARISON OF SWITCHING VOLTAGES FOR SELECTED SiO_2–INSULATOR COMPOSITIONS
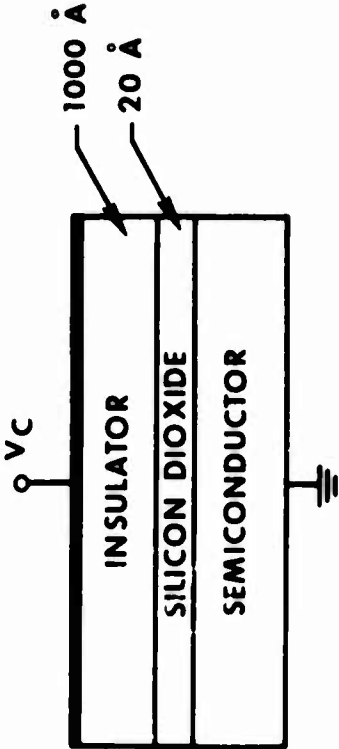
$$E_I = \frac{K_o}{K_I} E_o$$

$$V_C = E_o \left(X_o + \frac{K_o}{K_I} \times X_I\right)$$

INSULATOR	DIELECTRIC CONSTANT	INSULATOR FIELD WHEN SiO_2 FIELD $E_o \sim 7 \times 10^6$ V/CM	V_C–CHARGING VOLTAGE REQUIRED TO PRODUCE $E \sim 7 \times 10^6$ V/CM IN SiO_2	FILM THICKNESS
SiO_2	3.9	7×10^6 V/CM	—	20 Å
Si_3N_4	6.5	4.2×10^6 V/CM	43 V	1000 Å
Al_2O_3	9.5	3×10^6 V/CM	31 V	1000 Å
HfO_2	14	2×10^6 V/CM	21 V	1000 Å
$SrTiO_3$	80	3.5×10^5 V/CM	4.9 V	1000 Å

ductance which would not be the case if the surface mobility had been appreciably degraded by the process. The use of high temperatures during sputter cleaning tends to anneal out damage caused by ion bombardment.

One atmosphere of ultrapure oxygen was then bled into the vacuum chamber and the substrate was maintained at 600°C for one hour. This method reproducibly yields a 19 to 20Å tunnel barrier. Many samples were oxidized in this manner and measured with an ellipsometer. These measurements verified the high degree of reproducibility possible with this technique.

MIS capacitors fabricated with $SrTiO_3$ deposited directly onto the thermal oxide layer generally show only a small degree of charge trapping and the following step was introduced to enhance the flat band voltage shift due to trapping.

A small sputtering target was placed above the wafer which is held at 300°C and 120×10^{-3} torr was bled into the system after the atmosphere has been removed. A target of Ni was used to sputter 50 to 100Å of nitride to obtain a suitable trapping layer between the tunnel barrier and the high dielectric constant gate insulator. The small target was then moved out of the way and 1000Å of strontium titanate was deposited over the trapping layer. The process parameters for the strontium titanate were optimized with respect to overall device characteristics. For example, higher values of dielectric constant could be achieved with higher temperature, post deposition heat treatment. This procedure, however, caused the tunnel barrier to react with the strontium titantate thus degrading the memory effect. The parameters were varied to maximize resistivity and dielectric constant of the gate insulator within the constraints of overall device operation. The best process parameters for the strontium titanate found are the following: 20 millitorr of pure oxygen, substrate temperature of 400°C, a deposition rate of 35 Å/min, and a post deposition heat treatment of 15 min in pure O_2 at 750°C. The post depsotion heat treatment eliminates trapping due to surface states. Gold is alloyed into the back of the wafer to provide an ohmic contanct. Fifteen mil gold or aluminum dots are evaporated through a mask onto the high dielectric constant layer to complete the MIS capacitor.

The transistors were fabricated in the following manner. Boron was diffused into the water to form the source and drain of the transistors. Contact holes were opened up, platinum deposited and alloyed to form the ohmic contacts to the source and drain diffusions. This material will not oxidize, melt, or diffuse during the subsequent high temperature processing. Platinum silicide contacts are used because conventional alloying of aluminum at the end of fabrication, in a vacuum or inert gas can reduce the strontium titanate. Following the formation of the platinum silicide contacts, the gate region was opened and the wafer was placed in the sputtering chamber. The same deposition procedure was followed as with the MIS capacitor with one exception, the trapping layer was omitted. Aluminum was deposited and the gate electrode and contact pads were delineated.

8.3 Results and Discussion

8.3.1 Charge Storage Characteristics of $SrTiO_3$ MIS Capacitors

The deposition parameters for the strontium titanate were dictated by considerations in an attempt to optimize charge retention, switching speed and total flat-band voltage shift and reproducibility of the dielectric constant. Devices fabricated with a dielectric constant of 80 generally gave the best results. The breakdown voltage of the films was $> 2 \times 10^6$ V/cm. Figure 8-2 shows the current field characteristics of a $SrTiO_3$.

As mentioned earlier, structures fabricated with $SrTiO_3$ deposited directly on SiO_2 did not show an appreciable shift in flat-band voltage ($\sim 2V$). The switching and memory retention of a charge storage device depends on the nature of the trapping sites in the vicinity of the insulator-silicon dioxide interface. considerations, such as trap density, the spatial distribution of traps, and their distribution in energy affect device characteristics and are intimately related to the material combined with the silicon dioxide tunnel barrier. This is exemplified by the widely different switching characteristics of memory states exhibited by charge storage devices fabricated from silicon nitride-silicon dioxide (MNOS) (Ref. 8-3) and aluminum oxide-silicon dioxide (MAOS) (Ref. 8-4). In the aforementioned devices, device characteristics were optimized by variations in th deposition conditions of the insulating film.

A novel approach to the introduction of trapping centers was undertaken during the course of this study. It involved the sputtering of 50-100Å of a third material at the insulator-SiO_2 interface. The motivation to this approach was that the advantages of the high dielectric constant of $SrTiO_3$ could be retained in combination with the trapping characteristics of the material introduced. Experiments were performed where the interface layers of selected transition metal nitrides, carbides and sulfides were introduced by reactive sputtering. The choice of these materials was based primarily on the availability of pure metal targets and the ease of obtaining pure gases which allows synthesis of the compounds by reactive sputtering. A wide range of trapping characterisitics were observed and results obtained indicate that sputtering of "interface states" is a viable approach to the problem. See Appendix IV for additional data on HfO_2-SiO_2 structures with sputtered interface states.

The best results overall were obtained with 50Å of nickel nitride sputtered at the interface of 20Å SiO_2-1000Å $SrTiO_3$. The threshold for charge transfer was determined to be 6V in close agreement with the predicted value for a tunneling of charge through a 20Å SiO_2 barrier in combination with a 1000Å film with a dielectric constant of 80. The hysteresis in the capacitance-voltage characteristics (Fig. 8-3) show the shift in flat-band voltage for a dc bias ranging between +15 and -15V. The

FIG. 8-2

CURRENT-FIELD CHARACTERISTICS OF SrTiO₃

FIG. 8-3
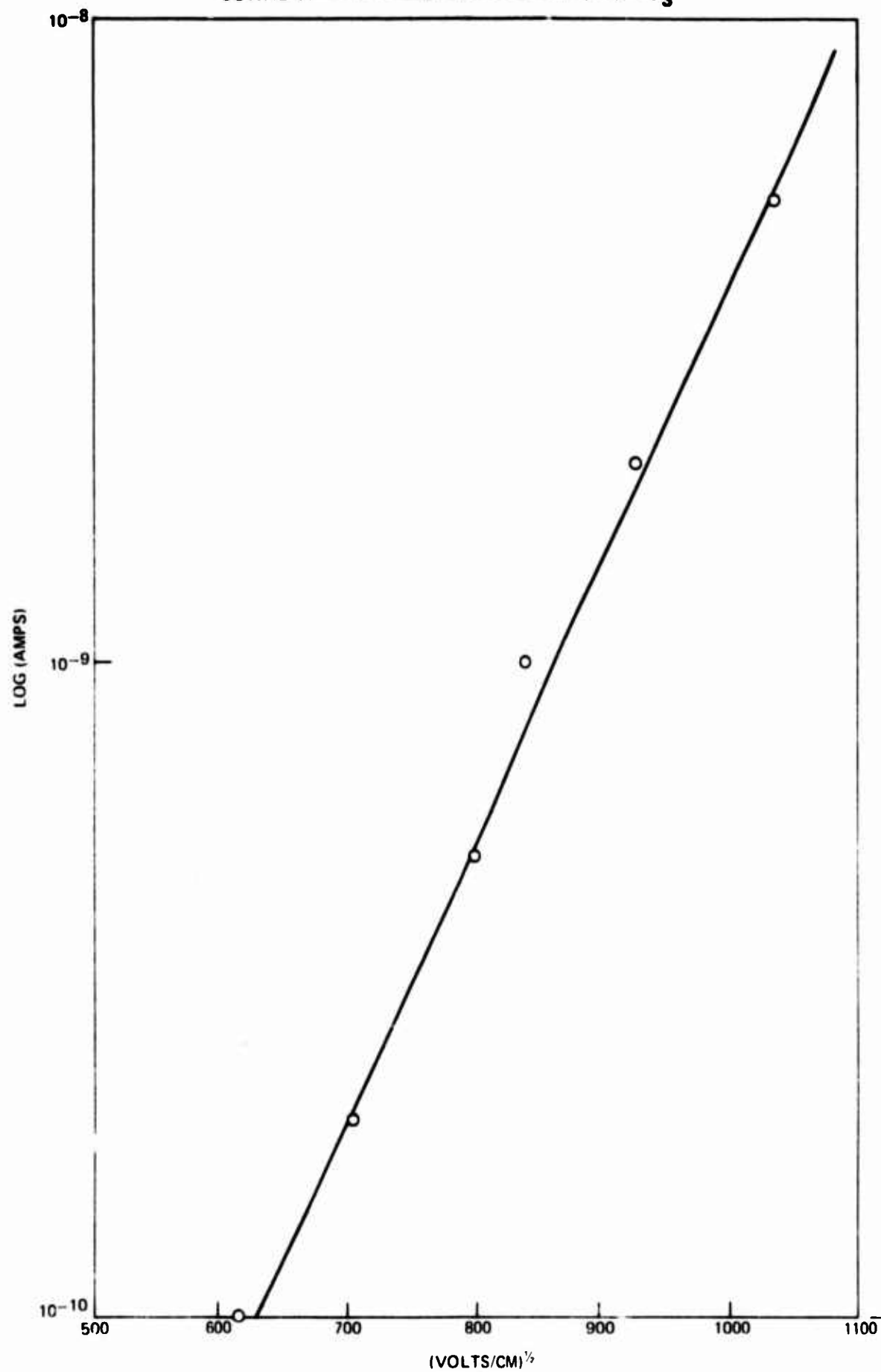
C-V CHARACTERISTICS OF 1000Å Sr Ti O₃ – 20 Å SiO₂ ON 10 Ω – CM n–TYPE SILICON
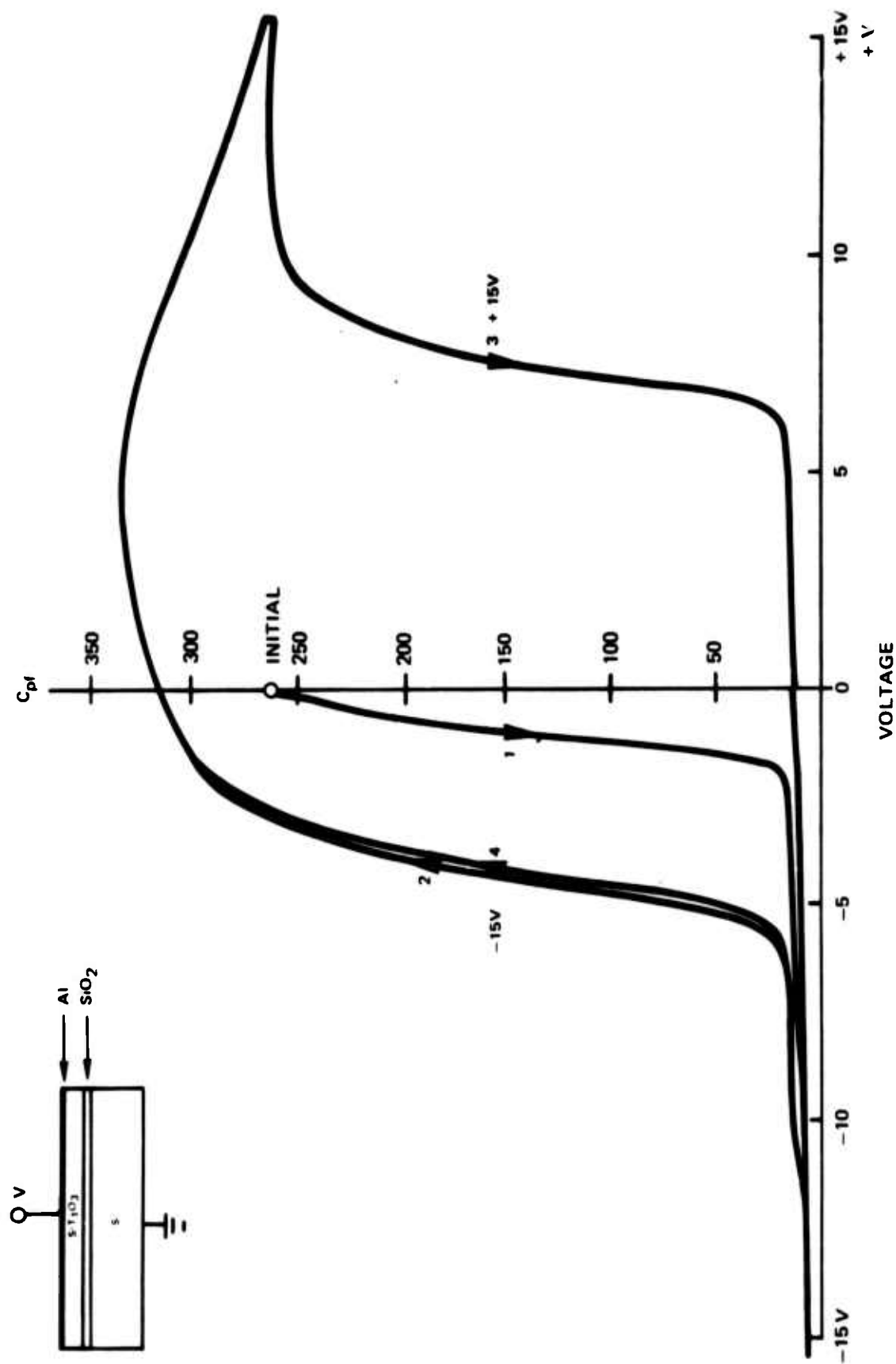
overall flat-band voltage shift is 11V. charge transfer characteristics are asymmetric under pulse bias. The flat-band voltage is shifted more readily by positive pulses applied to the gate. A flat band voltage shift of 1V could be obtained for +15V, 200 nsec pulses but a 20 μsec, -20V pulse is required to restore it to its initial state. The shift in flat band voltage to more positive values for positive pulses applied to the gate electrode is indicative that charge transfer is by tunneling of electrons from the n-type silicon into the traps at the interface. Flat-band voltage shifts as a function fo pulse duration and amplitude for positive pulses is illustrated in Figs. 8-4 and 8-5. The asymmetry in switching characteristics for positive and negative pulses is probably indicative of the asymmetric disposition of the trap levels with respect to the condution and valence bands of the silicon. The longer pulse duration required to clear the electrons from the traps is probably due to redistribution of charge away from the interface, which would require a longer time to clear the charge. The charge storage duration was less than a day. Devices charged to a flat band voltage of +5V decayed to near zero in about 24 hours. It is certain that device performance could be improved with regard to charge retention and switching characteristics. It must be emphasized that the results presented are based upon a limited investigation of sputtered interface states and that additional work is required to arrive at a better understanding of interface trap control.

8.3.2 Strontium Titanate Field-Effect Transistor

Insulated gate field effect transistors were fabricated using sputtered strontium titanate for the gate dielectric. The gate was a dual insulator structure comprised of 20Å of thermally grown silicon dioxide overladd with a 1000Å of sputtered strontium titanate. To our knowledge the devices fabricated in this manner may have the highest transconductance for an insulated gate field effect transistor of equivalent geometry and operating voltage. The transistors were p-channel devices fabricated on 10 Ω-cm n-type, (100) silicon. The channel length was 6 microns and the channel width was 30 microns. A transconductance of approximately 300 μmhos was obtained at a gate voltage of -2.0V and drain voltage of -1.5V. The effective dielectric constant of the composite gate insulator was 52, approximately 13 times greater than that of silicon dioxide. The transconductance is directly proportional to the dielectric constant. Turn on voltage for the transistors was -1.1V. Stability of the transistors under bias and temperature stress was good provided the bias voltage was kept below five volts. Gate voltages in excess of five volts resulted in some charge transfer and trapping at the SiO_2-$SrTiO_3$ interface. A shift in device threshold therefore resulted. The transfer characterisitcs are shown by Fig. 8-6. Figure 8-7 depicts the $SrTiO_3$ IGFET. The low voltage restriction on gate voltage may pose a problem for practical applications. Threshold voltage shifts of close to two volts may occur if the 5V bias level is exceeded.

8.4 Conclusions

(1) A dual insulator structure of 1000Å $SrTiO_3$-20Å SiO_2 has a low threshold voltage

PULSE DURATION VERSUS FLAT-BAND VOLTAGE SHIFT WITH PULSE AMPLITUDE AS A PARAMETER

FIG. 8–5
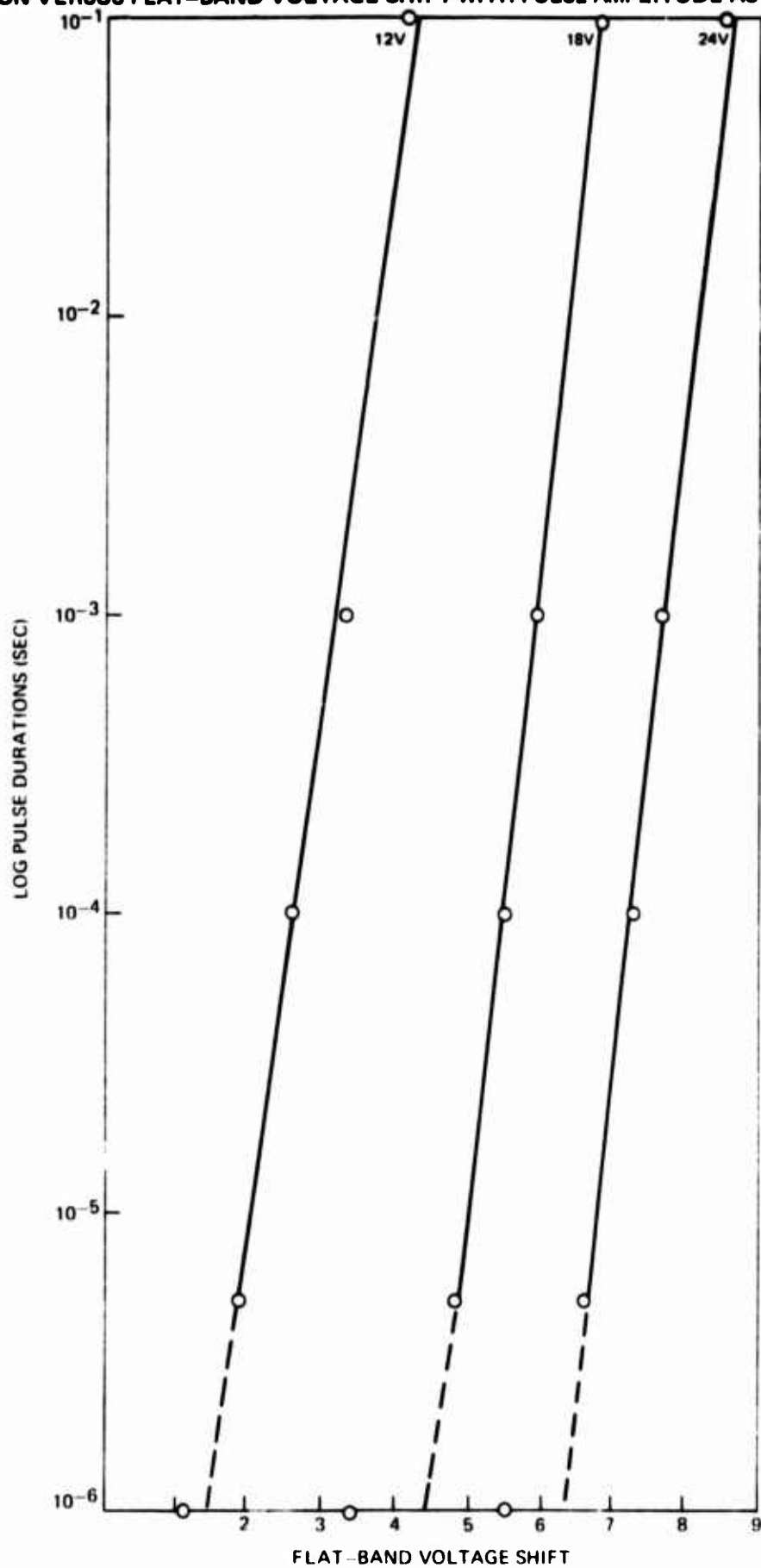
FLAT–BAND VOLTAGE SHIFT VERSUS PULSE VOLTAGE WITH PULSE LENGTH AS A PARAMETER

FLAT-BAND VOLTAGE SHIFT

FIG. 8-7
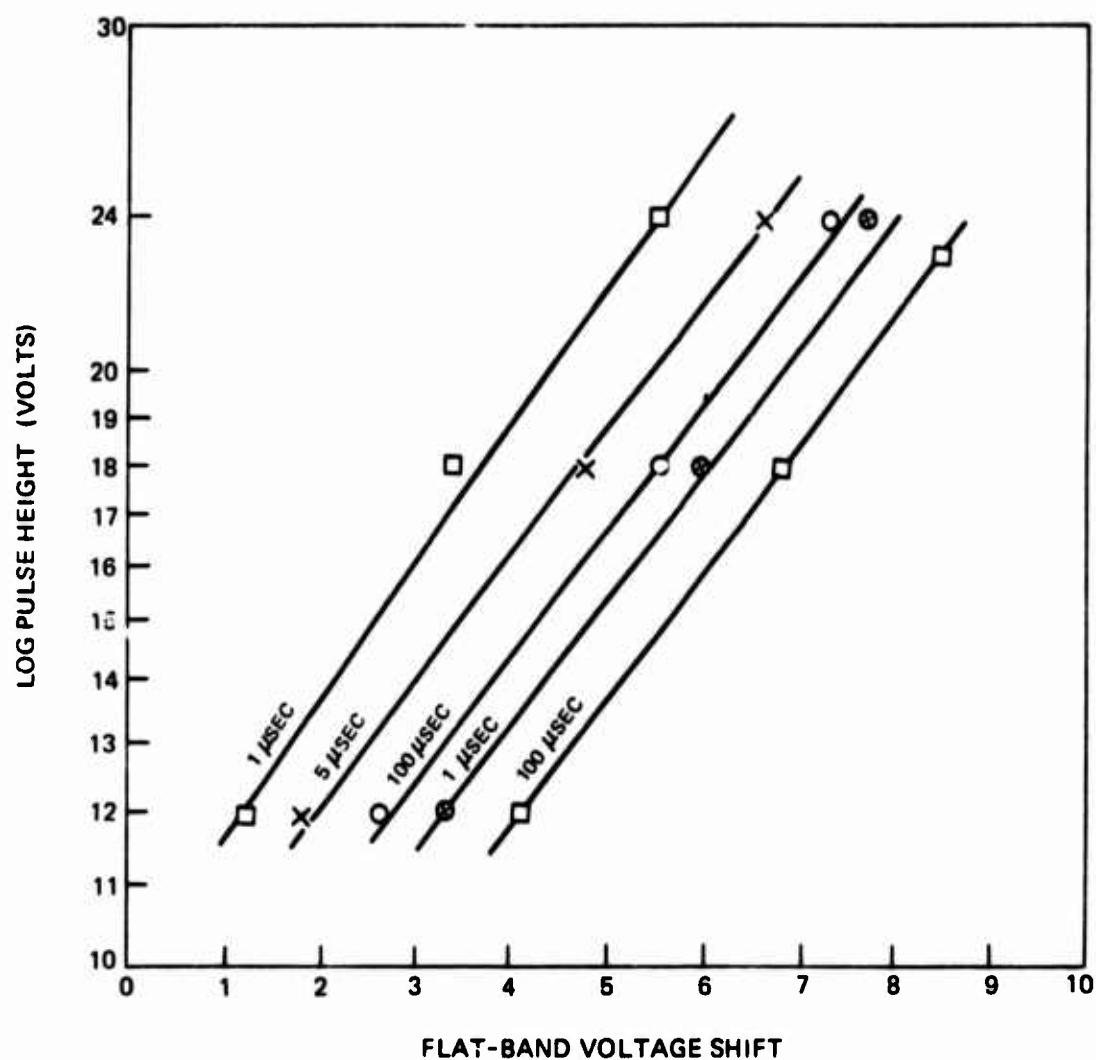
STRONTIUM TITANATE -IGFET

FIG. 8-6

TRANSFER CHARACTERISTICS OF SrTiO$_3$ - IGFET

GATE VOLTAGE (-0.2 VOLTS/STEP)
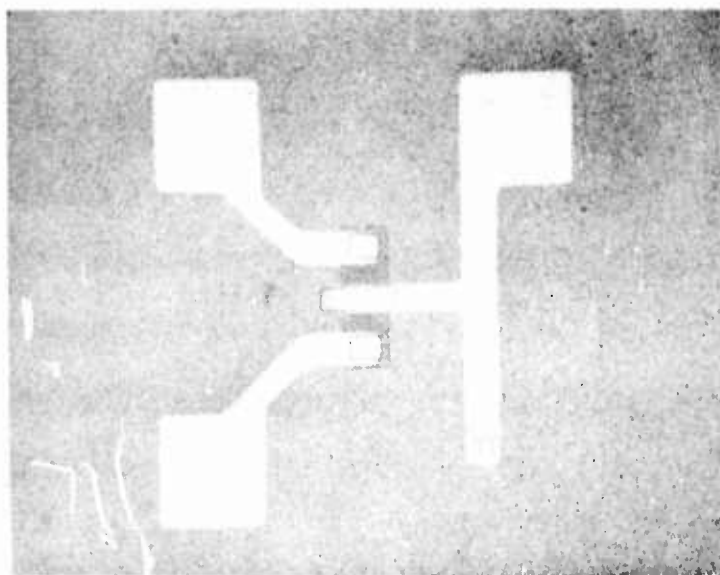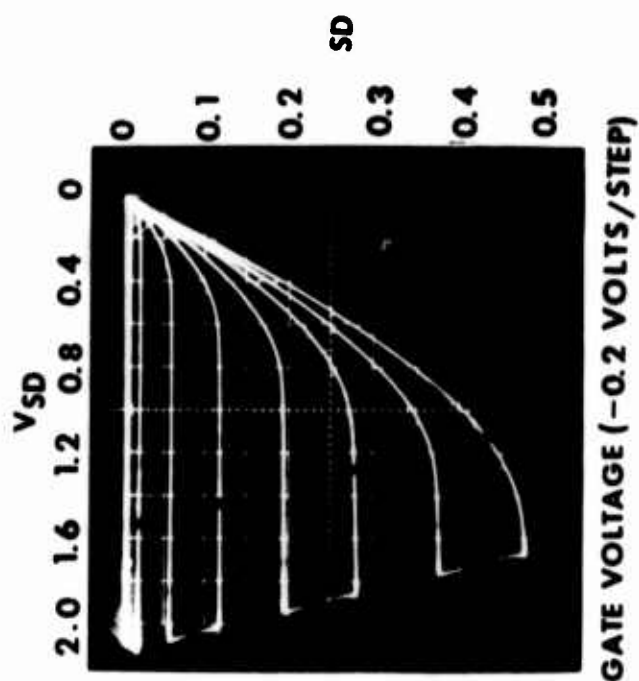
($\sim$5V) for transfer of charge to traps at the $SrTiO_3$-SiO_2 interface. Charge storage of current devices needs further improvement to enhance retention time.

(2) The sputtering of a third material at the $SrTiO_3$-SiO_2 interface has been proven to be a practical means of affecting charge trapping of these devices. Further work is required for device optimization.

(3) High transconductance, low threshold voltage, small geometry $SrTiO_3$ transistors can be fabricated by rf sputtering. Gate voltages must be restricted to values less than five volts to prevent threshold voltage shift due to charge trapping.

8.5 REFERENCES

8-1   Linz, A., Phys. Rev., 91, 753, (1953).

8-2   Pennebaker, W. B., IBM J. Res. Devel., 13, 686 (1969).

8-3   Wallmark, J. T., and J. H. Scott, RCA Rev., 30, 335, (1969).

8-4   Wada, T., K. Onoda, H. Ishiguro, and S. Nakanuma, IEEE J. Solid-State Circuits, SC-7, 375, (1972).

APPENDIX I

SUBSTRATE PREPARATION

The substrates used in this program for growing ZnO, AlN, TiO_2 and GaN were commercially procured single crystals of sapphire lithium niobate, magnesium aluminum spinel and silicon carbide.

The sapphire and the spinel were purchased from INSACO in wafer form and the surface finish was specified as 1 microinch. The lithium niobate was purchased from Linde also in polished wafer form. Figure AI-1 is an electron microscope surface replication of a typical as received sapphire substrate. Initially the sapphire was etched in 350°C phosphoric acid and subsequently annealed at 1200°C in air for two hours to remove polishing damage. However this proceedure seemed to add nothing significant to the quality of the film grown. This proceedure was later discontinued in favor of the following which yielded consistently clean substrates and apparently good surfaces for epitaxial growth. This proceedure was also used for the preparation of lithium niobate and magnesium aluminum spinel.

    i.   degrease in hot MOS grade trichloroethylene - several rinses
    ii. heat in H_2SO_4 until boiling commences, then let cool to room temperature
   iii. flush well in deionized water
    iv. dry in a stream of dry nitrogen

The silicon carbide substrates were random size unpolished crystals purchased from Norton Co. These substrates were prepared in the following manner.

    i.   degrease in hot MOS grade trichloroethylene - several rinses
    ii. etch in HF about 3 minutes to remove any SiO_2
   iii. flush well in deionized water
    iv. dry in a stream of dry nitrogen

Substrates were prepared as required for use and introduced directly into the sputtering chamber after cleaning. The chamber was then immediately evacuated.

TYPICAL AS RECEIVED SURFACE OF SAPPHIRE SINGLE CRYSTAL SUBSTRATE
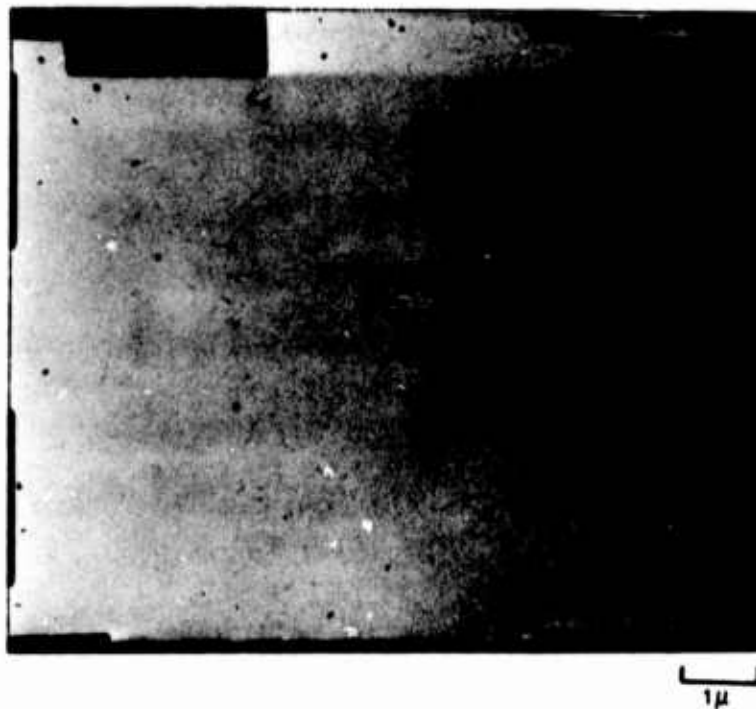
APPENDIX II

SUBSTRATE TEMPERATURE DETERMINATION

INTRODUCTION

One of the more difficult pieces of data for the experimenter in thin film vacuum deposition to obtain is substrate temperature during film growth. A common situation is found where a film is to be grown on one side of a planar substrate. The substrate surface must be exposed to the deposition source; therefore, the heating of the substrate must be arranged so as not to interfere with the line of sight path of the deposit. Systems utilizing radiation exclusively for heating and temperature monitoring must operate in the region where the substrate is strongly absorbent. For sapphire, this would require optics and energy source operating above 7μ wavelength. Systems operating above 7μ can be assembled and probably represent the ultimate in accuracy and cleanliness but at a cost which far exceeds the cost of performing the calibration outlined below.

The most common method of substrate heating is to place the substrate in contact with a solid heat source at the temperature desired. Various methods are used to insure that the substrate is at the same temperature as the source. Substrates can be held to the heater by gravity, mechanically clamped, or bonded with some good heat transfer medium. The most satisfactory method to ensure that the substrate follows the heater temperature is through the use of a bonding material. However, this method suffers from the fact that almost any bonding material will have an appreciable vapor pressure at elevated temperatures, thereby constituting a serious source of contamination.

EXPERIMENT

Through a series of experiments which involved the normal operations of loading the substrate in the deposition chamber and pumping down, we have found that a substrate simply held by gravity on a heater, while not necessarily achieving the same temperature as the heater, will repeatedly come up to very nearly the same equilibrium temperature. This says that correlation between the heater and the substrate temperatures does exist of sufficient reliability to generate a calibration curve. The process is more accurate at elevated temperatures. Figure AII-1 is a plot of the average substrate temperature as a function of the average heater temperature for the data taken in the vicinity of 1150°C heater temperature. Each point is the average of two substrate and three heater temperatures. The heater temperatures were taken next to each substrate and in between them. The substrates were silicon wafers and the heater was a flat tantalum strip, both about 0.025 cm thick. Temperature measurements were made through a pyrex window with an optical pyrometer.

REPEATABILITY OF SILICON SUBSTRATE TEMPERATURES
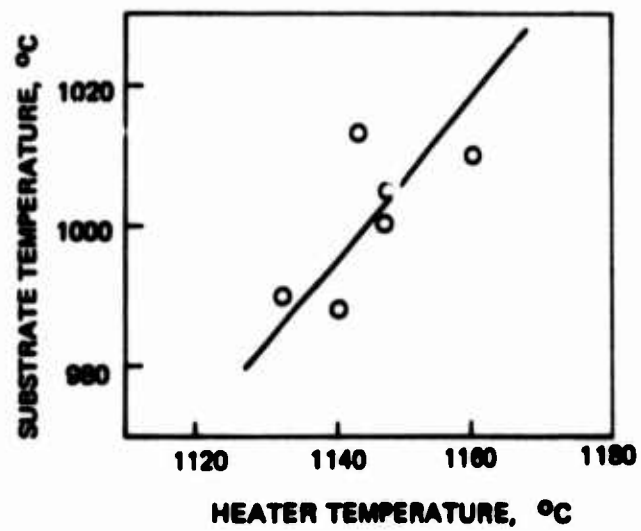
The problem of determining the temperature of transparent sapphire substrates becomes more complicated since an ordinary optical pyrometer cannot be used. The use of a thermocouple somehow attached to the substrate to perform a temperature calibration always leaves some doubt as to the quality of the contact or as to just what the thermocouple is measuring. The correlation between heater temperature and sapphire substrate temperature was established by measuring the change in length of a 0.051 cm thick c-axis oriented sapphire substrate for a given heater temperature. The substrate temperature was then inferred from values of the thermal linear expansion for sapphire parallel to the a-axis.

The heater was a tantalum strip heater, identical to those used in the earlier protion of this program. The heater temperature was determined with an optical pyrometer at temperatures above $800^{\circ}C$ and with a chromel-alumel thermocouple spot welded to the heater strip at temperatures below 800 C. At $800^{\circ}C$, agreement between the two was within $5^{\circ}C$.

The length measurements were made with a cathetometer capable of reading to 0.001 cm. Observed changes in sapphire length ranged from about 0.010 cm at $250^{\circ}C$ substrate temperature to 0.094 cm at $1400^{\circ}C$ substrate temperature. Observations were made in a nitrogen ambient at gas pressures of less than 2×10^{-3} Torr, 10^{-2} Torr, and 10^{-1} Torr. The thermal expansion data for c-axis oriented sapphire[1] used for this study are presented in Fig.AII-2. The calibration curves resulting from these measurements are shown in Fig. AII-3.

DISCUSSION

All curves lag the heater temperature considerably at the lower temperatures but rapidly approach it for heater temperatures above $1000^{\circ}C$. As expected, the low temperature lag is greater for lower gas pressures. As illustrated in Fig.AII-3, the effects of pressure are most pronounced between 2mTorr and 10mTorr. This points up the need for careful monitoring of the gas pressure during calibration and subsequent use when operating below 10mTorr.

A thin Al_2O_3 slide is sometimes used as a liner to reduce substrate contamination from the heater. At higher temperatures, the liner appears to cause a slight reduction of substrate temperature as compared to that obtained with the bare heater. A possible explanation of this phenomenon is that a high temperatures, where the principal method of energy transfer from the heater to the substrate is by radiation, the Al_2O_3 slide acts like an inferior intermediate radiator.

In practice, then, all one needs to do after determining the calibration curve is to monitor the heater temperature either with a thermocouple or an optical pyrometer and the substrate temperature can be deduced. Clearly, this calibration scheme can be used for any other substrate material for which thermal expansion data is known. However, it finds particular application for those materials which are transparent in the visible region.

LINEAR THERMAL EXPANSION OF SINGLE CRYSTAL Al₂O₃ PARALLEL TO THE A—AXIS. (REF. AII—1)
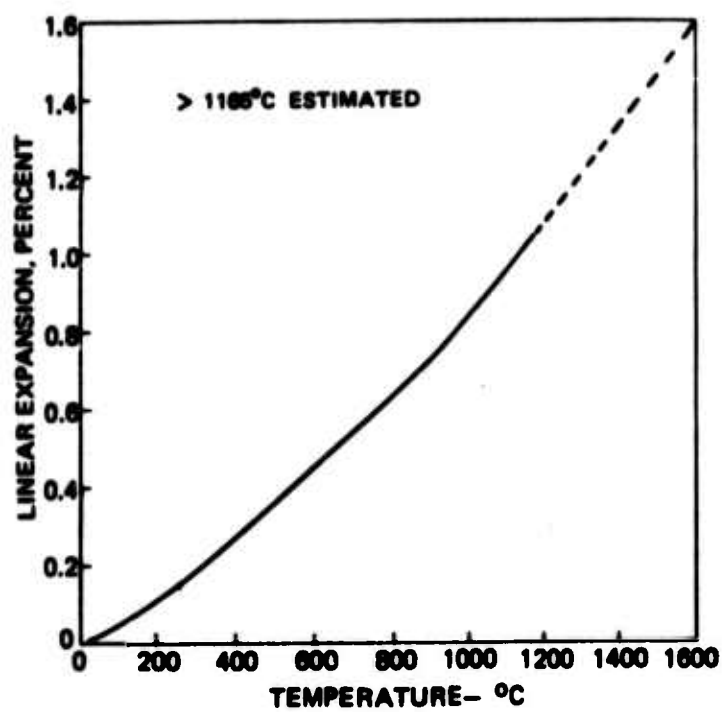
SAPPHIRE SUBSTRATE TEMPERATURE AS A FUNCTION OF
TANTALUM HEATER TEMPERATURE
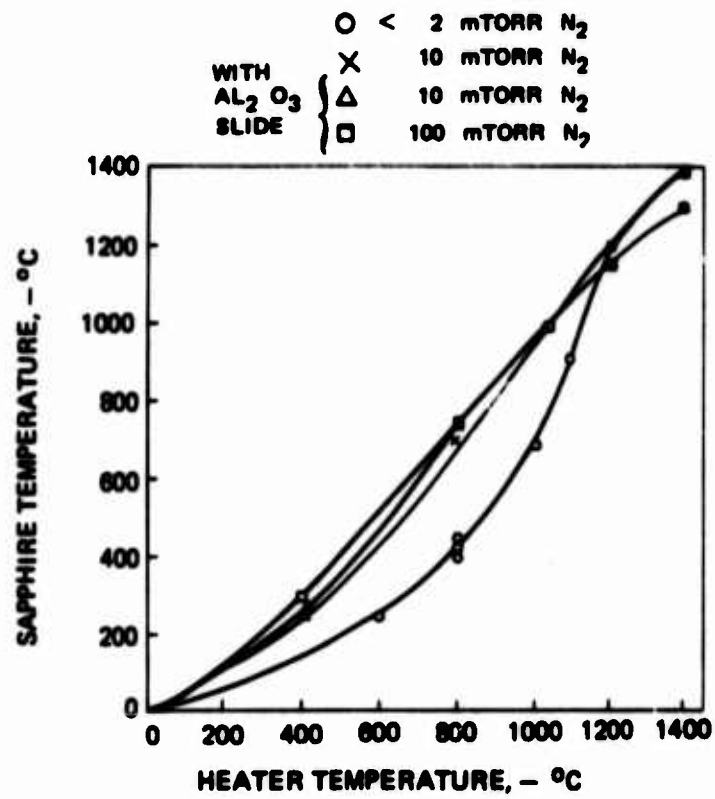
When looking through the published thermal expansion data for single crystal alumina, we were struck by the appreciable variation in the results among the various investigators (Ref.AII-1,2). The variation was particularly pronounced at high temperatures. At 1165°C, for example, it is estimated that the Wachtman, et.al. data is about 11.9% lower than the Campbell and Grain data for expansion parallel to the a-axis. The result of this is that for a heater temperature of 1200°C, the Campbell and Grain data implies a sapphire temperature of 1165°C for the expansion in one of the cases we measured. However, the Wachtman et.al. data implies a sapphire temperature of 1276°C which is inconsistent with out results. Our data tends to support the thermal expansion data of Campbell and Grain.

REFERENCES

AII-1. W. J. Campbell and C. Grain, "Thermal Expansion of Alpha-Alumina", U. S. Bur. Mines Rept. Invest., No. 5757 (1961).

AII-2. J. B. Wachtman, et.al., J. Amer. Ceram. Soc., 45 (7) 319 (1962).

APPENDIX III

TECHNIQUES FOR THIN FILM OPTICAL WAVEGUIDE EVALUATION

Facilities were setup for the study of optical waveguiding in thin films. Lasers covering the range of the spectrum from $0.633\mu m$ (red) to $3.39\mu m$ (infrared) were employed to characterize the waveguiding qualities of the films grown. Provisions were made for obtaining accurate attenuation measurements. Both prism and grating coupling techniques have been investigated. A series of amorphous Ta_2O_5 films were grown on glass substrates to provide samples with which to learn the experimental techniques of coupling to a thin film waveguide. In addition to the experimental studies, two computer programs were written to aid in the evaluation of the waveguide films and to serve as guides in the processing of the films.
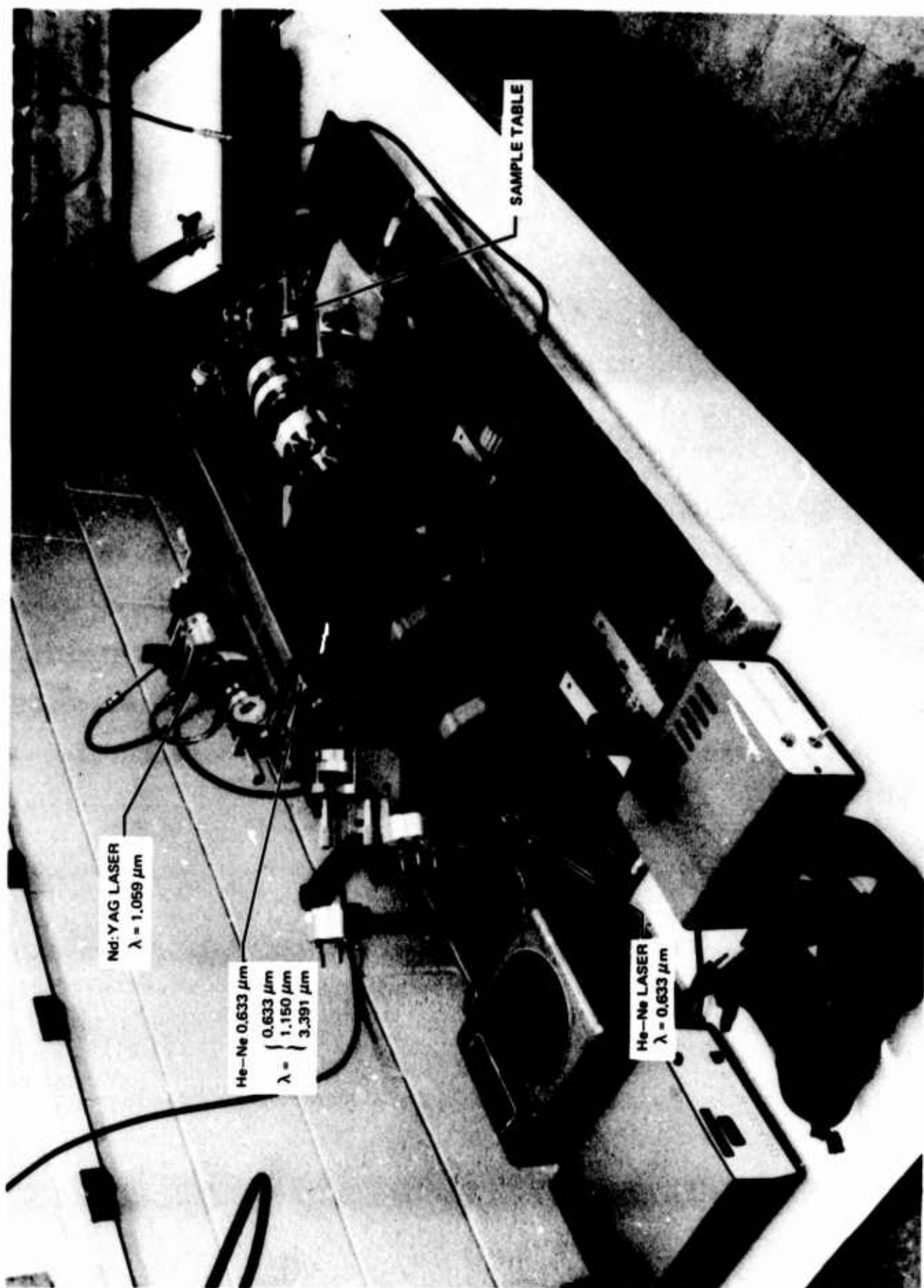
APPARATUS FOR OPTICAL WAVEGUIDE EVALUATION

A photograph of the apparatus used for study in waveguiding in thin films is shown in Fig. AIII-1. A small 0.5mW, $0.633\mu m$, HeNe laser is used for alignment purposes and for rough evaluation of newly made films. The larger He-Ne laser, with a stable output of 15mW at $0.633\mu m$, is used for most attenuation measurements. This unit has also been converted for use at $1.50\mu m$ and $3.391\mu m$, however, the output at these wavelengths proved to be too low for use in this study. A homemade Nd:YAG laser with an output of over 100mW at $1.059\mu m$ provided ample light for visual observation of the films using a small battery powered Varo infrared to visible converter. The ability to actually observe the guided wave via the converter greatly simplified the procedure of examining the films for waveguiding.
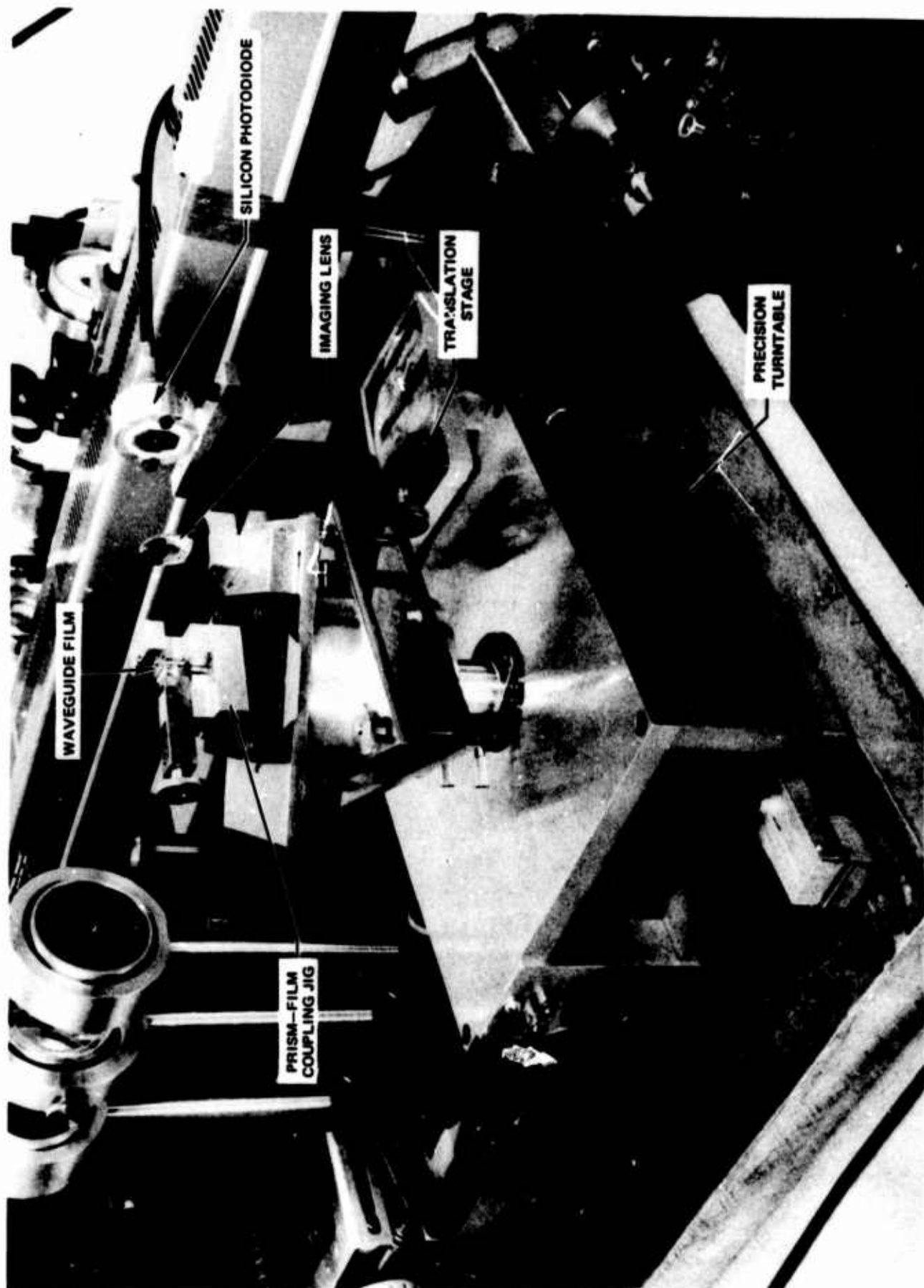
The sample table and attenuation measuring apparatus is shown in greater detail in Fig. AIII-2. A waveguide film on a small substrate is shown mounted in the prism-film coupling jig on top of the turntable. Provisions were made for properly orienting the plane of the film with respect to the laser beam. Light from one of the lasers was focused onto the coupling prism by a simple lens. The beam also passed through a polarizer and a 0.5° wedge that could be rotated about a horizontal axis and thus used to scan the prism-film contact region in a vertical direction. Angular resolution of the turntable was $\sim 0.01^{\circ}$ making possible accurate determination of the angles at which light is coupled into the film.

Light can be coupled into thin films using prisms or gratings, or the laser beam can be focused onto a cleaved or tapered edge of the film to obtain guiding. Prism and gratings have the advantage that any desired mode of light-wave propagation can be efficiently and selectively excited, and the difficult problem of focusing the beam onto the film edge is avoided. Attempts were made to edge

FIG. III—1

APPARATUS FOR STUDYING WAVEGUIDING IN THIN FILMS

SAMPLE TABLE

Nd: YAG LASER
$\lambda = 1.059 \ \mu m$

He—Ne 0.633 μm
$\lambda = \begin{cases} 0.633 \ \mu m \\ 1.150 \ \mu m \\ 3.391 \ \mu m \end{cases}$

He—Ne LASER
$\lambda = 0.633 \ \mu m$

FIG. III-2

SAMPLE TABLE & ATTENUATION MEASURING APPARATUS

couple 1.059μm light into a sputtered GaAs film; however, waveguide modes were not detected. The prism-film coupler was more widely used in the present study. The small jig shown in Fig. AIII-2 was used to apply pressure between the coupling prism and the thin film. A small round rod beneath the substrate, located $\sim$ 1mm back of the right angle corner of the prism (see Fig. IIIA-3), was used to local-ize the pressure between the prism and film and thus reduce the air gap between prism and film to a thickness small enough ($\geq \lambda/4$) for efficient coupling (Refs. AIII-1,2). This restriction on the size of the gap can be relaxed some-what by using an index matching fluid. For a given gap spacing, the addition of an index matching fluid will increase the coupling efficiency and these fluids have been used for just that purpose. The prisms used in this effort are 35° and 45° rutile prisms cut with the C-axis parallel to the right angle edge of the prism, and 45° SF61 glass prisms. With these prisms, waveguide modes with propa-gation constants (β/k) values as high as 2.37 for TM modes and 2.60 for TE modes can be accessed.

The facilities for fabricating photoresist grating couplers by an optical interference technique (Ref. AIII-3) are available and gratings have been produced with a periodicity of 0.5μm. Such gratings have been fabricated on Ta_2O_5 wave-guide films, but were not used extensively because of the simplicity and convenience of the prism-film coupling technique.

Attenuation measurements have been made in two ways. Originally, these measurments were made using a fiber optic technique similar to that described by Goell and Standley (Ref. AIII-4). One end of an 0.5mm dia. optical fiber is mounted on an x-y-z micro-positioner such that it can be positioned close (< 1mm separation) to the surface of the waveguide film and traversed in the plane of the film. The other end of the fiber is rigged so that the light output falls on the cathode of the photo-multiplier of a Pritchard photometer. The fiber optic probe is then used to measure the intensity of the light scattered from the guided beam as a function of distance along the beam. From this data the attenu-ation of the film in dB/cm, can readily be obtained. This method works well when large substrates are used. Many of the films in this study were grown on rather small substrates to conserve expensive substrate material and, under these conditions, the fiber optic probe technique is unsatisfactory.

An alternative method of measuring the light scattered from the guided mode uses a simple lens to form an image of the light streak in the film and a narrow slit in front of a photodetector is then scanned along the image (Ref. AIII-1). The experimental setup of this method is shown in Fig. AIII-2 and is illustrated schematically in Fig. AIII-3. A mechanical chopper modulated the laser beam and a phase sensitive amplifier was used to recover the low level signal from the photodetector. Corrections for image size were not necessary when a true size image was generated.

FIG. III-3

EXPERIMENTAL SETUP FOR OPTICAL ATTENUATION MEASUREMENTS
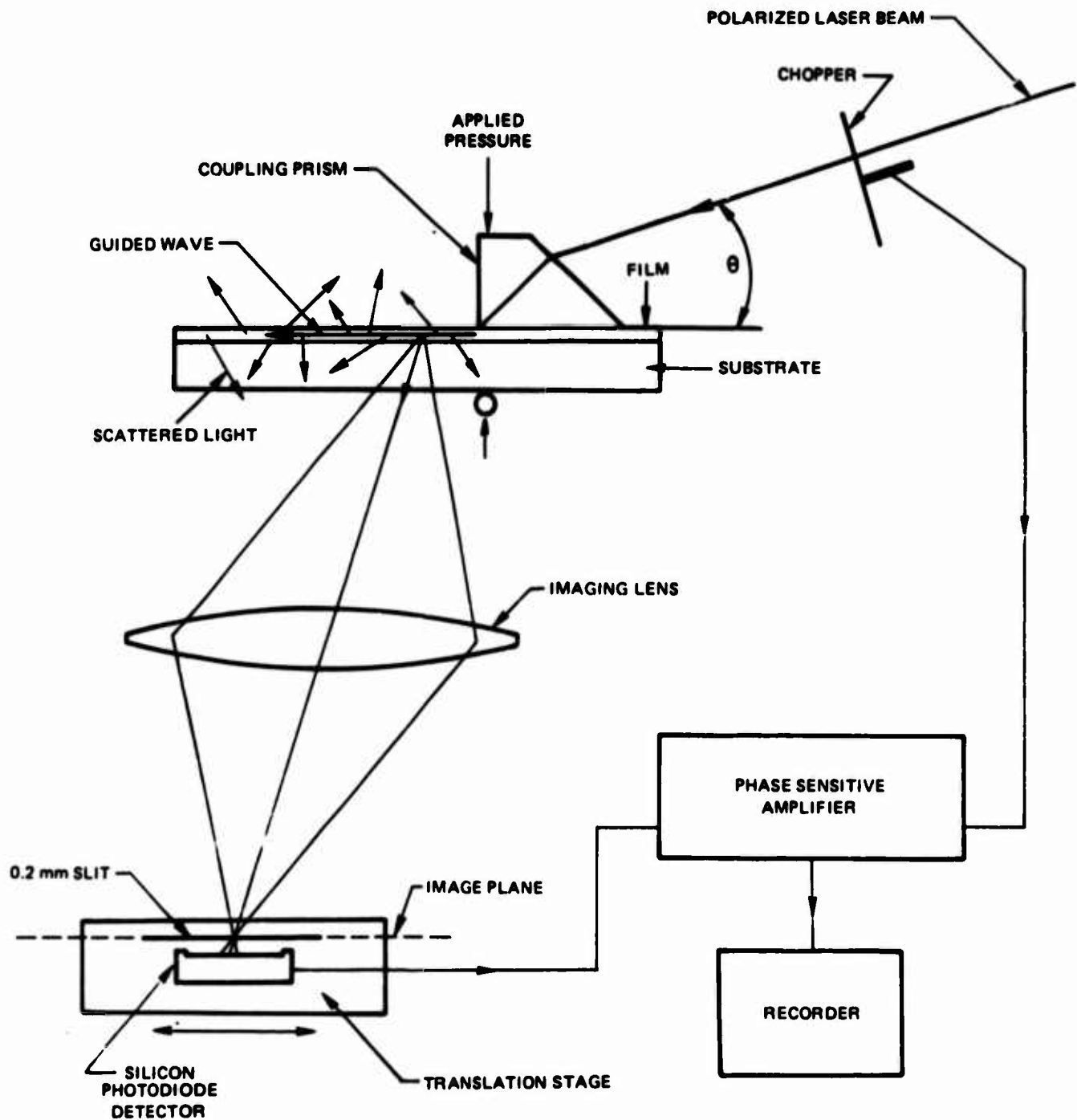
It was assumed, in using either of the two methods outlined above, that the scattering centers were uniformly distributed in the film. Both methods work well for losses as low as 1dB/cm. Below 1dB/cm, the variability in the location and strength of the scattering centers makes reliable measurements difficult. Measurements made on several Ta_2O_5 films using both methods showed good agreement. Losses for these films were typically 3dB/cm with some Ta_2O_5 films showing losses as low as 1dB/cm as reported by Tien (Ref. AIII-1).

COMPUTATIONAL AIDS TO THIN FILM WAVEGUIDE STUDIES

A knowledge of the angle and polarization of the incident laser beam for which guided modes are obtained in a given film enables one to compute the refractive index (N_F) and thickness (W) of that film. A computer program was written to perform this calculation. Using an estimated index as a starting point, the computer calculated a film thickness for each mode observed. The mean thickness and deviation were then calculated, and the computer then iterated on the index until the thickness deviation was minimized. This method provides an accurate way of determining both N_F and W of a thin film waveguide. Accuracies of 1% for N_F have been obtained (Ref. AIII-1).

In cases where the film supported only one waveguide mode, or only one mode could be coupled into the film because of prism or grating limitations, N_F and W can still be determined with the aid of another computer program written for this study. This second program computes the allowed modes for a film of given N_F and W. The $N_F \cdot W$ product of the film was first determined from measurements of the transmitted or reflected intensity versus wavelength. A series of computations were then made using values of N_F and W that gave the correct $N_F \cdot W$ product. The propagation constant, β/k, was then plotted versus N_F and the value of β/k for the observed mode used to pinpoint the tru N_F and W. This method was used for many of the TiO_2 films since they usually are only $\sim 0.5\mu m$ thick and often only 1 or 2 guided modes were observed.

REFERENCES

AIII-1. P. K. Tien, App. Opt., <u>10</u>, 2395 (1971).

AIII-2. The authors are indebted to Dr. Fritz Zernike of Perkin-Elmer Research Laboratories for his assistance during the initial stages of the optical waveguiding study.

AIII-3. M. L. Dakss, L. Kuhn, P. F. Hendrich and B. A. Scott, Appl. Phys. Lett., <u>16</u>, 523 (1970).

AIII-4. J. E. Goell and R. D. Standley, B.S.T.J., <u>48</u>, 3445 (1969).

Charge storage characteristics of MIS structures employing dual-insulator composites of HfO$_2$-SiO$_2$ and SrTiO$_3$-SiO$_2$ [†]

A. J. Shuskus, D. J. Quinn, and D. E. Cullen

United Aircraft Research Laboratories, East Hartford, Connecticut 06108

(Received 30 April 1973)

Two MIS versions have been fabricated employing rf-sputtered dual insulator structures comprised of 1000 Å HfO$_2$-20 Å SiO$_2$, and 1000 Å SrTiO$_3$-20 Å SiO$_2$. The high-dielectric-constant insulators in combination with a 20-A layer of silicon dioxide permit the transfer of charge by tunneling into traps at the dual-insulator interface to occur at considerably lower voltages than comparable structures employing silicon nitride or aluminum oxide. It was found that trap density and, hence, the degree of flat-band voltage shift could be altered by sputtering 50-Å layers of selected materials at the insulator-SiO$_2$ interface. The devices employing hafnium dioxide show promise in an application as a nonvolatile electrically alterable memory element. Although the strontium titanate devices exhibit a low threshold voltage for onset of charge transfer, the charge retention characteristics are poor.

Controlled charge storage in the gate dielectric of an insulated gate field effect transistor has been utilized as a nonvolatile electrically alterable store for digital data. Typical gate insulator structures reported to date consist of 10−100 Å of SiO$_2$ overlayed with 300−1000 Å of a second insulator. The SiO$_2$-Si$_3$N$_4$[1,2] and SiO$_2$-Al$_2$O$_3$[3,4] dual insulator structures have been at the focus of most studies. One major drawback of the above insulator combinations is the high operating voltage required for switching of memory states. In principle, the combination of a high-dielectric-constant insulator with silicon dioxide should yield devices with lower operating voltages since high electric field values can be developed across the silicon dioxide at a much lower voltage impressed across the MIS structures. A comparison of voltages V_c required for the onset of charge transfer with different insulator-SiO$_2$ combinations for a common structure is shown in Fig. 1. E_0, x_0 and E_i denote the field and thickness of the oxide and insulator, respectively. The dielectric constant values quoted for HfO$_2$ and SrTiO$_3$ are those obtained for sputtered films. An electric field intensity of 7×10^6 V/cm is assumed for tunneling of charge across the Si-SiO$_2$ barrier. Although the calculation is simplistic, it is found that it presents a valid basis of comparison for various insulator combinations. The results for the dual insulator combinations of HfO-SiO$_2$ and SrTiO$_3$-SiO$_3$ presented below tend to bear this out.
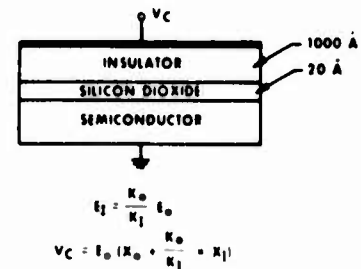
MIS capacitors were fabricated on 7- to 10-Ω cm (100) n-type silicon wafers. The 20-Å SiO$_2$ tunnel barrier was formed by thermal oxidation of the substrates in the vacuum system. The procedure used was the following.

Silicon wafers were placed in the vacuum system and the system was evacuated to 10^{-7} Torr. The substrate temperature was raised to 600 °C and sputter cleaned in 10 μ of ultrapure argon. 1 atm of oxygen was bled into the system, and the substrate was maintained at 600 °C for 1 h. The method reproducibly yielded a 20-Å silicon dioxide layer.

After preparation of the thermal oxide layer, 1000 Å of hafnium dioxide or strontium titanate was rf sputtered to complete the composite insulator. The hafnium oxide was prepared by reactive sputtering, and the SrTiO$_3$ was a ceramic target sputtered in an oxygen ambient.

Samples were then annealed in oxygen at 800 °C for 15 min, Ohmic contacts were alloyed to the back side, and 10-mil-diam aluminum dots were evaporated to complete the MIS structures.

Samples prepared in this manner with hafnium dioxide exhibited negligible flat-band shift up to bias levels approaching breakdown. Charge trapping characteristics of the devices could be modified by the sputtering of a third material at the SiO$_2$-insulator interface. In the fabrication of HfO$_2$-SiO$_2$ structures, the process was modified to reactively sputter hafnium nitride at a rate of 10 Å/sec for 5 sec onto the SiO$_2$ tunnel barrier prior to deposition of the reactively sputtered hafnium dioxide film. A typical C-V plot of an HfO$_2$-SiO$_2$ MIS capacitor with a nitrided interface subjected to dc polarizing voltages is illustrated in Fig. 2. No shift in flat-band voltage (V_{FB}) was discernible for bias voltage less than ±20 V, in agreement with the simple model. A positive shift in flat-band voltage was observed for a positive bias on the gate electrode, and a negative flat-band shift was observed for negative bias. The direction of flat-band shift with polarity is consistent with the transfer of electrons by tunneling between the silicon and traps at the HfO$_2$-SiO$_2$ interface. The shift in flat-band

$$t_i = \frac{K_o}{K_i} t_o$$

$$V_C = E_o (X_o + \frac{K_o}{K_i} x_i)$$

INSULATOR	DIELECTRIC CONSTANT	INSULATOR FIELD WHEN SiO$_2$ FIELD $E_o \sim 7 \times 10^6$ V/CM	V_C-CHARGING VOLTAGE REQUIRED TO PRODUCE $E = 7 \times 10^6$ V/CM IN SiO$_2$	FILM THICKNESS
SiO$_2$	3.9	7×10^6 V/CM	—	20 Å
Si$_3$N$_4$	6.5	4.2×10^6 V/CM	43 V	1000 Å
Al$_2$O$_3$	9.5	3×10^6 V/CM	31 V	1000 Å
HfO$_2$	14	2×10^6 V/CM	21 V	1000 Å
SrTiO$_3$	80	3.5×10^5 V/CM	49 V	1000 Å

FIG. 1. Threshold voltage V_c for onset of charge transfer by tunneling from silicon into traps at SiO$_2$-insulator interface for various SiO$_2$-insulator combinations.
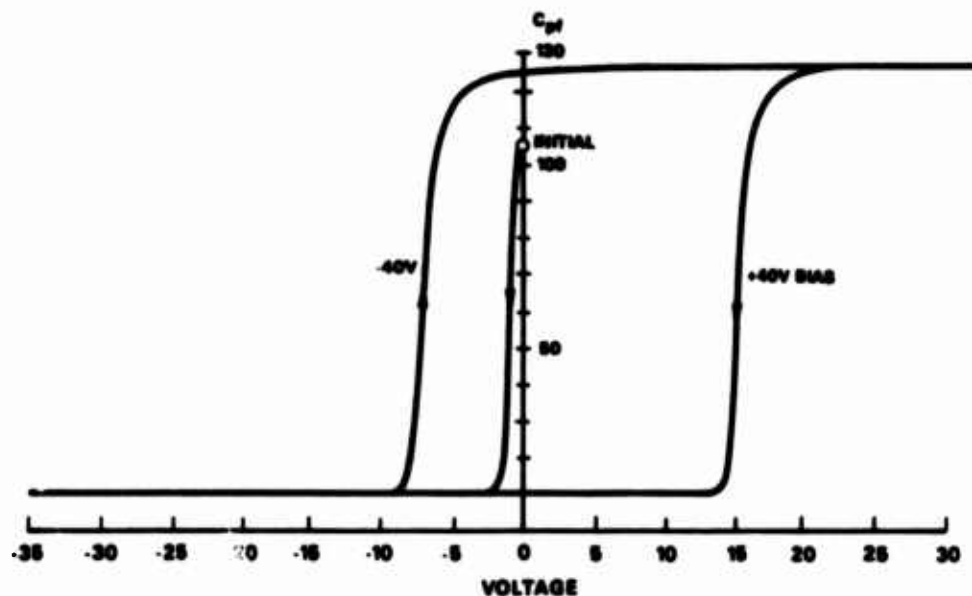
FIG. 2. *C-V* characteristics showing maximum flat-band shift for HfO₂-SiO₂ MIS structure with nitrided interface.

voltage is observed to be asymmetric with polarity and pulse duration. It is observed that positive values of flat-band shift are more readily obtained. Comparable shifts to more negative values require larger amplitudes and longer pulse durations. Typical device characteristics are the following: (i) 22-V threshold for onset of charge transfer; (ii) $\Delta V_{FB} = 22$ V for ±45-V gate bias; (iii) $\Delta V_{FB} = +6$ V for +50-V 1-μsec pulse; (iv) $\Delta V_{FB} = -9$ V for -100-V 100-μsec pulse; (v) Decay of Δ_{FB} at room temperature is 0.04 V/decade.

Devices made with SrTiO₃ directly on SiO₂ did not exhibit an appreciable flat-band shift with bias. Sputtering in Ar and N₂ did not result in generating many additional trap sites. A number of reactively sputtered nitrides and sulfides of selected transition metals were tested for enhancement of the charge trapping sites. The best results were obtained with nickel nitride as the trapping layer between the SiO₂ and SrTiO₃. Typical *C-V* characteristics for 20 Å SiO₂-50 Å nickel nitride-1000 Å strontium titanate MIS structures are shown in Fig. 3. Typical charge transfer and storage characteristics are the following: (i) 6-V threshold for the onset of charge transfer; (ii) $\Delta V_{FB} = 12$ V for ±15-V gate bias; (iii) $\Delta V_{FB} = +1$ V for +15-V 200-nsec pulse; (iv) $\Delta V_{FB} = -1$ V for -20-V 20-μsec pulse, (v) Devices charged
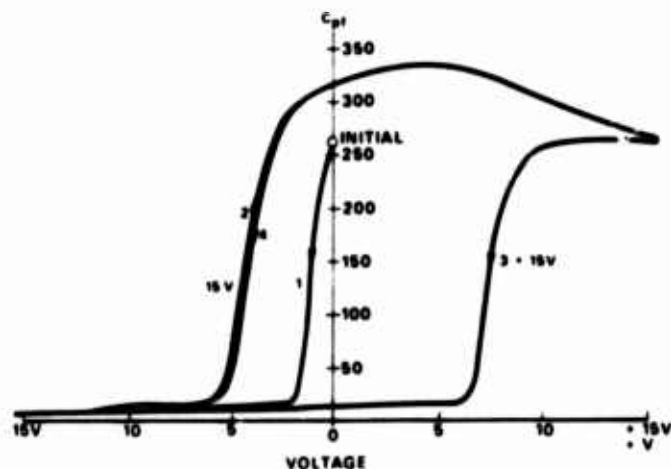
to a flat-band voltage of +5 V decayed to near zero in less than 24 h.

The direction of flat-band shift with bias voltage is consistent with tunneling of electrons rather than polarization phenomenon. The asymmetric charge switching characteristics for positive and negative pulses may be due in part to the asymmetric disposition of the trap levels with respect to the conduction and valence bands of the silicon. The longer pulse duration required to clear the electrons from the traps is probably due to the redistribution of charge away from the interface, which would require a longer time to clear the charge since conduction of charge would be required in addition to tunneling. The longer-term charge retention characteristics of the HfO₂ devices compared to those fabricated with SrTiO₃ are due to the superior insulating characteristics of hafnium oxide.

Laibowitz and Stiles[5] have reported on MIS structures where metal particles (30 Å) were introduced at the interface of a SiO₂-Al₂O₃ composite insulator structure. The flat-band voltage was controllable by tunneling of charge between the silicon and the metal particles. One of the drawbacks of the approach was the rapid decay of the stored charge. The reactively sputtered interface layer does not have this drawback, as demonstrated by the stability of the HfO₂ structures. This approach coupled with rf-sputtered high-dielectric-constant films holds promise for tailoring the charge transfer and storage characteristics of variable-threshold field effect transistors for nonvolatile memory applications with low-voltage switching of memory states.

The authors wish to acknowledge helpful discussions with D. H. Grantham and the technical assistance of F. Tarnowski.

[1] J. T. Wallmark and J. H. Scott, Jr., RCA Rev. (Radio Corp. Am.) 30, 335 (1970).
[2] D. Frohman-Bentchowski, Proc. IEEE 58, 1207 (1970).
[3] S. Nakanuma, T. Tsujide, R. Ishagari, K. Onada, T. Wada, and M. Nakagari, IEEE J. Solid-State Circuits SC-5, 203 (1970).
[4] T. Wada, K. Onada, H. Ishiguro, and S. Nakanuma, IEEE J. Solid-State Circuits SC-7, 375 (1972).
[5] R. B. Laibowitz and P. J. Stiles, Appl. Phys. Lett. 18, 267 (1971)

FIG. 3. *C-V* characteristics showing maximum flat-band shift for SrTiO₃-SiO₂ MIS structure with nickel nitride interface.